Study of Cations Effect on Microtubule Nucleation

By © Zahed Khatooni

A Thesis submitted to the School of Graduate Studies in partial fulfillment of the requirements for the degree of

Doctor of Philosophy in Pharmacy

School of Pharmacy

Memorial University of Newfoundland

January 2021

St. John's, Newfoundland and Labrador, Canada

Abstract

Microtubules (MT) are nanoscale-sized filaments actively involved in the segregation of chromosomes, the movement of vesicles, and the maintenance of eukaryotic cell morphology. The α, β-tubulin heterodimer is the building block of MTs, and γ-tubulin is the critical protein of the ring complex for MTs nucleation through direct interactions with the α, β-tubulin heterodimers. Molecular Dynamics (MD) simulation of GDP and GTP bound γ-tubulin monomer and dimer have been carried out in the presence of NaCl, $MgCl_2$, and $ZnCl_2$ as electrolytes.

In this study, the Mg^{+2}, Zn^{+2}, and Na^{+} effects on γ-tubulin conformation in GTP and GDP liganded and its unliganded monomer and dimer have been investigated. It has been found that both liganded and unliganded γ-tubulin monomer and dimer adapt curved and intermediate conformations relative to β-tubulin straight conformation.

The lattice model, which describes the role of lateral interactions in inducing the α, β-tubulin straightness, is an appropriate model for γ-tubulin dimers and monomers compared to the allosteric model.

Functional motions were observed for secondary structural segments of H2-H3 helices, M, and T5 loops, as well as H6-H7 segment of the N-terminal and the intermediate domains of the γ-tubulin. Also, H11 and H12 helices belonging to the C-terminal domain of γ-tubulin have been shown to contribute to the biological function.

At the GTP binding site, the existing Mg^{+2} compared to the Zn^{+2} and Na^{+} contribute to stronger electrostatic and L-J interactions between residues of the binding site and

nucleotides, either GTP or GDP. Residues of the GTP binding site that are interacting with oxygen atoms of α-γ phosphate, including Gln12, Cys13, Gly144, Thr145, and Gly146, exhibit stronger affinities for GTP and GDP compared to other residues in simulations. This MD result is consistent with wet-lab experiments in other organisms, such as yeast γ-tubulin.

The exact molecular position of the high-affinity metal-binding site, which plays a role in the function and stability of tubulins, was shown to be the oxygen atoms of β-γ phosphate of the GTP and GDP β phosphate in the binding site.

In conclusion: despite the same sequence and structural similarity, γ-tubulin adapts different conformations as compared to α or β tubulin. The lattice model appeared to better explain the straightness process compared to the allosteric model. The Mg^{+2} cations, due to their interactions, play a major role in γ-tubulin atomistic behavior compared to Na^{+} and Zn^{+2}.

Acknowledgments

I am very grateful to my supervisor Dr. Laleh Alisaraie for giving me the opportunity to pursue this research under her supervision. Without her guidance, encouragement, funding, as well as her support, I would not be able to complete the program and my thesis.

I would like to thank my supervisory committee, Dr. John Weber and Dr. Raymond A. Poirier, for their support.

I would like to thank the School of Pharmacy at Memorial University of Newfoundland.

I would like to thank the School of the Graduate Studies Memorial University of Newfoundland for its stipend support.

Table of Contents

CHAPTER 2 Impact of GTP and Ionic Conditions on Conformations of Unliganded and Liganded γ-Tubulin Monomer

CHAPTER 3 Effect of GTP, GDP and Ionic Conditions on Conformations of γ-Tubulin Dimer

List of Table

List of Figures

List of Abbreviations

ATP: Adenosine triphosphate

APC: adenomatous polyposis coli

ATB: Automated Topology Builder

Cdk: cyclid dependent kinases

CENP-E: Centromere protein E

dCOM: distance from center-of-mass

GDP: Guanosine diphosphate

GTP: Guanosine triphosphate

γTuSC: γ-tubulin small complex

γTuRC: γ-tubulin ring complex

ID: Intermediate domain

IF: Interface Interaction

μs: Microsecond

ms: Millisecond

TNF: Tumor necrosis factor

TGF: transforming growth factor

VEGF: Vascular endothelial growth factor

LJ: Lennard-Jones

LINCS: LINear Constraint Solver

MACF: microtubule actin cross-linking factor

MDB: methyl-CpG-binding domain

MTs: microtubules

MD: molecular dynamic

MOTC: microtubule organization center

mml: Milimol

NBD: nucleotide-binding domain

ns: nanosecond

nm: nanometer

NLS: nuclear localization signal

nM: nanomolar

NMR: nuclear magnetic resonance

OPLS-AA: optimized potentials for liquid simulations all-atom

PDB: Protein Data Bank

PCA: Principal Component Analysis

pm: picometer

SD: Steepest Descent

SASA: solvent accessible surface area

Ter: terminal

RB: retinoblastoma

RMSD: root mean square deviation

RMSF: root mean square fluctuation

vdW: van der Waals

CHAPTER 1

Introduction

1.1 Cancer

Cancer, malignant tumors, or neoplasms are defined as a group of diseases that enable cells to gain the unlimited ability to proliferate, grow in size, and spread throughout the human body. According to the World Health Organization (WHO), cancers were the second leading cause of death in 2015, killing more than 8 million patients, and an estimated 9.6 million deaths in 2018 worldwide.[1-3]

The hallmarks of the majority of cancers include persistent proliferation, resisting anti-growth factors, evading programmed death, promoting angiogenesis, and metastasis.[4, 5]

1.1.1 Origin and Initiation of Cancers

Cancer initiates and develops from a single cell in the body; the transformation of a normal into a cancerous cell is a multistep process that requires the alterations of several genes and their products.[6]

A somatic cell, through its genetic modifications, can be the origin of the malignancy.[7, 8] Genetic instability and mutation of somatic genes play an essential role in tumorigenesis.[9-12]

In addition to the mutation of genes, epigenetics and stem cells play significant roles in the initiation of cancer.[13] Both genetics and epigenetics regulate gene expression. The term epigenetics describes as heritable modifications that regulate the expression of genes without affecting the DNA sequences.[14]

Methylation of DNA, expression of non-coding regulatory RNA, and covalent modifications of histones are examples of the most well-understood epigenetic modifications. The main hallmarks of epigenetics include covalent modification of the cytosine base of DNA and deacetylation of the histones within nucleosomes, which downregulate gene expression.[15, 16]

The methylation of cytosine occurs mainly in the promoters of genes that contain CpG islands. The CpG islands are regions in the genome with high densities of cytosine and guanosine. The methylation at CpG islands silences genes, and if a downregulated gene is an anti-cancer one, it facilitates the growth of cancer cells. The methyl group transfer to cytosine bases is achieved by the activity of the DNA methyltransferase (DNMT) enzymes.[17, 18]

How methylation is chemically linked to gene silencing is related to the after-methylation process by which the methyl-CpG-binding domain recognizes and binds to the methylated DNA. The binding of the methyl-CpG-binding domain to DNA links methylated DNA to deacetylation of histones through the recruitment of the histone deacetylases.[19]

Stem cells are embryo cells; they are also found in mature tissues, which upon accumulation and alteration of their genes can cause cancer.[22,23]

Some features of stem cells are their resiliency to programmed cell death, self-renewal, which enables them to remain undifferentiated after multiple divisions, and, importantly, their ability to differentiate to various cell types.[20, 21]

1.1.2 Classification of Cancers

The National Institute of Health (NIH) estimates that about 200 different types of cancer are diagnosed in humans. A classification method for cancer is based on the starting point or the tissue from which cancer originated.[22] There are 6 types of cancers, including carcinoma with the epithelial origin, sarcoma refers to supportive and connective tissue cancer, myeloma arising from plasma cells, leukemia is a bone marrow cancer, lymphoma which is cancer of the glands of the lymphatic system, and mixed type with mixed originating cells.[22]

1.1.3 Apoptosis and Angiogenesis of Cancer Cells

Apoptosis refers to programmed or regulated cell death, which contributes to cell development as well. Apoptosis is not just a cell death; instead, it involves recruiting macrophages to remove or eat the apoptotic cells.[23]

Apoptosis or programmed cell death is a normal process during development because most overproduced cells or end-of-life cells have to be removed from the body. In addition, genetically damaged cells or older cells are a target of apoptosis as well.[24] Apoptosis of damaged cells, e.g., those with DNA damage, is triggered through P53 activity or by tumor necrosis factor (TNF) or death receptors expression.[25] However, cancer cells avoid apoptosis when the mutated P53 is unable to induce it, or the overexpression of the BCL-2 (Anti-apoptotic BCL-2) can help cancer cells to fight apoptosis.[26]

1.1.4 Cell Cycle

The cell cycle controls the proliferation of normal and cancerous cells; divides into interphase and meiosis/mitosis. During interphase, cell growth and DNA replication are major events, and while mitosis, the duplicated genome is isolated and directed toward two opposite cell poles. Genome isolation requires the assistance of proteins, which microtubules are the major ones. Mitosis is divided into four closely related stages of prophase, metaphase, anaphase, and telophases. **(Figure 1.1)**

During the prophase, the replicated chromosomes of the S phase are condensed. The chromosomes at this stage are composed of two genetically identical sister chromatids connected by their centromere. The condensation process is developed by aiding cohesin and condensing multiprotein complexes. In prophase, two centrosomes move toward opposite poles of the cell, generating the mitotic spindles to nucleate microtubules (MTs).[27] In metaphase, the nucleus membrane gradually disappears and causes the MTs to connect to the duplicated chromosomes directly. The process of nuclear membrane fragmentation is achieved through the phosphorylation of lamin proteins of the lamina. Lamina is a network of intermediate filaments that generate the structural scaffolding for the nucleus membrane. The main proteins of the nuclear lamina are lamin and prelamin.[28] **(Figure 1.1)**

The mitotic spindles are composed of three groups, astral, interpolar, and kinetochore microtubules (MTs). The astral MTs advance their plus end toward the cortex, interpolar MTs originate from one pole and end with the opposite pole, and kinetochore MTs are attached to chromosomes via kinetochore sites.

During anaphase, kinetochore MTs segregate the sister chromatids by pulling chromosomes against the microtubule organization center (MOTC). The highly dynamic MTs translate their growth and shrinking to the pulling forces to separate the chromosomes at their chromatids and move them toward the two opposite poles of the dividing cells. [29] (**Figure 1.1**)

The biological activity of MTs within cells depends on the regulatory proteins that interact and bind with them. Kinesin and dynein are examples of motor proteins that mediate the transport of vesicles alongside MTs. Other proteins, such as; adenomatous polyposis coli (APC), Microtubule actin cross-linking factor (MACF), and metazoan proteins, cross-link the MTs to the kinetochore.[30-32] After chromosome segregation, the last step of mitosis is the telophase. The isolated chromosomes decondense again, and the cytoplasm separates between two emerging cells while the cells undergo cytokinesis.[30] (**Figure 1.1**)

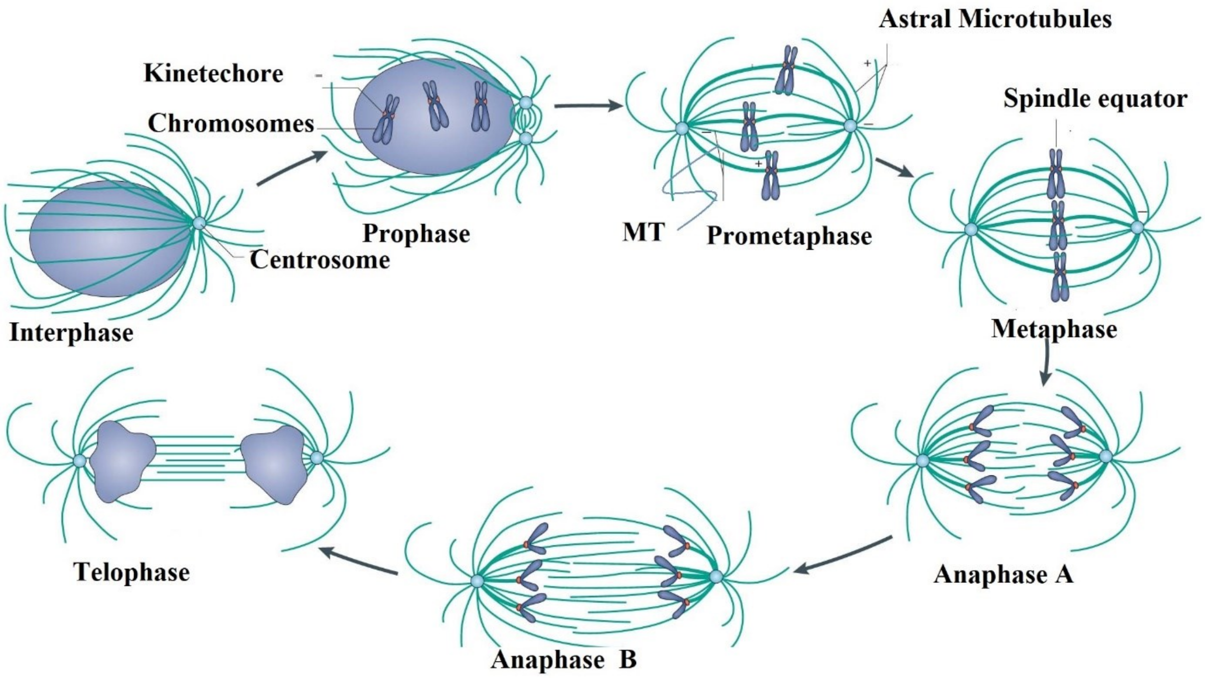

Figure 1.1: The schematic representation of the cell cycle. Four phases of mitosis are shown [33]. The figure is adapted with permission. Walczak et al., Nat Rev Mol Cell Biol 2010.

During the cell cycle, several checkpoints are available to prevent cell proliferation with abnormal size, broken genome, or in the presence of growth-restricting factors.[34]

However, during malignancy, cancer cells pass all restriction points of the cell cycle and undergo uncontrolled reproduction.

1.2 Cytoskeleton

The cytoskeleton is essential for cell survival; it prevents cells from deforming their morphology, maintains vesicle transport inside the cytosol, and contributes to cell movement.[35] The cytoskeleton physically and physiologically connects cells' cytoplasm to the extracellular matrix; it also organizes organelles within the cytoplasm. The three major proteins of the cytoskeleton are actin, intermediate filament (IF), and MTs.[36]

Actin, IF, and MTs, generate a strong network of proteins that are controlled by related regulatory proteins. These regulatory proteins include; nucleation-promoting that initiates generation of filaments, depolymerizing factors, capping proteins to terminate filament formation, as well as crosslinkers, and stabilizing proteins. The cytoskeleton constitutes ~ 25% of cytosol weight and around 35% of total cell proteins.[29, 36, 37] Actin, MTs, and IF filaments are distinguishable from each other, as they have different diameters, and their building blocks are not the same. The actin or microfilament is twisted two-strands with 8 nm to 9 nm in diameter. The actin subunits and α, β-tubulin heterodimer are building blocks of microfilaments and MTs. The IF differs from MTs and microfilaments in that it has no repetitive monomers in its structure. An example of IF is lamina; it generates the network around the genetic material on the nucleus membrane.[29, 37]

1.2.1 Microtubule and Its Functions

MTs are biopolymers that play an essential role in supporting cell structure and morphology.[38] MTs are ~ 13 protofilaments hollow tubes with 25 nm in diameter. Their function is important for the survival of the organisms and the maintenance of their biological shape.[39] MTs play a role in binding to chromosomes during metaphase and anaphase of mitosis and miosis, and in moving genetic material between dividing cells.[40, 41]

MTs originate from the centrosome or MTOC during interphase; in eukaryotic cells, there is only one MTOC. However, epithelial and plant cells contain several MTOCs. The

MOTC consists of the perpendicular arrangement of two centrioles. In addition to being highly dynamics MTs in replicating cells, MTs are also active in cilia and flagella, which are involved in cell motility. The two ends of the MT are called the plus and minus ends, which are in opposite directions to each other.[42] The plus and minus ends are associated with different regulatory proteins. MT is a polarized molecule as the α, β-tubulin heterodimer is polarized, its β-subunit is exposed at the plus end and the α subunit at the minus end.[43] The Biological function and dynamic behavior of MTs are related to the associated proteins that interact and bind to them.[29] MAP or MT associated proteins maintain their stabilization or destabilization. For instance, proteins such as adenomatous polyposis coli (APC), cytoplasmic linker associated proteins (CLASP), MAP1, MAP2, and Tau stabilize MTs. On the other hand, the katanin and kinesins gene family (KIF) induce depolymerization of MTs.[30, 44]

MAP is found at the wall and mostly at the plus end of the MTs; the plus end is more dynamic because it is exposed to interactions with MAP or kinetochore. However, the minus end is capped inside the MTOC, and it is in interaction with γ-tubulin, which is the main nucleator of MTs.[29]

The nanometer to micrometer movement of vesicles, organelles, and proteins inside the cytosol requires the MTs and their associated motor proteins such as kinesin and dynein.[45] Kinesin is a tetrameric protein with a molecular weight of 380000 composed of two heavy chains that bind ATP and MTs and two light chains attached to the membrane of the vesicle in which both heavy and light chains are connected through the coiled-coil helix.[46, 47] Binding of the light chain to the cytosolic cargo needs the mediating receptor, and movement of the particles needs the attachment of heavy chains of the kinesin to the wall of MTs and ATP hydrolysis, which power movement from the minus end toward the plus end.[45, 48, 49]

MT is polymerized by the tail to the head binding of the globular α, β-tubulin heterodimer with a molecular weight of ~ 55000, in which α-tubulin and β-tubulins are held together by non-covalent interactions. This tail to the head or longitudinal interactions generates protofilament if repeated for hundreds or thousands. Around 13 protofilaments are oriented laterally, side by side, to generate functionally active MTs tube.[50] MTs in neurons or nematodes have between 11 to 15 protofilaments instead of 13, doublet MTs in cilia and flagella, and triplet MTs in the basal body are discovered as well. The α, β-tubulin heterodimers have several isomers in different organisms and humans; they have around 45% sequence similarity.[51]

GTP binds α, β-tubulin heterodimer at its binding sites in both α-tubulin and β-tubulin. The GTP binding site can either be exchangeable or non-exchangeable for its bounded GTP; for instance, β-tubulin has an exchangeable site because its bounded GTP is hydrolyzed to GDP and Pi, while MT is polymerized.[52] However, the GTP binding site of α-subunit is non-exchangeable, as GTP remains intact without converting to GDP. The GTP-binding site of α-tubulin is located at the interface of α and β-tubulin.[53, 54]

1.2.2 Dynamic Instability of Microtubules

MTs are not static polymer inside the cytosol of eukaryotic cells. They are found with a high rate of changing from polymerization state or growth to depolymerization or catastrophe/shrinking.[55] This feature of MTs is defined as dynamic instability in which, after binding the GTP-bound α, β-tubulin to plus end, the polymerization continues until the catastrophe phase, through which the depolymerization rate is greater than the polymerization. After the catastrophe, the rescue phase will start when the rate of polymerization proceeds to disassembly.

The concentration of the GTP-bound α, β-tubulin heterodimer, and temperature contribute to the assembly and disassembly of the MTs as decreasing the temperature to 4° C induces depolymerization.[55, 56]

All MTs are not highly dynamic as the MTs of cilia and flagella are stable and not involved in cell proliferation. Availability of free GTP-bound α, β-tubulin heterodimers drives the formation of MTs at the plus end. Instantly after adding the GTP-tubulin to the plus end of the MTs, the hydrolysis of GTP to GDP starts. The dynamics of MTs changes from growth to catastrophe by releasing the GDP-dimers from the plus end of the MTs.[57] (**Figure 1.2**)

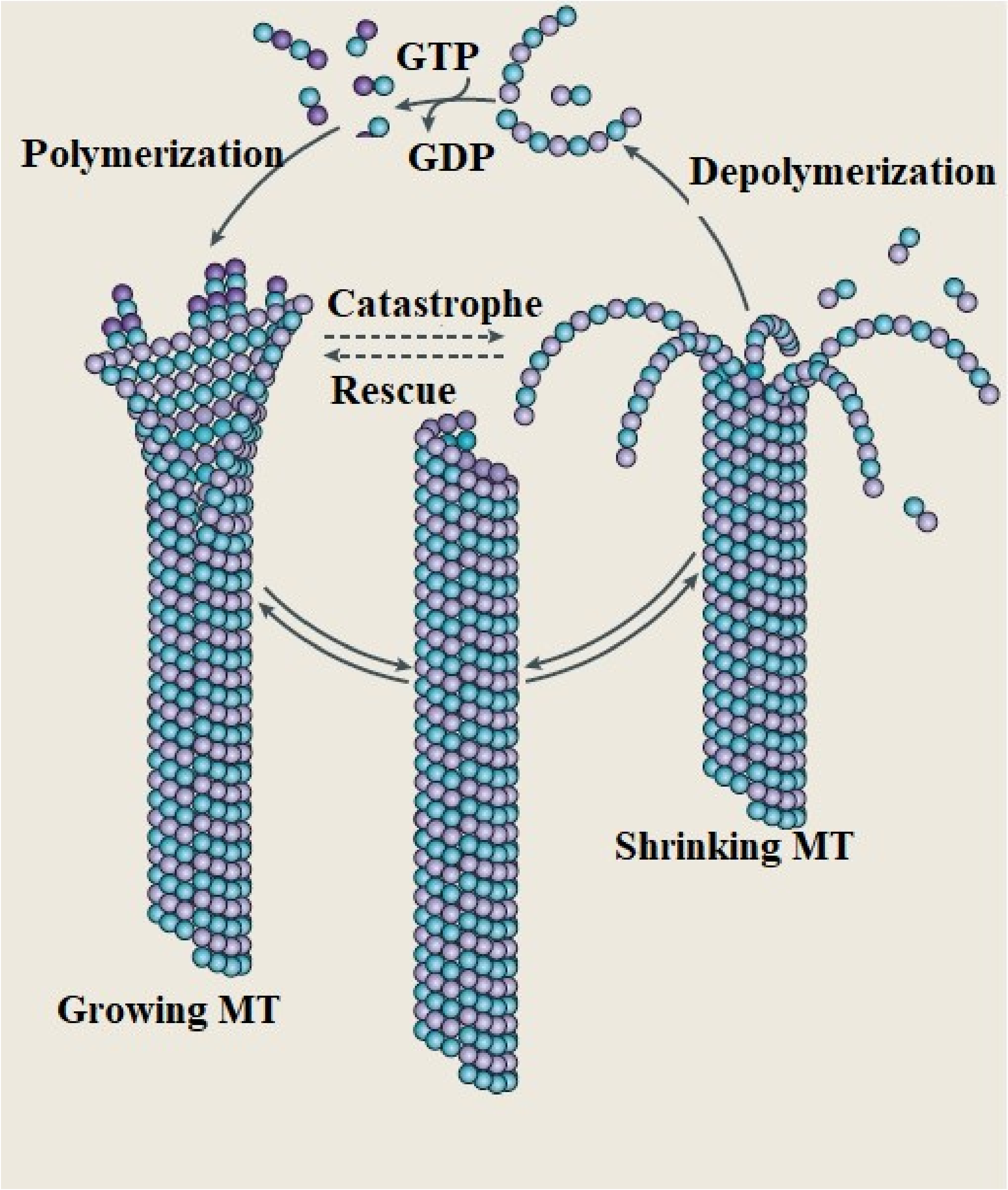

Figure 1.2: Dynamic instability of MTs. The hydrolysis of GTP to GDP at the plus end of MTs initiates the shrinking and release of the GDP-tubulin. The polymerization happened when the GTP-tubulin adds to the plus end of the MTs.[58] This figure is adapted with permission.

The conformation of α, β-tubulin heterodimer adapts a curved and straight state. The straight conformation is observed in MT lattice. The α, β-tubulin heterodimer crystal structure at 3.5 Å resolution with a GDP at β-tubulin, GTP at α-tubulin, and taxol have shown a straight conformation.[59, 60] Conde et al., Nature Reviews Neuroscience 2009.

The monomer of α or β-tubulin generates from the contribution of three domains of the N-terminal binding domain (NBD) (1-242), intermediate domain (ID) (243-381), and the C-terminal domain (382-445). The NBD is composed of six helices (H1-H6), six parallel beta-strands (S1-S6), and six loops, which are recognized as T1 -T6 loop. H8 to H10 helices, S7 to S10 strands form the ID, which is connected to NBD through the H7 helix. The C-terminal domain has two large helices of H11 and H12 that cross over both NBD and ID.[61] Considering three domains of α, β-tubulin heterodimer, it has been discovered that the intermediate domain heavily rearranges during straight to curved conversion. There is a controversy about the role of nucleotide (GTP) in the straightness or curvature of α, β-tubulin heterodimer. Two models discuss the GTP role and the protofilament lateral interactions as the main driving forces behind the transition from curved to straight conformations.[62]. **(Figure 1.3 & 1.4)**

According to the lattice model[63], the main driving force behind the straightness of α, β-tubulin is the lateral interactions of α-α and β-β tubulins within the protofilaments. Based on the lattice model, the free α, β-tubulin heterodimer adapts a curved conformation that is incompatible with the lattice of the MT, and a curved to straight rearrangement occurs upon its binding to the wall of the MT.[64] In contrast, the allosteric model[43] focuses on the impact of the GTP to induce straightness upon its binding to the binding site of α, β-tubulin heterodimers.[65] However, the research is lacking about γ-tubulin and whether the electrolytes impact its conformational changes or not.

The α, β tubulin heterodimer was the main target of studies about the curvature-straightness of MTs, γ-tubulin function, and its crystal conformations were gradually revealed afterward.[66] The majority of all studies about γ-tubulin are wet-lab experiments investigating various γ-tubulin aspects such as its nucleation ability, γ-complexes, its interactions with other proteins inside the MTOC or ring complex, its expression, and so on. MTs nucleation role of γ-tubulin contributes to a considerable number of studies about this protein. [67-74] The straightness or curvature of γ-tubulin crystal in the presence of the GTP analog was evaluated by Aldaz et al. through RMSD and alignment approaches. Dominant conformation was considered as curved by its crystal superimposition on curved and straight β-tubulins. [62] At their study, the 1SA0 was set as referenced curved, and for referenced straight, the 1JFF was used.

Chain A of 3CB2 has all critical residues that play a role in curved - straight conformational changes, and its missing residues are belonging to its loops. [63] Also, as in the dimer section, the dimer of γ-tubulin has to be studied; therefore, one reference γ-tubulin crystal, ‘3CB2’, which also is a dimer, was selected. [63] Two other crystal conformations for γ-tubulin are monomers, and 1Z5V is crystallized in association with GTPgammaS with several missing atoms and residues.[62] There are two conformations for the complete yeast small complex, among which 5FLZ was defined as an active state. In 5FLZ, two complete γ-monomers are in lateral interactions, and also it contains full longitudinal interactions with SPC97/98 that make this complex a suitable model. Another model (5FM1) is a low activity state. [73, 75]

The lattice and allosteric postulations on α, β tubulin conformations are subjects of several studies. In 2008 Rice et al. employed different approaches such as allocolchicine binding or SAXS analysis to evaluate the allosteric role of the GTP in inducing straight conformation, and in all examinations, the GTP was not an effective mediator causes straightness. They were mainly in favor of the lattice model. [63]

In another study by Peng et al., the free energy of the unassembled GDP-bounded α, β tubulin was -1 kJ/mol in favor of the curved conformation. Its binding to MT protofilament was in favor of straight conformation, consistent with the lattice model's prediction.[60]

However, in another study by Wang et al., the GTP interactions trigger the conformational rearrangements that cause adapting the straight conformation. In this study, instead of the GTP, non-hydrolyzable analog, GMPCPP was used. [65]

The reasons for using 1SA0 and 1JFF for reference conformations of curved and straight tubulins are as follows: apart from their 3.5 Å resolution, both proteins are almost complete, especially their segments that contribute to conversion from the straight to curved. [61] The straight conformation has one molecule of taxol, which restricts destabilization of MTs and hence adaptation of the curved state. GTP and GDP are bounded to non-exchangeable and exchangeable binding sites in the α and β subunits. The curved conformation is co-crystallized with colchicine, which destabilizes the MTs, and therefore adapting the curved conformation is most probable. There are also two GTPs in the chain A and C, two GDPs in the chain B and D were bound to the tetramer and made it a unique conformation.[76]

There are numerous tubulin structures deposited in the Protein Data Bank; however, not all of them are as 1SA0, and 1JFF perfectly adapted the curved and straight conformations. These two curved and straight conformations are also referenced of curved and straight conformations for several other studies.[60, 63, 77-79]

The source of domain classification came from the very pioneer work that crystalized the structure of the α, β-tubulin.[61]

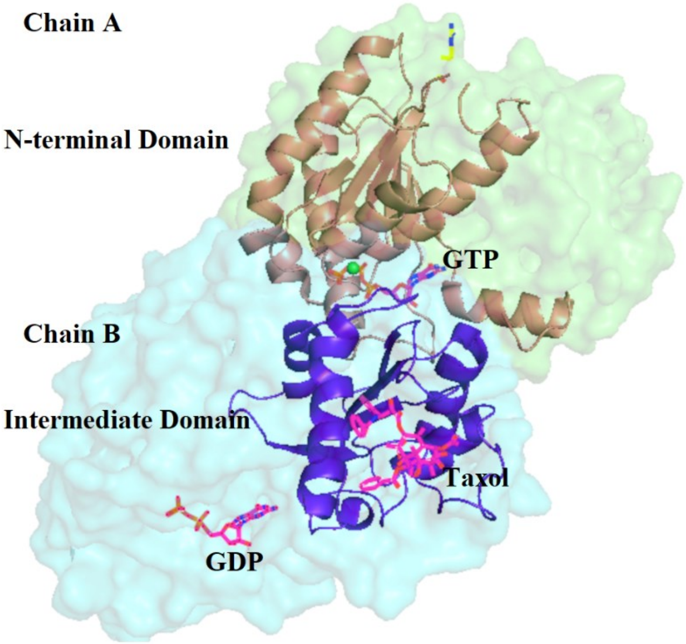

Figure 1.3: α, β tubulin heterodimer (1JFF) with highlighted N-terminal and intermediate domains. N-terminal nucleotide-binding domain in chain A is depicted in brown. The intermediate domain of chain B is colored in blue. The whole α, β tubulin heterodimer is in light cyan surface representation.

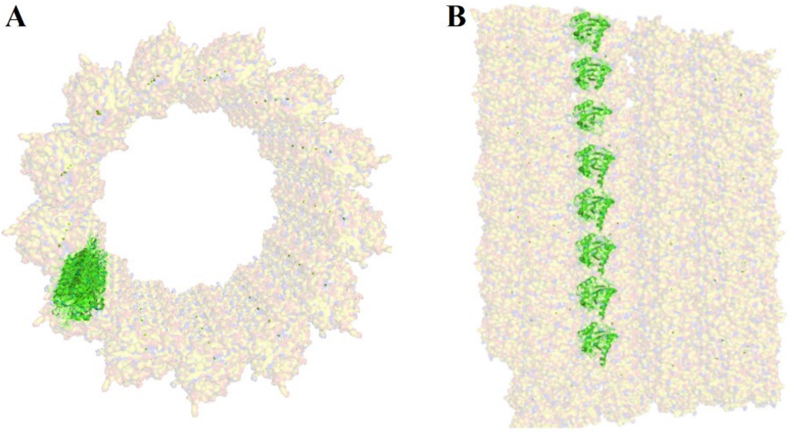

Figure 1.4: The structure of microtubule (6O2T) with the highlighted intermediate domain of α, β tubulin heterodimer. (**A**) the horizontal view of MT in which the intermediate domains of one protofilament is colored in green. (**B**) The vertical view of MT and the intermediate domain in green.

1.3 Computational Simulation

1.3.1 Molecular Dynamics Simulation

Molecular Dynamics (MD) simulation is a computational method to study the biological and non-biological properties of desired systems contain several thousand atoms. Biological systems could be various types of molecules such as water, protein, DNA, RNA, or ATP, and GTP. The properties of interest are diversely related to the MD systems, such as temperature or pressure. In biological systems, the study of conformational changes or the interactions between sets of molecules, e.g., DNA, protein, and a chemical molecule or ligand, are of interest.[80, 81]

Of major classes of computational simulations are Molecular Dynamics (MD) and Monte Carlo (MC) simulations. Properties that are impossible to be measured or studied in a wet lab can be evaluated by MD simulation, for instance, the position of each interacting water molecule in a bulk system of protein surrounded by water molecules. One difference between MD and MC simulations is the study of dynamic properties of systems that can be measured and visualized with MD techniques or the time-dependent response of systems to any intervention, such as changes in temperature or type of solvent.[81]

Using a theory for predicting the properties of systems before the invention of computational methods such as MD simulation was a common approach. However, the precision of theory was always in doubt because these theories are using few approximations. For example, to describe the transport properties of dilute gases, the Boltzmann equation was approximated. The computer simulation enables researchers to evaluate the theory's precision and to compare the MD results of a model with available data provided by experiments to predict the model's accuracy. Computer simulation is similar to an experiment designed for evaluating the accuracy of the theory. Nowadays, almost all theories will be tested by computer simulation before being applied in real conditions.[80, 81] During the MD simulation of a system with a large number of atoms with known X, Y, Z coordinates, e.g., from NMR or crystallography, step by step evaluation/solution of the classical equation of motion, Newton’s equation of motion, is required. The advantage of using the computational method for a system with more than two atoms is that an analytical solution of the equation of motion by hand is not possible.

For solving the equation of motion, one should be able to calculate the force acting on atoms. The force can be obtained by evaluating the potential energy of the system.[81]

MD simulation can handle a large number of atoms in the order of 10^5 or even larger. The time scale of simulations these days reaches μs and ms. The system of interest can also be rare gases or any kind of polymers, either biological or not.

For interaction evaluation, the molecular models such as the L-J or Coulomb models are employed. MD simulation is carried out inside a simulation box. Using smaller boxes significantly saves the CPU-time dedicated to simulation and reduces the required completion time. The main boxes, including cubic, rhombic dodecahedron, rhombic dodecahedron, or truncated octahedron.[81]

To avoid the boundary effect of the simulation box and to reduce the finite box size, there is no real boundary. Otherwise, a significant proportion of atoms interact with the simulation wall leading to the surface effect that those atoms do not contribute to the system's physical properties. The number of atoms that will be involved in the surface effect is $N^{-1/3}$ for the N atoms available in the simulation box.[80] In contrast with this, the simulation box is surrounded by an infinite number of its replica in all directions, the periodic boundary condition (PBC). Only one simulation box, which is the main one, is explicitly considered, and the other boxes are only images of the main simulation box. For instance, if a water molecule moves from the main box to another imaginary box, immediately a single water molecule from the adjacent imaginary box will enter the main simulation box.[80]

Conventional MD simulation is a force field (FF) simulation; FF is generally described as mathematical equations and their belonging parameters. The equations in FF relate the potential energy of the desired system to the coordinates of the atoms. The parameters are obtained from quantum mechanical, *ab-intio* calculations or by fitting to collected data from neutron spectroscopy, NMR, and X-ray experiments.[80-82]

There are several FFs that are different from each other due to different parameterization strategies and the complexity of their mathematical expressions. However, FFs should be able to reproduce the properties of interest. The CHARMM[83], Coarse-Grained Force Fields[84], GROMOS[85], and OPLSAA[86] are the names of some of the most applied and common FFs in MD simulations.

FF is used to evaluates the contribution of bonded and non-bonded intramolecular interactions into the potential energy of the system. The bonded terms are related to the contribution of bonds, angles, torsions, and impropers. Non- bonded contributions include L-J and electrostatic interactions.[81]

Most force fields contain parameters for different polar and non-polar solvents, common organic molecules, amino acids, carbohydrates, nucleic acids and are employed for calculation of the atomistic interaction of those molecules. However, if a FF is not parametrized for a specific molecule like RNA, it cannot be used for simulation of RNA; for instance, AMBER force fields are a proper choice for simulation of RNA. AMBER provides satisfactory descriptions of the structural and thermodynamic properties of both RNA and DNA. This FF is parametrized for RNA, DNA, and also proteins. GROMOS

56a_Carbo is a proper choice for the simulation of molecules, which contain beta-D-glucose.[87]

It should be mentioned that FFs are not for all classes of systems and compounds. For instance, water molecules with MD simulation have their own potentials, which are not based on the employed FF. For water, there are several models, such as SPCE, SPC, TIP3P, TIP4P, TIP5P. The SPC/E is a three-site water model that has three interaction points of two H and one O, similar to real water. The SPC model is similar to water as its partial charge for O and H is - 0.84 and + 0.42.[87]

The acting force ($\mathbf{F}_i$) on an atom is the negative derivative of potential energy with respect to its coordinates, $\mathbf{r}_i$.

$$\mathbf{F}_i = -\frac{\partial V}{\partial r_i} \qquad \textbf{(Equation 1.1)}$$

The potential energy is divided into bonded and non-bonded terms.[88]

$$\mathbf{V} = (\mathbf{r}_1, \mathbf{r}_2, \mathbf{r}_3, \ldots\ldots \mathbf{r}_N). \qquad \mathbf{V} = \mathbf{V}^{\text{bond}} + \mathbf{V}^{\text{non-bond}} \qquad \textbf{(Equation 1.2)}$$

Non-bonded interactions between atoms that are not covalently connected are modeled by Lennard-Jones and Coulombs.

Bonded interactions are composed of several terms:

$$\mathbf{V}_{\text{bon}} = V^{\text{bond}} + V^{\text{angle}} + V^{\text{har}} + V^{\text{trig}}. \qquad V_{\text{non-bon}} = V^{\text{LJ}} + V^{\text{VdW}}. \qquad \textbf{(Equation 1.3)}$$

Covalent bond interactions

The potential energy due to covalent bond interactions is calculated over the sum of all N_b bonds.[89]

$$V^{bond} = \sum_{n=1}^{Nb} \frac{1}{4} k_{bn} [b_n^2 - b_{0n}^2]^2. \qquad \textbf{(Equation 1.4)}$$

k_b and b_0 are bond constant, and bond length at equilibrium and N represents the number of bonds. The value of k_b and b_0 can be obtained through experimental spectroscopic and X-ray crystallography, respectively. b_n (bond length) is a variable that during simulation is changing and can have different values. **(Figure 1.5)**

The value of bond length (b_n) between two atoms of i and j with positions $\mathbf{r}_i$ and $\mathbf{r}_j$ for n^{th} bond between them is evaluated by using. (**Equation 1.5** & **Figure 1.5**)

$$b_n = r_{ij} = \sqrt{\boldsymbol{r}_{ij} \cdot \boldsymbol{r}_{ij}} \text{ and } \mathbf{r}_{ij} = \mathbf{r}_i - \mathbf{r}_j. \qquad \textbf{(Equation 1.5)}$$

Covalent Bond-Angle Interactions

The bond-angle potential energy calculated over the sum of all N_θ angles, N: number of all angles. θ_n refers to the value of the angle between atoms i, j, and k.[89]

$$V^{angle} = \sum_{n=1}^{N\theta} \frac{1}{4} k_{\theta n} [Cos\theta_n - Cos\theta_{0n}]^2 \qquad \textbf{(Equation 1.6)}$$

The values of θ_0 and k_θ are originated from spectroscopic and X-ray crystallography.

Improper Dihedral-Angle Interactions

Out of a plane, harmonic (har) or improper potential is used for potential energy of four contributing atoms (i, j, k, and l).

(Figure 1.5)

$$\mathrm{V}^{\mathrm{har}} = \sum_{n=1}^{N\xi} \frac{1}{2} K_{\xi n} \left[\xi_n - \xi_{n0}\right]^2$$ **(Equation 1.7)**

ξ is the value of the dihedral angle defined by i, j, k, l atoms, which can be calculated from:

$$\xi_n = \mathrm{sign}\xi\, arccos\left(\frac{\boldsymbol{r_{mj}} \cdot \boldsymbol{r_{qk}}}{r_{mj} r_{qk}}\right).$$ **(Equation 1.8)**

Torsional Dihedral-Angle Interactions (trig)

The potential energy of the torsional angle is calculated over the sum of all Nφ:

$$\mathrm{V}^{\mathrm{trig}} = \sum_{n=1}^{N_\varphi} K_{n\varphi}\left[1 + \cos(\delta_n)\cos(m_n \varphi_n)\right]$$ **(Equation 1.9)**

For the torsional dihedral angle, m_n is its multiplicity and δ_n (phase shift) is between 0 and π, for atoms of i, j, k, l, the φ is their dihedral angle.[89]

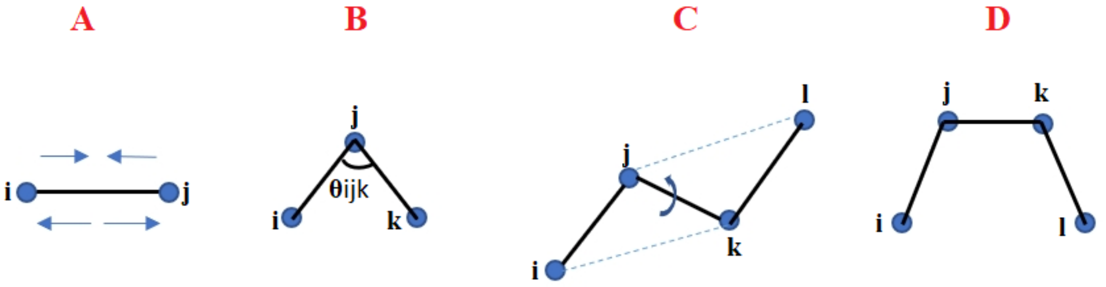

Figure 1.5: The schematic representation of covalent bond interactions. (**A**) Bond stretching between i and j atoms. (**B**) Angle bending between three atoms of i, j, and k. (**C**) The proper dihedral angle between the four atoms of i, j, k, and l. (**D**) The improper dihedral angle between atoms of i, j, k, and l.

Non-bonded interactions

Non-bonded interactions are calculated over the sum of all non-covalently bonded pairs of atoms.

van der Waals Interactions

Non-bonded van der Waals potential is evaluated as the sum of all non-bonded interacting atoms using the Lennard-Jones 12-6 interaction function.[89]

$$\mathbf{V}^{\mathrm{vdW}} = \sum_{pairs_{ij}} \left(\frac{\boldsymbol{C12}_{ij}}{r^{12}} - \frac{\boldsymbol{C6}_{ij}}{r^{6}}\right) \qquad \textbf{(Equation 1.10)}$$

C12 and C6 are related to the type of atom.

$$\mathrm{C12}_{\mathrm{ij}} = \sqrt{C12_{ij}.C12_{jj}} \text{ and } \mathrm{C6}_{\mathrm{ij}} = \sqrt{C6_{ii}.C6_{jj}} \qquad \textbf{(Equation 1.11)}$$

Electrostatic Interactions

By applying equation 1.12, "Coulomb equation," the electrostatic interaction can be evaluated.

$$\mathbf{V}^{\mathrm{c}} = \sum_{\mathrm{pairs}_{\mathrm{i,j}}} \frac{q_i q_j}{4\pi\varepsilon_0\varepsilon_1 r_{ij}} \qquad \textbf{(Equation 1.12)}$$

ε_1 and ε_0 are relative permittivity of the medium, in which the atoms are embedded, and dielectric permittivity of vacuum, respectively. q is the partial charge for atoms, and c is used for Coulomb. The actual distance between two atoms of i and j with the position of **r**i and **r**j is *r*ij.[89]

To start MD simulation, the first step is assigning the initial position and velocity to all atoms of the system of interest. The atoms should not be too close to each other to prevent any overlap and atomic clashes among them. This can be done by putting atoms at the cubic lattice by which, for available atoms, the random position will be assigned, or in many cases, the initial positions of atoms are from the crystallography or NMR data. NMR and crystallography contain the initial position of atoms in X, Y, Z coordinates. However, some of the atoms and their bond lengths or angles from crystallography or NMR studies are found close or far from equilibrated values. Therefore, energy minimization (EM) is a necessary step before the production run.[81]

The purpose of energy minimization (EM) or geometry optimization is to start the simulation with a stable structure with low potential energy.

By carrying out the EM, one makes sure that there are no atomic clashes and that the system is at low potential energy surface either at a local or global minima. This can be achieved by utilizing one of EM algorithms to find the minima at the energy surface of the system.

EM is a stepwise numerical process in which the structure becomes closer to its minimum energy surface at each step by changing the bond length and dihedral angles. If the new conformer has larger potential energy, the movement will be rejected, and again from the previous conformation, the EM will be continued until finding an energy minima.[87]

At the local minima or local maxima, the first derivative of potential energy with respect to the coordinates of atoms is zero. However, the second derivative at any minimum is positive, and at any maximum, it is negative.[81]

To simplify the above-mentioned example, if one considers the potential energy surface as a function of the X coordinate, at any stationary point, the result of the first derivative of the potential energy with respect to the X coordinate is zero.[90]

$$\frac{dV(x)}{dx} = 0$$ **(Equation 1.13)**

However, the second derivative with respect to X at any minimum with low potential energy will be greater than 0 (Eq 1.15).

$$\frac{d^2V(x)}{dx} > 0$$ **(Equation 1.14)**

In MD simulation, there are 3N coordinates; the second derivates with respect to the coordinates of all atoms create a 3N*3N matrix, which is called Hessian Matrix.[82] Newton-Raphson method of carrying out EM evaluating the first and second derivatives. In the Steepest Descent (SD) method (algorithm for EM), the second derivative is not evaluated; therefore, this method is faster. In the SD method, the geometry of the molecule modifies by changing the value of angles, torsions, and bond length step-by-step in order to reach the local minima.[90]

The calculation of the force acting on atoms is the most time-consuming step during MD. In a system with N atoms, if just an interaction of one atom with its closest atom is considered, the N(N-1)/2 pair interactions should be evaluated.

After evaluating force, as discussed earlier, Newton's equation of motion will be integrated at each step of the MD simulation.[80]

There are several algorithms in conventional MD simulations for integrating the equation of motion. The integrator predicts the trajectory or new positions of the atoms at each step. The integrator should be fast enough because, with MD simulations, the speed of the calculations is crucial. Any equation with a large number of parameters takes more time compared to an equation that has a smaller number of parameters. Another feature of the equation of motion is accuracy, and the algorithm should be able to conserve energy with the least energy drift.

One popular integrator is Leap-Frog algorithm.

$$r(t+\Delta t) = 2r(t) - r(t-\Delta t) + \frac{1}{m}\boldsymbol{F}(t)\Delta t^2 + O(\Delta t^4) \qquad \textbf{(Equation 1.15)}$$

The next position $r(t+\Delta t)$ is related to Δt or time step, m or mass of the atoms, and also the acting force according to equation 1-15.[80]

The value of Δt or time step is affecting the accuracy of the MD calculation. It is better to have a small Δt to obtain accurate integration of the equation of motion, but the time of simulation never ends for a small time step. The problem with large Δt is that the resultant simulation may be unstable with the large energy drift.[82]

1.3.2 Molecular Docking

Molecular docking is used to find the mode(s) of binding or interactions between X and Y. X, in most cases, is a small molecule, which is called a ligand, and Y is the known cavity or binding site on the surface of the known protein.[91-93] The ligand can also be a small peptide[94], and peptide-RNA/DNA docking is also possible.[95]

Molecular docking is a useful technique in finding a lead compound in computational drug design.[96, 97] Two steps in molecular docking are essential; search algorithm and scoring functions. The first step is to search the conformational and configurational space of the ligand-protein complex. For example, if a docking tool is flexible for ligand, it has numerous conformations by considering torsional (dihedral), translational, and rotational degrees of freedom. The second step is ranking the modes of binding or solutions, according to their binding energy, which they have with the target. The accuracy and speed of conformational space searching and prediction of correct binding energy are fundamental steps in molecular docking.[98]

Docking tools employ different algorithms for searching the conformational space and also evaluation of the binding energies. Most of the available docking tools are searching the configurational space of a ligand by modifying its angles, bond lengths, and torsions, which enables them to find the conformation of the ligand that interacts with high affinity to the binding site. However, rigid docking rotates and translates the ligand, but torsional degrees of freedom will also be considered with flexible docking tools. The first model of interaction between protein and ligand was proposed by Emil Fischer in which he described the ligand as a key that fits into its binding site, the lock. Emil Fischer's model does not account for the induced fit or conformational changes due to the allosteric effects.[99] Based on Fischer's model, both ligand and protein are considered to be rigid bodies. Another model from Koshland brings the famous term "induces fit" into the account. Accordingly, the binding and interactions between ligand and protein induce conformational changes in the structure of the protein that eventually leads to a better match of the two molecules.

Studies show that proteins are found with several conformations "an ensemble of conformations" rather than just one important or functional conformation.[100, 101] The algorithms by which the docking tools evaluate the binding affinities between ligand and proteins are categorized as a force field, knowledge-based and empirical methods. With the Force Field (FF), the binding energies between ligand and protein are calculated by evaluating the L-J and Coulomb interactions.[102] The accuracy of the FF method is very much dependent on the parametrization of the FF. Several docking tools utilize FF for scoring function; among them, Dock[103] Atuodock[104], and Gold are some examples.[105, 106] The FlexX[107], Glide[108], x-Score, and SCORE use empirical methods of evaluating the scoring function. ITScore, PMF, and DrugScore benefit from the knowledge-based scoring function.[109]

FlexX is a docking tool that applies an incremental construction strategy for docking, which includes three main steps. First, a part of the ligand, the base fragment, is selected; it contains OH, NH, N, O interaction sites matched with the binding site of the protein. The rest of the ligand will be broken into small fragments from single rotatable acyclic bonds. The second step is base placement, through which the base fragment is docked into the binding site. The rest of the ligand is incrementally added to the base fragment, and the different modes of interactions between the ligand and the binding site are evaluated. The scoring function is based on the Böhm algorithm.[110]

The scoring function of FlexX docking tool calculates the energy between the ligand and its receptor.[110] (Eq 1-17)

$$\Delta G = \Delta G0 + \Delta G_{rot} \times \mathrm{N_{rot}} + \Delta Ghb \sum\nolimits_{neutral\ H-bond} f(\Delta R, \Delta\alpha 0) + \Delta Gio \sum\nolimits_{ionic-int} f(\Delta R, \Delta\alpha 0) + \Delta Garo \sum\nolimits_{naro-int} f(\Delta R, \Delta\alpha 0) + \Delta Glipo \sum\nolimits_{lipo.cont} f(\Delta R)$$

(Equation 1.16)

Any deviation from the ideal geometry will be penalized by $\Delta R, \Delta\alpha$ function. N_{rot} is the number of acyclic rotatable bonds that are fixed, and $\Delta Ghb, \Delta Gio\ and\ \Delta Garo$ referring to the contribution of H-bonds, electrostatic and aromatic interactions in the free binding energy, respectively.

1.3.3 An Introduction to Principal Component Analysis

It has been found collective motions in proteins play a significant role in their functions or that relate to proteins function. The proteins' functions, such as substrate binding, product release, allosteric regulations, and hinge bending [111] are examples of collective motion. These motions are different from local motions, which are not related to the biological functions. Therefore, the majority of the motions related to the functions of proteins are collective rather than local.[112, 113]

Under equilibrium conditions, a protein is not confined to one conformation. But, an ensemble of conformations describes an equilibrium state. Some ensemble conformations have high potential energy and are not thermodynamically stable, and some others are found near a local energy minimum close to global minima. They are separated from each other by a very low energy barrier. The most functional conformations are those with the potential energy close to the global minima. These functional conformations are very dynamic and easily converted into each other.[99]

The native state has several microstates with the same secondary conformations, but the atomic coordinates are not the same. For instance, the value for φ (**phi**) and ψ (**psi**), the bond length, and the angles of the two microstates differ from each other. During MD simulation, these microstates are continuously converted into each other due to changes in the bond length, dihedrals, and angles. These conversions between conformations can actively drive the movements of the domains involved in the allosteric and functional movement of proteins. Differentiation of collective motion from local motions is useful in structural biology for recognizing important segments and find out their biologically related motions.[114]

Several million conformations have been generated over each set of MD simulations. Systematic changes in variables such as bond length, dihedrals, and angles during the integration of the Newton equation of motion per each 2 fm in MD simulations generate a new coordinate/conformation. It is impossible to visualize each conformation and compare it with another one. It is important to know how to discover the most important conformations. The functional movements involved in the sampling of collective sub-states are found in the low frequency of mode spectrum. The low-frequency mode is called global or essential mode. Principal Component Analysis (PCA) can be used to extract concreted fluctuations with a large amplitude mode.[115]

PCA is an orthogonal linear transformation that is used to transform collected data from MD simulations in cartesian coordinates to new collective coordinates. The main goal of carrying out the PCA is to find the major route or direction of conformational changes. As discussed, MD simulation generates a large number of data; by doing PCA; the first few PC axes include the highest variance in MD data (the highest proportion of variance). Therefore, it is easier to interpret them and get insights into the major and greatest conformational changes and variance among them.[113, 116]

With MD data, the first step is to generate a covariance matrix (C-matrix), which is a $p \times p$ matrix. To remove translational and rotational motions that are not related to function, conformations fit the reference one. For obtaining the C-matrix, the average structure $\langle X_i \rangle$ of the *i*th atom is measured throughout the MD simulation. The covariance between the *i*th and *j*th atoms can be evaluated as described in equation 1.17.[115]

$C_{ij} = \frac{1}{n}\sum_{k=1}^{n} (X_{ik} - \langle X_i \rangle)(X_{jk} - \langle X_j \rangle)$ $i = 1, 2, \ldots., p$ $j = 1, 2, \ldots, p$ **(Equation 1-17)**

The diagonalizing of the C-matrix gives a variance of each coordinate. The C-matrix is a symmetric matrix because each column and row shows the coordinates of the same conformation in the same order.[115] For example, the 5th row has the same data point as the 5th column.

The next step after generation of symmetric $3N \times 3N$ C-matrix is its diagonalization by the eigenvector decomposition method: $C = T \Lambda T^{T}$ **(Equation 1-18)**

Where T represents the matrix of the column eigenvectors, and Λ is the diagonal matrix of the corresponding eigenvalues, which is the mean square displacement of their corresponding eigenvectors. Eigenvalue shows the magnitude of the displacement, and each eigenvector is a principal component of the displacement.[117, 118]

The main questions that this study is interested in investigating and answering are as follow:

Study the impact of various cations at low mM concentrations on the conformations of monomer and dimer of γ-tubulin as the major nucleator of MTs, and reveals whether cations can induce conformational changes in the structure of γ-tubulin or not.

It has been shown that cations induce aggregation of proteins, but the nature of interactions between them and proteins at the atomistic level is not well understood.

Mg^{+2} influences the interactions between GTP and α, β-tubulin heterodimer, and has a role in the assembly of MTs. However, the exact role of those interactions has not yet been revealed. Mg^{+2} and Zn^{+2} both can bind the GTP binding site, but Mg^{+2} is the dominant cations for unknown reasons.

Determination of the exact position of the high-affinity binding site and the major residues that interact with GTP and GDP in their binding sites are also investigated.

The binding of GTP induces conformational changes on the β-tubulin, but the impact of GTP and GDP binding on the conformation of γ-tubulin is not well addressed.

Zn^{+2} binds to tubulin and, similar to Mg^{+2}, induces the self-assembly of MTs; however, the resulting polymer would be a sheet of protofilaments rather than an MT tube, and the main reason behind which is still elusive. This study aims to investigate the cations' impact on GTP binding site interactions and to compare the electrostatic and L-J energies of GTP with its binding site, as well as evaluating the structural stability of γ-tubulin with each of these cations. The straightness and curvature of the γ-tubulin conformation have not been addressed since the effect of the cations is not well known; it is still elusive whether γ-tubulin adapts the straight conformation or not.

Whether GTP induces straight conformation or the lattice model is still a controversial discussion.

1.4 Bibliography

1. Alibert C, Goud B, Manneville JB: **Are cancer cells really softer than normal cells?** *Biology of the cell* 2017, **109**(5):167-189.
2. Small W, Jr., Bacon MA, Bajaj A, Chuang LT, Fisher BJ, Harkenrider MM, Jhingran A, Kitchener HC, Mileshkin LR, Viswanathan AN *et al*: **Cervical cancer: A global health crisis**. *Cancer* 2017, **123**(13):2404-2412.
3. Bray F, Ferlay J, Soerjomataram I, Siegel RL, Torre LA, Jemal A: **Global cancer statistics 2018: GLOBOCAN estimates of incidence and mortality worldwide for 36 cancers in 185 countries**. *CA Cancer J Clin* 2018, **68**(6):394-424.
4. Hanahan D, Weinberg RA: **Hallmarks of cancer: the next generation**. *Cell* 2011, **144**(5):646-674.
5. Pfeffer CM, Singh ATK: **Apoptosis: A Target for Anticancer Therapy**. *International journal of molecular sciences* 2018, **19**(2).
6. Nowell PC: **The clonal evolution of tumor cell populations**. *Science (New York, NY)* 1976, **194**(4260):23-28.
7. Visvader JE: **Cells of origin in cancer**. *Nature* 2011, **469**(7330):314-322.
8. Rycaj K, Tang DG: **Cell-of-Origin of Cancer versus Cancer Stem Cells: Assays and Interpretations**. *Cancer Research* 2015, **75**(19):4003-4011.
9. Alexandrov LB, Stratton MR: **Mutational signatures: the patterns of somatic mutations hidden in cancer genomes**. *Current opinion in genetics & development* 2014, **24**:52-60.
10. Lengauer C, Kinzler KW, Vogelstein B: **Genetic instabilities in human cancers**. *Nature* 1998, **396**(6712):643-649.
11. Samuels Y, Wang Z, Bardelli A, Silliman N, Ptak J, Szabo S, Yan H, Gazdar A, Powell SM, Riggins GJ *et al*: **High Frequency of Mutations of the PIK3CA Gene in Human Cancers**. *Science (New York, NY)* 2004, **304**(5670):554-554.
12. Davies H, Bignell GR, Cox C, Stephens P, Edkins S, Clegg S, Teague J, Woffendin H, Garnett MJ, Bottomley W *et al*: **Mutations of the BRAF gene in human cancer**. *Nature* 2002, **417**(6892):949-954.
13. Bu Y, Cao D: **The origin of cancer stem cells**. *Frontiers in bioscience (Scholar edition)* 2012, **4**:819-830.
14. Sharma S, Kelly TK, Jones PA: **Epigenetics in cancer**. *Carcinogenesis* 2009, **31**(1):27-36.
15. Moutinho C, Esteller M: **MicroRNAs and Epigenetics**. *Advances in cancer research* 2017, **135**:189-220.
16. Gibney ER, Nolan CM: **Epigenetics and gene expression**. *Heredity* 2010, **105**:4.

17. Jin B, Robertson KD: **DNA methyltransferases, DNA damage repair, and cancer**. *Adv Exp Med Biol* 2013, **754**:3-29.
18. Kareta MS, Botello ZM, Ennis JJ, Chou C, Chedin F: **Reconstitution and mechanism of the stimulation of de novo methylation by human DNMT3L**. *The Journal of biological chemistry* 2006, **281**(36):25893-25902.
19. Clouaire T, Stancheva I: **Methyl-CpG binding proteins: specialized transcriptional repressors or structural components of chromatin?** *Cell Mol Life Sci* 2008, **65**(10):1509-1522.
20. Kreso A, Dick John E: **Evolution of the Cancer Stem Cell Model**. *Cell Stem Cell* 2014, **14**(3):275-291.
21. Beck B, Blanpain C: **Unravelling cancer stem cell potential**. *Nature reviews Cancer* 2013, **13**(10):727-738.
22. **Cancer Classification**. 2010.
23. Nagata S: **Apoptosis and Clearance of Apoptotic Cells**. *Annual review of immunology* 2018, **36**:489-517.
24. Fuchs Y, Steller H: **Programmed cell death in animal development and disease**. *Cell* 2011, **147**(4):742-758.
25. Elmore S: **Apoptosis: a review of programmed cell death**. *Toxicologic pathology* 2007, **35**(4):495-516.
26. Matsuura K, Canfield K, Feng W, Kurokawa M: **Metabolic Regulation of Apoptosis in Cancer**. *Int Rev Cell Mol Biol* 2016, **327**:43-87.
27. Hagstrom KA, Meyer BJ: **Condensin and cohesin: more than chromosome compactor and glue**. *Nature reviews Genetics* 2003, **4**(7):520-534.
28. Ottaviano Y, Gerace L: **Phosphorylation of the nuclear lamins during interphase and mitosis**. *The Journal of biological chemistry* 1985, **260**(1):624-632.
29. Lodish UH: **Molecular Cell Biology**: W.H. Freeman; 2016.
30. Tamura N, Draviam VM: **Microtubule plus-ends within a mitotic cell are 'moving platforms' with anchoring, signalling and force-coupling roles**. *Open biology* 2012, **2**(11):120132.
31. Leung CL, Sun D, Zheng M, Knowles DR, Liem RK: **Microtubule actin cross-linking factor (MACF): a hybrid of dystonin and dystrophin that can interact with the actin and microtubule cytoskeletons**. *J Cell Biol* 1999, **147**(6):1275-1286.
32. Ciossani G, Overlack K, Petrovic A, Huis in 't Veld PJ, Koerner C, Wohlgemuth S, Maffini S, Musacchio A: **The kinetochore proteins CENP-E and CENP-F directly and specifically interact with distinct BUB mitotic checkpoint Ser/Thr kinases**. *Journal of Biological Chemistry* 2018.
33. Walczak CE, Cai S, Khodjakov A: **Mechanisms of chromosome behaviour during mitosis**. *Nat Rev Mol Cell Biol* 2010, **11**(2):91-102.

34. Slavov N, Botstein D: **Coupling among growth rate response, metabolic cycle, and cell division cycle in yeast**. *Molecular biology of the cell* 2011, **22**(12):1997-2009.

35. Birchmeier W: **Cytoskeleton structure and function**. *Trends in Biochemical Sciences* 1984, **9**(4):192-195.

36. Fletcher DA, Mullins RD: **Cell mechanics and the cytoskeleton**. *Nature* 2010, **463**(7280):485-492.

37. Dugina V, Alieva I, Khromova N, Kireev I, Gunning PW, Kopnin P: **Interaction of microtubules with the actin cytoskeleton via cross-talk of EB1-containing +TIPs and γ-actin in epithelial cells**. *Oncotarget* 2016, **7**(45):72699-72715.

38. Shelanski ML, Gaskin F, Cantor CR: **Microtubule assembly in the absence of added nucleotides**. *Proc Natl Acad Sci U S A* 1973, **70**(3):765-768.

39. Stephens RE, Edds KT: **Microtubules: structure, chemistry, and function**. *Physiological Reviews* 1976, **56**(4):709-777.

40. Forth S, Kapoor TM: **The mechanics of microtubule networks in cell division**. *The Journal of Cell Biology* 2017, **216**(6):1525-1531.

41. McEwen BF, Heagle AB, Cassels GO, Buttle KF, Rieder CL: **Kinetochore Fiber Maturation in PtK1 Cells and Its Implications for the Mechanisms of Chromosome Congression and Anaphase Onset**. *The Journal of Cell Biology* 1997, **137**(7):1567-1580.

42. Wu J, Akhmanova A: **Microtubule-Organizing Centers**. *Annual review of cell and developmental biology* 2017, **33**:51-75.

43. Wang H-W, Nogales E: **Nucleotide-dependent bending flexibility of tubulin regulates microtubule assembly**. *Nature* 2005, **435**(7044):911-915.

44. Grimaldi AD, Maki T, Fitton BP, Roth D, Yampolsky D, Davidson MW, Svitkina T, Straube A, Hayashi I, Kaverina I: **CLASPs are required for proper microtubule localization of end-binding proteins**. *Dev Cell* 2014, **30**(3):343-352.

45. Hirokawa N, Noda Y, Tanaka Y, Niwa S: **Kinesin superfamily motor proteins and intracellular transport**. *Nature Reviews Molecular Cell Biology* 2009, **10**(10):682-696.

46. Nogales E: **A structural view of microtubule dynamics**. *Cell Mol Life Sci* 1999, **56**(1-2):133-142.

47. Hirokawa N: **Kinesin and Dynein Superfamily Proteins and the Mechanism of Organelle Transport**. *Science (New York, NY)* 1998, **279**(5350):519-526.

48. Sheetz MP, Vale R, Schnapp B, Schroer T, Reese T: **Movements of vesicles on microtubules**. *Annals of the New York Academy of Sciences* 1987, **493**:409-416.

49. Uemura S, Kawaguchi K, Yajima J, Edamatsu M, Toyoshima YY, Ishiwata Si: **Kinesin–microtubule binding depends on both nucleotide state and loading direction**. *Proceedings of the National Academy of Sciences* 2002, **99**(9):5977-5981.

50. Solomon F: **Analyses of the Cytoskeleton in Saccharomyces cerevisiae**. *Annual Review of Cell Biology* 1991, **7**(1):633-662.
51. Burns RG: **α-, β-, and γ-tubulins: Sequence comparisons and structural constraints**. *Cell Motility* 1991, **20**(3):181-189.
52. Carlier MF, Didry D, Valentin-Ranc C: **Interaction between chromium GTP and tubulin. Stereochemistry of GTP binding, GTP hydrolysis, and microtubule stabilization**. *The Journal of biological chemistry* 1991, **266**(19):12361-12368.
53. Nogales E, Wolf SG, Downing KH: **Structure of the αβ tubulin dimer by electron crystallography**. *Nature* 1998, **391**(6663):199-203.
54. Mandelkow EM, Mandelkow E, Milligan RA: **Microtubule dynamics and microtubule caps: a time-resolved cryo-electron microscopy study**. *The Journal of Cell Biology* 1991, **114**(5):977-991.
55. Mitchison T, Kirschner M: **Dynamic instability of microtubule growth**. *Nature* 1984, **312**(5991):237-242.
56. Borisy G, Heald R, Howard J, Janke C, Musacchio A, Nogales E: **- Microtubules: 50 years on from the discovery of tubulin**. 2016, **- 17**:-.
57. and AD, Mitchison* TJ: **MICROTUBULE POLYMERIZATION DYNAMICS**. *Annual Review of Cell and Developmental Biology* 1997, **13**(1):83-117.
58. Conde C, Cáceres A: **Microtubule assembly, organization and dynamics in axons and dendrites**. *Nature Reviews Neuroscience* 2009, **10**(5):319-332.
59. Downing KH, Nogales E: **Tubulin structure: insights into microtubule properties and functions**. *Current opinion in structural biology* 1998, **8**(6):785-791.
60. Peng LX, Hsu MT, Bonomi M, Agard DA, Jacobson MP: **The free energy profile of tubulin straight-bent conformational changes, with implications for microtubule assembly and drug discovery**. *PLoS computational biology* 2014, **10**(2):e1003464-e1003464.
61. Löwe J, Li H, Downing KH, Nogales E: **Refined structure of αβ-tubulin at 3.5 Å resolution**. *Journal of Molecular Biology* 2001, **313**(5):1045-1057.
62. Aldaz H, Rice LM, Stearns T, Agard DA: **Insights into microtubule nucleation from the crystal structure of human γ-tubulin**. *Nature* 2005, **435**(7041):523-527.
63. Rice LM, Montabana EA, Agard DA: **The lattice as allosteric effector: structural studies of alphabeta- and gamma-tubulin clarify the role of GTP in microtubule assembly**. *Proceedings of the National Academy of Sciences of the United States of America* 2008, **105**(14):5378-5383.
64. Buey RM, Díaz JF, Andreu JM: **The Nucleotide Switch of Tubulin and Microtubule Assembly: A Polymerization-Driven Structural Change**. *Biochemistry* 2006, **45**(19):5933-5938.

65. Wang HW, Nogales E: **Nucleotide-dependent bending flexibility of tubulin regulates microtubule assembly**. *Nature* 2005, **435**(7044):911-915.

66. Oakley CE, Oakley BR: **Identification of γ-tubulin, a new member of the tubulin superfamily encoded by mipA gene of Aspergillus nidulans**. *Nature* 1989, **338**(6217):662-664.

67. Horio T, Uzawa S, Jung MK, Oakley BR, Tanaka K, Yanagida M: **The fission yeast gamma-tubulin is essential for mitosis and is localized at microtubule organizing centers**. *J Cell Sci* 1991, **99 (Pt 4)**:693-700.

68. Joshi HC: **Gamma-tubulin: the hub of cellular microtubule assemblies**. *BioEssays : news and reviews in molecular, cellular and developmental biology* 1993, **15**(10):637-643.

69. Masuda H, Shibata T: **Role of gamma-tubulin in mitosis-specific microtubule nucleation from the Schizosaccharomyces pombe spindle pole body**. *J Cell Sci* 1996, **109 (Pt 1)**:165-177.

70. Dráberová E, D'Agostino L, Caracciolo V, Sládková V, Sulimenko T, Sulimenko V, Sobol M, Maounis NF, Tzelepis E, Mahera E *et al*: **Overexpression and Nucleolar Localization of γ-Tubulin Small Complex Proteins GCP2 and GCP3 in Glioblastoma**. *Journal of neuropathology and experimental neurology* 2015, **74**(7):723-742.

71. Sallin P, Jaźwińska A: **γ-tubulin is differentially expressed in mitotic and non-mitotic cardiomyocytes in the regenerating zebrafish heart**. *Data in brief* 2015, **3**:71-77.

72. Farache D, Jauneau A, Chemin C, Chartrain M, Rémy MH, Merdes A, Haren L: **Functional Analysis of γ-Tubulin Complex Proteins Indicates Specific Lateral Association via Their N-terminal Domains**. *The Journal of biological chemistry* 2016, **291**(44):23112-23125.

73. Greenberg CH, Kollman J, Zelter A, Johnson R, MacCoss MJ, Davis TN, Agard DA, Sali A: **Structure of γ-tubulin small complex based on a cryo-EM map, chemical cross-links, and a remotely related structure**. *J Struct Biol* 2016, **194**(3):303-310.

74. Lin TC, Neuner A, Flemming D, Liu P, Chinen T, Jäkle U, Arkowitz R, Schiebel E: **MOZART1 and γ-tubulin complex receptors are both required to turn γ-TuSC into an active microtubule nucleation template**. *J Cell Biol* 2016, **215**(6):823-840.

75. Greenberg CH, Kollman J, Zelter A, Johnson R, MacCoss MJ, Davis TN, Agard DA, Sali A: **Structure of gamma-tubulin small complex based on a cryo-EM map, chemical cross-links, and a remotely related structure**. *J Struct Biol* 2016, **194**(3):303-310.

76. Ravelli RBG, Gigant B, Curmi PA, Jourdain I, Lachkar S, Sobel A, Knossow M: **Insight into tubulin regulation from a complex with colchicine and a stathmin-like domain**. *Nature* 2004, **428**(6979):198-202.

77. Mulder AM, Glavis-Bloom A, Moores CA, Wagenbach M, Carragher B, Wordeman L, Milligan RA: **A new model for binding of kinesin 13 to curved microtubule protofilaments**. *The Journal of cell biology* 2009, **185**(1):51-57.

78. Moores CA, Milligan RA: **Visualisation of a kinesin-13 motor on microtubule end mimics**. *Journal of molecular biology* 2008, **377**(3):647-654.

79. Li Z, Alisaraie L: **Microtubules dual chemo and thermo-responsive depolymerization**. *Proteins* 2015, **83**(5):970-981.

80. Frenkel D, Smit B: **Understanding molecular simulation : from algorithms to applications**. San Diego: Academic Press; 2001.

81. Leach AR: **Molecular modelling : principles and applications**. Harlow: Pearson/Prentice Hall; 2009.

82. Abraham MJ, Murtola T, Schulz R, Páll S, Smith JC, Hess B, Lindahl E: **GROMACS: High performance molecular simulations through multi-level parallelism from laptops to supercomputers**. *SoftwareX* 2015, **1-2**:19-25.

83. Brooks BR, Brooks CL, 3rd, Mackerell AD, Jr., Nilsson L, Petrella RJ, Roux B, Won Y, Archontis G, Bartels C, Boresch S *et al*: **CHARMM: the biomolecular simulation program**. *Journal of computational chemistry* 2009, **30**(10):1545-1614.

84. Barnoud J, Monticelli L: **Coarse-grained force fields for molecular simulations**. *Methods in molecular biology (Clifton, NJ)* 2015, **1215**:125-149.

85. Scott WRP, Hünenberger PH, Tironi IG, Mark AE, Billeter SR, Fennen J, Torda AE, Huber T, Krüger P, van Gunsteren WF: **The GROMOS Biomolecular Simulation Program Package**. *The Journal of Physical Chemistry A* 1999, **103**(19):3596-3607.

86. Jorgensen WL, Tirado-Rives J: **The OPLS [optimized potentials for liquid simulations] potential functions for proteins, energy minimizations for crystals of cyclic peptides and crambin**. *Journal of the American Chemical Society* 1988, **110**(6):1657-1666.

87. Hess B, Kutzner C, van der Spoel D, Lindahl E: **GROMACS 4: Algorithms for Highly Efficient, Load-Balanced, and Scalable Molecular Simulation**. *Journal of Chemical Theory and Computation* 2008, **4**(3):435-447.

88. Emile Apol RA, Herman J.C. Berendsen, Aldert van Buuren, P¨ar Bjelkmar, Rudi van Drunen, Anton Feenstra, Sebastian Fritsch, Gerrit Groenhof,: **GROMACS USER MANUAL**. 2015.

89. Oostenbrink C, Villa A, Mark AE, Van Gunsteren WF: **A biomolecular force field based on the free enthalpy of hydration and solvation: The GROMOS force-field parameter sets 53A5 and 53A6**. *Journal of Computational Chemistry* 2004, **25**(13):1656-1676.

90. Standard JM: **Energy Minimization Methods**. September 9, 2015.

91. Ayaz Mahmood D, Shafia M: **- Molecular Docking: Approaches, Types, Applications and Basic Challenges**. 2017.

92. Shoichet BK, McGovern SL, Wei B, Irwin JJ: **Lead discovery using molecular docking**. *Current Opinion in Chemical Biology* 2002, **6**(4):439-446.

93. Kuntz ID, Blaney JM, Oatley SJ, Langridge R, Ferrin TE: **A geometric approach to macromolecule-ligand interactions**. *Journal of Molecular Biology* 1982, **161**(2):269-288.
94. Ciemny M, Kurcinski M, Kamel K, Kolinski A, Alam N, Schueler-Furman O, Kmiecik S: **Protein–peptide docking: opportunities and challenges**. *Drug Discovery Today* 2018, **23**(8):1530-1537.
95. Yan Y, Zhang D, Zhou P, Li B, Huang S-Y: **HDOCK: a web server for protein–protein and protein–DNA/RNA docking based on a hybrid strategy**. *Nucleic Acids Research* 2017, **45**(W1):W365-W373.
96. Abagyan R, Totrov M: **High-throughput docking for lead generation**. *Current Opinion in Chemical Biology* 2001, **5**(4):375-382.
97. Schneider G: **Virtual screening: an endless staircase?** *Nature Reviews Drug Discovery* 2010, **9**:273.
98. Lee K, Czaplewski C, Kim S-Y, Lee J: **An efficient molecular docking using conformational space annealing**. *Journal of Computational Chemistry* 2005, **26**(1):78-87.
99. Nelson DL, Cox MM, Lehninger AL: **Lehninger, principles of biochemistry**. Basingstoke; New York: Macmillan Higher Education ; W.H. Freeman; 2017.
100. Koshland DE: **Application of a Theory of Enzyme Specificity to Protein Synthesis**. *Proceedings of the National Academy of Sciences of the United States of America* 1958, **44**(2):98-104.
101. Monod J, Wyman J, Changeux J-P: **On the nature of allosteric transitions: A plausible model**. *Journal of Molecular Biology* 1965, **12**(1):88-118.
102. Shoichet BK, Leach AR, Kuntz ID: **Ligand solvation in molecular docking**. *Proteins: Structure, Function, and Bioinformatics* 1999, **34**(1):4-16.
103. Ewing TJ, Makino S, Skillman AG, Kuntz ID: **DOCK 4.0: search strategies for automated molecular docking of flexible molecule databases**. *J Comput Aided Mol Des* 2001, **15**(5):411-428.
104. Goodsell DS, Morris GM, Olson AJ: **Automated docking of flexible ligands: applications of AutoDock**. *Journal of molecular recognition : JMR* 1996, **9**(1):1-5.
105. Verdonk ML, Cole JC, Hartshorn MJ, Murray CW, Taylor RD: **Improved protein-ligand docking using GOLD**. *Proteins* 2003, **52**(4):609-623.
106. Huang S-Y, Grinter SZ, Zou X: **Scoring functions and their evaluation methods for protein–ligand docking: recent advances and future directions**. *Physical Chemistry Chemical Physics* 2010, **12**(40):12899-12908.
107. Kramer B, Rarey M, Lengauer T: **Evaluation of the FLEXX incremental construction algorithm for protein-ligand docking**. *Proteins* 1999, **37**(2):228-241.

108. Friesner RA, Banks JL, Murphy RB, Halgren TA, Klicic JJ, Mainz DT, Repasky MP, Knoll EH, Shelley M, Perry JK *et al*: **Glide: a new approach for rapid, accurate docking and scoring. 1. Method and assessment of docking accuracy**. *Journal of medicinal chemistry* 2004, **47**(7):1739-1749.

109. Pagadala NS, Syed K, Tuszynski J: **Software for molecular docking: a review**. *Biophys Rev* 2017, **9**(2):91-102.

110. Rarey M, Kramer B, Lengauer T, Klebe G: **A Fast Flexible Docking Method using an Incremental Construction Algorithm**. *Journal of Molecular Biology* 1996, **261**(3):470-489.

111. van Aalten DM, Amadei A, Linssen AB, Eijsink VG, Vriend G, Berendsen HJ: **The essential dynamics of thermolysin: confirmation of the hinge-bending motion and comparison of simulations in vacuum and water**. *Proteins* 1995, **22**(1):45-54.

112. Berendsen HJ, Hayward S: **Collective protein dynamics in relation to function**. *Current opinion in structural biology* 2000, **10**(2):165-169.

113. Bahar I, Chennubhotla C, Tobi D: **Intrinsic dynamics of enzymes in the unbound state and relation to allosteric regulation**. *Current opinion in structural biology* 2007, **17**(6):633-640.

114. Singh R, Weikert T, Basa S, Moerschbacher BM: **Structural and biochemical insight into mode of action and subsite specificity of a chitosan degrading enzyme from Bacillus spec. MN**. *Scientific reports* 2019, **9**(1):1132-1132.

115. Stein SAM, Loccisano AE, Firestine SM, Evanseck JD: **Chapter 13 Principal Components Analysis: A Review of its Application on Molecular Dynamics Data**. In: *Annual Reports in Computational Chemistry.* Edited by Spellmeyer DC, vol. 2: Elsevier; 2006: 233-261.

116. Bahar I, Lezon TR, Bakan A, Shrivastava IH: **Normal mode analysis of biomolecular structures: functional mechanisms of membrane proteins**. *Chem Rev* 2010, **110**(3):1463-1497.

117. Prathamesh M.: **Applications of Principal Component Analysis (PCA) in Materials Science**. 2012.

118. Sittel F, Jain A, Stock G: **Principal component analysis of molecular dynamics: On the use of Cartesian vs. internal coordinates**. *The Journal of Chemical Physics* 2014, **141**(1):014111.

CHAPTER 2

Impact of GTP and Ionic Conditions on Conformations of Unliganded and Liganded γ-Tubulin Monomer

2.1 MD Simulation of Unliganded γ-Tubulin Monomer Under $MgCl_2$, $ZnCl_2$, and NaCl Ionic Conditions

2.1.1 Introduction

2.1.1.1 Role of Cations in Cells and their Impact on Proteins

All macromolecules such as proteins, carbohydrates, lipids, and nucleic acids are exposed to an aqueous environment containing several types of ions, where K^+, Na^+, Cl^-, Mg^{+2}, Ca^{+2}, and Zn^{+2} are just a few of them. Cations interact with biomolecules and play significant roles, such as stabilization of protein complexes, signal transduction, hormone secretion, muscle contraction, and regulatory functions in the immune system. [1-4] How cations interact with γ-tubulin, and the main segments or domains of interactions mainly remains elusive.[5-7] Mg^{+2} is an important metal cation inside the cytoplasm and nucleus. It is a cofactor for kinases such as pyruvate kinase, hexokinase, and glucose 6-phosphatase.[7, 8] Mg^{+2} promotes ATP hydrolysis; also, it interacts with phosphoproteins. [7, 8] Other electrolytes such as Na^+ and Cl^- are abundant outside the cytoplasm.[9] Zn^{+2} is an essential catalytic and structural cofactor for alcohol dehydrogenase, carboxypeptidase, and carbonic anhydrase.[10] In addition, Zn^{+2} has a functional activity in zinc finger transcription factors by stabilizing the whole structure of the zinc finger motif. Zinc fingers are the most abundant transcriptional factors involved in regulating thousands of genes through their sequence-specific binding to DNA.[11]

The ion concentration and salt-protein interaction on protein solubility have been known for a long time. Salts at higher concentrations induce the precipitation of soluble proteins, a process of salting-out that disrupts the interactions of proteins and water molecules.[12]

The effect of available cations and anions of the cytoplasm on internal interactions and the conformation of proteins is mostly unknown. Studies show that changing the ionic strength of Ca^{+2} induces conformational changes in the Calmodulin.[13]

However, what is the impact of various cations at mM concentration on the conformation of proteins in the general or specific family of proteins, or whether different ionic conditions can induce any conformational alterations in the structure of proteins remained elusive. Genetic mutations affect the function and biological role of proteins; many diseases such as Sickle-Cell Anemia and Cystic Fibrosis are examples of mutation.[14] Point mutations for even one base/one residue can deactivate a protein, but there is no detailed explanation about the impact of cations on the functions and conformations of proteins as they have electrostatic interaction with the residues of proteins.[14]

The physiological concentration of cations relates to clinical disorders, such as cancers and neurodegenerative diseases. Compared to normal cells, higher Na^+ concentration was detected in carcinoma in which the ratio of Na^+/K^+ in cancer cells was five-times higher than in normal cells.[15]

Lateral interactions between rod-like proteins, include MTs, F-actin, and condensation of DNA molecules, are shown to be stimulated by divalent and trivalent cations.[16, 17] Aggregation will be reversed using counter-anion particles such as nucleoside phosphates.[16,17]

Deviation of physiological concentration of metals that causes their binding or dissociation can affect the activity of a specific protein. Therefore, their concentration should be maintained in the physiologic ranges. It has been shown that the filamentous M13 and fb bacteriophages, which are rod-like proteins, aggregate in the presence of < 100 mml/L of Mg^{+2} and Ca^{+2} cations.[18] This is an indication of the impact of cations on molecular interactions, but the nature of these interactions at the atomistic level is not well understood.[18]

Aggregation of amyloid-β peptide is common in Alzheimer, and α-synuclein aggregation has been reported in Parkinson. Cu^{+2} and Fe^{+3} cations play roles in both of the mentioned aggregations.[19, 20] Several metalloproteinases are the target of drug development against a diverse range of diseases. Histone Deacetylase, Hepatite C protease, and Glycoxalse, which are Zn^{+2}-metalloproteinases, targeted for cancer therapy and hepatite C treatment, respectively.[21] Mg^{+2}-metalloproteinase, like integrase, is targeted for AIDS treatment.[21] The concentration of Na^{+} in plasma ranges from 136 mml/L to 146 mml/L and from 98 mml/L to 107 mml/L for Cl^{-} anion.[22] However, the concentration of Mg^{+2} in plasma is lower than Na^{+} with ~1 - 2 mml/L. The above-mentioned concentrations are in plasma; however, inside the mammalian cells, the overall concentration of all cations are around ≥ 140 mml/L as compare to the used concentration here is higher. In this study, the overall goals for selecting the ~ 129 mml/L for NaCl and 65 mml/L for $MgCl_2$ are not to compare it exactly with inside or outside the cytoplasm or plasma but to select a range close to the cumulative concentrations of all other cations which are not available here. For instance, the K^+ concentration in the mammalian cell is ~ 139 mml/L.[23]

Both Mg^{+2} and Zn^{+2} compete for interaction to proteins, but what are the differences between their effect are not well-known specifically about γ-tubulins.[24] Mg^{+2} and Zn^{+2} do not participate in any redox reaction. The charge of cations plays a key role in charge-dipole and charge-charged interactions, and the higher valance cations make stronger interactions.[25]

Large ionic radius of metals results in low charge density and less favorable attraction with ligands or lower metal-binding energy. Zn^{+2} is a better electron acceptor because the charge transfer from a ligand to Zn^{+2} is more favorable than Mg^{+2}. Studies have shown that Zn^{+2} can dislodge Mg^{+2} from its interaction with a protein, but Mg^{+2} cannot replace Zn^{+2}.[24] Also, based on the "Irving–Williams" series, the stability of metal complexes is higher with Zn^{+2} compared to that of Mg^{+2}.[26, 27] Compared to Mg^{+2}, the concentration of Zn^{+2} is much lower in the cytosol with ~ 0.016 mml/L, which is ~ 1-2 mml/L for Mg^{+2}.[28]

Small molecules or ligands modulate the function of proteins; for instance, GTP is a ligand in the tubulin family.[29, 30] GTP binds to α, β-tubulin heterodimer, α-tubulin carries a non-exchangeable binding site for GTP, which is called N-site in which GTP is not hydrolyzed to GDP. [31] The E-site is located on β-tubulin in which GTP is hydrolyzed during folding and polymerization of MTs.[31]

Depending on whether the two molecules of GTP are both in the N and E-sites or one GTP bound to the N-site, two or one high-affinity metal-binding site is available that reversibly binds Mg^{+2}. Other divalent metals, such as Zn^{+2} and Mn^{+2}, can also bind and compete with Mg^{+2} to occupy the binding site, but Mg^{+2} is the main cation for unknown reasons.[32] Mg^{+2} influences GTP and α, β-tubulin interactions, and MTs assembly; however, the nature of those interactions is not revealed yet.[32]

The GTP role at the N-site is structural and contributes to the stability of α, β-tubulin heterodimer.[32] The Mg^{+2} dissociation induces the functional inactivity of the tubulin dimer and GTP release. Binding of Mg^{+2} to the N-site is also needed for the MTs assembly.[33]

The α, β-tubulin heterodimer with bound GTP to both N and E-sites consists of two high-affinity metal binding sites for divalent cations such as Mg^{+2}. [34, 35] Those with GDP inside the E-site has only one high-affinity metal binding site for Mg^{+2}. This indicates that Mg^{+2} binding depends on the γ-phosphate availability.[34, 35] However, the possibility of existing other high-affinity metal-binding sites and their potential functions remain elusive, which is investigated in this study.

The conformation of β-tubulin is shown to be related to the GTP or GDP binding. The binding of GTP induces conformational changes in β-tubulin.[36-38] Whether conformational changes upon GTP binding to γ-tubulin induce in Mg^{+2} or Zn^{+2} simulations compared to unliganded simulations are unknown.

Other divalent cations such as Zn^{+2} or Mn^{+2} also interact with the E and N-sites. The apparent association constant of Mn^{+2} is greater than that of Mg^{+2}. It is $0.7\text{-}1.1 \times 10^{6}\ M^{-1}$ for Mg^{+2} and $4.1\text{-}\ 4.9 \times 10^{7}\ M^{-1}$ for Mn^{2+}.[34, 39]

Zn^{+2} and Co^{+2} bind to tubulins and induce self-assembly of MTs; however, the resulting polymer would be a sheet of protofilaments rather than a tube.[34, 39, 40] The Mg^{+2} is necessary for GTPase activity of FtsZ protein as well.[41]

GTP binding to γ-tubulin indicates that the nucleotide has both functional and structural roles. Binding of GTP is essential for interactions between γ-tubulin and α-tubulin, nucleation, and organization of MTs.[42] GTP is not necessary for the component recruitment of the ring complex; both *in vivo* and *in vitro* studies reveal that the role of γ-tubulin in the nucleation of MTs is strongly dependent on the binding of GTP to the protein.[42] This emphasizes the GTP structural role as mutations of the GTP binding site in yeast γ-tubulin defect yeast γ-tubulin and MTs interactions.[42] And it was shown that binding of GTP to yeast Tub4 is essential for the viability of an organism. With ATP synthases enzyme, Mg^{+2} induces conformational changes that lead to the re-positioning of Ala158 towards the catalytic site during the transition state of ATP synthesis.[43] The binding properties of GDP and GTP to β and γ-tubulin are almost similar. The affinities of β-tubulin and γ-tubulin for GTP are 64.50 ± 6.30 nM and 58.40 ± 12.60 nM, respectively.[44] and for GDP are 1.13 ± 0.20 μM for γ-tubulin, 1.55 ± 0.25 μM for β-tubulin.[44]. These features of γ-tubulin make it likely that upon its interaction with α-tubulin, its GTPase activity stimulated by α-tubulin in a similar pattern to that of the exchangeable binding site in β-tubulin. However, hydrolyzes mechanism and protein activation for the GTPase activity of γ-tubulin has not been fully addressed.[44] This study aims to survey the effect of Mg^{+2}, $Zn^{+2,}$ and Na^{+} cations on the conformational changes of γ-tubulin. Investigating the impact of cations on interactions within the GTP binding site and comparing the electrostatic and L-J interactions of GTP with its binding site, as well as evaluating the structural stability of γ-tubulin with these cations will be addressed.

2.1.1.2 γ-Tubulin and its Structure

The three-dimensional structure of γ-tubulin is similar to that of α, β-tubulin heterodimer; they have 35% of sequence similarity.[45] Similar to β-tubulin, the γ-tubulin is composed of three domains that can be recognized on its structure. N-terminal nucleotide-binding domain (Met1-Thr242), intermediate domain (Arg244-Asn380), and C-terminal domain (His381-Gln451).[45]

The nucleotide-binding domain (NBD) (Met1-Thr242) at the N-terminal of γ-tubulin is composed of six parallel beta-strands (S1-S6), six helices (H1-H6), and six loops (T1-T6 loop) that bridges the strands to the H1-H6 helices. T1-T6 loops are in interactions with the GTP/GDP nucleotide.[45, 46] The NBD joins the intermediate domain (Arg244-Asn380) through H7 helix (225Phe - Leu243). The core helix (H7 helix) is an indicator of curvature or straightness of conformation of the tubulin family that will be discussed later in detail.[44, 47] The second domain, the intermediate domain (ID), is smaller than NBD and comprises the H8 to H10 helices and the S7 to S10 strands.

Two long helices with the opposite orientation at their C and N-terminal create the C-terminal domain (C-ter). These two helices include the H11 helix (Ser385-Lys400) and the H12 (Asp419-Ala437), cross both intermediate domain and N-terminal nucleotide-binding domain.[44, 48] (**Figure 2.1 and Table 2.1**)

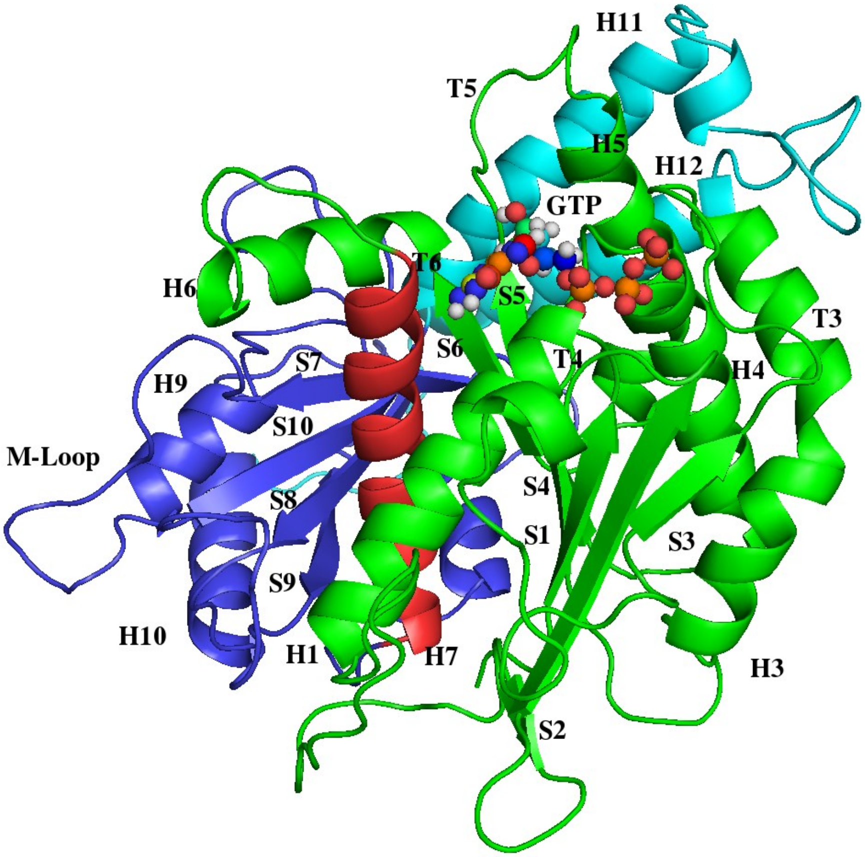

Figure 2.1: The structure of γ-tubulin. The N-terminal domain is colored in green, the intermediate domain in blue, C-terminal domain in cyan. The H7 core helix is depicted in red.

Domains	Residue	Secondary Elements	Known Function	Secondary Elements	Known Function
N-terminal	1Met-242Thr			**S4**Gly134-Ser140	NBD
		S1Ile5-Leu10	Centrosome localization/NBD	**S5**Leu165-Phe172	NBD
		S2Ala64-Asp68	NBD	**S6**Cys201-Asp206	NBD
		S3Ile91-Leu93	NBD	**H4**Thr145-Arg160	NBD
		H1 Gly11-Glu28	NBD	**H5**Gln184-Gln197	NBD
		H2Arg72-Asn79	NBD	**H6**Asn207-Asp216	NBD
		H3Trp104-Asp127	NBD	**T4**Ile141-Gly144	NBD
		T1Met1-Glu4	NBD	**T5**Pro173-Gln184	NBD
		T2Leu69-Pro71		**T6**Asn188-Asp200	NBD
		T3Ser94-Asn103		**H7** Phe225-Leu243	
		T7Thr240-Asp252			
Intermediate Domain	Arg244-Asn380	**H8**Leu253-Leu260		**S7**Phe268-Tyr273	
		H9Val290-Leu298		**S8**Tyr317-Gln325	
		H10 Pro330-Arg343		**S9**Ile356-Ser361	
		M loop Thr274-289Thr		**S10**Ser374-His381	
C-terminal Domain	His381-Gln451	**H11**Ser385-Lys400	NLS[49]		
		H12 Asp419-Ala437	Centrosome localization[50]		

Table 2.1: Three domains of γ-tubulin with their helices, loops, and beta-stands. N-terminal, Intermediate, and C-terminal domains of γ-tubulin. The NBD; nucleotide-binding domain. NLS: Nuclear localization signal.[44, 45, 51]

2.1.1.3 γ-Tubulin and Nucleation of Microtubules

The γ-tubulin is a member of the tubulin family of proteins on chromosome 17, 17q21.[52] *Homo-sapiens* have two genes for γ-tubulin[53], *TUBG1,* and *TUBG2* on chromosome 17 and a pseudogene on chromosome 7. The sequence similarity of *TUBG1* and *TUBG2* is about 97.3%, and both express γ-tubulin in various tissues, including the colon, heart, ovary, muscle, lung, testicle, liver, kidney, and stomach.[52] The γ-tubulin is a conserved member of the tubulin family that was discovered in 1989 in *Aspergillus nidulansand* as a product of the *mipA* gene.[51]

The centrosome is one of the main organelles associated with the γ-tubulin within cells that initiates nucleation of MTs and is involved in several cellular processes, including mitosis, segregation of chromosomes, and cell movement.[54]

The centrosome is composed of a perpendicular arrangement of two centrioles, plus around 100 different proteins. Its proteins mainly are mitotic regulators, spindle checkpoints, cytoskeletal regulators, microtubule-associated proteins, mRNA processors.[55, 56]

The γ-tubulin is a key component of two complexes of proteins: γ-tubulin small complex (γTuSC) and γ-tubulin ring complex (γTuRC); both γTuSC and γTuRC are actively involved in the nucleation of microtubules.[57-59] (**Figure 2.2**)

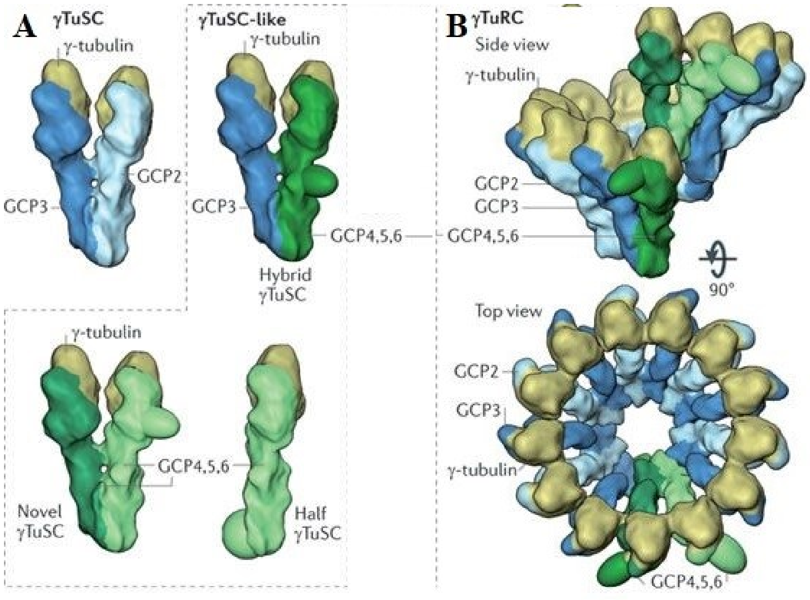

Figure 2.2: Structure of γTuSC and γTuRC. (**A**) The γTuSC is composed of two γ-tubulin in lateral interactions and GCP2 and GCP3 proteins. The whole γTuRC is generated from a ring of γTuSC-like from two γ-tubulin and proteins, include GCP2, GCP3, GCP4, GCP5, and GCP6. (**B**) The γTuRC on the side and top views with the γ-tubulin on top and GCP2, GCP3, GCP4, GCP5, as well as GCP6 proteins in interaction with it. The GCP4, GCP5, and GCP6 are represented in green. GCP2 or GCP3 is shown in blue and γ-tubulin in yellow color.[60] This figure is adapted with permission. Kollman et al., Nature Reviews Molecular Cell Biology 2011.

The MTs nucleation is achieved by the centrosome and centrosome independent through Agumin complex; and, in both, γ-tubulin has a central role.[61, 62]

γTuRC is a ring-shaped complex of at least seven proteins with a diameter of 25 nm located at the microtubule organization center. The size of the ring corresponds to 13 protofilaments of MTs. During nucleation, the γTuRC caps the negative end of microtubules at the centrosome, and the α, β-tubulin binds the γ-tubulin on the top of γTuRC. The α, β-tubulin heterodimer, and the γTuRC interactions need the α subunit. (**Figure 2.2**)

The whole γTuRC complex stabilizes through the interaction between the α, β-tubulin heterodimers, and the γ-tubulin. γ-tubulin acts as a mediator between α, β-tubulin heterodimers, and other members of the γTuRC. The composition of γTuRC in mammals and frogs is similar; in mammalian cells, the counterparts of yeast Spc97/98 are hGCP2 and hGCP3. The number of γ-containing complexes in frog is about 10-13, and in humans is estimated to be 12-16 monomers. Both hGCP2/3 are conserved in the γ-tubulin ring complex from yeast to humans; this indicates the functional importance of these proteins. [63] Other proteins that are members of γTuRC in *Homo-sapiens* cells are hGCP4, hGCP5, and hGCP6. There are multiple copies of GCP2, GCP3, and GCP4 and a single copy of GCP5.[63]

Off all GCPs, proteins, GCP2, GCP3, and GCP4[64] are more conserved. The other members of γTuRC are MOZART1, MOZART2A/B, which due to their small size, remain unknown with the other subunits of γTuRC. MOZARTs are conserved components of γ TuRC, are different from GCPs, and do not share similar sequences or homology with them.[63] MOZART1 is a conserved evolutionary protein[63]. Yeast homolog of MOZART1 is essential for the recruitment of γ-tubulin containing complex to MTOC.[65]

NEDD1 is a centrosomal protein associated with γTuRC; its role is important for centrosomal targeting. However, the assembly of the ring complex can be implemented without NEDD1.[66]

Nucleation of microtubules and formation of mitosis spindle failed in cells with inactivated γ-tubulin. In *Drosophila* embryo extracts, γTuRC is not the only γ-tubulin containing complex; the cytosolic γ-tubulin can be found as part of another complex called the γ-tubulin small complex (γTuSC). γTuSC is a hetero-tetrameric complex composed of the homodimer of γ-tubulin, and two homologous Spc97 and Spc98 proteins. The molecular mass of γTuRC is seven times that of γTuSC, with 15 nm Stokes radius compared to 7 nm Stokes radius of γTuSC.[67, 68] (**Figure 2.2**)

Excluding γ-tubulin, other proteins of both complexes are different as well. γTuSC is a structural scaffolding for the assembly of γTuRC. Dgrips 84 and 91 (Drosophila γ-ring proteins) were discovered in both complexes (ring and small complex), which in γTuRC are called Spc97/98p.[69]

γTuSC is universally conserved in all eukaryotes; it consists of two copies of γ-tubulin and Spc97p and Spc98p proteins. The C-terminal of Spc97 and Spc98 directly interacts with γ-tubulin. γTuSC resembles a Y-shape that GCP2/3 (γ-tubulin complex proteins 2 and 3) form its arms, and two γ-tubulins are located in lobes at the tips of the two arms in contact with GCP2/3.[70] (**Figure 2.2**)

In both γTuRC and γTuSC complexes, the γ-tubulin is cross-links to the GTP molecule. There are two γ-tubulin in γTuSC laterally in interaction, which is further assembled into γ-TuRC and supporting the view that γTuSC can be a scaffold for the formation of γTuRC.

[69, 70] Both small and ring complexes are able to promote nucleation. However, the γTuRC nucleates MTs 25 times faster than γTuSC. [71] The role of GCP subunits of γTuSC is enough for centrosomal microtubule nucleation. It has been shown that the role of specific γTuRC proteins like GCP4/5 and GCP6 is the activation of nucleation activity and stabilization of the ring structure.[71]

2.1.2 Experimental Set-Up of MD Simulations of Unliganded and GTP-liganded γ-Tubulin Monomer

The γ-tubulin crystal structure of chain A with 2.3 Å resolution, PDB[72] entry of 3CB2[73], and UniProt code of P23258 was retrieved from the Protein Data Bank. The missing atoms were added by employing the Swiss-Pdb Viewer[74] and the missing residues by using the Pymol tool.[75]

Inserted missing residues include: Thr278, Asp279, Gln280, Ser281, Val282, and Ala283 belong to the M loop, Arg311, Gln312 of H8-S9 loop, Leu367, Pro368, Ser369, Ala370, His371 belong to the S9-S10 loop, and Gly447, Thr448, Gln449, Glu450, as well as Gln451 of the C-terminal loop.

Then chain A was subjected to 6 sets of simulations for the unliganded monomer and GTP liganded monomer as main experiments. Two repetitions were carried out using GROMACS 4.5.7 package[76] and GROMOS 96, 53A6[77] force field, all for 200 ns in the presence of NaCl, $MgCl_2$, and $ZnCl_2$ for each set. The “md” integrator with a 2 fs time step was applied, and Linear Constraint Solver (LINCS) [78] was used to constrain all bond lengths. The protein was embedded into the cubical solvent box with SPC[79] water molecules. A distance of 1 nm was assigned between the protein surface and the box edge.

Non-bonded interactions, including Van der Waals and electrostatic, were modeled using Lennard–Jones and electrostatic potentials, respectively. A cut-off distance of 1.4 nm was assigned to both Lennard–Jones and electrostatic interactions. The calculations of electrostatic interactions contributing to energies and forces were carried out based on the Particle Mesh Ewald algorithm.[80]

First, all simulations were energy minimized to relax internal constraints using the steepest descent method prior to MD simulation. The all-bonds position restraint was done for 2 ns after energy minimization, and 10 ns equilibration simulation was carried out. The time constant for pressure coupling was set to 1.0 ps with the compressibility of 4.5e-5 bar at a 300 K temperature. The protein and non-protein groups were coupled separately to a temperature bath of 300K with a time constant of 0.1 ps that was kept constant by temperature coupling with Bussi’s thermostat. Using an energy minimized structure, second and third trajectories were produced for evaluating the accuracy of the first set. In sets two and three, velocities were assigned differently at random for position restraint. However, all other parameters were the same in the second and third rounds of repeated simulations. MD simulations were performed on the high-performance computer clusters of the ACENET, Graham, and West Grid Consortium. The convergence point of the simulations was after 110-130 ns, and for all simulations, the last 50 ns from 150 ns to 200 ns were selected for analysis.

The atomistic behavior of GTP-bound γ-tubulin was modeled by MD simulation in the concentration of ~129 mml/L of NaCl and ~ 65 mml/L of $MgCl_2$ and $ZnCl_2$ in the presence of docked GTP at its binding site. (**Table 2.2**)

The united atom topology of GTP was obtained from the Automated Topology Builder (ATB) repository.[81] Docking of GTP into its binding site of γ-tubulin was achieved by using FlexX. [82] The ranking of an energetically favorable docking pose is based on their total binding energy, which was calculated based on Böhm scoring function.[83]

Simulation	**RUN**	**MD length**	**Salt Con mml/L**
# 1	**NaCl**	**200 ns**	**~ 129**
# 2	**$MgCl_2$**	**200 ns**	**~ 65**
# 3	**$ZnCl_2$**	**200 ns**	**~ 65**

Table 2.2: Simulations set up and concentration of the electrolyte with each simulation.

2.1.3 Results and Discussion

2.1.3.1 Definition of Curvature and Straightness and their Quantitative Analysis

α, β-tubulin heterodimer adapts straight and curved conformations distinguished through their superimposition.[44, 47, 84, 85]

The α, β-tubulin with straight conformation, serves as a building block of MTs. [45] MTs has lateral interactions between α-α and β-β homodimers,[45] longitudinal interactions between non-similar proteins of α-β tubulin. (**Figure 2.3**)

However, curved conformation has shown rearrangements with intermediate domain (Arg244-Asn380) that differentiates it from straight conformation. One of the distinct rearrangements during straight to curved conversion is the deviation of the core H7 helix

(Asp224-Phe242) that is shown by measuring the distance from the center of mass (dCOM) for H7 helix from S6 strand.[44] (**Figure 2.3**)

In curved conformation, weak lateral interactions exist at the protofilament of MTs, and they are no longer involved in the stability of the protofilament.[86]

Considering α, β-tubulin domains, the intermediate domain encounters a larger alteration of its conformation while converting from curved to straight conformation. The NBD and C-terminal domains, in contrast, behave as rigid units and do not undergo conformational rearrangements as much as the intermediate domain does.

In β-tubulin, the most affected secondary structure segments during curved to straight conversion are with helices such as H6 (Ala206-Ile215), H7 (Asp224-Phe242), and H10 (Glu325-Ser338) as well as the intermediate domain strands of S7 (Met267-Pro272), S8 (Val313-Arg320), S9 (Ile356-Leu361), S10 (Asn373-Ile381).[47] (**Figure 2.3)**

The loops that contribute to the rearrangement from curved to straight conversion include M (Pro272-Leu289), H1-S2 (His28-Ile47), T5 (Ser172-Try183), and H6-H7 (Lys216-Gly223) loops with β-tubulin.[47]

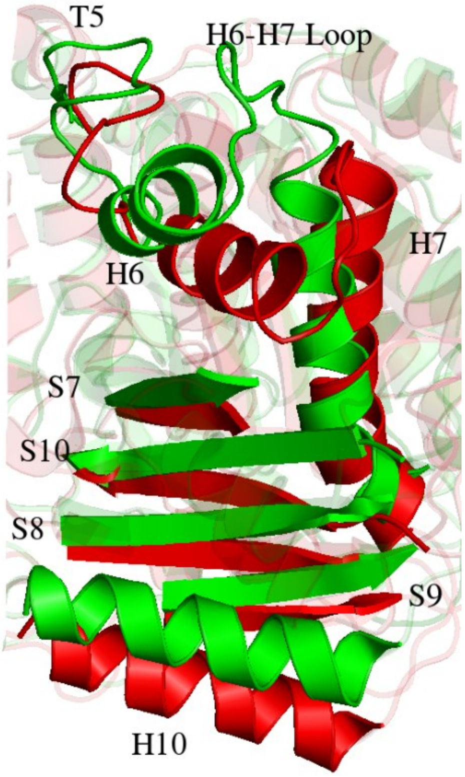

Figure 2.3: Conformation of the curved and straight β-tubulin. The structural superimposition of straight β-tubulin on curved β-tubulin. The straight β-tubulin (1JFF) is colored in red, and the curved β-tubulin (1SA0) is colored in green. H6 (Ala206-Ile215), H7 (Asp224-Phe242), and H10 (Glu325-Ser338). S7 (Met267-Pro272), S8 (Val313-Arg320), S9 (Ile356-Leu361), S10 (Asn373-Ile381)). M (Pro272-Leu289), H1-S2 (His28-Ile47), T5 (Ser172-Try183) and H6-H7 (Lys216-Gly223) loops of β-tubulin

The curved (1SA0) and straight (1JFF) α, β-tubulin superimposition shows that the two α-subunits of curved or straight tubulins are uniformly organized with no variation in conformation of their domains compared to β-tubulin. (**Figure 2.4**)

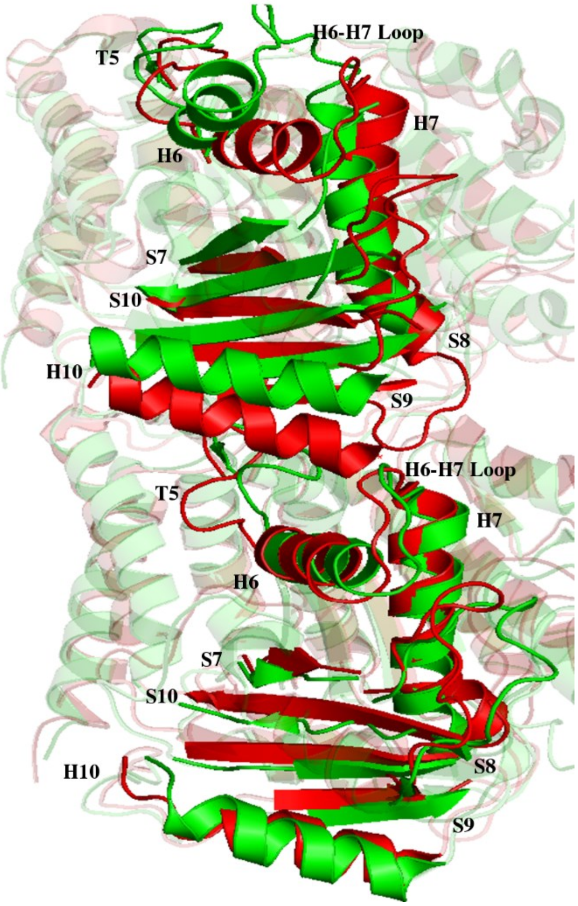

Figure 2.4: Superimposition of straight α, β-tubulin heterodimer on its curved conformation. The straight α, β-tubulin heterodimer (1JFF), is colored in red, and its curved conformation (1SA0) is depicted in green.

To quantitatively address the curved and straight conformations, distance from center the of mass (dCOM) between H7 helix (Phe225-Leu231) N-terminal and S6 strand (Cys201-Asp206) for available crystal conformations was evaluated. The curved β-tubulin has a distinct curvature, especially within the N-terminal of the H7 helix, compared to the straight conformation. The S6 strand is selected because it does not rearrange during the conversion between straight and curved conformations. Hence it is instead a stable secondary structure segment of the γ-tubulin. (**Figure 2.5**)

The dCOM for the H7 helix and S6 strand with available crystal structures shows 1.5 Å differences between β-curved (1SA0) and β-straight (1JFF). (**Table 2.3**)

The dCOM values of the H7 (Phe225-Leu231) helix from the S6 (Cys201-Asp206) strand of γ-tubulin is considered a curved conformation for 1.6 nm or lower and a straight for a value more than 1.7 nm. This evaluation is based on the superimposition of conformation of γ-tubulin on both curved and straight β-tubulin. Intermediate conformation shows similarity in both straight and curved β-tubulin, and its dCOM of H7 helix from the S6 strand is between the curved and straight with a value from 1.6 nm - 1.7 nm.

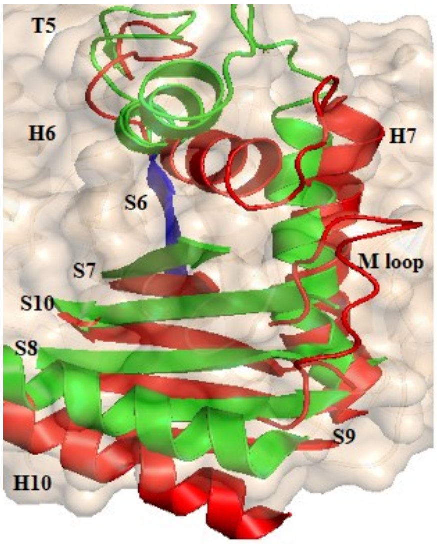

Figure 2.5: The position of H7 helix and S6 strand with respect to each other.

The H7 helix of both curved (1SA0) and straight (1JFF) β-curved are superimposed over each other and colored in green and red, respectively. The S6 strand is colored blue.

Crystal structure	**1JFF (Chain B)** **H7: 225-231** **S6:200-203**	**1SA0 (Chain B)** **H7: 228-234** **S6:200-203**	**3CB2 (Chain A)** **H7: 226-231** **S6:201-206**	**3CB2 (Chain B)** **H7: 226-231** **S6:201-206**	**1Z5V** **H7: 226-231** **S6:201-206**	**1Z5W** **H7: 226-231** **S6:201-206**
dCOM H7-S6 (nm)	1.66	1.5	1.59	1.54	1.56	1.57

Table 2.3: The dCOM of H7 helix and S6 strand for crystal conformations of β and γ-tubulin. For crystal structure of β-curved, β-straight, and γ-tubulin the dCOM of H7 and S6 is measured.

The straightness and curvature related to the conformation of the γ-tubulin have not been addressed since the effect of the ionic condition is not known; it is still elusive whether this protein adapts the straight conformation or not. Another uncertainty is whether GTP affects the dominant conformation of the γ-tubulin or not. Also, the impact of cations on the conformational changes and the curvature of γ-tubulin will be addressed here.[44]

Root means square deviation (RMSD) of the backbone atoms of γ-tubulin was evaluated during 200 ns of every set of MD simulations. The RMSD was conducted to evaluate protein stability during 200 ns of MD simulations. It demonstrates that the $ZnCl_2$ simulation converged at 110 ns, $MgCl_2$, and NaCl at 130 ns. Each MD simulation with different cations had a different path on its energy surface, and they run independently. Therefore, they showed different convergence times. For all MD simulations, the last 50 ns simulations are stable with minimum fluctuation of ~ ± 0.03 nm and are converged among all simulations. Therefore, for all MD simulations, the data analysis was carried out for the last 50 ns from 150 ns to 200 ns. (**Figure 2.6**)

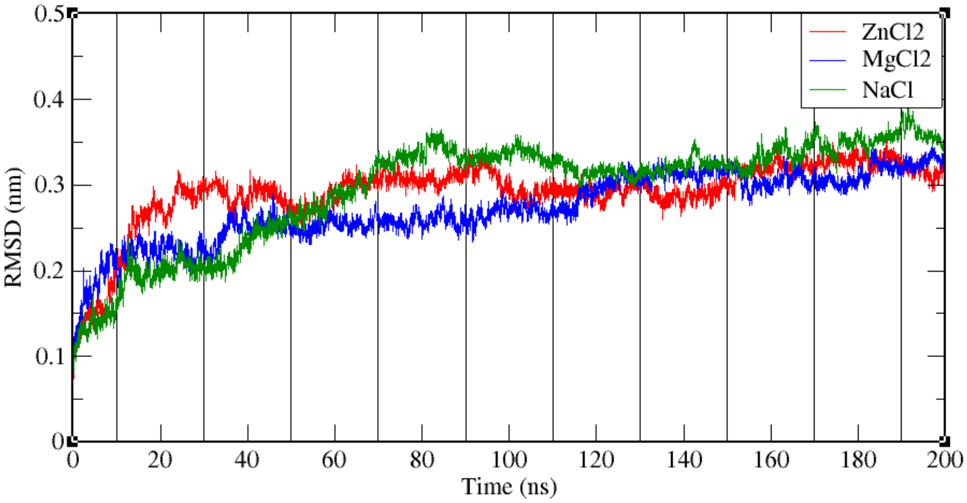

Figure 2.6: The RMSD plot of backbone atoms of γ-tubulin with unliganded (no substrate) MD simulations. The RMS deviation under $MgCl_2$, NaCl, and $ZnCl_2$ within 200 ns of each set of MD simulations are colored in blue, green, and red, respectively.

2.1.3.2 Dominant Conformation of Unliganded γ-tubulin Monomer

In this study, to address the conformational changes of γ-tubulin, its structure is superimposed on the straight (1JFF) and curved (1SA0) β-tubulin. Evaluated segments rearrange during curved to straight transition, including H6 (Asn207-Asp216), H7 (Phe225-Leu243), and H10 (Pro330-Arg343) helices as well as the intermediate domain strands of S7 (Phe268-Tyr273), S8 (Tyr317-Gln325), S9 (Ile356-Ser361), S10 (Ser374-His381). The loops that contribute to conversion from curved to straight conformation are composed of M (Thr274-289Thr) loop, T5 (Pro173-Gln184), and H6-H7 (Arg217-Ser224) loops.

Contributing segments to straightness and curvature were superimposed on the same secondary structure segments of both straight (1JFF) and curved (1SA0) β-tubulin for comparison. Also, the H7 helix (Phe225-Leu231) and S6 strand (Cys201-Asp206) dCOM was measured and compared with the dCOM of the H7 helix and the S6 strand of the known curved (1SA0) and straight (1JFF) β-tubulin crystal structure.

The H7 helix from S6 strand dCOM of γ-tubulin in the $MgCl_2$ simulation is fluctuating ~ 1.56 nm from 150 to 180 ns and at the range of 1.57 ns to 1.59 nm from 180 ns to 200 ns of $MgCl_2$ trajectory. It is about 1.50 nm for NaCl and 1.53 nm in the $ZnCl_2$. The fluctuation in $ZnCl_2$ at 168 ns increases the dCOM of H7 helix and the S6 strand to 1.64 nm resembling the intermediate conformation. The dCOM of the H7 helix and S6 strand of the known curved and straight α, β-tubulin heterodimers are 1.5 nm and 1.65 nm, respectively. (**Figure 2.7 and Table 2.3**)

By evaluating dCOM of H7 helix and S6 strand during the last 50 ns of MD simulations, it is concluded the curved conformation is dominant in all three simulations, and intermediate conformation was seen at some points in the trajectory. (**Figure 2.7 and Table 2.3**)

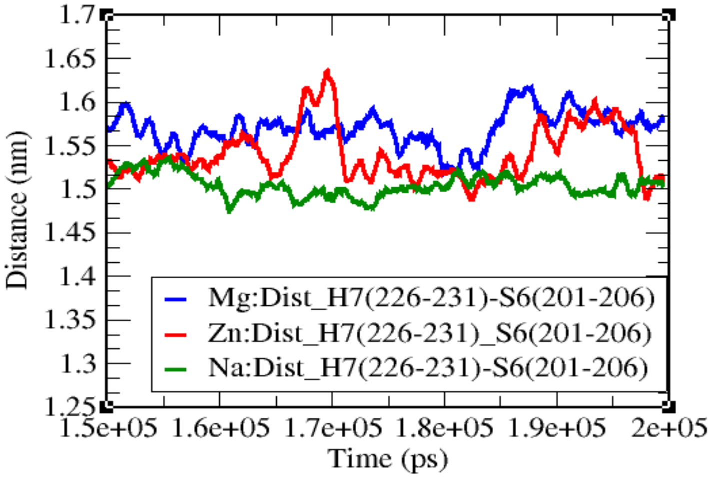

Figure 2.7: The dCOM of H7 helix (Phe225-Leu231) and the S6 strand (Cys201-Asp206) in unliganded MD simulations. The dCOM is evaluated from 150 ns to 200 ns of all three

trajectories. The distances with $MgCl_2$ is colored in blue. Those for $ZnCl_2$ are colored in red. Green is used for distances in NaCl.

In the $MgCl_2$ simulation, 200 ns conformation of its trajectory was extracted and superimposed over straight (1JFF) and curved (1SA0) β-tubulins. Next, the contributing helices and strands of γ-tubulins to straightness and curvature compared to reference conformations (chain B of 1JFF and chain B of 1SA0). Upon superimposition, the conformation of the H7 helix of γ-tubulin is aligned to the H7 helix of curved β-tubulin compared to the straight conformation of β-tubulin. (**Figure 2.8**)

The H6 helix is aligned to the curved β-tubulin as well. The three beta-strands of the intermediate domain S7 to S9 specifically, S7 (Phe268-Tyr273), S8 (Tyr317-Gln325), and S9 (Ile356-Ser361) are well organized in the same positions as the S7 to S9 strands of curved β-tubulin.

The conformation of the H10 (Pro330-Arg343) helix of γ-tubulin is aligned with none of the H10 helices of curved or straight β-tubulin. It can be deduced that the conformation of γ-tubulin at 200 ns of $MgCl_2$ simulation adapts a curved conformation. (**Figure 2.8**)

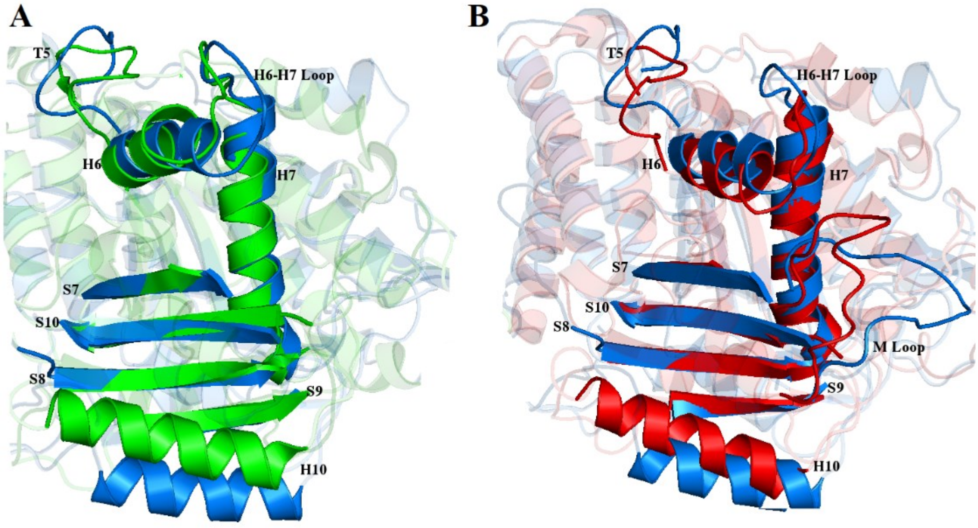

Figure 2.8: Superimposition of γ-tubulin in $MgCl_2$ simulation on curved (1SA0) and straight (1JFF) β-tubulin. A conformation of the trajectory of γ-tubulin at 200 ns in $MgCl_2$ colored in blue superimposed on β-curve (1SA0) and β-straight (1JFF). (**A**) Curved β-tubulin is colored green. (**B**) Straight β-tubulin colored in red.

In the $ZnCl_2$ simulation, the 200 ns conformation was superimposed over both the curved and straight β-tubulin. The conformation of the H6 and H7 helices, intermediate domain strands are aligned to the curved β-tubulin (1SA0). (**Figure 2.9**)

The conformation of γ-tubulin at 200 ns of $ZnCl_2$ adapts to the curved structure.

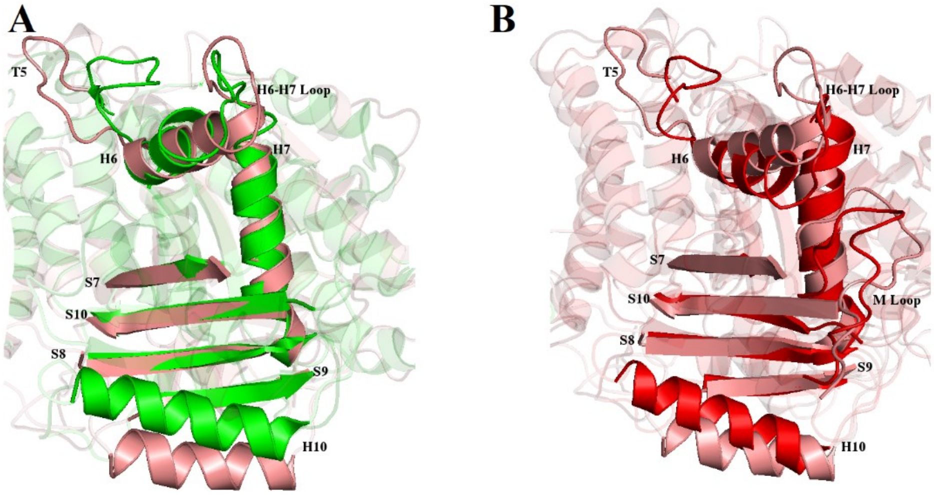

Figure 2.9: Superimposition of γ-tubulin in the $ZnCl_2$ simulation on curved (1SA0) and straight (1JFF) β-tubulin. A conformation γ-tubulin at 200 ns in $ZnCl_2$ colored in pink. (**A**) Curved β-tubulin (1SA0) is colored in green. (**B**) Straight β-tubulin(1JFF) colored in red.

In the NaCl simulation, a 200 ns conformation of the trajectory was extracted for analysis of its curvature and straightness based on the known curved (1SA0) and the straight (1JFF) conformations of β-tubulin. (**Figure 2.10**)

The H7 (Phe225-Leu231) helix of γ-tubulin is well-aligned with the H7 helix of the curved β-tubulin compared to that of the straight conformation, especially at the N-terminal. The conformation of the H7 represents the curved conformation, and as it was discussed, the dCOM of H7 and S6 is ~ 1.5 nm, which resembles the curved conformation. (**Figure 2.10**)

The H6 helix (Asn207-Asp216) and beta-strands orientations for S7 (Phe268-Tyr273), S8 (Tyr317-Gln325), S9 (Ile356-Ser361), and S10 (Ser374-His381) are aligned to their counterpart at curved β-tubulin as well. In conclusion, the γ-tubulin under NaCl condition is largely found to be aligned to the curved β-tubulin in comparison to that of straight conformation of β-tubulin. (**Figure 2.10**)

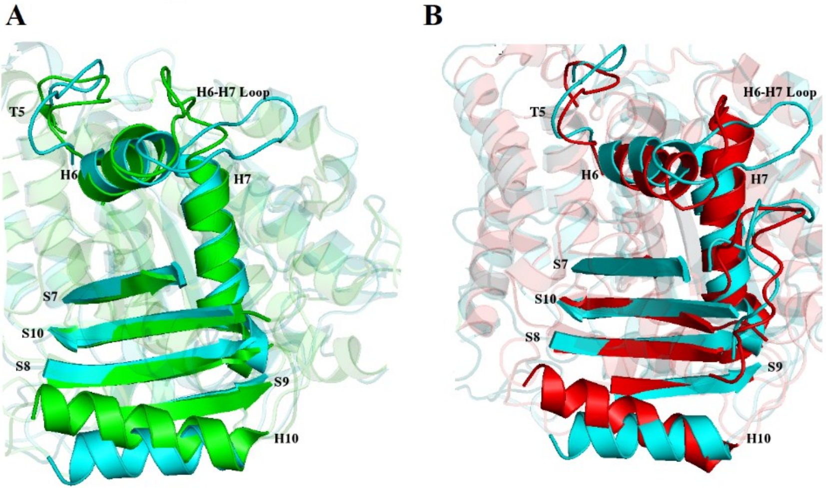

Figure 2.10: Superimposition of γ-tubulin in NaCl simulation on curved (1SA0) and straight (1JFF) β-tubulin. A conformation of the trajectory of γ-tubulin at 200 ns under NaCl colored in cyan superimposed on β-curve (1SA0) and β-straight (1JFF). (**A**) Curved β-tubulin is colored in green. (**B**) Straight β-tubulin colored in red.

None of the repeated simulations show exactly the same value of dCOM between the H7 and the S6 strand as the main experiments, but most conformations are intermediate and curved. The set one of repeated simulation in unliganded $MgCl_2$ has large fluctuations at 153 ns, 166 ns, 170 ns, and 189 ns that the dCOM of H7 and S6 reached 175 nm, 176 nm, 177 nm, and 179 nm, respectively. For the second set in $MgCl_2$, it fluctuates around 1.6 nm until 180 ns and ~ 1.5 nm from 180 ns – 200 ns, shows major seen conformation is intermediate. For set one of unliganded $ZnCl_2$ until 185 ns, the dCOM is ~ 163 nm, and for the rest of the simulation and also for set two, it is around 1.52 nm with curved conformation. The unliganded NaCl has dCOM of H7, and S6 ranges from 157 nm – 160 nm of intermediate conformation from 150 ns to 200 ns for set one, and for set two, it is about 156 nm of curved conformation. **(Figure A1 - A3)**

2.1.3.3 Conformational Stability of γ-Tubulin Under Ionic Conditions

To address the role of electrolytes in the γ-tubulin structural stability, residues that lost contribution to helicity were counted at150 ns, 160 ns, 170 ns, 180 ns, 190 ns, and 200 ns, as well as the cluster conformation. Cluster conformation was obtained after clustering the last 50 ns of each MD simulation and then extracting the conformation with the lowest RMSD compared to all other conformation from 150 ns to 200 ns. For each conformation, all helices were extracted and compared with the reference crystal conformation of γ-tubulin (chain A of PDB of 3CB2). (**Figure 2.11**)

The helices in the $MgCl_2$ simulation are more stable and retain their helical shape. The number of residues of all 12 helices over 7 mentioned conformations of γ-tubulin that lost their contribution to the secondary conformation in the NaCl simulation was 20, and in the $ZnCl_2$ simulation, it was 26. The number of these residues in the $MgCl_2$ simulation was 10. These numbers are averaged over 7 aforementioned conformations, at 150 ns, 160 ns, 170 ns, 180 ns, 190 ns, and 200 ns, as well as the lowest RMSD at the last 50 ns. The average describes sums of residues that lost their contribution to the helical structure at the 7 aforementioned conformations divided by 7.

Gly11, Gln12, and Cys13 at 150 ns and lowest RMSD conformations not contributing to the helicity of H1 helix (Gly11-Glu28) in the $MgCl_2$ simulation. (**Figure 2.11**)

In NaCl simulation, three residues, including Glu125, Ala126, Asp127 of the H3 helix (Trp104-Asp127), and Phe225, Ser226, Glu227 in H7 (Phe225-Leu243) helix for all seven aforementioned conformations have lost their helicity. Also, in NaCl simulation, H2 (Arg72-Asn79) helix residues of Arg72, Val73, Ile74, and His75 at 180 ns and lowest RMSD conformations, as well, five H12 (Asp419-Ala437) residues of Asp419, Glu420, Met421, Asp422 and Thr423 at 160 ns and 180 ns have lost their contribution in a helical conformation. In the $ZnCl_2$ simulation, three residues of Arg72, Val73, Ile74 of N-terminal and Leu78, Asn79 of C-terminal of H2 (Arg72-Asn79) helix at 170 ns, 180ns, 190ns, 200 ns, and the lowest RMSD have lost their contribution to helicity. Ser239, Thr240, and Thr241 at 160 ns, Thr240, T241, Thr242, and L243 of H7 helix (Phe225-Leu243) at the lowest RMSD conformation have found to be part of the loop. The H12 helix (Arg72-Asn79) unfolded at 170ns, 180ns, 190ns, 200 ns, and the lowest RMSD conformation for 6 residues of Asp419, Glu420, Met421, Asp422, Thr423, and Ser424. (**Figure 2.11 and 2.12**)

The H12 helix in $ZnCl_2$ and NaCl simulations is unfolded into loops for six residues, including Asp419, Glu420, Met421, Asp422, Thr423, and Ser424, and 4 residues of Asp419, Glu420, Met421, Asp422, respectively. However, the conformation is intact in the $MgCl_2$ simulation. (**Figure 2.11 & 2.12**)

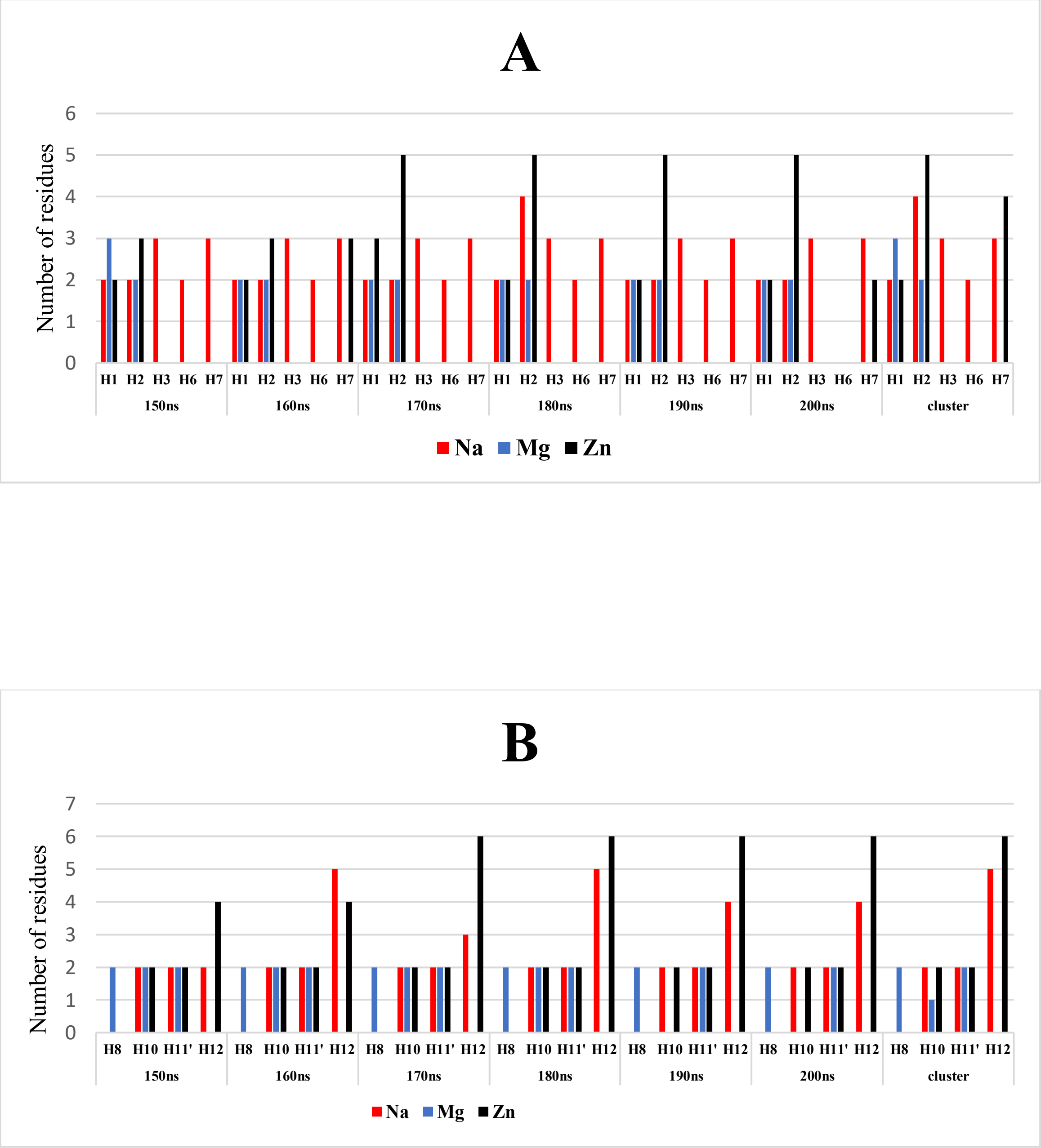

Figure 2.11: The conformational instability of the γ-tubulin for seven conformations in each simulation. The number of residues that lost their helicity for helices of γ-tubulin at 7 conformations (lowest RMSD conformation and conformations at 150ns, 160ns, 170ns, 180ns, 190nsand, and 200 ns) colored in red in NaCl, blue in $MgCl_2$, and black in the

$ZnCl_2$ simulation. (**A**) The number of residues that lost their contribution to helical conformation in helices H1, H2, H3, H6, and H7. (**B**) The number of residues that lost their contribution to helical conformation in helices H8, H10, H11, and H12.

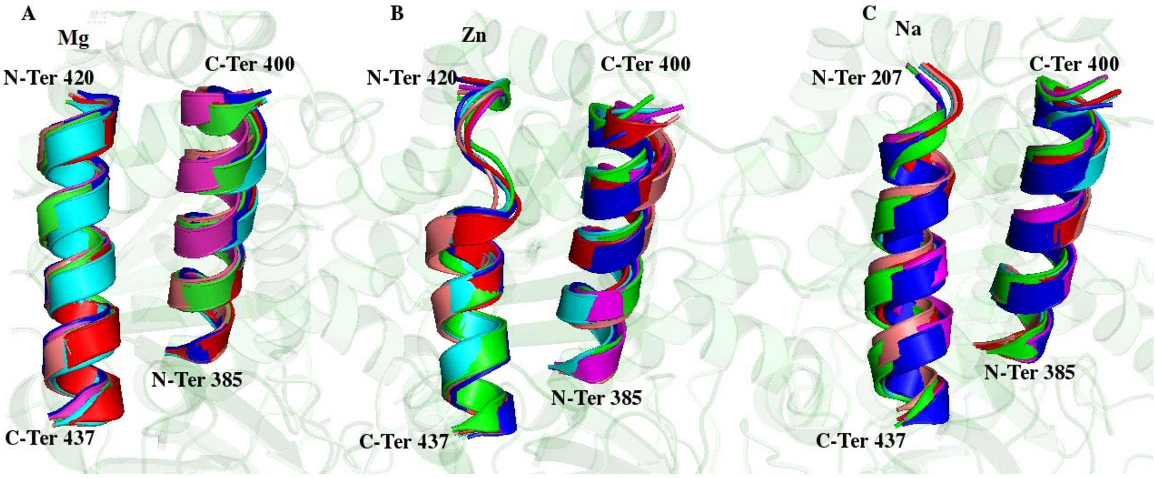

Figure 2.12: Slight conformational changes of helices of the C-terminal domain. The conformational changes of major helices of the C-terminal domain at 6 frames of the last 50 ns of all simulations. (**A**) H11 and H12 in the $MgCl_2$ simulation. (**B**) $ZnCl_2$ simulation and (**C**) NaCl simulation. Conformations at 150 ns, 160 ns, 170 ns, 180 ns, 190 ns, and 200 ns are colored in green, cyan, magenta, blue, orange, and red, respectively.

2.1.3.4 *Homo-sapiens* and Yeast γ-Tubulin in Active γTuSC

In yeast, the nucleation of MTs is achieved through γTuSC.[87] The γTuSC in *homo-sapiens* serves as a scaffold for the assembly of a more complicated complex (composed of

6-7 γTuSC), known as ring complex. With γTuSC, the two γ-tubulins interact laterally with each other and longitudinally interact SPC monomers.[87] (**Figure 2.13**)

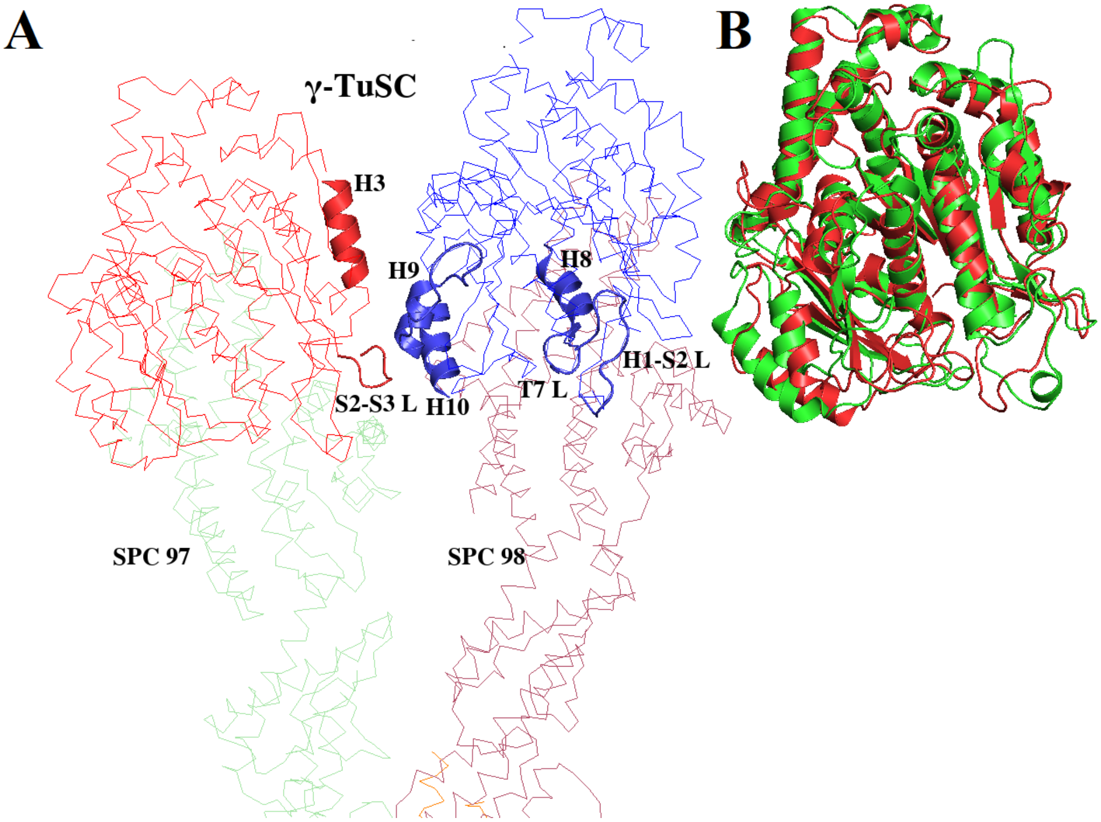

Figure 2.13: Structure of yeast γTuSC. (**A**) Two yeast γ-tubulins are colored in red and blue; their lateral interactions are depicted in cartoons for both monomers. (**B**) Structural superimposition of *homo-sapiens* γ-tubulin in red on to yeast γ-tubulin in green.

Homo-sapiens and yeast γ-tubulins are identical for 40% of their sequences. Hence, the three-dimensional conformations of both proteins are similar. The two monomers of the yeast dimer are in their functional and active conformations. Therefore, their secondary structure segments can be used as reference conformation to evaluate whether the secondary structure segments of *homo-sapiens* γ-tubulin are in their active shape or not.

Helices and loops of yeast γ-tubulin at γTuSC (PDB: 5FLZ) which contribute to lateral interactions with adjacent γ-tubulin are including the H3 (Trp104-Asp127), H8 (Leu253-Leu260), H9 (Val290-Leu298), H10 (Pro330-Arg343) helices, and the T7 (Thr240-Asp252), H1-S2 (His29-Arg47) and M (Thr274-289Thr) loops. They are interacting with secondary structure segments within the γTuSC (PDB: 5FLZ). (**Figure 2**.**13**)

Homo-sapiens conformation was compared to one yeast γ-tubulin monomer at γTuSC (PDB: 5FLZ) that contributes to the lateral interactions within the γTuSC. The reason for this comparison is that the γTuSC is an active complex; its helices and loops are in their functional and active forms. Therefore, it is possible to study the effect of cations on the conformations of *homo-sapiens* γ-tubulin.

Two *homo-sapiens* conformations were selected in each simulation; the first one was 200 ns conformation, and the second was the lowest RMSD conformation at the last 50 ns (cluster). With each simulation, the lowest RMSD at last 50 ns and 200 ns conformations were superimposed on yeast γ-tubulin of γTuSC for RMSD evaluation. (**Figure 2.14**)

Large dissimilarities in the orientations of the secondary structure segments of *homo-sapiens* γ-tubulin from the yeast γ-tubulin are found with the H1-S2 (His29-Arg47) and M (Thr274 - Thr289) loops. The dCOM of Glu39 of H1-S2 (His29-Arg47) belonging to the $MgCl_2$ simulation at 200 ns from Pro40 of the same loop of yeast γ-tubulin was 8.7 Å. The conformation of γ-tubulin at 200 ns and the lowest RMSD in $MgCl_2$ simulation is not aligned to the reference T7 loop. As it was mentioned, the reference conformation is the crystal structure of the yeast γ-tubulin. The M loop (Thr274 - Thr289) of both conformations of all simulations in NaCl, $MgCl_2$, and $ZnCl_2$ is not fully aligned to the M loop of the yeast γ-tubulin. (**Figure 2.14**)

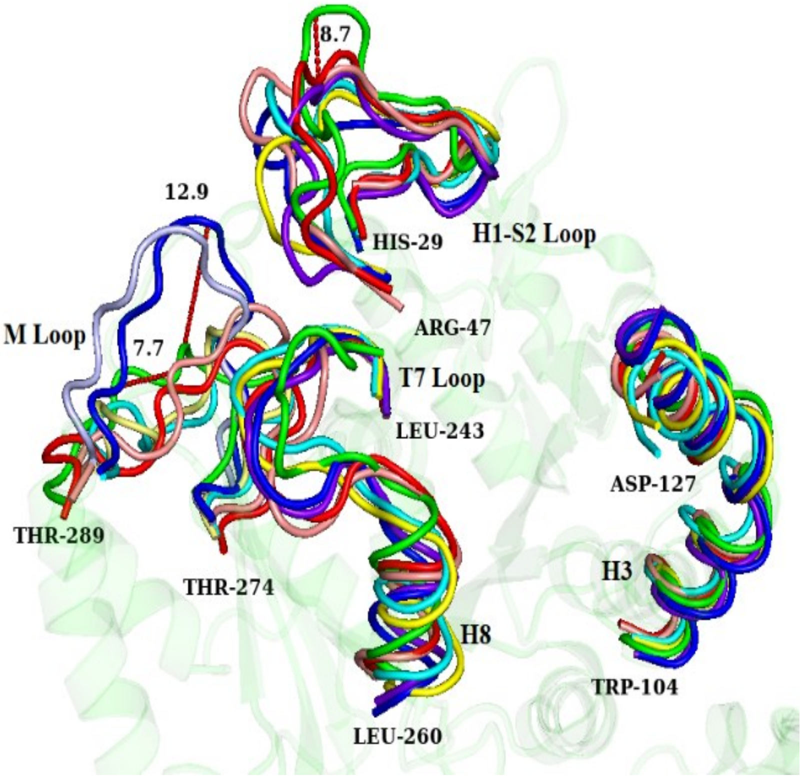

Figure 2.14: Structural superimposition of two conformations of *homo-sapiens* γ-tubulin on the yeast γ-tubulin, overall, three conformations. The (cluster) lowest RMSD of the last 50 ns and 200 ns conformation in three MD simulations superimposed over the reference conformation of yeast γ-tubulin of γTuSC (PDB: 5FLZ) colored in green. The lowest RMSD of the last 50 ns and conformation at 200 ns are respectively colored in

blue and purple-blue when representing $MgCl_2$, red and pink when representing $ZnCl_2$, and yellow and cyan are used for the NaCl simulation.

To obtain a better evaluation of electrolytes' role in inducing conformational changes in γ-tubulin comparable to that of active γ-tubulin at yeast γTuSC (PDB: 5FLZ). The RMSD of interacting regions of *homo-sapiens* γ-tubulin include (H3, H8, H10, T7, M loops) at two aforementioned conformations of the lowest RMSD of the last 50 ns and 200 ns were measured using the yeast γ-tubulin as a reference structure. (**Figure 2.15**)

The H3 (Trp104-Asp127) and H10 (Pro330-Arg343) helices are found having low RMSD from the reference yeast γ-tubulin in all three simulations ($ZnCl_2$, $MgCl_2$, and NaCl simulations); specifically, in the $ZnCl_2$ simulation, they have RMSD values of 0.4 Å and 0.4 Å for the lowest RMSD conformation respectively. The RMSD of H3 (Trp104-Asp127) and H10 (Pro330-Arg343) helices in the $ZnCl_2$ simulation for conformation at 200 ns were 1.3 Å and 1.2 Å, respectively. In $MgCl_2$ simulation, the H3 (Trp104-Asp127) and the H10 (Pro330-Arg343) had the RMSD of 0.7 Å and 0.8 Å for the lowest RMSD conformation at last 50 ns, respectively, and in NaCl simulation, they had RMSD of 0.6 Å for the conformation with the lowest RMSD. (**Figure 2.15**)

Also, the T7 (Thr240-Asp252) loop and the H8 (Leu253-Leu260) helix have a smaller RMS deviation with 1.2 Å and 1.4 Å for the lowest RMSD and conformation at 200 ns in the $ZnCl_2$ simulation, being 2.5 Å for both conformations under $MgCl_2$. Their RMSD was 2.6 Å and 2.5 Å in NaCl simulation for the conformation with the lowest RMSD and conformation at 200 ns, respectively. The M loop (Thr274-Thr289) and the H1-S2 loop

(His29-Arg47) have lower and larger RMSD values in NaCl simulation. The RMSD of M loop in NaCl simulations for lowest RMSD and last frame conformation at 200 ns were 1.4 Å and 1.1 Å respectively, and the RMSD of H1-S2 (His29-Arg47) loop were 3.0 Å and 2.5 Å for lowest RMSD and last frame conformations at 200 ns in NaCl simulation respectively. (**Figure 2.15**)

For H3 (Trp104-Asp127), H8 (Leu253-Leu260), H9 (Val290-Leu298), H10 (Pro330-Arg343) helices, T7 (Thr240-Asp252), H1-S2 (His29-Arg47), and M (Thr274-Thr289) loops, the sums of RMSD in the $ZnCl_2$ simulation were 6.6 Å and 6.5 Å for the lowest RMSD at last 50 ns and conformation at 200 ns. However, these values for $MgCl_2$ are 8.5 Å and 7.8 Å, and in NaCl they were 8.5 Å and 7.4 Å for the conformation with the lowest RMSD at the last 50 ns and last frame at 200 ns, respectively. It can be concluded that the orientations of the interacting secondary structure segments of γ-tubulin within a small yeast complex resemble the same secondary structure segments with the *homo-sapiens* γ-tubulin in the $ZnCl_2$ simulation with larger deviations seen in the $MgCl_2$ simulation. (**Figure 2.15**)

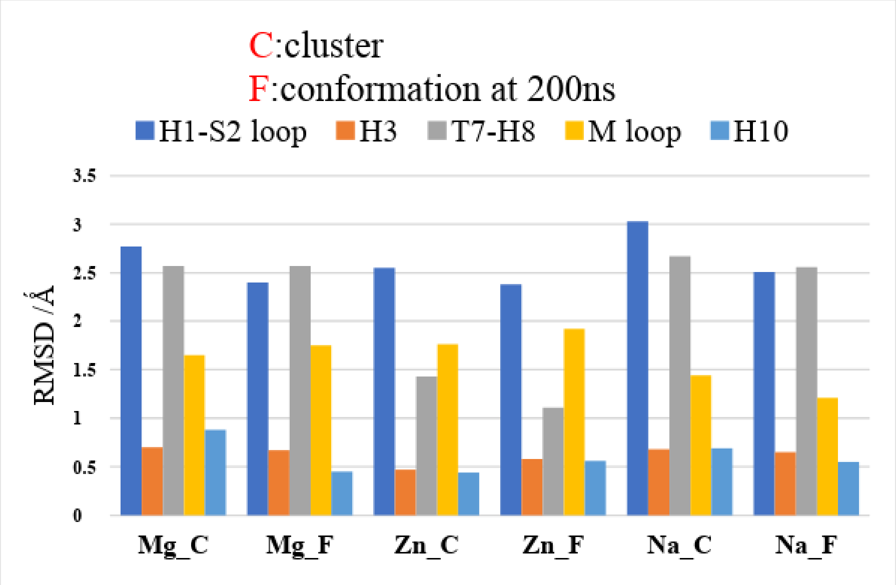

Figure 2.15: The RMSD of selected secondary structure segments of two conformations of *homo-sapiens* γ-tubulin from the yeast γ-tubulin. Two conformations of the *homo-sapiens* γ-tubulin include a conformation at 200 ns and also the conformation with the lowest RMSD at the last 50 ns conformation for all three simulations (MgCl2, $ZnCl_2$, and NaCl).

2.1.3.5 Interactions of Cations with γ-Tubulin

The minimum distance at which the cations interact with the protein, as well as their electrostatic energy with the γ-tubulin were evaluated to study how they interact with the protein in different simulations. The minimum distance evaluates the smallest distance between atoms of two predetermined molecules or atoms. [88] One group is set to γ-tubulin, and another group to the cations at each different simulation.

The minimum distances between Na^+ and γ-tubulin fluctuated around 2.5 Å - 3.5 Å. In contrast to Na^+, Mg^{+2} and Zn^{+2} interact at large distances of 3.6 Å – 4.1 Å, which was also stable for 150 ns to 200 ns of their MD trajectories. (**Figure 2.16 A**)

In addition, in the Mg^{2+} simulation, the minimum distances between Mg^{+2} and the three domains were also measured. The results reveal that the nucleotide-binding domain (NBD) and C-terminal domains interact at close distances to the Mg^{+2} compared to the intermediate domain. The minimum distances of Mg^{+2} from the N-terminal domain are stable at 3.9 Å. The value is about the same for the C-terminal domain, fluctuating at 152 ns and from 175 ns to 188 ns, which increasing it to 4.9 Å. The minimum distances of Mg^{+2} from the intermediate domain fluctuate around 6.1 Å from 150 ns to 175 ns and reach 4.1 Å at 178 ns; it rises to 10 Å at 190 ns. (**Figure 2.16 B**)

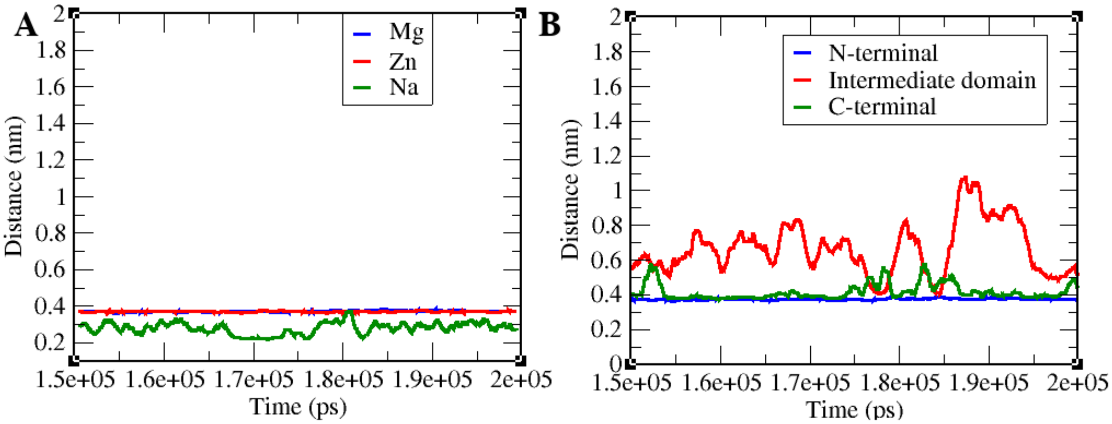

Figure 2.16: Minimum distances between cations and γ-tubulin. (**A**) minimum distances between Mg^{2+} (blue), Zn^{2+} (red), Na^+ (green) and γ-tubulin. (**B**) Minimum distances between Mg^{2+} and intermediate domain (red), N-terminal (blue), and C-terminal domain (green).

While the minimum distances between Na$^+$ and γ-tubulin are less than Mg^{+2} and Zn^{+2}, strong electrostatic energy with -1700.6 kJ/mol is observed between Zn^{+2} and protein. **(Figure 2.17)**

It is noticeable that NaCl concentration is twice as high as the MgCl$_2$ and ZnCl$_2$ with ~ 129 mml/L. The electrostatic energy between Na$^+$ and γ-tubulin is around ~ -500.3 kJ/mol and ~ -1500.9 kJ/mol between Mg^{2+} and protein. (**Figure 2.17**)

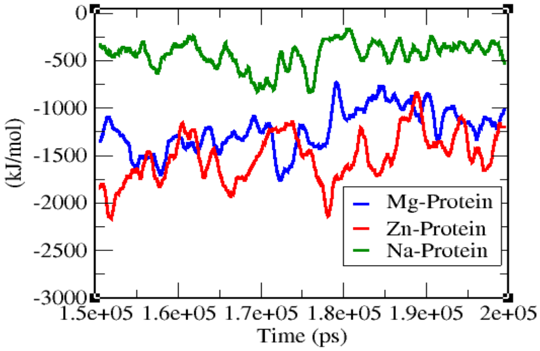

Figure 2.17: The electrostatic energy between Na$^+$, Mg^{+2}, Zn^{+2}, and γ-tubulin. The electrostatic energy from 150 ns to 200 ns is colored in blue, red, and green for MgCl$_2$, ZnCl$_2$, and NaCl, respectively.

The electrostatic energy between the intermediate domain and Zn^{+2}, Mg^{+2}, and Na$^+$ is less than -6 kJ/mol. The C-terminal electrostatic energy with cations in NaCl, MgCl$_2$, and ZnCl$_2$ simulations is -88.9 kJ/mol, -244.3 kJ/mol, and -446.5kJ/mol, respectively. For the NBD, the electrostatic energy is fluctuating around -340.8 kJ/mol, -1063.2 kJ/mol and -976.4 kJ/mol in NaCl, MgCl$_2$' and ZnCl$_2$ simulations. NBD interacts more strongly with cations regardless of their charges, and weaker electrostatic interactions have been found between the intermediate domain (ID) and cations of the three simulations. (**Figure 2.18**)

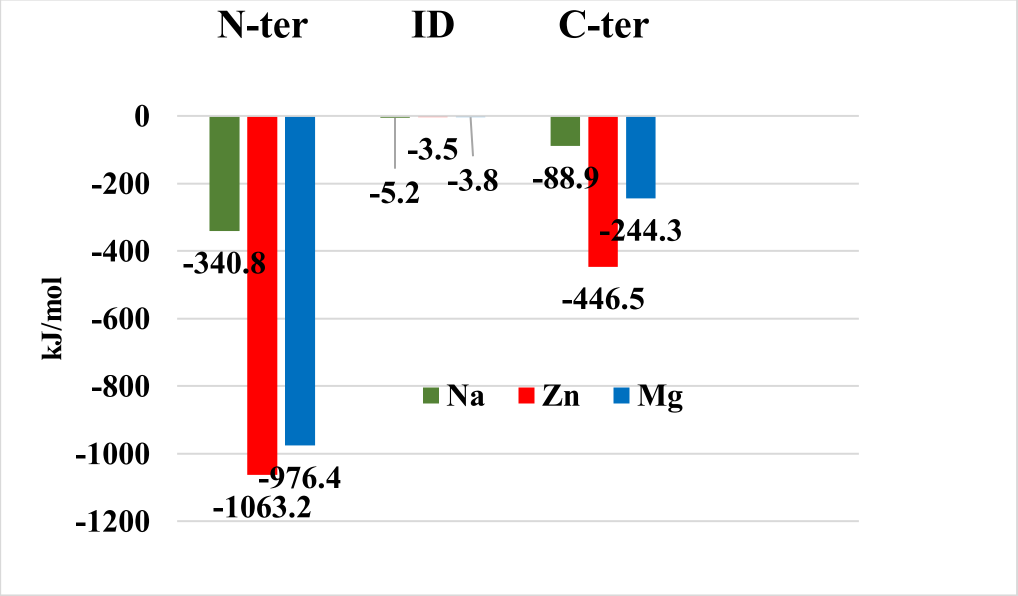

Figure 2.18: The electrostatic energy between cations and three domains of γ-tubulin. The electrostatic energy between cations and each domain is colored in red for $ZnCl_2$, green in NaCl, and blue for $MgCl_2$ simulations. ID: intermediate domain. N-ter: N-terminal. C-ter: C-terminal

2.1.3.6 GTP Binding Site

The GTP binding site at NBD of the γ-tubulin is created by the contribution of S2 (Ala64-Asp68), S4 (Gly134-Ser140), S5 (Leu165-Phe172) strands. The H1 (Gly11-Glu2), H3 (Arg72-Asn79), H4 (Thr145-Arg160), and H7 (Phe225-Leu243) helices as well as the T3 (Ser94-Asn103) the T5 (Pro173-Gln184) loops.

It was found in unliganded NaCl simulation movement of the T5 loop toward the H3 and

H7 helices resulting in the limited accessibility of the GTP binding site. This observation was seen at 173 ns of NaCl simulation. **(Figure 2.19 A**)

In an unliganded $MgCl_2$ simulation with intermediate conformation the GTP binding site was seen to be accessible compared to the NaCl simulation. This was observed in $MgCl_2$ at186 ns with an intermediate conformation, which shows the GTP binding site forms an accessible state, which probably accommodates GTP. (**Figure 2.19 B**)

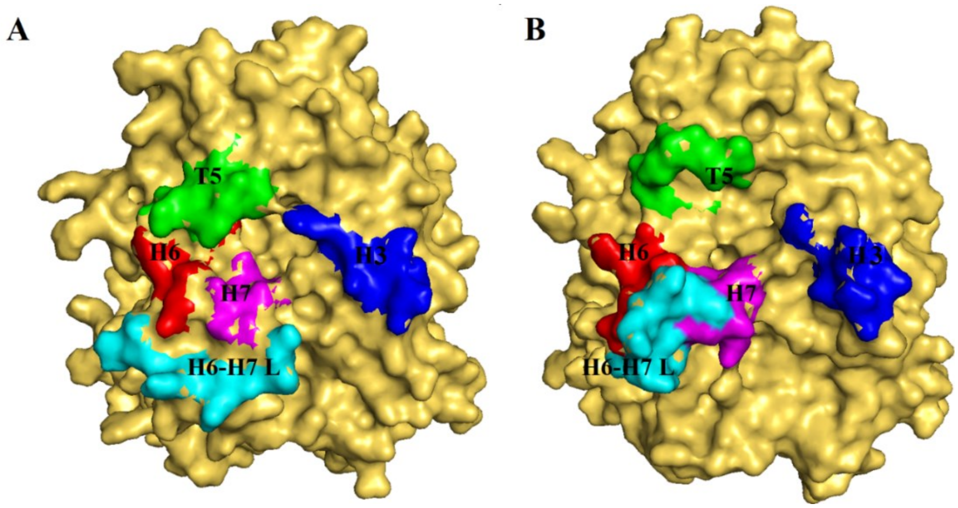

Figure 2.19: Conformations of the GTP binding site in unliganded $MgCl_2$ and NaCl simulations. **(A)** A non-accessible conformation of the GTP binding site at 173 ns of NaCl simulation. (**B)** Accessible state of the GTP binding site at 186 ns of the $MgCl_2$ simulation. The T5 loop and H3 helix colored in green and blue, respectively. The H6, H6-H7 loop, and H7 are depicted in red, cyan, and magenta, respectively.

The dCOM between Asp180 of the T5 from the Arg72 of the H3 and the Glu177 of the T5 from the Gln277 of the H7 helix were evaluated. These measurements were made to investigate how T5 loop movement toward H3 and H7 contributes to the accessibility of the binding site. The dCOM of Asp180 from Arg72 fluctuated around 1.1 nm from 175 ns to 200 ns with lower distances at 170 ns and 195 ns. (**Figure 2.20 B**)

However, in the $ZnCl_2$ simulation, the dCOM of Asp180 from Arg72 fluctuated around 2.2 nm from 160 ns to 200 ns. In the $MgCl_2$ simulation, from 170 to 195 with 1.6 nm, and at 200 ns it has a value of 1.5 nm. This shows how the T5 loop moves toward the H3 helix and, as shown, affects the availability of the GTP binding site. (**Figure 2.20 B**)

Also, the Glu177 dCOM from the Gln227 was measured to better reveal how the contribution of T5 loop movement induces a not-accessible state. The dCOM of Glu177 and Gln 227 in NaCl simulation fluctuated around 1.3 nm, and in $MgCl_2$ simulation, it changed around 1.8 nm. Around 2.4 nm in $ZnCl_2$ simulation, which showed ~ 0.5 nm and ~ 0.9 nm larger in $MgCl_2$ and $ZnCl_2$ compared to NaCl. (**Figure 2.20 A**)

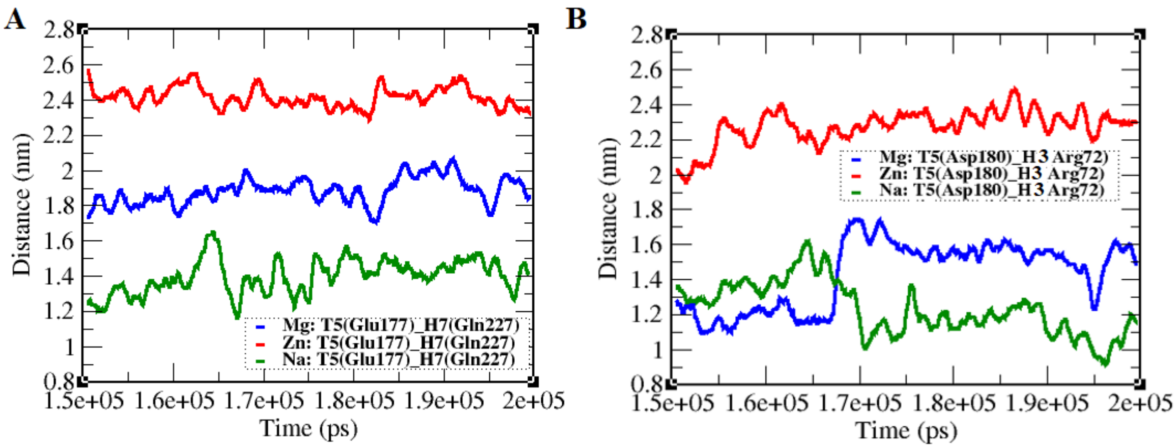

Figure 2.20: The dCOM of Glu177 from Gln227 and Asp180 from Arg72. (**A**) the dCOM of Glu177 of the T5 loop from Gln227 belongs to H7 helix. (**B**) the dCOM of Asp180 of

the T5 loop from Arg72 of H3 helix. The dCOM is colored in green, blue, and red for NaCl, MgCl2, and $ZnCl_2$ simulation, respectively.

2.2 MD Simulation of GTP-Bound γ-Tubulin Monomer Under NaCl, $MgCl_2$, and $ZnCl_2$ Ionic Conditions

The RMSD of backbone atoms during the course of the MD simulations were measured. The reference structure was set to the last conformation of the equilibrium simulation.

The convergence point in $MgCl_2$ simulation is at 60 ns, while both $ZnCl_2$ and NaCl converge at 138 ns. For three simulations, the last 50 ns are considered for evaluation and analysis of the obtaining data. (**Figure 2.21**)

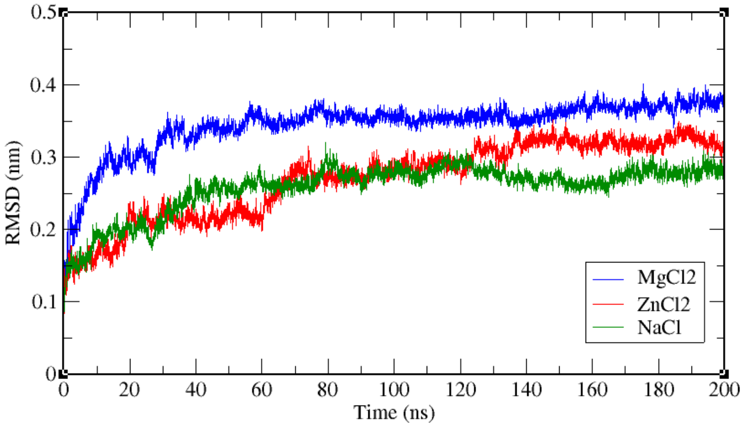

Figure 2.21: The RMSD of the backbone atoms of the γ-tubulin under GTP-bound simulations. The RMSD of $ZnCl_2$ is represented in red, NaCl in green, and blue for $MgCl_2$.

2.2.1 Impact of Cations and GTP on Dominant Conformation of γ-Tubulin

Whether GTP induces straightness on the tubulins' conformation still remains elusive and is not addressed especially with the *homo-sapiens* γ-tubulin. For assessing the straightness and curvature of GTP-bound γ-tubulin during MD simulations, the distances from dCOM of H7 helix (Phe225-Leu231) and the S6 strand (Cys201-Asp206) strand were monitored for three simulations from 150 ns to 200 ns. The dCOM of the H7 helix (Phe225-Leu231) and S6 strand (Cys201-Asp206) in the NaCl simulation starts at 1.67 nm at 150 ns, then decreases to 1.60 nm at 153 ns and for the rest of the simulation from 155 ns to 195 ns fluctuated from 1.68 nm - 1.70 nm. The dCOM of H7 and S6 in NaCl simulation shows that the intermediate conformation is dominant. **(Figure 2.22 and Table 2.3)**

The H7 helix (Phe225-Leu231) and S6 strand (Cys201-Asp206) dCOM, in $MgCl_2$ simulation, fluctuates between 1.55 nm - 1.58 nm from 150 ns to 200 ns and therefore resemble a curved conformation with the dCOM lower than 1.6 nm. (**Figure 2.22**)

In $ZnCl_2$ at 150 ns, it is 1.60 nm, then reaches 1.70 nm at 155 ns, and after that, it decreases to around 1.57 nm until the end of the simulation. Therefore in $ZnCl_2$ simulation, the curved conformation is dominant as the dCOM of the H7 and the S6 is less than 1.6 nm, but the intermediate conformation was also observed at 155 ns with dCOM of 1.6 nm. (**Figure 2.22**)

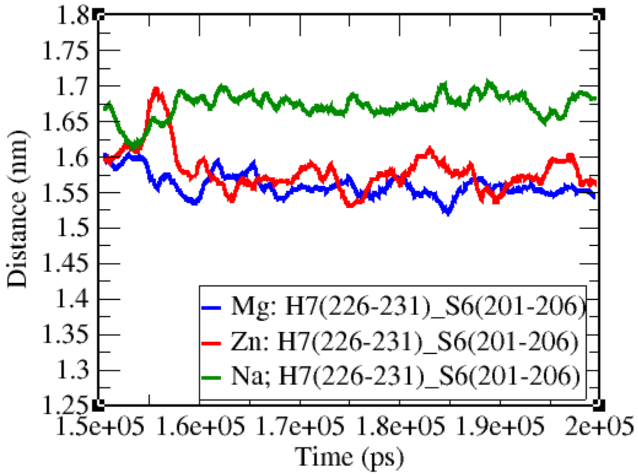

Figure 2.22: The dCOM of H7 helix and S6 strand in GTP-bound simulations. The dCOM of H7 and S6 was represented in blue for $MgCl_2$, in green for NaCl, and red for $ZnCl_2$.

As an example, for every set of simulations, one conformation of their trajectories (e.g., a conformation of γ-tubulin from $MgCl_2$, NaCl, or $ZnCl_2$ simulations) at 200 ns was selected in order to determine its curvature or straightness. **(Figure 2.22 & 2.23)**

As mentioned, the secondary structure segments including H6 (Asn207-Asp216), H7 (Phe225-Leu243), H10 (Pro330-Arg343) helices and the intermediate domain strands of S7 (Phe268-Tyr273), S8 (Tyr317-Gln325), S9 (Ile356-Ser361), S10 (Ser374-His381) as well as loops include M (Thr274-289Thr), T5 (Pro173-Gln184) and H6-H7 (Arg217-Ser224), contributing to the rearrangement from curved to straight conversion. (**Figure 2.3 and Table 2.3**)

The GTP-bound γ-tubulin in $MgCl_2$ at 200 ns was superimposed on both curved (1SA0) and straight (1JFF) conformations of the β-tubulin. (**Figure 2.23**)

Four beta-strands of the intermediate domain, S7 – S10, are aligned to their counterpart at the curved β-tubulin. The conformation of the H6 helix (Asn207-Asp216) is aligned to the H6 helix of the straight β-tubulin. The H7 helix is aligned to the H7 helix of curved β-tubulin. The M (Thr274-289Thr) and T5 (Pro173-Gln184) loops are superimposed to that of M and T5 loops of the straight conformation. (**Figure 2.23**)

In conclusion, it can be said that by considering other secondary structure segments such as S7 to S10 strands, H6, and H7 helices, the overall conformation of the γ-tubulin at 200 ns in GTP-MgCl$_2$ simulation exists as curved conformation. (**Figure 2.23**)

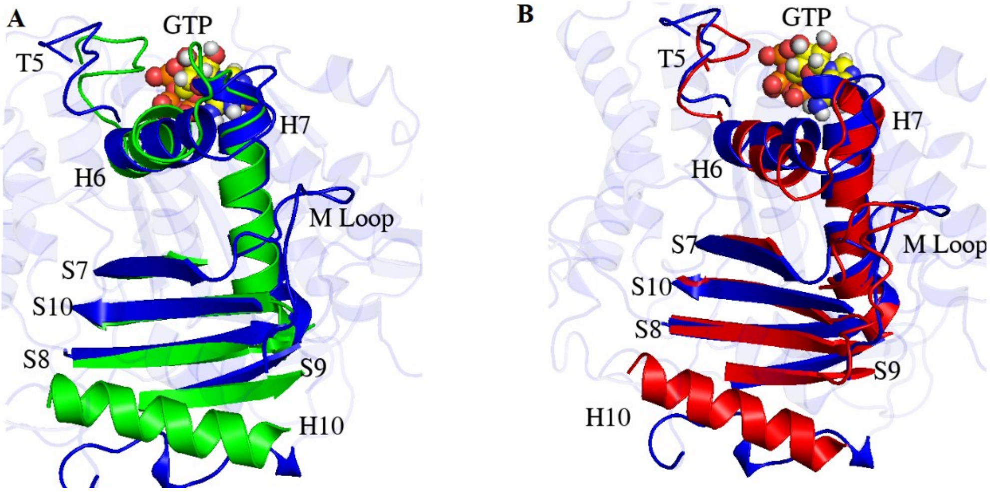

Figure 2.23: Superimposition of the monomer of GTP-bound γ-tubulin on curved (1SA0) and straight (1JFF) β-tubulin in MgCl$_2$ simulation. The 200 ns conformation of γ-tubulin in GTP-MgCl$_2$ colored in blue superimposed on β-curve (1SA0) and β-straight (1JFF). (**A**) Curved β-tubulin (1SA0) is colored in green. (**B**) Straight β-tubulin colored in red (1JFF).

In $ZnCl_2$, the 200 ns conformation was superimposed on the straight (1JFF) and the curved (1SA0) conformations of the β-tubulin. (**Figure 2.24**)

The H6 (Asn207-Asp216) and H7 (Phe225-Leu243) helices are aligned to the H6 and H7 helices of the curved β-tubulin (1SA0). The intermediate domain strands of γ-tubulin such as S7 (Phe268-Tyr273), S8 (Tyr317-Gln325), S9 (Ile356-Ser361), S10 (Ser374-His381), and H10 helix (Pro330-Arg343) over the shown superimposition are arranged in a direction that is not similar to the straight or curved conformations of the β-tubulin, the intermediate conformation explains their shape. (**Figure 2.24**)

The orientations of the M (Thr274-289Thr) and T5 (Pro173-Gln184) loops are aligned with their counterparts with the curved conformation of the β-tubulin. It can be concluded that curved conformation is dominant for conformation at 200 ns of the $ZnCl_2$ simulation. (**Figure 2.24**)

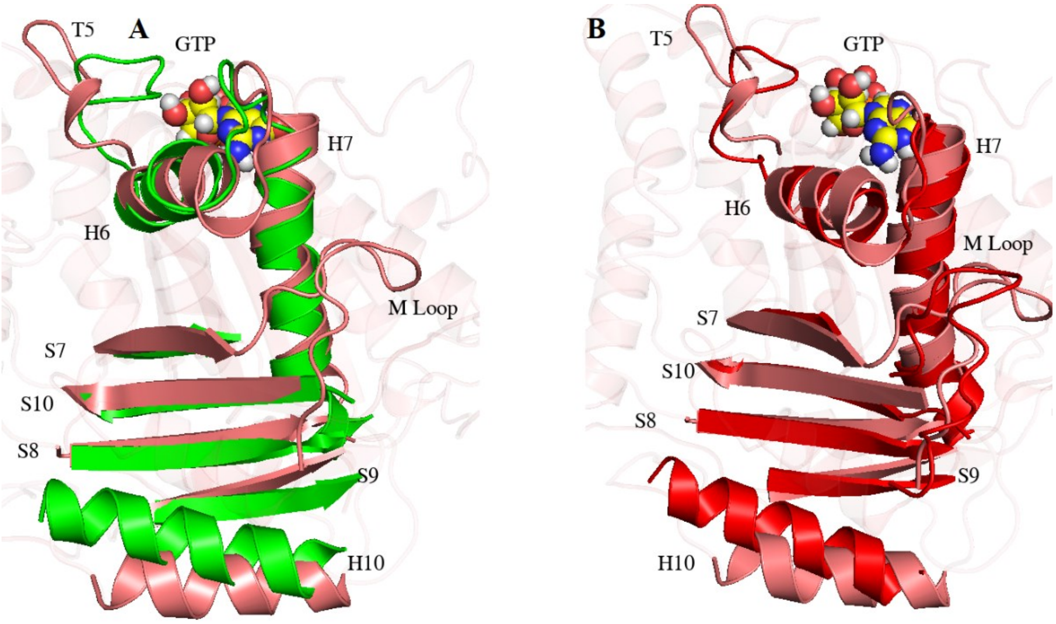

Figure 2.24: Superimposition of GTP-bound γ-tubulin on curved (1SA0) and straight

(1JFF) β-tubulin in $ZnCl_2$ simulation. The 200 ns conformation of γ-tubulin in GTP-bound under $ZnCl_2$ colored in pink superimposed on β-curve (1SA0) and β-straight (1JFF). (**A**) Curved β-tubulin is colored in green (1SA0). (**B**) Straight β-tubulin colored in red (1JFF).

In NaCl, the conformation of γ-tubulin at 200 ns was extracted and superimposed onto the curved and straight β-tubulin. After superimposition, it can be seen that the H7 helix is not aligned to the H7 helix of the curved and straight β-tubulin rather, it adapts the intermediate conformation. (**Figure 2.25**)

However, other secondary structure segments, such as the beta-strands of S7 (Phe268-Tyr273), S8 (Tyr317-Gln325), S9 (Ile356-Ser361), and S10 (Ser374-His381) are aligned to the curved conformation of β-tubulin. This is an indication of an intermediate conformation that structurally adapted a shape close to both the curved and straight conformations. (**Figure 2.25**)

The dCOM of H7 helix (Phe225-Leu231) from the S6 strand (Cys201-Asp206) in NaCl simulation is 1.7 nm ranging from 150 ns to 200 ns, and it has been said that it resembles an intermediate conformation. The conformation of γ-tubulin at 200 ns of NaCl simulation is rather similar to an intermediate conformation. (**Figure 2.25**)

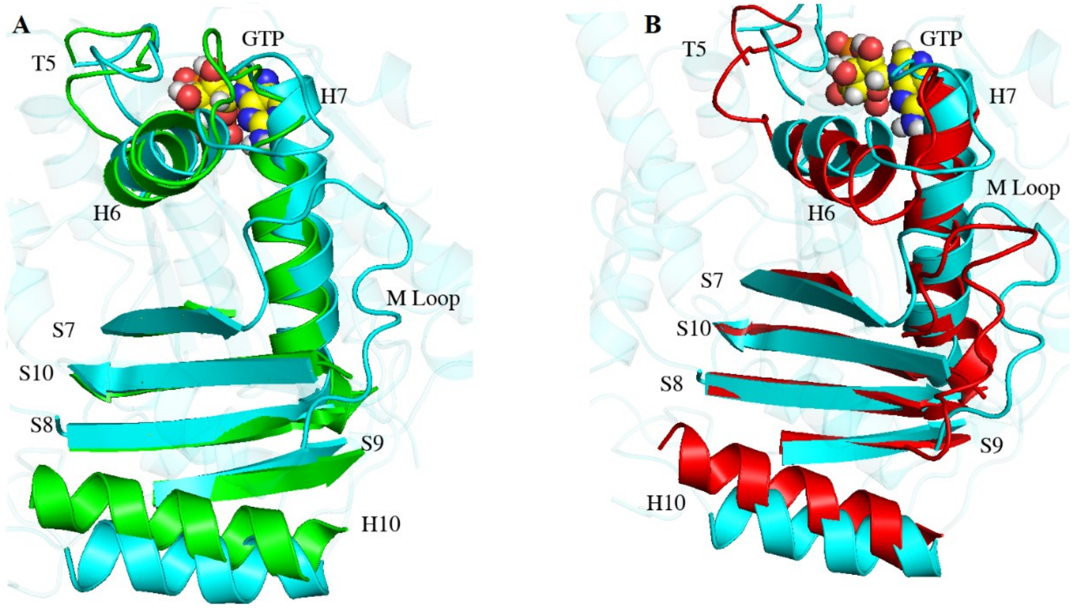

Figure 2.25: Superimposition of GTP-bound γ-tubulin in NaCl simulation on curved (1SA0) and straight (1JFF) β-tubulin. The 200 ns conformation of γ-tubulin of GTP-bound in NaCl simulation colored in cyan superimposed on β-curved (1SA0) and β-straight (1JFF). (**A**) Curved β-tubulin (1SA0) is colored in green. (**B**) Straight β-tubulin (1JFF) is colored in red.

2.2.2 Allosteric or lattice Model

Disagreement among advocates of the allosteric and lattice models about the major forces behind the conversion from curved to straight conformation in β-tubulin exists. The allosteric model discusses GTP allosteric effect, but the lattice model postulates the lateral interactions[73] between the α, β-tubulin heterodimer is the main effective force.[60]

The role of GTP and whether it can induce straightness with γ-tubulin is not known and was investigated in this study. (**Figure 2.26**)

The H7 helix is the major player that represents straight and curved conformations.[47]

With three GTP-liganded simulations, it was shown that the curved and intermediate conformations were the major observed conformations. This means that the GTP effect does not induce straightness on γ-tubulin. (**Figure 2.22-2.25**)

For 50 ns, the whole trajectory was investigated by measuring the H7 and S6 dCOM, and no straight conformation was observed as a result of the GTP interactions. (**Figure 2.22**)

The dCOM of the H7 helix and the S6 for the $MgCl_2$ simulation demonstrate no changes for liganded compared to the unliganded simulation with dCOM of ~ 1.55 nm – 1.60 nm, and similarly to the $ZnCl_2$ simulation, the curved conformation was most seen conformers with dCOM less than 1.6 nm. (**Figure 2.26**)

The GTP-liganded γ-tubulin in the NaCl simulation is not straight as the dCOM of H7 helix (Phe225-Leu231) from the S6 strand (Cys201-Asp206) is around 1.69 nm, but it is higher than that of the unliganded NaCl simulation with 1.5 nm. The GTP-bound γ-tubulin adapted an intermediate conformation in NaCl simulation. (**Figure 2.26**)

The repetition of set one for GTP-liganded in $MgCl_2$ had the dCOM of the H7 and S6 of ~ 1.64 nm of intermediate conformation and around 1.55 nm for the curved conformation in set two from 150 ns – 200 ns. The curved conformation for both the repetition sets in $ZnCl_2$ is dominant from 150 ns to 200 ns. For both sets in NaCl the curved conformation is dominant apart from a fluctuation at 180 ns and 195 ns. **(Figure A4 - A6)**

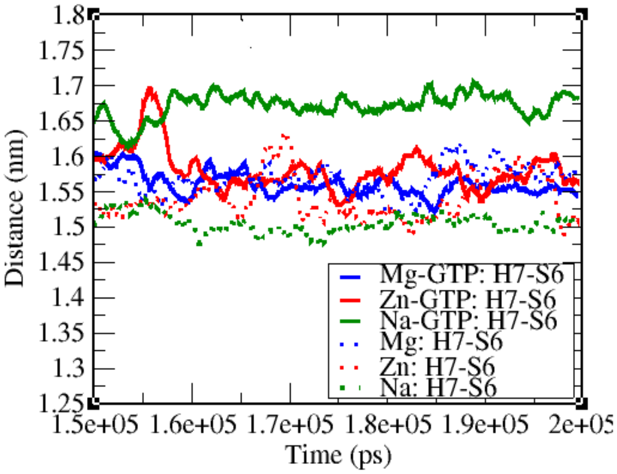

Figure 2.26: The dCOM of H7 helix and the S6 strand of liganded and unliganded simulations. The dCOM from 150 to 200 ns, colored in blue, red, green in liganded γ-tubulin and dash-blue, dash-red, and dash green in unliganded γ-tubulin, respectively, for $MgCl_2$, NaCl, and $ZnCl_2$ simulations.

The GTP main interaction sites with the H7 helix are through purin ring with Phe225 and Ile228. (**Figure 2.27**)

The interaction energy of Phe225 and Ile228 with GTP in $MgCl_2$ is -31.1 kJ/mol and -0.6 kJ/mol, respectively, and in NaCl is -37.3 kJ/mol and -2.1 kJ/mol, respectively. However, GTP interactions with Thr145 and Gly13 is much stronger than Ile228 or Phe225 with ~ -171.3 kJ/mol and -122.8 kJ/mol in $MgCl_2$, which shows that the interaction energy of GTP with H7 as compared to other residues is not strong. (**Figure 2.31**)

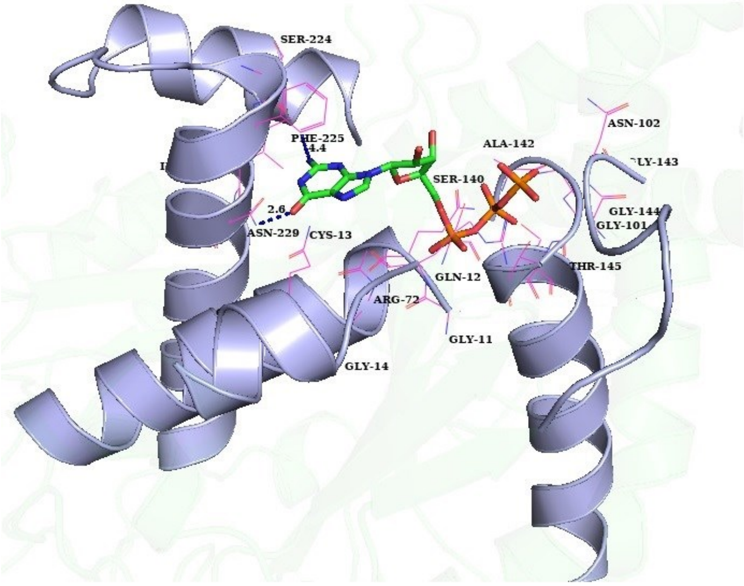

Figure 2.27: Bounded GTP in its interaction with the H7 helix. The GTP is depicted in a green stick. Phe225 and Ile228 are shown in magenta line representation.

Other helices and loops such as S7 to S10 strands and H10 helix contribute to the straightness and curvature, but none of which are in the interaction site of the GTP; they are part of the intermediate domain. Accordingly, the GTP binding has not induced straight conformation, and hence the lattice model, which emphasizes the lateral interaction, is a more reliable model. (**Figure 2.26 & 2.27**)

2.2.3 High Affinity-Metal Binding Sites in γ-Tubulin

GTP binds to either α or β-tubulins; the high-affinity metal-binding site was determined as a binding site for GTP. [31] The question arises about the exact location and involved atoms in creating the high-affinity metal-binding site.

The result showed that with all three MD simulations, one Mg^{+2}, one $Zn^{+2,}$ and two Na^{+} interact at fixed distances of Og-Ob atoms of GTP. (**Figure 2.28 and 2.29**)

Two Na^{+} atoms are associated with O1g and O3g atoms of GTP at a close distance of 2.1 Å and 3.1 Å within the last 50 ns of NaCl simulation, respectively. The interaction of Na^{+} from O3g is stable for the last 50 ns at 2.1 Å. The Na^{+} and O1g distances have fluctuations at 153 ns and 175 ns, and for the rest of the simulation, remains at ~ 3.1 Å. (**Figure 2.28 & 2.29**)

The Mg^{+2} interacts ~ 3.6 Å from the O3g atom, and Zn^{+2} about 4.0 Å, with fluctuation at 162 ns, increasing the distances to 5.0 Å. Therefore, the high-affinity metal-binding site is the GTP binding site in which, upon GTP binding, it accommodates one divalent or two monovalent cations to oxygen atoms of the β-γ phosphate. (**Figure 2.28**)

With all the 6 sets of repetitions of GTP liganded simulations, one divalent cation and two monovalent cations were accommodated into the GTP binding site in interaction with the oxygen atoms of the β-γ phosphate. This further proves the exact location of the high-affinity binding site in γ-tubulin. **(Figure A7 – A9)**

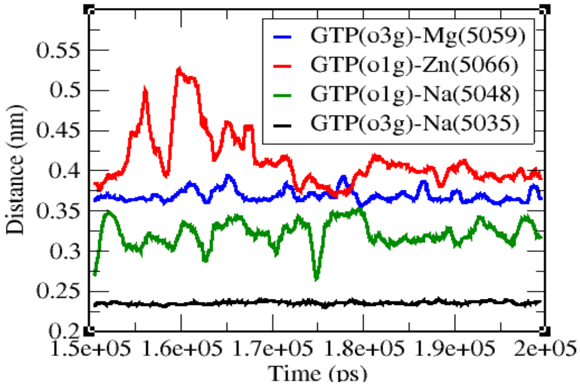

Figure 2.28: The distances between cations inside the GTP binding site from oxygen atoms of β-γ phosphate of GTP. The distances between Mg^{2+}, Zn^{2+}, and Na^{+} with respect to the oxygen atoms of β-γ phosphate are colored in blue, red, green, and black, respectively. The number in parenthesis is related to the conducted simulations in this study. They are the code determined for all atoms in the current study.

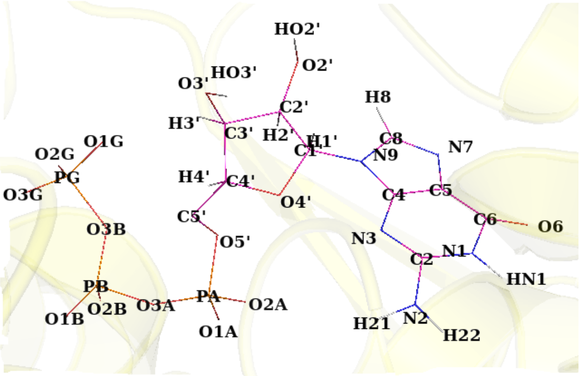

Figure 2.29: Structure of GTP with all atoms and their name label.

2.2.4 Interactions Among Residues, Water molecules, and Cations Within the GTP Binding Site

It was shown that one divalent and two monovalent cations of Zn^{+2} and Mg^{+2} interact with three oxygen atoms of GTP (Oa1, Oa2, Ob1, Ob2, Og1, Og2, and Og3). (**Figure 2.28)**

However, how accommodation of different cations affects the interactions within the binding site is not very well understood. The only difference of the GTP binding site with each simulation is the interaction of two Na^+, one $Zn^{+2,}$ and Mg^{+2} with three elements of GTP, residues of the binding site, and water molecules.

The nature of the interactions between residues of the GTP binding site, water molecules, GTP, and cations inside the GTP binding site are not answered elsewhere.

The sums of the electrostatic and L-J interaction energy between GTP and γ-tubulin are -1452.5 kJ/mol, -1371.1 kJ/mol, and -1424.2 kJ/mol in $MgCl_2$, $ZnCl_2$, and NaCl simulations, respectively. In this evaluation, two groups were selected, one group is GTP, and the other one is γ-tubulin. The interaction energies between GTP and each residue of the binding site will be discussed in detail later. The obtained values show that GTP interacts more strongly with γ-tubulin in the $MgCl_2$ simulation by -81.4 kJ/mol than in the $ZnCl_2$ simulation; this could be an indication that why Mg^{+2} is the major cation found in interaction with GTP and ATP.[43, 89, 90] (**Figure 2.30 and 2.31**)

Although the evaluations do not demonstrate which residues have the strongest interaction energy with GTP, the interaction energy of residues of the binding site and GTP will be addressed in detail later. (**Figure 2.30 and 2.31**)

The sum of the electrostatic and L-J interactions between each binding site residue and GTP was calculated to determine GTP interaction energy. Three residues of *homo-sapiens* γ-tubulin, including Gln12, Thr145, and Cys13, have strong interaction energy with GTP. **(Figure 2.31)**

Interestingly, with yeast γ-tubulin, Tub4, a mutation study revealed that Gln12, Cys13, and Thr145 play a key role in GTP interactions due to their high binding constant [91], which is consistent with the evaluations performed in this study.

The interaction energy between Gln12 and GTP is considerably strong in the $MgCl_2$ simulation, with a value of -238.8 kJ/mol as compared to -198.8 and -176.2 kJ/mol in NaCl and $ZnCl_2$ simulations, respectively. The interaction energy for Thr145 with three simulations of $MgCl_2$, $ZnCl_2$ and NaCl simulations is -171.3 kJ/mol, -170.0 kJ/mol, -163.5 kJ/mol, respectively. whereas, for Cys13 the value of energy is -122.8 kJ/mol, -125.7 kJ/mol, -120.1 kJ/mol, in $MgCl_2$, $ZnCl_2$ and NaCl simulations respectively. With γ-tubulin of the *Tetrahymena thermophila*, the mutation of Thr146 and Arg72 is lethal for the organism. Thr145 forms the strongest interaction energy with *homo-sapiens* γ-tubulin with all three simulations[91] consistent with *Tetrahymena thermophila* study. Thr145 and Arg72 have shown considerable interaction energy to GTP as mentioned above; for Arg72, its mutation has been shown to be lethal in *Tetrahymena thermophila.*[91]

Ala100, Ser147, and Gly101 have been found with large dissimilarities in their interaction energy with GTP among three simulations. The interaction energy for Ala100 is +3.7 kJ/mol, -90.6 kJ/mol and +1.3 kJ/mol in $MgCl_2$, $ZnCl_2$ and NaCl simulations, respectively. While in $MgCl_2$, NaCl and $ZnCl_2$ simulations, the interaction energy between Ser147 and GTP is -120.5 kJ/mol, -5.2 kJ/mol, and -123.8 kJ/mol, respectively. (**Figure 2.31**)

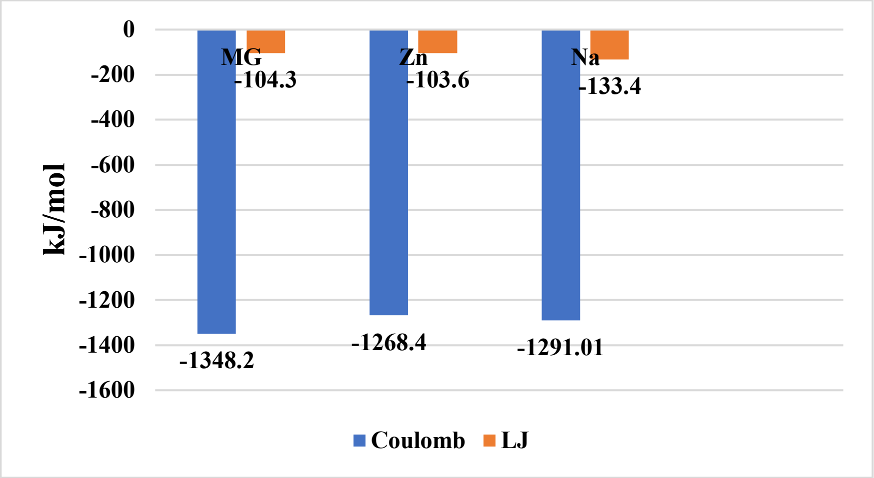

Figure 2.30: The sums of electrostatic and L-J interactions between GTP and γ-tubulin from 150 ns to 200 ns. The electrostatic and L-J energy is colored in orange and blue, respectively.

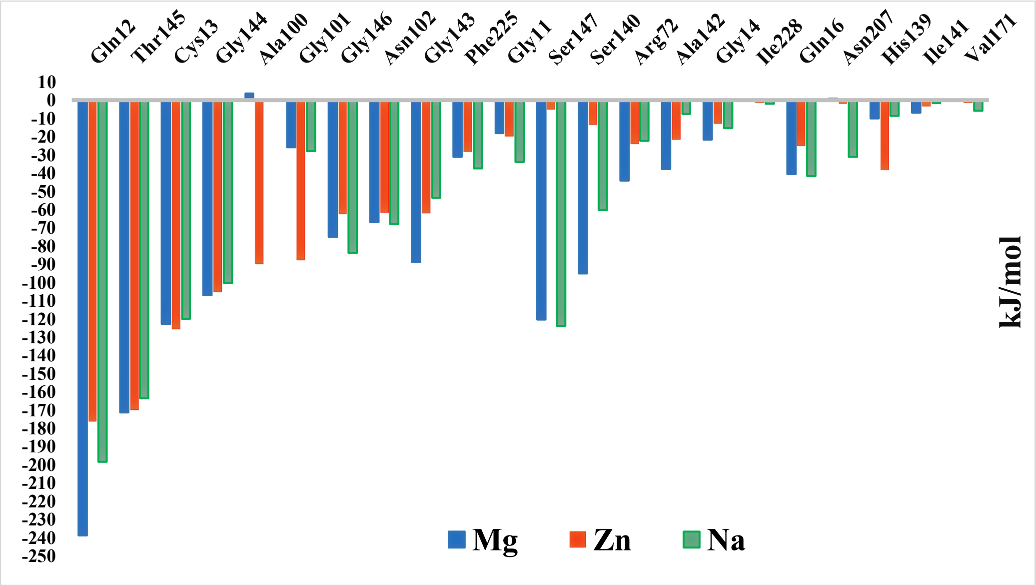

Figure 2.31: Interaction energy between each residue of the binding site and GTP from 150 ns to 200 ns. The interaction energy is colored in red for $ZnCl_2$, blue for $MgCl_2$, and green for NaCl simulation.

The interaction energy between Arg72 and GTP is -44.1 kJ/mol, -24.1 kJ/mol, and -22.2 kJ/mol, in $MgCl_2$, $ZnCl_2$, and NaCl respectively. All three simulations were carefully investigated in order to find out the origin of the differences between them.

The position and distances of Arg72 and Ala100 have changed from GTP. The changes of Ala100 was due to the deviation of the T3 loop (Ser94-Asn103) from the GTP, and for Arg72, its sidechain rotated towards the GTP. In the $MgCl_2$ simulation, Arg72 of γ-tubulin decreases the distance between its guanido group and $O_{1\text{-}2\text{-}3}G$ atoms of GTP (from 12 Å - 3 Å). Arg72 was found at a distance from $O_{1\text{-}2\text{-}3}G$ at 53 ns ~ 12 Å; at 100 ns, the gap is halved to 6 Å. At 153 ns, the 6 Å was also halved to 3 Å, and the atoms of guanido group of Arg72 exist at 3.1 Å from the O2g atom of GTP. (**Figure 2.32**)

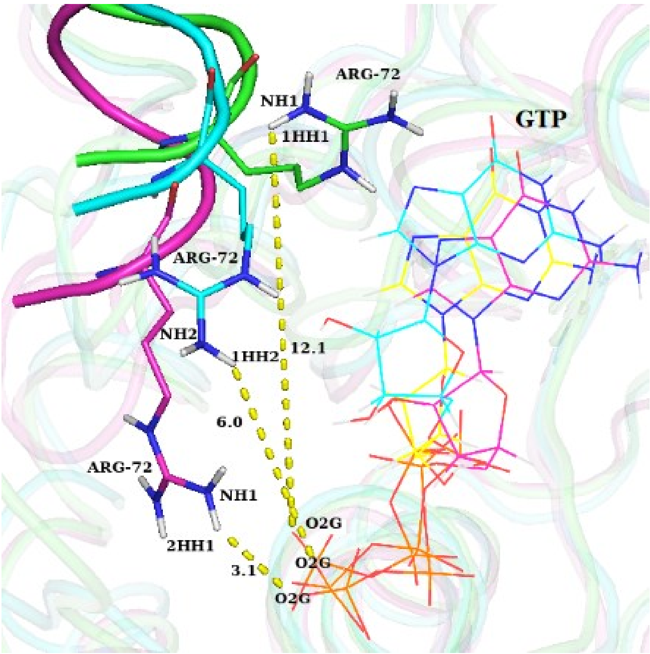

Figure 2.32: The distance of the sidechain of Arg72 from the γ phosphate of GTP in the $MgCl_2$ simulation. The Arg72 distances were shown at (**A**) 53 ns colored in green, 100 ns colored in cyan, and 153 ns colored in magenta with respect to $O_{1\text{-}2\text{-}3}G$ atoms of γ phosphate of the GTP.

Ala100 is a residue of the T3 loop (Ser94-Asn103), and the position of this residue at each simulation with respect to the γ phosphate atom of GTP changes due to fluctuations of the T3 loop (Lys93-Asn102). (**Figure 2.33 B**)

The dCOM of Ala100 from γ phosphate atom of GTP in three simulations was measured to uncover its different IE in each simulation. The dCOM of Ala100 and γ phosphate in the $ZnCl_2$ simulation was stable in the range of 4.0 Å - 4.5 Å from 150 ns to 200 ns. The value of dCOM of Ala100 and γ phosphate, for $MgCl_2$ and NaCl simulations, is almost twice that of $ZnCl_2$ ~ 8 Å and ~ 7 Å, respectively. (**Figure 2.33 B**)

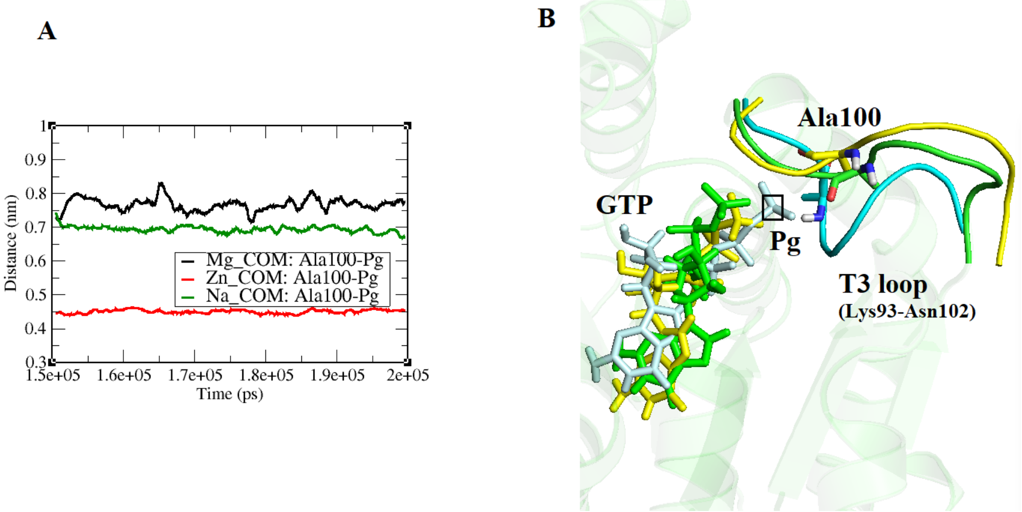

Figure 2.33: The position of Ala100 with respect to GTP. (**A**) dCOM of Ala100 from GTP γ phosphate. (**B**) Movement of T3 loop (Ser94-Asn103) towards the GTP. The Ala100 is depicted in the stick, and the T3 loop from $MgCl_2$, $ZnCl_2$, and NaCl are colored in green, cyan, and yellow, respectively.

At the GTP binding site, the oxygen atoms connected to β-γ phosphate of GTP (Og and Ob) mediate the interaction between the GTP with accommodated cations at stable distances. **(Figure 2.28 and 2.29)**

To study the effect of accommodated cations on GTP interactions, the interaction energy between GTP β-γ oxygens, water molecules, and binding site residues were evaluated. The β-γ phosphate oxygens of GTP including O1b, O2b, O1g, O2g, and O3g. It was discussed that the cations interact mainly with GTP β-γ phosphate oxygens (**Figure2.28 - 2.34**)

The sum of the electrostatic and L-J energy between GTP β-γ oxygens and the binding site residues is strong in $MgCl_2$ and $ZnCl_2$ simulations. The interaction energy between β-γ oxygens and GTP binding site in $MgCl_2$ simulation is -826.2 kJ/mol and -890.1 kJ/mol in $ZnCl_2$ simulation; this value reduces to -722.1 kJ/mol in NaCl simulation. These differences are attributed to the role and interactions of the accommodated cations at the GTP binding site because the only difference with the GTP binding site in each simulation is the accommodation of different cations. (**Figure 2.34 A-B and 2.28**)

Also, this finding reveals that compared to the whole molecule of GTP, just five oxygen atoms of β-γ phosphate account for 56.8% of the interaction energy between GTP and residues of the binding site in $MgCl_2$ simulation, 64.9% in $ZnCl_2$, and 50.7% in NaCl simulation. (**Figure 2.30 and 2.34 A-B**)

The presence of cations at the GTP binding site affects the interactions between GTP and water molecules. (**Figure 2.34 A and B**)

The value of the interaction energy between oxygen groups of β-γ phosphate, including O1b, O2b, O1g, O2g, O3g, and water molecules in $MgCl_2$ and $ZnCl_2$ simulations is -375.2 kJ/mol and -412.6 kJ/mol, respectively, and -188.5 kJ/mol for NaCl simulation. Therefore, the interaction energy between oxygen groups of β-γ phosphate, water molecules, and residues of the binding site indicates how the accommodated cations affect interactions of the GTP with other factors such as water and residues. In all cases, the availability of divalent cations tunes the interaction energy between the oxygen atoms of GTP with either water or residues of the binding site. (**Figure 2.34 A and B**)

This finding is useful to understand the Mg^{+2} role in the α, β-tubulin stability, and in GTP hydrolysis. Accordingly, it can be deduced that Mg^{+2} contributes to strong interactions between the nucleotide and other elements at the binding site, such as water and residues. The GTPase activity of *homo-sapiens* γ-tubulin has not been described in detail, but the interactions between oxygen groups of β-γ phosphate are important in developing the GTPase reaction, and existing of Mg^{2+} can foster the efficient interaction between the residues of the binding site and GTP. The nature of GTPase activity is a nucleophilic reaction, and at this reaction, water plays a key role.[92] It has been shown that water makes stronger interactions when cations such as Mg^{+2} is available in interactions with the oxygen atoms of GTP at the binding site. (**Figure 2.34 A-B and 2.28**)

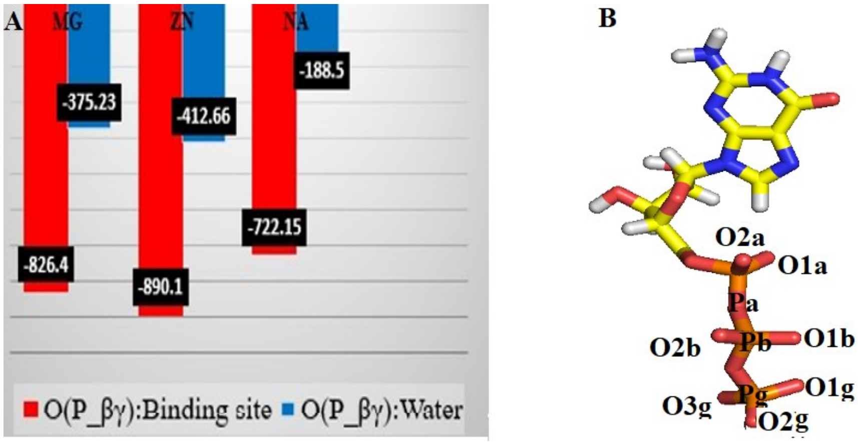

Figure 2.34: The interaction energy between oxygen atoms of β-γ phosphate of GTP with the binding site and water molecules. (**A**) The sums of L-J and electrostatic interaction between oxygen atoms of β-γ phosphate of GTP with the binding site and water molecules colored in red and blue, respectively. (**B**) Structure of GTP, the oxygen atoms of β-γ phosphate are marked.

More investigation has revealed that the number of interactions and H-bonds between three oxygen atoms of γ phosphate of GTP (O1g, O2g, and O3g) with respect to the binding site are different with each simulation. (**Figure 2.35 A and B**)

The number of H-bonds and interactions between O1g, O2g, and O3g and GTP binding site were monitored from 150 ns to 200 ns. Notably, the number of interactions and H-bonds in $ZnCl_2$ simulation were distinctly more compared to those of the Mg^{2+} and NaCl observations. (**Figure 2.35A and B**)

Throughout this study, for H-bonds and the number of interactions, the cut-off distance of 4 Å is assigned. It has been shown that moderate and weak H-bond is most effective in protein.[93] The distance for making a moderate to weak H-bonds is ~ 2.5 Å – 4 Å, which generates around < 4 kcal/mol – 15 kcal/mol energy.[93]

For distances between cations and residues of the protein, 4 Å – 4.5 Å is used for all evaluations in the subsequent sections. There are no reference distances; however, after looking at the conformations, it was found that several interactions fall between 4 Å – 4.5 Å; therefore, the maximum cut-off was set to 4.5 Å.

The number of interactions changed from 40 to 45 in $ZnCl_2$ simulation in contrast to 35 and 25 interactions in $MgCl_2$ and NaCl simulations, respectively, from 150 ns 200 ns. The number of interactions does not measure which atoms are in interaction with each other. Instead, all atoms that fall into the cut off distance of 4 Å will be counted.

The number of H-bonds is higher in $ZnCl_2$ simulations with ~ 7 to 8 from 150 ns to 200 ns. This value is 5 and 4 for $MgCl_2$ and NaCl simulations, respectively. (**Figure 2.35 A and B**)

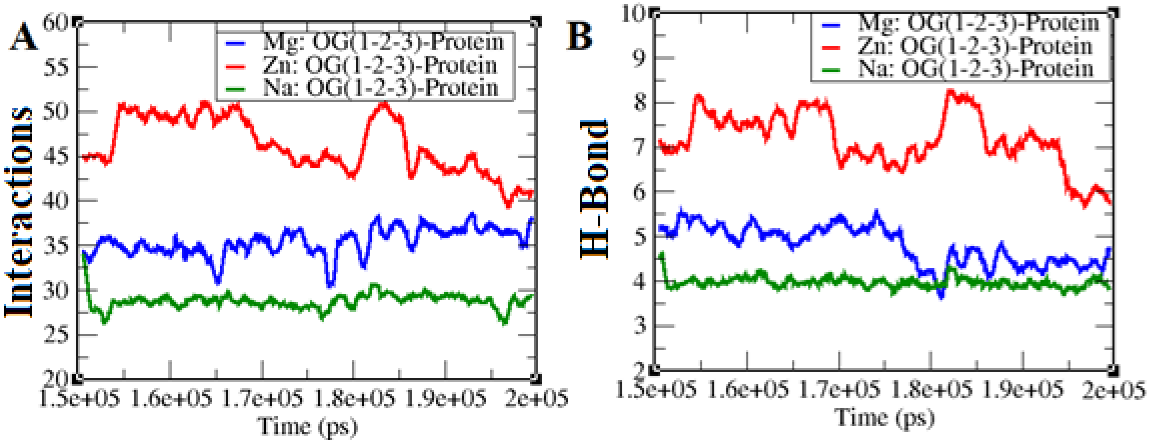

Figure 2.35: The number of interactions and H-bond between the oxygen atoms of γ phosphate (O1g, O2g, and O3g of GTP) and GTP binding site of γ-tubulin. (**A**) The number

of interactions in $MgCl_2$ colored in blue in $ZnCl_2$ is represented in red and green in NaCl simulation. (**B**) number of H-bond.

The first set of repetitions has ~ 35, 25, and 30 interactions between γ phosphate oxygens and residues of the binding site in $ZnCl_2$, NaCl, and $MgCl_2$, respectively. The number of H-bonds between γ phosphate oxygens and residues of the binding site in the first set of repetitions is ~ 4 H-bonds in NaCl and, with large fluctuations around 5 for $ZnCl_2$ and $MgCl_2$. The number of H-bond for the second set almost fluctuating from 3 – 5 for three simulations, higher by one for NaCl at 150 ns and 200 ns. **(Figure A14 - A16)**

To study how the cations interact with the GTP-bound γ-tubulin, the 200 ns conformations of protein with all simulations were extracted, and all interacting cations at ≤ 4.5 Å were found out. Then the interactions between residues and cations were monitored for the last 50 ns from 150 ns to 200 ns.

At 200 ns of $MgCl_2$ simulation, five Mg^{+2} cations were found near the γ-tubulin. The Mg^{+2} cations interacted at 3.9 Å to Asp120, 4.3 Å of Glu58, 2.1 Å to Asp130, at 4.4 Å to Glu38, and at 3.7 Å to Asp127. (**Figure 2.36**)

At the first set of repetition in $MgCl_2$, Glu116 at 4.1 Å, Glu402 at 3.8 Å, Asp433 at 4.3 Å, and Asp123 at 3.7 Å were found at ≤ 4.5 Å of protein. (**Figure A18**)

It should be noted that the above-mentioned interactions are found with only an examined conformations, and their interaction can be stable or not. The minimum distance between Mg^{+2} and Asp130 is stable at a distance of 2.0 Å for the last 50 ns. The interactions of all other Mg^{+2} to Asp120, Glu58, Glu38, and Asp127 are not stable; they show large fluctuations and interact at less than 4.5 Å to the γ-tubulin at 200 ns. (**Figure 2.37**)

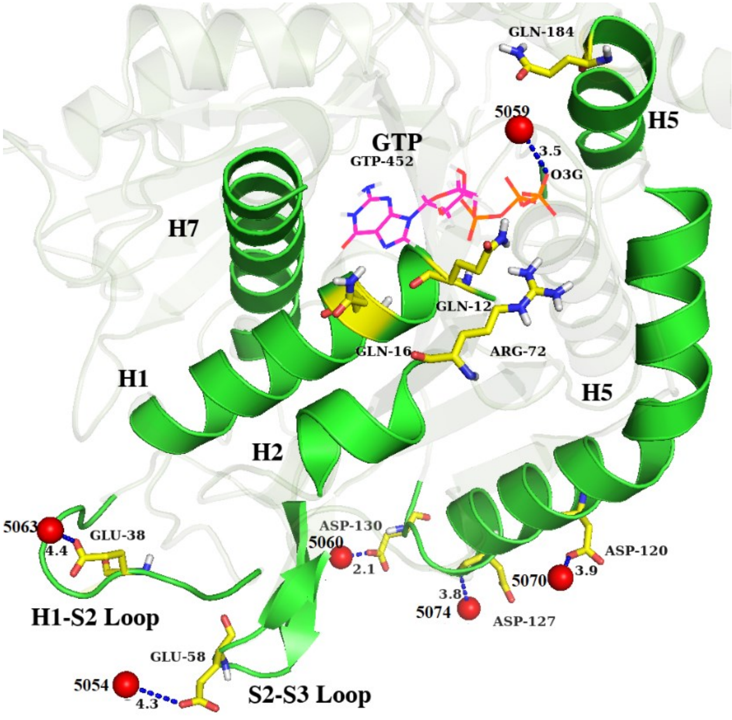

Figure 2.36: The conformation of γ-tubulin at 200 ns with interacting Mg^{+2} at ≤ 4.5 Å. The conformation of γ-tubulin under Mg^{2+} at 200 ns colored in green, Mg^{+2} is colored in sphere red, and interacting residues at a stick representation. The GTP in stick representation with its interacting Mg^{2+} in red.

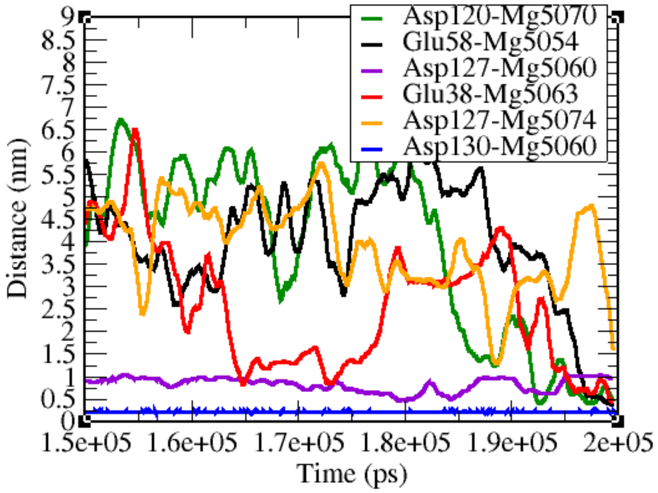

Figure 2.37: The minimum distances between Mg^{+2} cations and residues of the γ-tubulin. The minimum distances between Asp120, Asp127, Glu58, Glu38, and Asp130 with Mg^{2+} cations from 150 ns to 200 ns.

Also, the conformation of γ-tubulin at 200 ns of Zn^{2+}simulation was extracted to study all interacting Zn^{+2} at ≤ 4.5 Å. (**Figure 2.38).**

Zn^{+2} cations were found at 3.8 Å to Glu38, 3.7 Å of Glu112, 4.3 Å to Glu89, 3.9 Å to Glu4, and 3.8 Å to Glu116.

Interacting residues at ≤ 4.5 Å of the Zn^{+2} cations in set one includes Asp49 at 4.4 Å, Glu116 at 4 Å, Asn102 with the distance of 4 Å, and Val37 at 4.3 Å from the Zn^{+2}. (**Figure A17)**

The minimum distance between Zn^{+2} and Glu4 is ~ 2 – 4 nm from 150 ns to 180 ns; occurred at 180 ns, this value decreases to around 5 Å, and Zn^{+2} interacts with stable interactions until 200 ns with respect to Glu4. The minimum distance from Zn^{+2} to Glu38 changes ~ 4 Å from 180 ns to 200 ns. (**Figure 2.39**)

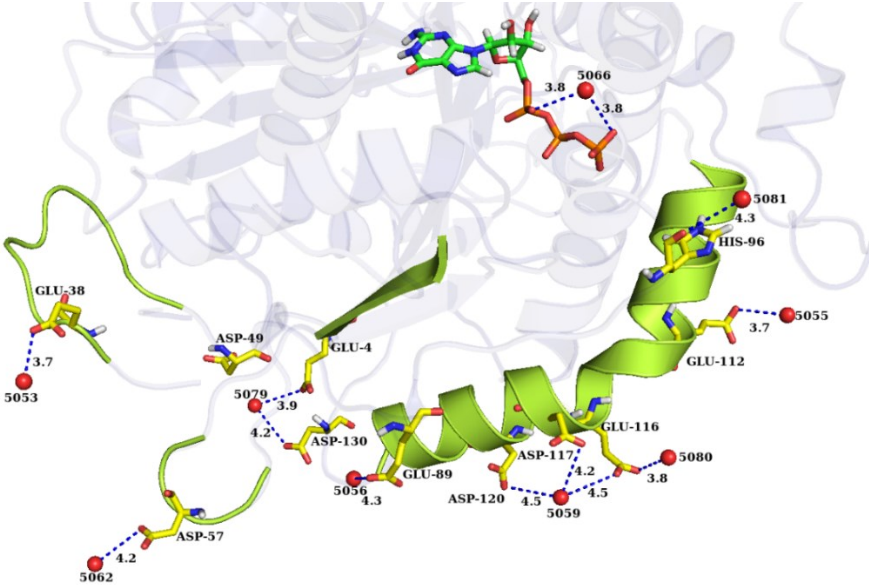

Figure 2.38: The conformation of γ-tubulin at 200 ns with interacting Zn^{+2} at ≤ 4.5 Å. Zn^{+2} is colored in sphere red and interacting residues in stick. The GTP in stick representation with its interacting Zn^{+2} to O1g and O2a in red.

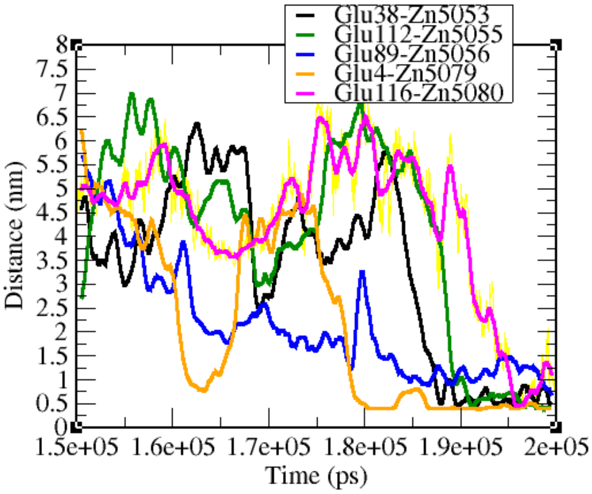

Figure 2.39: The minimum distances between Zn^{+2} cations and residues of the γ-tubulin. The minimum distances between Asp, Glu with Zn^{+2} from 150 ns to 200 ns.

Four Na^{+} cations were found to be in interaction with γ-tubulin at 200 ns of NaCl simulation. Na^{+} cations were found at 3.8 Å to Glu95, 3.9 Å of Asp120, 4.1 Å to Gly128, and at 4.5 Å to Thr215. (**Figure 2.40**)

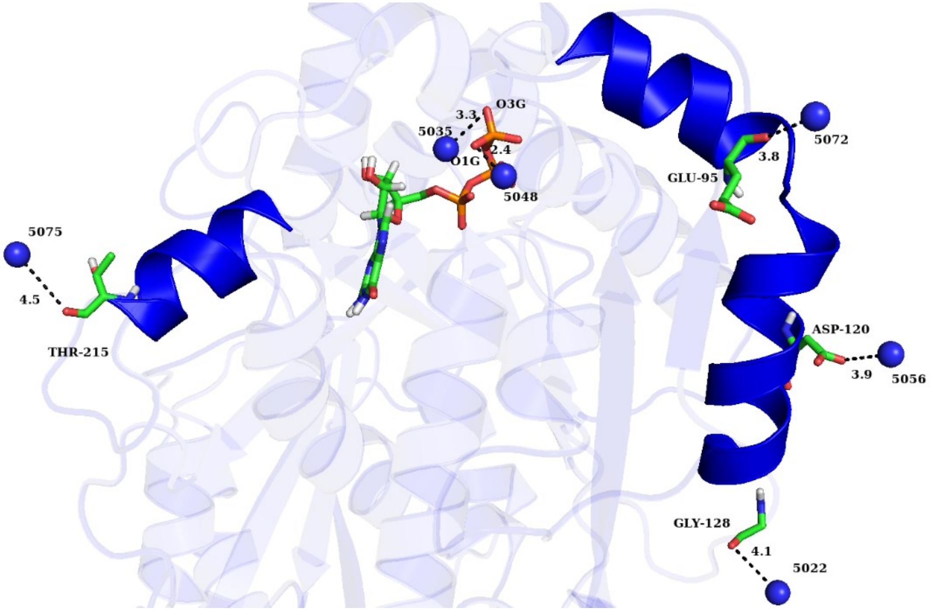

Figure 2.40: The conformation of γ-tubulin with interacting Na^{+} at ≤ 4.5 Å. The conformation of γ-tubulin in NaCl simulation at 200 ns, cations are colored in sphere blue and interacting residues with the stick. The GTP in stick representation with its interacting Na^{+} to O1g and O3g in blue as well.

For all the three liganded (GTP) and unliganded simulations, the electrostatic energies between domains and cations were calculated and compared to reveal the role of the cation in interactions to domains. (**Figure 2.41)**

The N-terminal (1-242) and C-terminal (381-451) of γ-tubulin interacts with strong electrostatic energies with both divalent (Mg^{+2} and Zn^{+2}) and monovalent cations (Na^{+}). In unliganded simulations, the electrostatic energy between Mg^{+2}, $Zn^{+2,}$ and Na^{+} with the N-terminal domain is -976.4 kJ/mol, -1063.2 kJ/mol, and -340.8 kJ/mol, respectively. They are -3.8 kJ/mol, -3.5 kJ/mol, and -5.2 kJ/mol with intermediate domain (343-380), and -244.3 kJ/mol, -446.5 kJ/mol, and -88.9 kJ/mol for the C-terminal domain. Upon binding of the GTP, the electrostatic energy was increased around three times with intermediate domains in liganded $ZnCl_2$ and $MgCl_2$ simulations to -15.2 kJ/mol and -27.3 kJ/mol, respectively, and reached ~ zero value in liganded NaCl simulation. Two reasons can be mentioned as to why zero, the intermediate domain with three GTP liganded and unliganded simulations, has weaker electrostatic energy with cations. Na^{+} interact with weaker energy as it is shown above, and the second reason is the intermediate domain, as shown in Figure 2.1 is located between the NBD and C-terminal domain and is not accessible for interaction with cations. (**Figure 2.41**)

GTP Binding also increased the electrostatic interactions between the $Mg^{2+}$and N-terminal to -1350.2 kJ/mol compared to the unliganded simulation, which was -976.4 kJ/mol. Although the electrostatic energy between the N-terminal domain with the liganded simulations in NaCl and $ZnCl_2$ simulations decreased compared to that of unliganded studies by -15.2 kJ/mol and - 115.1 kJ/mol, respectively. (**Figure 2.41**)

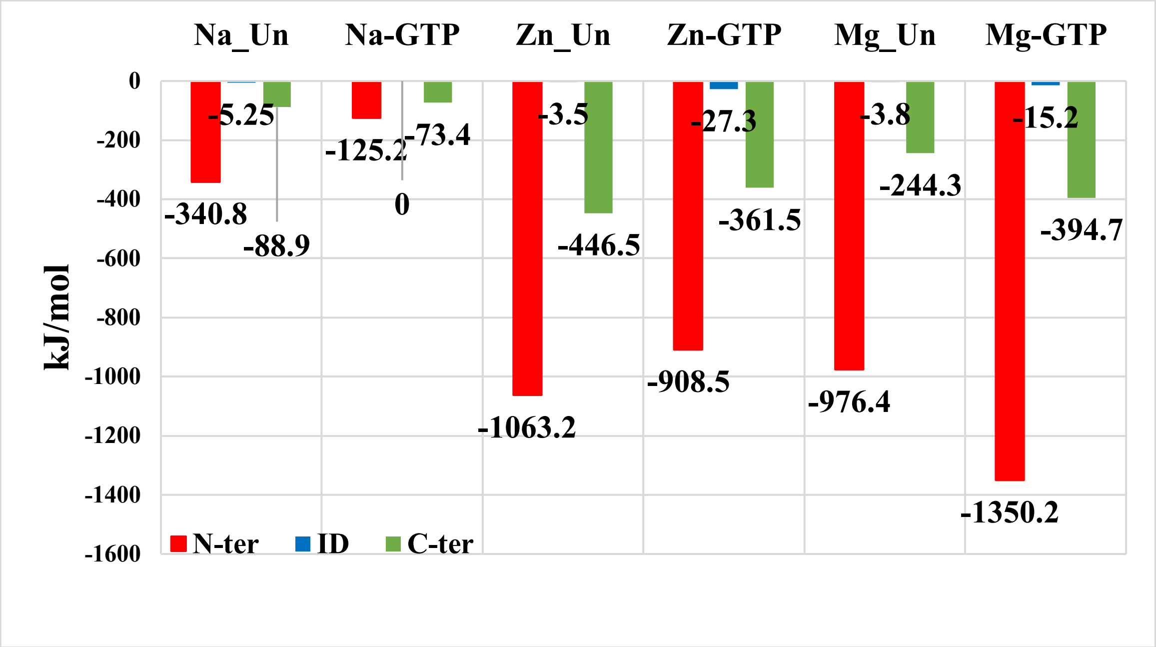

Figure 2.41: The electrostatic energy between three domains of the liganded and unliganded γ-tubulin. The electrostatic energy between the C-terminal (C-ter in green), N-terminal (N-ter in red), and Intermediate domain (ID in blue) of γ-tubulin and cations (Mg^{+2}, Zn^{+2}, and Na^{+}) from 150 ns to 200 ns of liganded (GTP) and unliganded (Un) simulations.

2.2.5 Role of Zn^{+2} in MTs Sheet Formation

When Zn^{+2} has a high concentration of 5×10^{-5} mol/L, pure tubulins form a non-functional sheet instead of a hollow tube of MTs. [40] One possible reason for inducing the sheet is suggested to be the Zn^{+2} - Cys interaction. The role of interaction between Cys and Zn^{+2} can be one possibility that will be investigated here. Other than that, it has been shown that the Zn^{+2} role is well established in its interactions with the GTP and the residues of its binding site. (**Figure 2.28-2.36**)

Cys residues of γ-tubulin include Cys13, Cys 26 belong to H1, Cys 138 of S4, Cys 201 for S6, Cys 316 at H8-S9 loop, and Cys 392 of H11 helix. In order to investigate whether the interaction of Zn^{2+} with Cys can be strong enough or not to affect the whole conformation of the protein, the cumulative radial distribution between the $Zn^{2+,}$ Mg^{2+}, at each simulation and all six Cys of the γ-tubulin were evaluated. The cumulative Radial Distribution Function (RDF) gives the average number of cations at a distance "r" with regard to each Cys residue. Accordingly, it was found that the closest distance in which Zn^{2+} interacts with the Cys is for Cys13 at around 9 Å for one Zn^{2+} cation (the Y-axis gives the number of cations). For the other five Cys residues (Cys26, Cys138, Cys201, Cys316, and Cys392), the interaction starts at 10 Å, which cannot be considered to be effective enough to have an impact on the conformation or the function of the protein. Because the energy of interaction when their distance drops to 8.0 Å - 1.0 Å is less than 0.01 kcal/mol for two charged particles, however, here, the Cys has no charge, and the energy can be even weaker than 0.01 kcal/mol.[94] The cumulative RDF between the Mg^{2+} and Cys residues show almost the same pattern as Cys13 interact at 8.5 Å – 9.0 Å for one Mg^{2+} and the rest of Cys residues interact at distances greater than 1.0 Å - 4.5 Å. (**Figure 2.42 A & B**)

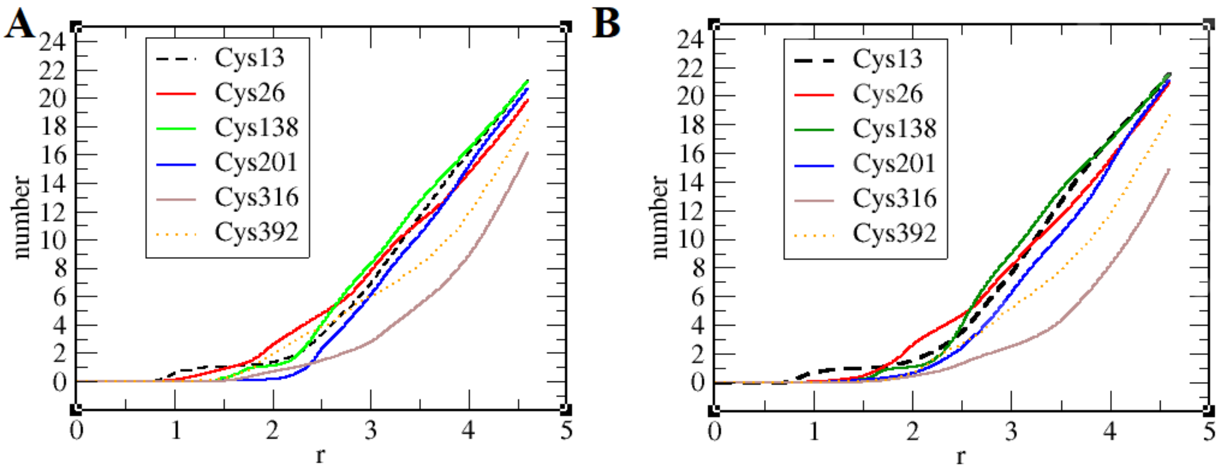

Figure 2.42: The cumulative RDF between Zn^{2+}, Mg^{+2}, and Cys. (**A**) The cumulative radial distribution between Zn^{2+} all six residues of the Cys and (**B**) between Mg^{2+} and Cys residues.

Solvent-accessible surface area for a molecule is a surface area that is accessible for solvent or, in other words, the total area of a molecule subtracting from its area in contact with other neighboring molecules. Greater SASA means lower interatomic interactions. Calculated SASA is the total SASA, which evaluates both hydrophilic and hydrophobic interactions.

Major differences were observed in the C-terminal domains in which the simulations, including Zn^{2+}, have a larger SAS area compared to NaCl or $MgCl_2$ simulations. The SAS area for unliganded simulation fluctuates between 46 nm^2 to 47 nm^2 in $ZnCl_2$ simulation, 44 $nm^{2,}$ and 46 nm^2 in $MgCl_2$ and NaCl simulations, respectively. Upon GTP binding in three simulations, a small increase of 2 nm^2 to 3 nm^2 is observed; hence, the $ZnCl_2$

simulation with SAS area of 50 nm^2 has a larger SAS area for its C-terminal as compared to $MgCl_2$ or NaCl with 46 nm^2 and 49 nm^2 in liganded simulations. (**Figure 2.43**)

In the $ZnCl_2$ simulation, a higher number of interactions and H-bonds were observed between GTP and γ-tubulin compared to $MgCl_2$ and NaCl. Also, the stronger interaction energy between GTP and water with -412.66 kJ/mol, the higher unfolded residues as well as larger SAS area were seen in $ZnCl_2$ simulation.

Therefore, It can be deduced that the formation of MTs sheet cannot be solely directed to the interaction of Cys with Zn^{+2} as it has been shown it has weaker interaction energy and RDF. However, it relatively can be directed to the overall interactions and impact of the Zn^{+2} as a divalent cation in its interaction with the GTP binding site, C-terminal domain, and negatively charged residues of the Asp and Glu.

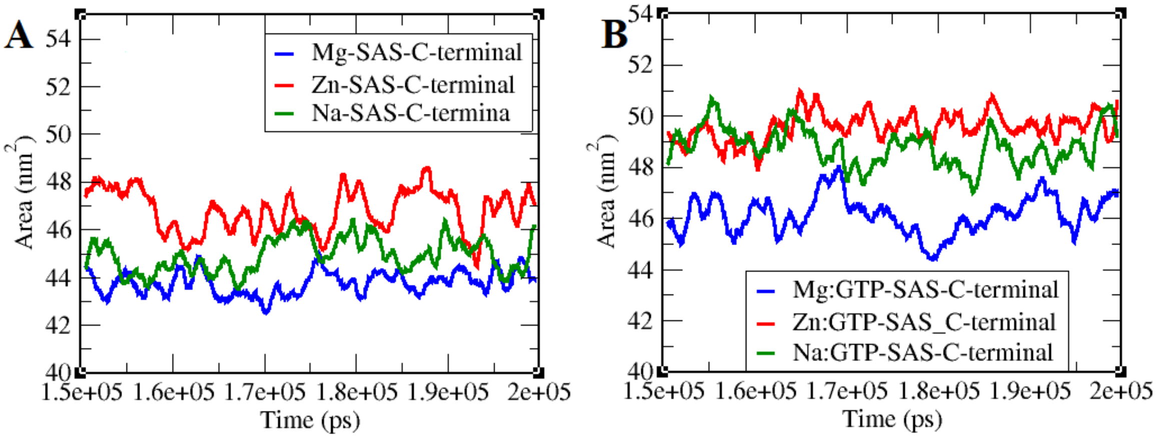

Figure 2.43: Solvent Accessible Surface Area (SAS) for the C-terminal domain of γ-tubulin in both liganded (GTP) and unliganded MD simulations. **(A)** The SAS area for unliganded and (**B**) for liganded MD simulations.

2.3 Discussion

Cation interactions were found to be dependent on their charges, and they occur at various distances. The minimum distance of interaction between Mg^{+2}, Zn^{+2}, and protein was at the range of 3.8 Å to 4.1 Å larger than Na^{+}, in the range of 2 Å – 2.5 Å. The major interactions were mostly with negatively charged residues such as Asp and Glu, belonging to N-ter and C-ter domains of the γ-tubulin, which compose of several critical helices such as H11, H2, and H1, all vital for its function. Although the interactions were at closer distances to Na^{+}; the interaction energy was stronger for divalent cations compared to Na^{+}. The intermediate domain exhibited insignificant interaction with cations in three simulations. Therefore it can be said the C-ter, and N-ter domains are the main interaction sites with cations. The position of the ID between N-ter, and C-ter domains makes it a non-accessible interaction segment for cations. The electrostatic energy between the intermediate domain and Zn^{+2}, Mg^{+2}, and Na^{+} is -3 kJ/mol to -5 kJ/mol, in all simulations. The electrostatic energy between cations and C-terminal for $MgCl_2$, $ZnCl_2$, and NaCl simulations is -244.3 kJ/mol, and -446.5kJ/mol, -88.9 kJ/mol, respectively. The N-ter domain composes of 243 residues and is exposed to charged particles of an aqueous environment, its interaction with cations is stronger than C-ter and ID domains.

Distance from COM of N-terminal of H7 helix and S6 strand was selected to address the straightness and curvature of γ-tubulin as a different measure from superimposing of conformations. The S6 strand is located at the N-ter of the γ-tubulin and does not undergo conformational rearrangement when the conversion occurs between straight and curved states. In unliganded simulations, the curved conformation was dominant in three simulations, and intermediate conformation was observed in both divalent simulations, but the curved conformation was well established, and the straight state was not detected. This can be assumed that the active conformation of the γ-tubulin in the small or ring complex is the curved conformation, but the exact functional conformation of γ-tubulin is still a mystery.

In addition to intermediate and curved conformations, the protein stability was also measured, and it has been noticed that conformation of the γ-tubulin monomer in the $MgCl_2$ simulation is more stable with a higher conserved helical shape compared to simulations performed in the presence of Na^+ and Zn^{+2} cations. This is consistent with the studies that show Mg^{+2} stabilizes the structure of α, β tubulin. The number of residues of helices in 7 conformations of γ-tubulin whose secondary conformations were lost was twice in Zn^{+2} and Na^+ simulations as compared to the Mg^{+2} simulation. This indicates the impact of the cations in γ-protein structural integrity or, in general, it can be directed to globular proteins.

The structural comparison of *homo-sapiens* γ-tubulin and yeast γ-tubulin (PDB: 5FLZ) was carried out; the yeast monomer is in its active state inside the small complex, which was used as a reference conformation. Most secondary segments, including H3, H8, and H10 of *homo-sapiens,* are structurally comparable and well-aligned to their counterparts of the yeast protein. These segments are contributing to lateral and longitudinal interactions of the small complex.

Two distinct states were observable in GTP binding site; they relate to the straightness and curvature of the γ-tubulin monomer. The curved conformation in Na^+ simulation exhibited a non-accessible state compared to the intermediate conformation in Zn^{+2} and Mg^{+2} simulations which was accessible for GTP. It was seen that the secondary segments generating the GTP binding site were interacting with each other in closer distances in the curved conformation compared to the intermediate conformation. The dCOM between Gln227 of H7 helix from Glu177 of T5 loop was measured to reveal how the contribution of T5 loop movement induces a non-accessible state; in NaCl simulation, it fluctuated around 1.3 nm, and in $MgCl_2$ simulation, it was around 1.8 nm and around 2.4 nm in $ZnCl_2$ simulation. The movement of the T5 loop in α, β tubulin switching between conversion from curved to straight conformation and, as it was seen in γ-tubulin, it affects the accessibility of the GTP binding site. The question about its role in GTPase activity of the γ-tubulin still remained unanswered.

The GTP-bound γ-tubulin adapts the intermediated conformation in Na^+ simulation, and in both Mg^{+2} and Zn^{+2} simulations, its dominant conformation was curved. Based on trajectory analysis, no straight conformation was induced as a result of GTP interactions in three $MgCl_2$, $ZnCl_2$, or NaCl simulations. In GTP liganded simulation, the dCOM of the H7 helix from the S6 strand is around 1.69 nm in Na^+ simulation, which totally resembles the intermediate but not straight conformation. The dCOM of H7 from S6 in the $MgCl_2$ simulation with ~ 1.55 nm – 1.60 nm demonstrates no changes for liganded compared to its unliganded simulation. In $ZnCl_2$ simulation, the curved conformations were most seen conformers with dCOM less than 1.6 nm. This finding is strongly in favor of the lattice model that states GTP effect is not the main force behind tubulins' straightness.

The Zn^{+2} effects in γ-tubulin are directly related to its interactions with negatively charged residues, and as it was shown, Zn^{+2} induces slight conformational changes that rather destabilize the secondary structure of the protein. The number of unfolded residues in the Zn^{+2} simulation was two times as the Mg^{+2}, and the SASA in the Zn^{+2} simulation was higher than Mg^{+2} and Na^{+} simulations. It can be concluded that the Zn^{+2} impact on MTs sheet formation cannot be directly attributed to its interaction with the Cys residues as the RDF evaluation shows that the closest interaction between Zn^{+2} and Cys is around 1 nm, which can not be considered as strong and effective interactions.

The γ-tubulin high-affinity metal-binding site in GTP liganded simulations was defined to be the GTP β-γ oxygens. In all three GTP-liganded simulations, stable interactions were observed between cations and Og-Ob atoms of the GTP. Two Na^{+}, one Zn^{+2}, and one Mg^{+2} were accommodated to the GTP binding site. It was observed that Mg^{+2} at the GTP binding site contributes to the stronger interactions between all components of the GTP binding site, such as waters, residues, and GTP with each other. The sums of electrostatic and L-J interaction energies between GTP and γ-tubulin are -1424.2 kJ/mol, -1371.1 kJ/mol, and -1452.5 kJ/mol in NaCl, $ZnCl_2$, and $MgCl_2$ simulations, respectively. The sums of electrostatic and L-J interaction energies between oxygen atoms of β-γ phosphate of GTP and residues of the GTP binding site are stronger in $MgCl_2$ and $ZnCl_2$.

The interaction energy between β-γ oxygens and GTP binding site in $MgCl_2$ simulation is -826.2 kJ/mol and -890.1 kJ/mol in $ZnCl_2$ simulation; this value reduces to -722.1 kJ/mol in NaCl simulation. These differences are attributed to the role and interactions of accommodated cations at the GTP binding site because the only difference in the GTP binding site in each simulation was the accommodation of different cations.

2.4 Conclusions

The curved conformation was found to be dominant in unliganded simulations in most analyzed trajectories time in $MgCl_2$, NaCl, and $ZnCl_2$. Most of the time, from 150 ns to 200 ns, the dCOM of H7 and S6 was not more than 1.55 nm in NaCl simulation. However, it reached 1.60 nm at some point in simulations contain $MgCl_2$ at 186 ns and 167 ns of $ZnCl_2$ simulation. Two significant impacts of cations can be highlighted in $MgCl_2$' $ZnCl_2$, and NaCl simulations. First, In addition to curved, the intermediate conformation observed in $MgCl_2$ simulation from 186 ns to 200 ns and at167 ns to 170 ns in which the dCOM of H7 and S6 was larger than 1.6 nm in $ZnCl_2$. Second, the impact of monovalent cations was to maintain the curvature with γ-tubulin without converting the conformation from curved to an intermediate or straight conformation, as the simulation in the NaCl had a lower dCOM of H7 helix and S6 strand.

Homo-sapiens γ-tubulin with intermediate or curved conformations differ in terms of the states of the GTP binding site in the presence of divalent or monovalent cations. Intermediate conformation in $MgCl_2$ and $ZnCl_2$ simulations show an accessible state for the GTP binding site. This is in contrast to the curved γ-tubulin acquiring the inaccessible binding site in NaCl simulation. The reason for acquiring the limited-access state with the curved γ-tubulin is due to the movement of the T5 loop with respect to the N-terminal of the H7 and H3 helices. The Asp180 from the Arg72 dCOM, and Glu177 from Gln277 were with a lower value in NaCl curved conformation compared to that of $MgCl_2$ and $ZnCl_2$ simulations. The dCOM of Asp180 from Arg72 helix fluctuated around 1.15 nm from 175 ns to 200 ns with shorter distances at 170 ns and 195 ns for 1.0 nm in NaCl simulation.

However, in $ZnCl_2$ simulation, the dCOM of Asp180 from Arg72 fluctuated around 2.2 nm from 160 ns to 200 ns, and in the $MgCl_2$ simulation, it has a value of ~ 1.6 nm. This shows how T5 loop moves toward the H3 helix and, as shown, affects the availability of the GTP binding site for either binding or unbinding GTP.

The electrostatic interactions between the N-terminal domain and the cations are -340.8 kJ/mol, -1063.2 kJ/mol, and -976.4 kJ/mol in NaCl, $MgCl_2$, and $ZnCl_2$ simulations, respectively. It was found that both interactions and electrostatic energy between cations and the intermediate domain are weaker in value than the N-terminal and C-terminal domains. Electrostatic energy of -3.5 kJ/mol was seen between Zn^{+2} and intermediate domain compared to -1063.2 kJ/mol between NBD and Zn^{+2} cations that are considerable differences. The intermediate domain is located between NBD and C-ter domain and is relatively no accessible for interactions. The structural stability of γ-tubulin in ionic conditions was evaluated by measuring the number of residues of all the 12 helices (H1 to H12) that lost their contribution to the helicity of the protein. In the $MgCl_2$ simulation, the secondary conformation of γ-tubulin is more stable compared to the NaCl and $ZnCl_2$ simulations. The counted number of residues that are not part of the helices were double in NaCl with 20 and 26 in $ZnCl_2$ simulations compared to simulation in $MgCl_2$ with an average of 10 residues. The H12 (Asp419-Ala437) helix at the C-terminal of the γ-tubulin in both NaCl and $ZnCl_2$ simulations has lost its secondary conformations for Asp419, Glu420, Met421, Asp422, Thr423, Ser424 and was stable in $MgCl_2$ simulation.

Simulation of the GTP-bound monomer of *homo-sapiens* γ-tubulin further advances the knowledge about the three-dimensional conformation of γ-tubulin, the differences between the role of various cations inside the cells, and providing more data in favor of the lattice model.

γ-tubulin straightening was not induced due to the GTP impact as the allosteric model predicted. The conversion from curved to intermediate conformation was observed in NaCl simulation and only moderately from 153 ns to 155 ns in $ZnCl_2$ simulation. Otherwise, the curved conformation was the dominant conformation.

GTP does not have a strong effect on converting curved to straight conformation relatively with all simulations. Of all the loops and helices that contribute to the conversion from curved to straight conformation, it has been shown that GTP just interacts with the H7 helix, and that interaction is not charged-charged; rather, interactions between the C-H atoms of the purin ring with the Phe225 and Ile228 sidechain. Therefore, the allosteric model, which emphasizes the GTP role in straightening the conformation of the tubulins, is not a reliable model according to the obtained data. The lattice model, which discusses the straightening as a consequence of lateral interactions, is more consistent with the available outputs of these MD simulations.

γ-tubulin conformational changes differ from β-tubulin while adapting curved or intermediate conformations. For instance, after superimposition of γ-tubulin on β-tubulin, H10 helix of γ-tubulin is not aligned with H10 helix of curved or straight β-tubulins. One reason attributed to sequence dissimilarities that changes the position of secondary structure segments between γ-tubulin and β-tubulins. The H10 helix of γ-tubulin starts at residue Pro330 and ends at Arg343; whereas, in β-tubulin, the H10 initiates at Glu325 and terminates at Ser338. This might indicate that the γ-tubulin function inside the ring or small complex is independent of the conformational changes from the curved to straight similar to the β-tubulin as the straight conformation was not observed.

The GTP binding site with *homo-sapiens* γ-tubulin acts as a high-affinity metal-binding site that accommodates two Na^+ and one divalent Zn^{+2} or Mg^{+2} cations with the stable interaction to $O_{1\text{-}2\text{-}3}G$ atoms of the β-γ phosphate. The stable interactions between two Na^+ at 2.5 Å of γ oxygens and one divalent cation at 3 Å – 4 Å distances were observed. Therefore, the exact position of the high-affinity metal-binding site is the oxygen atoms of β-γ phosphate.

The different cations that are accommodated to the GTP binding site are affecting the strength of interactions inside the binding site between water, residues of the binding site, and the GTP. The interaction energy between the oxygen atoms of β-γ phosphate and water molecules inside the binding site is stronger when with Zn^{2+} and Mg^{2+} cations for -412.6 kJ/mol, -375.2 kJ/mol, respectively, compared to -188.5 kJ/mol in NaCl simulation. The interaction energy between β-γ oxygens and residues of the binding site are stronger in $MgCl_2$ and $ZnCl_2$ simulations with -826.4 kJ/mol and -890.1 kJ/mol, respectively, as compared to -722.15 kJ/mol of NaCl simulation.

The results are consistent with yeast and *Tetrahymena thermophila* studies that investigated the mutation effect of GTP binding site. This further reveals that the key residues in interaction with GTP are the same for *homo-sapiens*, yeast tub4, and *Tetrahymena thermophila*. The top three residues with the highest interaction energy with GTP are Gln12, Thr145, and Cys13; they play a significant role in the binding of GTP with yeast tubulin.

The SAS areas of C-ter in the $ZnCl_2$ simulation are higher with both liganded and unliganded simulations by 3 - 5 nm^2 from 150 ns to 200 ns, and it was shown Zn^{+2} strongly interact with the protein. The formation of MTs sheet cannot be solely directed to the interaction of Cys residues with Zn^{+2} as it was shown it has weak interaction energy and RDF with the Zn^{+2} cations. However, it relatively can be directed to the overall interactions and impact of the Zn^{+2} as a divalent cation and its interaction with GTP binding site, C-ter domain, and negatively charges residues of the Asp and Glu. It was shown a higher number of interactions by 10, and H-bonds by 3 were observed between GTP and γ-tubulin in $ZnCl_2$ system compared to $MgCl_2$ and NaCl. Also, stronger interaction energy between GTP and water with -412.66 kJ/mol, a large number of unfolded residues of 26 were observed in $ZnCl_2$ simulation.

2.5 Bibliography

1. Pandey S, Zhang W, Assmann SM: **Roles of ion channels and transporters in guard cell signal transduction**. *FEBS Letters* 2007, **581**(12):2325-2336.
2. Haase H, Rink L: **Signal transduction in monocytes: the role of zinc ions**. *Biometals : an international journal on the role of metal ions in biology, biochemistry, and medicine* 2007, **20**(3-4):579-585.
3. Ohtsuki I: **Calcium ion regulation of muscle contraction: the regulatory role of troponin T**. *Molecular and cellular biochemistry* 1999, **190**(1-2):33-38.
4. Stojilkovic SS, Tabak J, Bertram R: **Ion channels and signaling in the pituitary gland**. *Endocr Rev* 2010, **31**(6):845-915.
5. Kuboniwa H, Tjandra N, Grzesiek S, Ren H, Klee CB, Bax A: **Solution structure of calcium-free calmodulin**. *Nature Structural Biology* 1995, **2**(9):768-776.
6. Prasad AS: **Zinc: an overview**. *Nutrition* 1995, **11**(1 Suppl):93-99.
7. De Bondt HL, Rosenblatt J, Jancarik J, Jones HD, Morgant DO, Kim S-H: **Crystal structure of cyclin-dependent kinase 2**. *Nature* 1993, **363**(6430):595-602.
8. Nelson DL, Cox MM, Lehninger AL: **Lehninger, principles of biochemistry**. Basingstoke; New York: Macmillan Higher Education ; W.H. Freeman; 2017.
9. Nepal N, Arthur S, Sundaram U: **Unique Regulation of Na-K-ATPase during Growth and Maturation of Intestinal Epithelial Cells**. *Cells* 2019, **8**(6).
10. Maret W: **Zinc biochemistry: from a single zinc enzyme to a key element of life**. *Advances in nutrition (Bethesda, Md)* 2013, **4**(1):82-91.
11. Jen J, Wang Y-C: **Zinc finger proteins in cancer progression**. *Journal of Biomedical Science* 2016, **23**(1):53.
12. Duong-Ly KC, Gabelli SB: **Salting out of proteins using ammonium sulfate precipitation**. *Methods in enzymology* 2014, **541**:85-94.
13. Negi S: **Effect of Calcium Ion Removal, Ionic Strength, and Temperature on the Conformation Change in Calmodulin Protein at Physiological pH**. *Journal of Biophysics* 2014, **2014**:9.
14. White MB, Amos J, Hsu JM, Gerrard B, Finn P, Dean M: **A frame-shift mutation in the cystic fibrosis gene**. *Nature* 1990, **344**(6267):665-667.
15. Nagy IZ, Lustyik G, Nagy VZ, Zarandi B, Bertoni-Freddari C: **Intracellular Na+:K+ ratios in human cancer cells as revealed by energy dispersive x-ray microanalysis**. *J Cell Biol* 1981, **90**(3):769-777.
16. Shklovskii BI: **Wigner Crystal Model of Counterion Induced Bundle Formation of Rodlike Polyelectrolytes**. *Physical Review Letters* 1999, **82**:3268-3271.

17. Tang JX, Wong S, Tran PT, Janmey PA: **Counterion induced bundle formation of rodlike polyelectrolytes**. *Berichte der Bunsengesellschaft für physikalische Chemie* 1996, **100**(6):796-806.
18. Tang JX, Janmey PA, Lyubartsev A, Nordenskiöld L: **Metal Ion-Induced Lateral Aggregation of Filamentous Viruses fd and M13**. *Biophysical Journal* 2002, **83**(1):566-581.
19. Viles JH: **Metal ions and amyloid fiber formation in neurodegenerative diseases. Copper, zinc and iron in Alzheimer's, Parkinson's and prion diseases**. *Coordination Chemistry Reviews* 2012, **256**(19):2271-2284.
20. Leal SS, Botelho HM, Gomes CM: **Metal ions as modulators of protein conformation and misfolding in neurodegeneration**. *Coordination Chemistry Reviews* 2012, **256**(19):2253-2270.
21. Rouffet M, Cohen SM: **Emerging trends in metalloprotein inhibition**. *Dalton Trans* 2011, **40**(14):3445-3454.
22. OpenStaxMarch 6: **Anatomy and Physiology**.
23. Lodish H BA, Zipursky SL, et al. : **Molecular Cell Biology. 4th edition**. *New York: W H Freeman* 2000.
24. Dudev T, Lim C: **Metal Selectivity in Metalloproteins: Zn2+ vs Mg2+**. *The Journal of Physical Chemistry B* 2001, **105**(19):4446-4452.
25. Oostenbrink C, Villa A, Mark AE, Van Gunsteren WF: **A biomolecular force field based on the free enthalpy of hydration and solvation: The GROMOS force-field parameter sets 53A5 and 53A6**. *Journal of Computational Chemistry* 2004, **25**(13):1656-1676.
26. Irving H, Williams RJP: **Order of Stability of Metal Complexes**. *Nature* 1948, **162**(4123):746-747.
27. Foster AW, Osman D, Robinson NJ: **Metal preferences and metallation**. *The Journal of biological chemistry* 2014, **289**(41):28095-28103.
28. Suhy DA, Simon KD, Linzer DIH, O'Halloran TV: **Metallothionein Is Part of a Zinc-scavenging Mechanism for Cell Survival under Conditions of Extreme Zinc Deprivation**. *Journal of Biological Chemistry* 1999, **274**(14):9183-9192.
29. Wade RH: **On and around microtubules: an overview**. *Molecular biotechnology* 2009, **43**(2):177-191.
30. Burns RG: **Identification of two new members of the tubulin family**. *Cell motility and the cytoskeleton* 1995, **31**(4):255-258.
31. Burns RG: **Kinetics of GTP hydrolysis during the assembly of chick brain MAP2-tubulin microtubule protein**. *Biochem J* 1991, **277 (Pt 1)**(Pt 1):239-243.
32. Menendez M, Rivas G, Diaz JF, Andreu JM: **Control of the structural stability of the tubulin dimer by one high affinity bound magnesium ion at nucleotide N-site**. *The Journal of biological chemistry* 1998, **273**(1):167-176.

33. Grover S, Hamel E: **The magnesium-GTP interaction in microtubule assembly**. *European journal of biochemistry* 1994, **222**(1):163-172.

34. Correia JJ, Beth AH, Williams RC: **Tubulin exchanges divalent cations at both guanine nucleotide-binding sites**. *Journal of Biological Chemistry* 1988, **263**(22):10681-10686.

35. Monasterio O: **Fluorine-19 nuclear magnetic resonance measurement of the distance between the E-site GTP and the high-affinity magnesium in tubulin**. *Biochemistry* 1987, **26**(19):6099-6106.

36. Sternlicht H, Yaffe MB, Farr GW: **A model of the nucleotide-binding site in tubulin**. *FEBS Letters* 1987, **214**(2):226-235.

37. Wang HW, Nogales E: **Nucleotide-dependent bending flexibility of tubulin regulates microtubule assembly**. *Nature* 2005, **435**(7044):911-915.

38. Mandelkow EM, Mandelkow E, Milligan RA: **Microtubule dynamics and microtubule caps: a time-resolved cryo-electron microscopy study**. *The Journal of Cell Biology* 1991, **114**(5):977-991.

39. Himes RH, Lee YC, Eagle GR, Haskins KM, Babler SD, Ellermeier J: **The relationship between cobalt binding to tubulin and the stimulation of assembly**. *The Journal of biological chemistry* 1982, **257**(10):5839-5845.

40. Larsson H, Wallin M, Edström A: **Induction of a sheet polymer of tubulin by Zn2+**. *Experimental Cell Research* 1976, **100**(1):104-110.

41. Rivas G, López A, Mingorance J, Ferrándiz MaJ, Zorrilla S, Minton AP, Vicente M, Andreu JM: **Magnesium-induced Linear Self-association of the FtsZ Bacterial Cell Division Protein Monomer: THE PRIMARY STEPS FOR FtsZ ASSEMBLY**. *Journal of Biological Chemistry* 2000, **275**(16):11740-11749.

42. Gombos L, Neuner A, Berynskyy M, Fava LL, Wade RC, Sachse C, Schiebel E: **GTP regulates the microtubule nucleation activity of γ-tubulin**. *Nature Cell Biology* 2013, **15**:1317.

43. Ko YH, Hong S, Pedersen PL: **Chemical mechanism of ATP synthase. Magnesium plays a pivotal role in formation of the transition state where ATP is synthesized from ADP and inorganic phosphate**. *The Journal of biological chemistry* 1999, **274**(41):28853-28856.

44. Aldaz H, Rice LM, Stearns T, Agard DA: **Insights into microtubule nucleation from the crystal structure of human γ-tubulin**. *Nature* 2005, **435**(7041):523-527.

45. Löwe J, Li H, Downing KH, Nogales E: **Refined structure of αβ-tubulin at 3.5 Å resolution11Edited by I. A. Wilson**. *Journal of Molecular Biology* 2001, **313**(5):1045-1057.

46. Li Z, Alisaraie L: **Microtubules dual chemo and thermo-responsive depolymerization**. *Proteins* 2015, **83**(5):970-981.

47. Ravelli RBG, Gigant B, Curmi PA, Jourdain I, Lachkar S, Sobel A, Knossow M: **Insight into tubulin regulation from a complex with colchicine and a stathmin-like domain**. *Nature* 2004, **428**(6979):198-202.
48. Nogales E, Downing KH, Amos LA, Löwe J: **Tubulin and FtsZ form a distinct family of GTPases**. *Nature Structural Biology* 1998, **5**(6):451-458.
49. Eklund G, Lang S, Glindre J, Ehlen A, Alvarado Kristensson M: **The nuclear localization of γ-tubulin is regulated by SadB-mediated phosphorylation**. *Journal of Biological Chemistry* 2014.
50. Leask A, Stearns T: **Expression of Amino- and Carboxyl-terminal γ- and α-Tubulin Mutants in Cultured Epithelial Cells**. *Journal of Biological Chemistry* 1998, **273**(5):2661-2668.
51. Oakley CE, Oakley BR: **Identification of γ-tubulin, a new member of the tubulin superfamily encoded by mipA gene of Aspergillus nidulans**. *Nature* 1989, **338**(6217):662-664.
52. Wise DO, Krahe R, Oakley BR: **The gamma-tubulin gene family in humans**. *Genomics* 2000, **67**(2):164-170.
53. Yuba-Kubo A, Kubo A, Hata M, Tsukita S: **Gene knockout analysis of two γ-tubulin isoforms in mice**. *Developmental Biology* 2005, **282**(2):361-373.
54. Kellogg DR, Moritz M, Alberts BM: **The centrosome and cellular organization**. *Annu Rev Biochem* 1994, **63**:639-674.
55. Kalt A, Schliwa M: **Molecular components of the centrosome**. *Trends in cell biology* 1993, **3**(4):118-128.
56. Doxsey S, Zimmerman W, Mikule K: **Centrosome control of the cell cycle**. *Trends in cell biology* 2005, **15**(6):303-311.
57. Kollman JM, Polka JK, Zelter A, Davis TN, Agard DA: **Microtubule nucleating γ-TuSC assembles structures with 13-fold microtubule-like symmetry**. *Nature* 2010, **466**:879.
58. Zheng Y, Wong ML, Alberts B, Mitchison T: **Nucleation of microtubule assembly by a γ-tubulin-containing ring complex**. *Nature* 1995, **378**(6557):578-583.
59. Moritz M, Braunfeld MB, Guénebaut V, Heuser J, Agard DA: **Structure of the γ-tubulin ring complex: a template for microtubule nucleation**. *Nature Cell Biology* 2000, **2**(6):365-370.
60. Kollman JM, Merdes A, Mourey L, Agard DA: **Microtubule nucleation by γ-tubulin complexes**. *Nature Reviews Molecular Cell Biology* 2011, **12**:709.
61. Hsia KC, Wilson-Kubalek EM, Dottore A, Hao Q, Tsai KL, Forth S, Shimamoto Y, Milligan RA, Kapoor TM: **Reconstitution of the augmin complex provides insights into its architecture and function**. *Nat Cell Biol* 2014, **16**(9):852-863.
62. Goshima G, Mayer M, Zhang N, Stuurman N, Vale RD: **Augmin: a protein complex required for centrosome-independent microtubule generation within the spindle**. *The Journal of cell biology* 2008, **181**(3):421-429.

63. Murphy SM, Preble AM, Patel UK, O'Connell KL, Dias DP, Moritz M, Agard D, Stults JT, Stearns T: **GCP5 and GCP6: two new members of the human gamma-tubulin complex**. *Molecular biology of the cell* 2001, **12**(11):3340-3352.
64. Zheng Y, Wong ML, Alberts B, Mitchison T: **Nucleation of microtubule assembly by a gamma-tubulin-containing ring complex**. *Nature* 1995, **378**(6557):578-583.
65. Masuda H, Mori R, Yukawa M, Toda T: **Fission yeast MOZART1/Mzt1 is an essential gamma-tubulin complex component required for complex recruitment to the microtubule organizing center, but not its assembly**. *Molecular biology of the cell* 2013, **24**(18):2894-2906.
66. Haren L, Remy M-H, Bazin I, Callebaut I, Wright M, Merdes A: **NEDD1-dependent recruitment of the γ-tubulin ring complex to the centrosome is necessary for centriole duplication and spindle assembly**. *The Journal of Cell Biology* 2006, **172**(4):505-515.
67. Vinh DB, Kern JW, Hancock WO, Howard J, Davis TN: **Reconstitution and characterization of budding yeast gamma-tubulin complex**. *Molecular biology of the cell* 2002, **13**(4):1144-1157.
68. Geissler S, Pereira G, Spang A, Knop M, Soues S, Kilmartin J, Schiebel E: **The spindle pole body component Spc98p interacts with the gamma-tubulin-like Tub4p of Saccharomyces cerevisiae at the sites of microtubule attachment**. *The EMBO journal* 1996, **15**(15):3899-3911.
69. Oegema K, Wiese C, Martin OC, Milligan RA, Iwamatsu A, Mitchison TJ, Zheng Y: **Characterization of two related Drosophila gamma-tubulin complexes that differ in their ability to nucleate microtubules**. *The Journal of cell biology* 1999, **144**(4):721-733.
70. Choy RM, Kollman JM, Zelter A, Davis TN, Agard DA: **Localization and orientation of the gamma-tubulin small complex components using protein tags as labels for single particle EM**. *J Struct Biol* 2009, **168**(3):571-574.
71. Kollman JM, Polka JK, Zelter A, Davis TN, Agard DA: **Microtubule nucleating gamma-TuSC assembles structures with 13-fold microtubule-like symmetry**. *Nature* 2010, **466**(7308):879-882.
72. Berman HM, Westbrook J, Feng Z, Gilliland G, Bhat TN, Weissig H, Shindyalov IN, Bourne PE: **The Protein Data Bank**. *Nucleic Acids Research* 2000, **28**(1):235-242.
73. Rice LM, Montabana EA, Agard DA: **The lattice as allosteric effector: structural studies of alphabeta- and gamma-tubulin clarify the role of GTP in microtubule assembly**. *Proceedings of the National Academy of Sciences of the United States of America* 2008, **105**(14):5378-5383.
74. Waterhouse A, Bertoni M, Bienert S, Studer G, Tauriello G, Gumienny R, Heer FT, de Beer TAP, Rempfer C, Bordoli L *et al*: **SWISS-MODEL: homology modelling of protein structures and complexes**. *Nucleic Acids Res* 2018, **46**(W1):W296-w303.
75. **The PyMOL Molecular Graphics System, Version 1.2r3pre, Schrödinger, LLC.**

76. Abraham MJ, Murtola T, Schulz R, Páll S, Smith JC, Hess B, Lindahl E: **GROMACS: High performance molecular simulations through multi-level parallelism from laptops to supercomputers**. *SoftwareX* 2015, **1-2**:19-25.

77. Scott WRP, Hünenberger PH, Tironi IG, Mark AE, Billeter SR, Fennen J, Torda AE, Huber T, Krüger P, van Gunsteren WF: **The GROMOS Biomolecular Simulation Program Package**. *The Journal of Physical Chemistry A* 1999, **103**(19):3596-3607.

78. Hess B, Bekker H, Berendsen HJC, Fraaije JGEM: **LINCS: A linear constraint solver for molecular simulations**. *Journal of Computational Chemistry* 1997, **18**(12):1463-1472.

79. Leach AR: **Molecular modelling : principles and applications**. Harlow: Pearson/Prentice Hall; 2009.

80. Essmann U, Perera L, Berkowitz ML, Darden T, Lee H, Pedersen LG: **A smooth particle mesh Ewald method**. *The Journal of Chemical Physics* 1995, **103**(19):8577-8593.

81. Malde AK, Zuo L, Breeze M, Stroet M, Poger D, Nair PC, Oostenbrink C, Mark AE: **An Automated Force Field Topology Builder (ATB) and Repository: Version 1.0**. *Journal of Chemical Theory and Computation* 2011, **7**(12):4026-4037.

82. Rarey M, Kramer B, Lengauer T, Klebe G: **A Fast Flexible Docking Method using an Incremental Construction Algorithm**. *Journal of Molecular Biology* 1996, **261**(3):470-489.

83. Bohm HJ: **The development of a simple empirical scoring function to estimate the binding constant for a protein-ligand complex of known three-dimensional structure**. *J Comput Aided Mol Des* 1994, **8**(3):243-256.

84. Downing KH, Nogales E: **Tubulin structure: insights into microtubule properties and functions**. *Current opinion in structural biology* 1998, **8**(6):785-791.

85. Nogales E, Wolf SG, Downing KH: **Structure of the alpha beta tubulin dimer by electron crystallography**. *Nature* 1998, **391**(6663):199-203.

86. Sept D: **Microtubule Polymerization: One Step at a Time**. *Current Biology* 2007, **17**(17):R764-R766.

87. Greenberg CH, Kollman J, Zelter A, Johnson R, MacCoss MJ, Davis TN, Agard DA, Sali A: **Structure of gamma-tubulin small complex based on a cryo-EM map, chemical cross-links, and a remotely related structure**. *J Struct Biol* 2016, **194**(3):303-310.

88. Hess B, Kutzner C, van der Spoel D, Lindahl E: **GROMACS 4: Algorithms for Highly Efficient, Load-Balanced, and Scalable Molecular Simulation**. *Journal of Chemical Theory and Computation* 2008, **4**(3):435-447.

89. Rudack T, Xia F, Schlitter J, Kotting C, Gerwert K: **The role of magnesium for geometry and charge in GTP hydrolysis, revealed by quantum mechanics/molecular mechanics simulations**. *Biophys J* 2012, **103**(2):293-302.

90. Mistou MY, Cool RH, Parmeggiani A: **Effects of ions on the intrinsic activities of c-H-ras protein p21. A comparison with elongation factor Tu**. *European journal of biochemistry* 1992, **204**(1):179-185.
91. Shang Y, Tsao C-C, Gorovsky MA: **Mutational analyses reveal a novel function of the nucleotide-binding domain of γ-tubulin in the regulation of basal body biogenesis**. *The Journal of Cell Biology* 2005, **171**(6):1035-1044.
92. Carvalho ATP, Szeler K, Vavitsas K, Åqvist J, Kamerlin SCL: **Modeling the mechanisms of biological GTP hydrolysis**. *Archives of Biochemistry and Biophysics* 2015, **582**:80-90.
93. Jeffrey GA: **An introduction to hydrogen bonding**. *Oxford University Press* 1997.
94. Lee KK, Fitch CA, García-Moreno E B: **Distance dependence and salt sensitivity of pairwise, coulombic interactions in a protein**. *Protein Sci* 2002, **11**(5):1004-1016.

CHAPTER 3 Effect of GTP, GDP, and Ionic Conditions on Conformations of γ-Tubulin Dimer

3.1 MD Simulation of Unliganded γ-Tubulin Dimer Under $MgCl_2$, $ZnCl_2$, and NaCl Ionic Conditions

3.1.1 Introduction

Homo-sapiens γ-dimer is co-crystallized with GDP in both chains A and B. Among higher eukaryotes such as *homo-sapiens*, γTuSC is a scaffold for the generation of a massive γTuRC complex, which can nucleate MTs at a higher rate than that of γTuSC.[1-4] γTuRC contains repeated pairs of γ-tubulin in lateral interactions. [5, 6]The nucleation of MTs relies on the γ-containing complex of proteins; γTuSC is mainly functional in yeast MTs nucleation and as a template for γTuRC in *homo-sapiens*.[7] The γTuSC and γTuRC complexes are examples of these γ-containing complexes. However, how the complex of proteins with γ-tubulin develops the nucleation of MTs is not fully understood[8] despite many advances in determining the involving subunits which are involved in the process of nucleation.[8]

The main controversy is about the orientation of γ-tubulin in γTuRC. The protofilament and template are two proposed models that discuss γ-tubulin related nucleation of MTs from two different perspectives. None of these models are universally accepted or rejected.[9-11] Based on the template model, 12 to 14 monomers of γ-tubulin are laterally arranged into 6 to 7 γTuSC-like complex. γ-tubulin longitudinal interactions at the top of the γTuSC are with the α-subunit of α, β-tubulin heterodimers, during nucleation of MTs and at the opposite bottom end of the γTuSC, they interact with GCP2, GCP3, GCP4, GCP5 proteins.[2] According to the template model, there is no way that γ-tubulin contributes to the MTs protofilament.[2] (**Figure 3.1**)

In the protofilament model, γ-tubulins interactions inside γ-complex are longitudinal.[10] The lateral interactions are between α, β-tubulin, and γ-tubulin, and accordingly, γ-tubulin contributes to the structure of the MTs protofilament. Thus in the protofilament model, the γ-tubulin advances into the protofilament and will be part of it at the minus end of MTs.[10] (**Figure 3.1**)

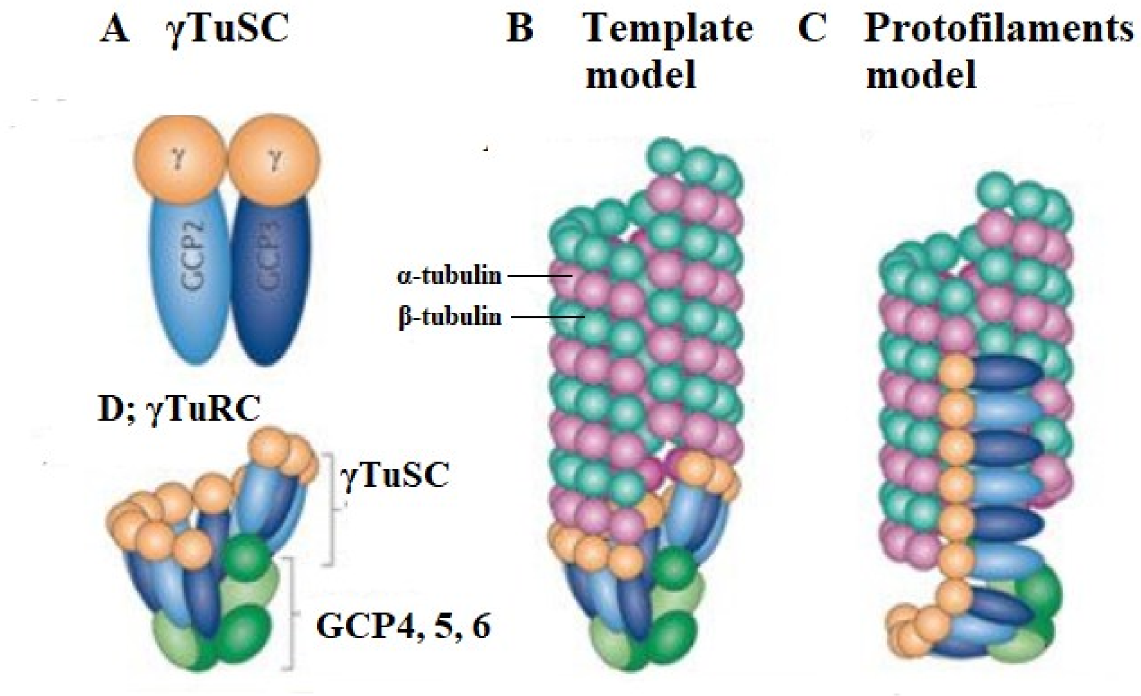

Figure 3.1: Template and protofilament models. (**A and D**) The γTuSC and γ-TuRC with the γ-tubulin on top in yellow. (**B**) Representation of the template model in which γTuRC

nucleate the MTs through the interaction between γ-tubulins on top with the α subunit. (**C**) The schematic representation of the protofilament model in which the lateral interactions between γ-tubulin and both α-and β-tubulin occur. This figure has been adapted by permission.[2] Kollman et al., Nature Reviews Molecular Cell Biology 2011.

The conformation of the existing (5FLZ) yeast γTuSC is different from the crystal structure of a *homo-sapiens* γ-tubulin dimer (3CB2).[12] **(Figure 2.13)**

The three-dimensional conformation of *homo-sapiens* and yeast γ-tubulins have a 40% sequence identity. The way that two monomers generate a dimer in each organism varies from another one. Upon superimposition of *homo-sapiens* γ-protein dimer on yeast γTuSC, noticeable variation can be observed. First, *homo-sapiens* dimer and yeast dimer lateral interactions are not sharing the same segments. In other words, different helices and loops generate the interface interactions between them (dimer of yeast and *homo-sapiens* γ-tubulin), and that will be discussed later.[1] The main variations between them are secondary segments orientation for the H6, H7 helices, and intermediate domain strands of S7 to S10. (**Figure 3.2**)

In the yeast γ-dimer at γTuSC (PDB code: 5FLZ), the two H7 helices of both yeast γ-tubulins are parallel with respect to their Y-axis, and their N-terminals are directed upward in both of them. With *homo-sapiens* γ-tubulin, the H7 helices are not parallel but positioned in opposite N to C terminal directions.[1, 13, 14] (**Figure 3.2 and 3.3 A)**

The lateral interactions between two γ-tubulin homodimers within the γTuSC of yeast are achieved through H3 (Trp104-Asp127), H8 (Leu253-Leu260), H9 (Val290-Leu298), H10 (Pro330-Arg343) helices, and T7 (Thr240-Asp252), H1-S2 (His29-Arg47) as well as M (Thr274-Thr 289) loops. (**Figure 2.13)**

The interface interactions in *homo-sapiens* γ-dimer generate through H8 (Leu253-Leu260), H10 (Pro330-Arg343) helices, the C-terminal tail for Try443-Trp446, and T7 (Thr240-Asp252) loop. (**Figure 3.3**)

It is worth mentioning that in yeast, the γTuSC is the main complex involved in the nucleation of MTs, and it is known that with this complex, only two γ-tubulin monomers interact laterally.[2]

As with other organisms such as *homo-sapiens*, γTuSC is not effective as to the high demand of MTs generation, and a more effective complex is needed for nucleation[2]. In *homo-sapiens*, γTuRC is taking the role of being the main complex involved in nucleation. However, the detailed orientation of γ-tubulin with *homo-sapiens* complexes is not known.

A comparison of *homo-sapiens* γ-tubulin dimer with the α, β-tubulin heterodimer has shown that they are arranged the same way compared to the axis of their H7 helix (Phe225-Leu243), which is parallel to each other. The main differences between them were observed with the direction of their monomers.[2, 15] (**Figure 3.4 A and B)**

The direction of the N-terminal of the H7 helix of the α, β-tubulin heterodimer is upwards and looks like an arrow. This is different in the *homo-sapiens* dimer in which the direction of the N-terminal of the H7 helix of chain A is oppositely arranged compared to chain B. (**Figure 3.4 A and B)**

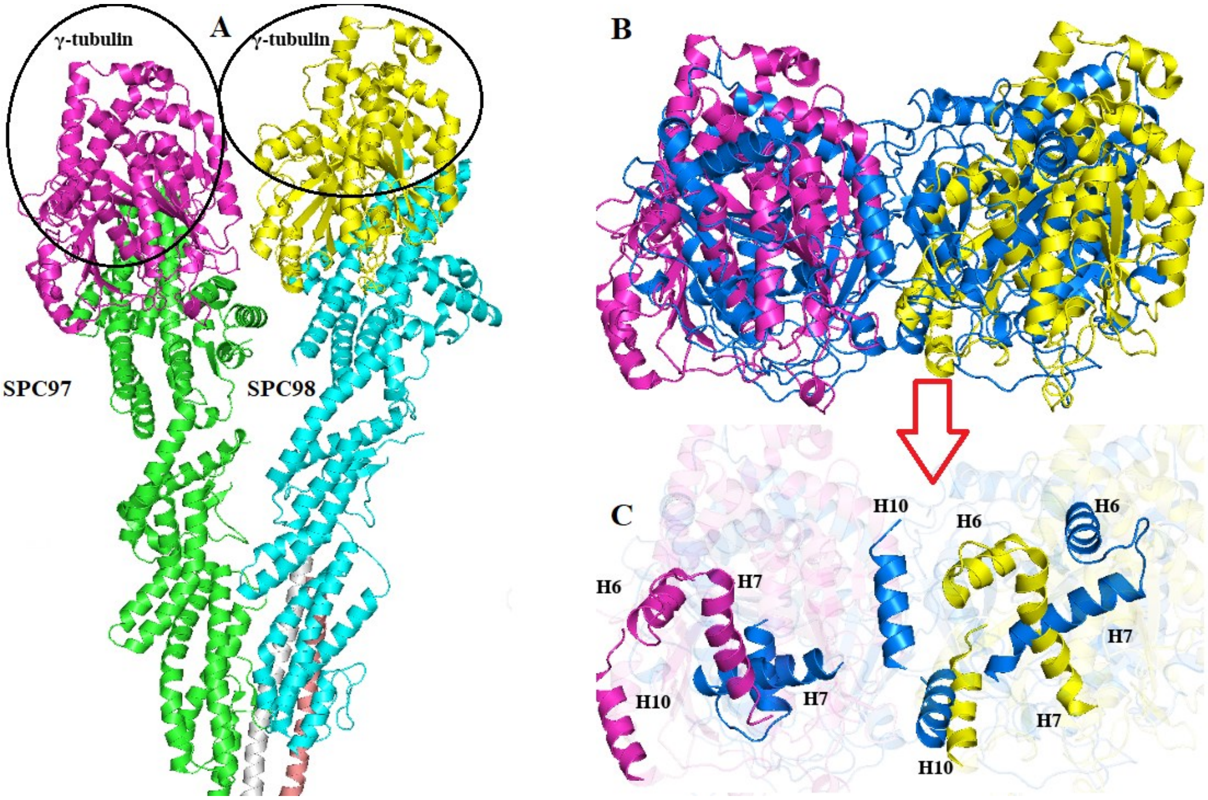

Figure 3.2: Comparison of a γ-tubulin dimer in *homo-sapiens* and yeast dimer at γTuSC. **(A)** Yeast γ-tubulin dimer inside the small complex; two monomers of γ-tubulin are colored in magenta and yellow. (**B**) The alignment of *homo-sapiens* γ-tubulin dimer on to the γ-tubulin dimer in a γTuSC; the *homo-sapiens* γ-tubulin for both chains are colored in blue, yeast γ-tubulin are colored in magenta and yellow. **(C)** The orientation of the secondary segment structure of H7 and H10 after superimposition of two dimers on each other. The same coloring is used for section A for sections B and C with γ-TuSC, two monomers of

γ-tubulin are colored in magenta and yellow, and the *homo-sapiens* γ-tubulin for both chains are colored in blue.

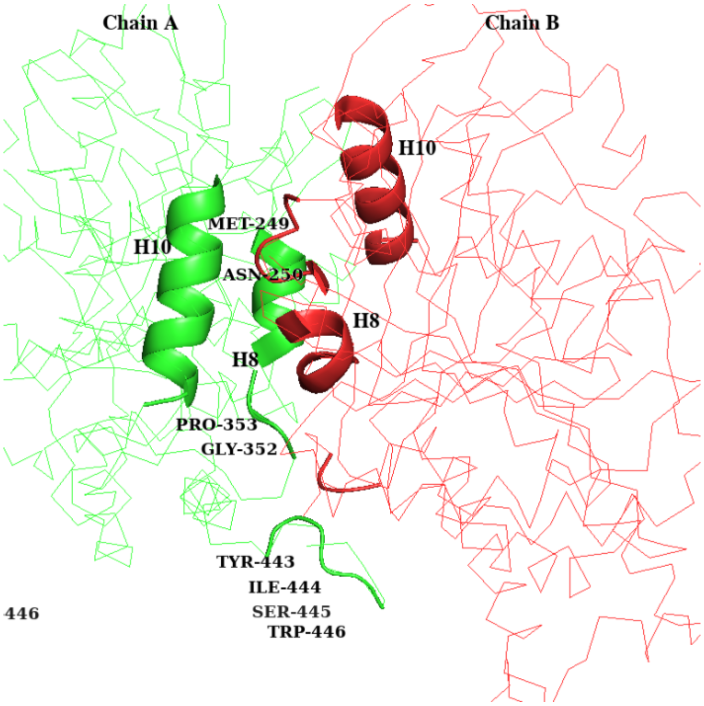

Figure 3.3: Contributing helices and loops in the interface interactions of chains A and B in the *homo-sapiens* γ-tubulin dimer. Chain A is colored in green and chain B in red. The interface elements are shown in cartoon representation for each chain.

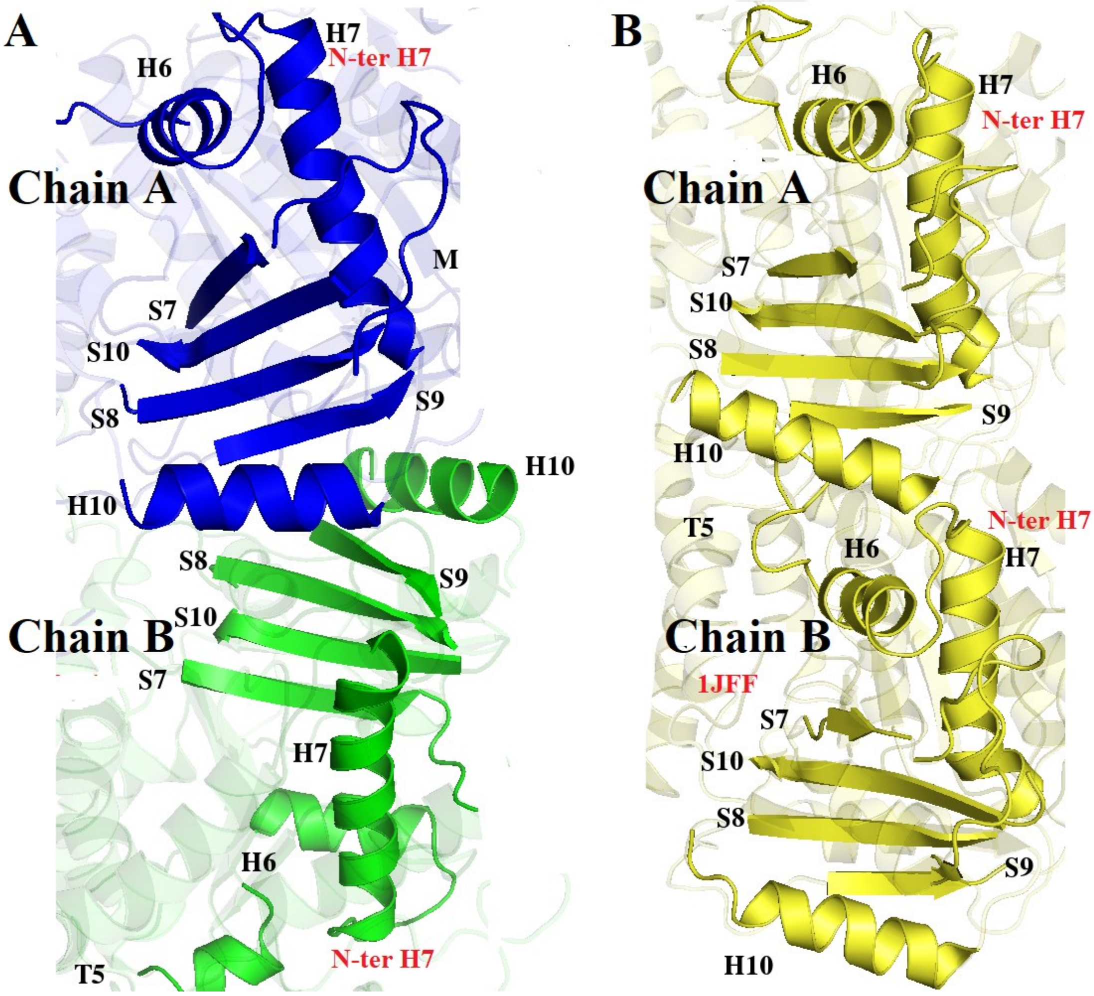

Figure 3.4: Comparison of α, β-tubulin heterodimer with the dimer of γ-tubulin. (**A**) the γ-tubulin dimer. (**B**) α, β-tubulin heterodimer (1JFF). N-ter: N-terminal with both A and B.

The role of GTP in β-tubulin is both structural and functional as GTP is hydrolyzed to GDP. In α-tubulin, GTP does not contribute to the function of the protein, and its role is structural.[16-18] The affinity of *homo-sapiens* γ-tubulin for GTP and GDP is in the same range as β-tubulin, as explained in chapter two. However, other than that, there is little information about the role of GTP in *homo-sapiens* γ-tubulin.[19] The role of GTP is well studied in yeast Tub4, and it discussed that the GTP is essential for proper nucleation of MTs.[19] Also, in yeast γ-tubulin, the nucleation of MTs is dependents on GTP because mutation of residues at the GTP binding site impairs the nucleation.[20]

In section 3.1.1 the *homo-sapiens* and yeast γ-tubulin structural dissimilarities in γTuSC were discussed. Here the focus will be on investigating the ability of GDP and GTP to induce straight conformation. It remains elusive which conformation, the straight or the curved is active in *homo-sapiens* γTuSC, in γTuRC or whether the transition from curved to straight occurs in γ-tubulin dimer or not. The cation's role in interface interactions and the high-affinity binding site with conformation of GDP-bounded dimer will be investigated.

β-tubulin hydrolyzes GTP immediately after binding to the plus end of MTs. The mechanism by which the tubulin family of proteins hydrolyzes the GTP is not fully known.[21] It is unclear whether tubulins use an activating protein or independently hydrolyze GTP. Evidence of the hydrolyzing activity of γ-tubulin and the possible involvement of activating protein is unknown.[19]

3.1.2 Experimental Set-Up of MD Simulation of GTP and GDP Liganded of γ-Tubulin Dimer

The crystal structure of a *homo-sapiens* γ-tubulin dimer with the PDB code of 3CB2[1] [22] and UniProt code of P23258 is obtained from the protein data bank. This structure has missing atoms with both A and B chains, which were added to the dimer by employing the Swiss-PDB Viewer.[23] The missing residues were added using Pymol tool.[24] The missing residues for chain A include Thr278, Asp279, Gln280, Ser281, Val282, Val283, Arg311, Gln312, Leu367, Pro368- Ser369, Ala370, His371, Gly447, Thr448, Gln449, Glu450, Gln451, and for chain B Gly97, Gly98, Thr278, Asp279, Gln280, Ser281, Val282, Ala283, Ser284, Val285, Arg286, Aly308, Arg309, Asp310, Arg311, Gln312, Lys344, Ser369, Ala370, His371, Gly447, Thr448, Gln449, Glu450 and Gln451. Gromos 53A6 was used to generate the topology of the γ-dimer [25], "md" integrator with a 2 fs time step was applied, and Linear Constraint Solver (LINCS)[26] was used to constrain all bond lengths. The protein was embedded in the cubical solvent box with SPC water model. A distance of 1 nm was assigned between the protein and the box edge. Non-bonded interactions, including van der Waals and electrostatic, were modeled using Lennard–Jones and electrostatic potentials, respectively. A cut-off distance of 1.4 nm was assigned to both Lennard–Jones and electrostatic interactions. The calculations of electrostatic interactions contributing to energy and forces were carried out based on the Particle Mesh Ewald algorithm.[27]

All simulations were energy minimized to relax the internal constraints by using the steepest descent method prior to the simulation. The Position Restraint (PR) was applied for 2 ns after the energy minimization. 10 ns equilibration simulation was performed before starting the production run. The time constant for pressure coupling was set to 1.0 ps with the compressibility of 4.5e-5 bar at a 300 K temperature. Protein and the non-protein groups were coupled to a temperature bath of 300K with a time constant of 0.1, which was kept constant by temperature coupling with Bussi's thermostat.[28] The calculations were performed on high-performance computer clusters of ACENET, Graham, and West Grid Consortium. The Automated Topology Builder (ATB) repository was used to generate the united atom topology of GDP and GTP compatible with the Gromos family of force fields. ATB employs quantum mechanical calculations for generating the force filed descriptions of the ligands.[29] Docking of GTP into its binding site on chain A and chain B of the γ-tubulin dimer was achieved by using the FlexX tool[30] (version 2.1.3) of LeadIT. FelxX uses an incremental construction algorithm. The ranking of an energetically favorable docking pose is based on their total binding energy, which was calculated based on the Böhm scoring function.[31]

GDP coordinates were obtained from the original crystal conformation of 3CB2, and the protonation states of GTP and GDP were set to -4 and -3, respectively.[1, 32, 33]

3.1.3 Results and Discussion

To evaluate the structural stability of the γ-dimer, the RMS deviations of the backbone atoms for A and B chains in 200 ns were measured. The reference conformation was set to the last frame of the equilibrium simulation that was carried out for 10 ns before the production run. The RMSD for chain A of NaCl increases gradually from the start point to a maximum of 3.5 Å at 100 ns, then with a low fluctuation of 0.2 Å - 0.3 Å ends up at

200 ns. The RMSD for chain B in NaCl simulation rises from 3.7 Å at 104 ns, then decreases to 2.8 Å at 150 ns, which is its convergence point and with no subsequent large fluctuations. (**Figure 3.5 A and B)**

The RMSD of chain A in the $ZnCl_2$ simulation increases gradually to 3 Å at 65 ns and is relatively stable from its convergence point at 150 ns to the end of the simulation at 200 ns. The convergence point for chain A in $MgCl_2$ simulation is at 145 ns. (**Figure 3.5 A**)

The RMSD of chain B of the $ZnCl_2$ simulation gradually increases to 3.5 Å until 200 ns. Chain B in $MgCl_2$ simulation has a lower RMS deviation compared to the $ZnCl_2$ simulation, and its RMSD increases to 2.5 Å, which is its convergence point at 80 ns. It has no high fluctuations afterward until the end of the trajectory at 200 ns. (**Figure 3.5 B**)

For all simulations, the last 50 ns from 150 to 200 were considered for data analysis of the unliganded dimers.

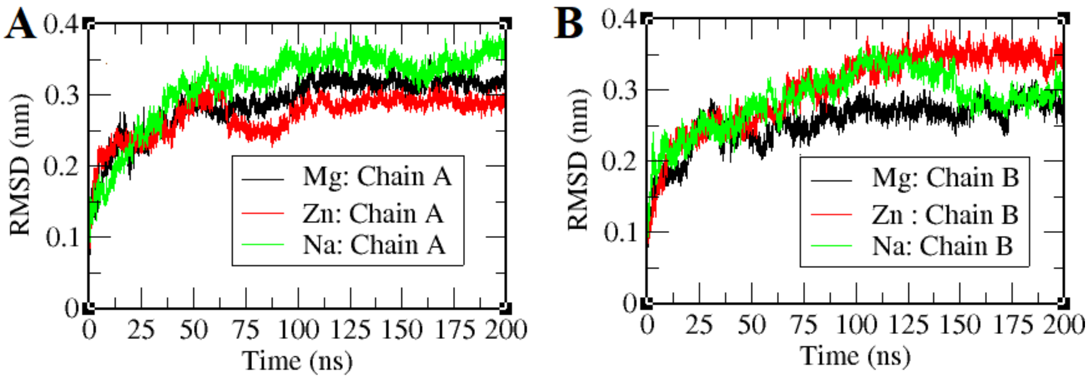

Figure 3.5: The root mean square deviation (RMSD) of backbone atoms of the residues for chain A and chain B of the unliganded γ-tubulin dimer. (**A**) the RMSD of chain A. (**B**) the RMSD of chain B. For both chains, the RMSD of $MgCl_2$ simulation is colored in black, red in $ZnCl_2$ and NaCl in green.

3.1.3.1 Interactions Between Chain A and B Under Three Different Ionic Conditions

The role of cations in the polymerization of a complex of proteins remains mostly elusive. There are studies that link the aggregation of proteins such as amyloid-beta (Aβ) and α-synuclein to Ca^{+2}, Fe^{+3} cations.[34-36] The electrostatic and L-J interaction energy between chains A and B of the γ-tubulin dimer was calculated for the last 50 ns of the simulations to assess how the interaction energies differ in each simulation. The electrostatic energy between chain A and B of the γ-tubulin fluctuates around -1500.2 kJ/mol, and -1400.5 kJ/mol in $MgCl_2$ and $ZnCl_2$ simulations, respectively, and about -1250.3 kJ/mol in NaCl simulation from 150 ns to 200 ns. Also, the L-J energy between chains A and B is stronger for the $MgCl_2$ simulation with a value of -840.0 kJ/mol, -750.3 kJ/mol in $ZnCl_2$, and -550.0 kJ/mol in NaCl simulation. (**Figure 3.6 A & B)**

The abovementioned interactions are the average over the last 50 ns. For instance, in $MgCl_2$ simulation, the electrostatic energy between A and B chain starts at -1430.5 kJ/mol at 150 ns then increases to -1780.2 kJ/mol at 165 ns. From 168 ns to 172 ns it is around -1570.6 kJ/mol; until 200 ns, it has many fluctuations. However, the amount is larger than that of $ZnCl_2$ and NaCl simulations. (**Figure 3.6 A)**

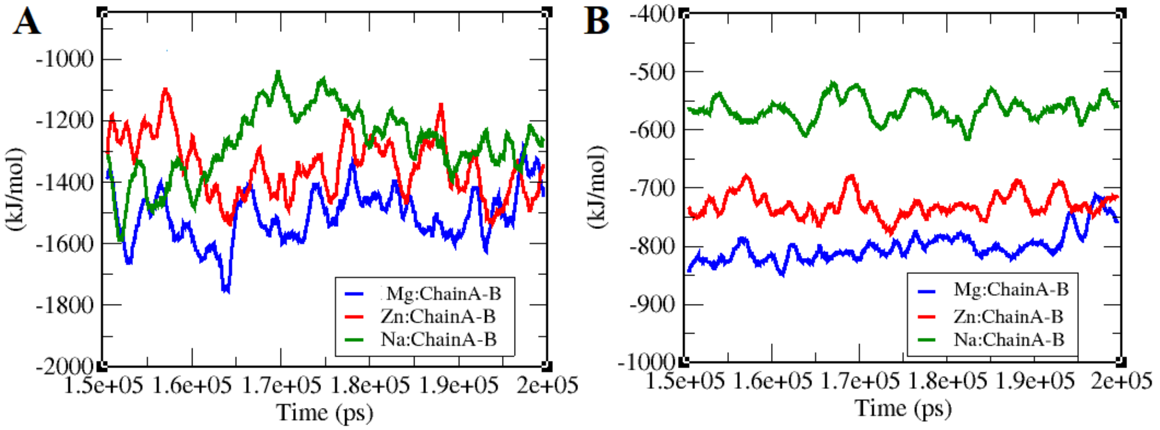

Figure 3.6: The average electrostatic and L-J interactions between chains A and B. (**A**) The electrostatic interaction energy. (**B**) The L-J interaction energy. The interaction energy is colored in blue, red, and green for $MgCl_2$, $ZnCl_2$, and NaCl simulations, respectively.

The average electrostatic interaction energy between Na^+ and γ-dimer are fluctuating around - 453.5 kJ/mol for chain A and -333.2 kJ/mol for chain B. (**Figure 3.7)**

In contrast to Na^+, Mg^{+2} and Zn^{+2} have stronger electrostatic energy with chain A, which are -1982.4 kJ/mol and -2022.1 kJ/mol, respectively. It Was -2143.2 kJ/mol for chain B in Mg^{+2} and being -1745.9 kJ/mol for Zn^{+2} simulations. (**Figure 3.7)**

The average electrostatic energy between Zn^{+2} and Mg^{+2}, and each chain are four times higher than Na^+ simulations, -1982.4 kJ/mol in $MgCl_2$ simulation and -2021.1 kJ/mol in $ZnCl_2$ simulation for chain A compared to the -453.5 kJ/mol in NaCl simulation. (**Figure 3.7)**

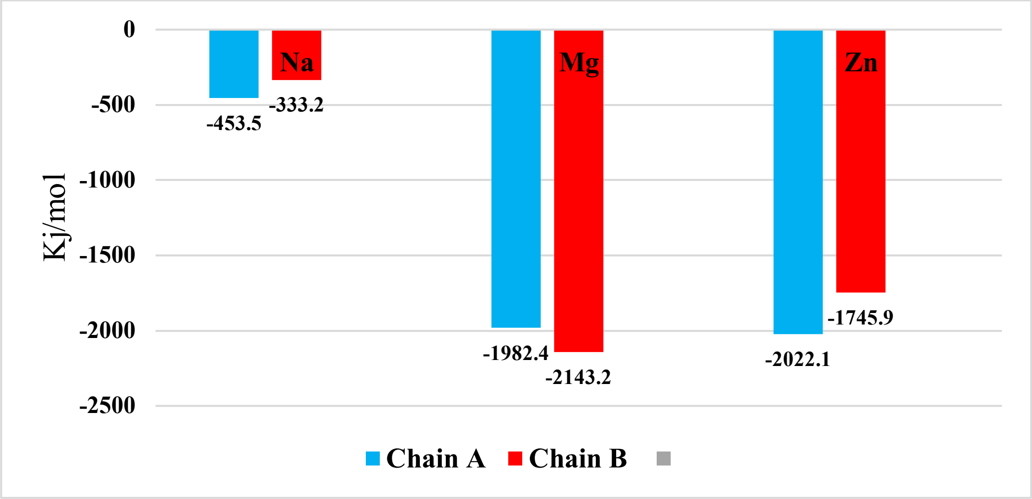

Figure 3.7: The average electrostatic energy between chains A and B with cations at each simulation from 150 ns to 200 ns. The interaction energy is colored in blue for chain A and in red for chain B.

The side chains of the oppositely charged residues, such as Asp, Glu, Arg, and Lys, affect dimer's interactions and motions. The cations contribute to the dynamic motion of both A and B chains through their electrostatic interaction energies.

To understand how cations affect the dynamics of the dimer, the number of interactions and H-bonds between A and B chains were evaluated. The number of interactions evaluates any interactions at a distance of ≤ 4 Å between two determined groups of atoms. These interactions can be between charge atoms or non-polar ones.

The number of interactions between the residues of chains A and B at ≤ 4 Å is 100 times higher in the $MgCl_2$ simulation compared to the other two simulations containing $ZnCl_2$ and NaCl. Chain A makes around 700 - 720 interactions with that of chain B in the $MgCl_2$ simulation from 150 ns to 200 ns. **(Figure 3.8 A)**

The number of interactions dropped to around 600 in both $ZnCl_2$ and NaCl simulation, which shows that higher interaction was generated between two chains in $MgCl_2$ simulation. It was also shown that the electrostatic and L-J interaction energies between chains A and B in the $MgCl_2$ simulation were -1500.2 kJ/mol and -840.0 kJ/mol, respectively, stronger than the NaCl simulation. The number of H-bonds at 4 Å cut-off between the A and B chains ranging from 30 - 33 H-bonds in the $MgCl_2$ simulation. (**Figure 3.8 B & 3.6**)

In NaCl, the number of H-bonds between A and B chains is around 19 - 20, and in the $ZnCl_2$ simulation fluctuates about 22 - 25. (**Figure 3.8 B**)

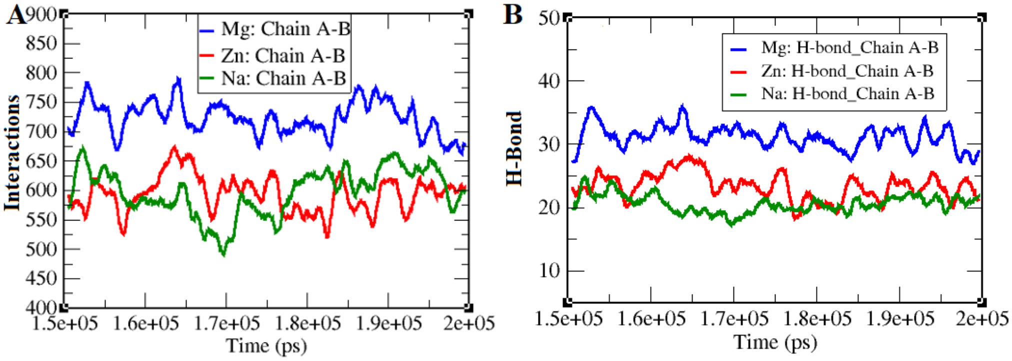

Figure 3.8: The number of interactions and H-bonds between chain A and chain B. **(A)** The number of interactions at ≤ 4 Å between chain A and B with three simulations. (**B**) The

number of H-bonds at ≤ 4 Å between chains A and B with three simulations. They are colored in blue, green, and red in $MgCl_2$, NaCl, and $ZnCl_2$ simulations, respectively.

It was shown that γ-dimer in $MgCl_2$ and $ZnCl_2$ simulations make stronger interactions with cations compared to NaCl. Chains A and B have a larger number of interactions, H-bond, and L-J as well as electrostatic energy. (**Figure 3.6 - 3.8**)

These differences are attributed to the role of divalent cations and their interactions with the protein, which will be shown later with residues of the protein. The role of cations should be considered as a cumulative role during the course of simulations.

γ-dimer secondary structure segments that contribute to the interface interactions are the H8 (Leu253-Leu260), H10 (Pro330-Arg343) helices of both chains, the C-terminal tail of the γ-tubulin from Try443-Trp446, and Met249, Asn250, Gly352, Pro353 and the residues of T7 (Thr240-Asp252) loop. (**Figure 3.3**)

The H10 helix (Pro330-Arg343) in the intermediate domain (Arg244-Asn380) rearranges during the transition from the straight to curved conformation. With the γ-tubulin dimer, the H10 helix plays a role in the interface interactions with both chains. But to what extent the H10 helices (Pro330-Arg343) of both chains contribute to the interface interactions is unknown. (**Figure 3.3 and 3.9**)

Thus, to evaluate the H10 helix's role in interface interactions, the electrostatic energy between the H10 helix of chain A from the whole chain B and the H10 helix of chain B from the whole chain A was analyzed in $MgCl_2$ simulation. At this evaluation, the H10 helix was considered as one group and the opposite chain as another group. The $MgCl_2$ simulation was selected for the purpose of this evaluation because it had stronger electrostatic and L-J interactions between A and B chains with -1500.2 kJ/mol and -840.0 kJ/mol compared to the NaCl and $ZnCl_2$ simulations. (**Figure 3.6 and 3.9**)

The average electrostatic interaction energy between the H10 helix of chain A from the whole chain B fluctuates from ~ -350.5 kJ/mol to -380.5 kJ/mol. The average electrostatic energy between the H10 helix of chain B and the whole chain A is about -100.5 kJ/mol from 150 ns 173 ns and -200.5 kJ/mol from 185 ns until 200 ns. Their sum, or in other words, the contribution of both the H10 helices in electrostatic interactions between chains A and B of the dimer, is ~ -575.2 kJ/mol. (**Figure 3.9**)

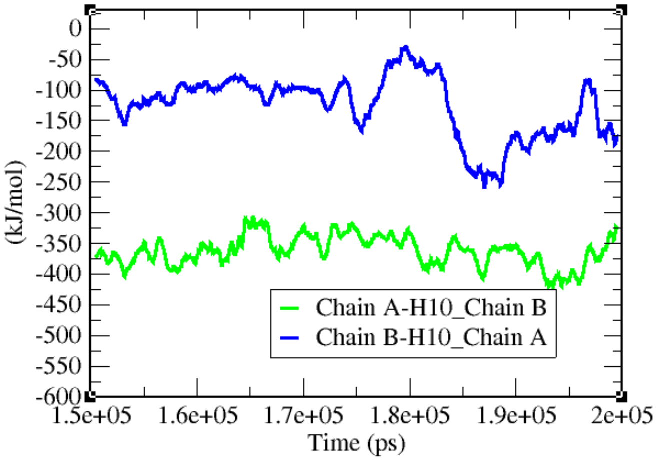

Figure 3.9: The electrostatic interactions between H10 helix and the opposite chain. The electrostatic energy between the H10 helix of chain A from whole chain B colored in green and electrostatic energy between the H10 helix of chain B from whole chain A in blue.

3.1.3.2 Straight or Curved Conformation of Chains A and B of the γ-Dimer

α, β-tubulin heterodimer, is adapting straight and curved conformations distinguishable from each other by their structural superimposition.[13, 37, 38] The α, β-tubulin heterodimer with a straight conformation is a building block of the dynamically active MTs with lateral interactions between the α-tubulin (α-α) and β-tubulin (β-β).[14] Their longitudinal interactions are with their non-similar monomers (i.e., α-with β-tubulin). (**Figure 2.5 and 3.10**)

However, the curved conformation has shown rearrangements that are mostly in the intermediate domain (Arg244-Asn380), which is different from the straight conformation. One of the distinct rearrangements from straight to curved conversion is the core H7 helix (Asp224-Phe242). (**Figure 2.5 and 3.10**)

To quantitatively study dimer curvature and straightness, the dCOM between the N-terminal of the H7 helix (Phe225-Leu231) and the S6 strand (Cys201-Asp206) for the available crystal conformations were evaluated. The curved β-tubulin has distinct curvature, especially within the N-terminal of the core H7 helix compared to the straight conformation. The S6 is selected because it is relatively stable during the conformational change from straight to curved conformation. Hence it is, therefore, the stable secondary structure segment of the γ-tubulin. (**Figure 3.10**)

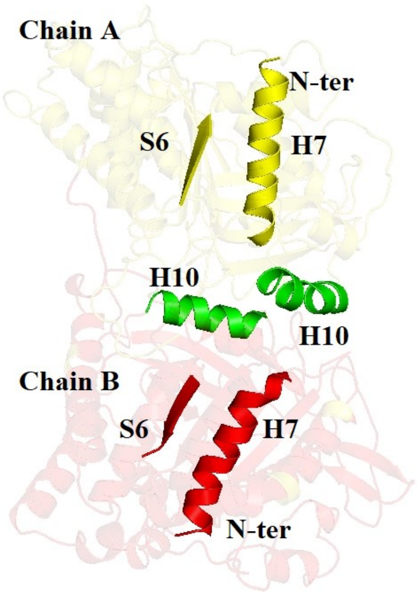

Figure 3.10: Chain A and B of the γ-tubulin dimer with the position of H7, H10, and S6 with respect to each other. The chain A secondary segments are colored in yellow and red for chain B.

The dCOM from H7 helix and the S6 strand with the available crystal structures show 1.5 Å difference between β-curved (1SA0) and β-straight (1JFF). (**Table 2.3**)

On the basis of H7 and the S6 dCOM evaluation of curved (1SA0) and straight (1JFF) β-tubulin, the dCOM of the H7 helix and the S6 strand of the γ-tubulin dimer is considered to be a curved conformation for ≤ 1.6 nm, and straight for a value more than 1.70 nm. The intermediate conformation has a dCOM of H7 (Phe225-Leu231) helix and S6 strand (Cys201-Asp206) between the curved (1.60 nm) and straight conformation (1.70 nm) with the value between 1.60 nm – 1.70 nm. (**Table 2.3**)

After monitoring the dCOM of the H7 helix (Phe225-Leu231) and the S6 strand (Cys201-Asp206) in chain A, the curved conformation was seen to be a dominant conformation in three simulations. Form approximately 50 ns, the H7 and the S6 dCOM of chain A fluctuates in the range of 1.58 nm - 1.59 nm in three simulations. There are fluctuations that decrease it in $MgCl_2$ simulation to 1.5 nm at 165 ns. (**Figure 3.11 A**)

In chain B of the γ-tubulin dimer, the intermediate conformation is dominant in NaCl and $ZnCl_2$ simulations and a curved conformation in the $MgCl_2$ simulation. The dCOM of H7 helix and the S6 strand in the NaCl simulation is ~ 1.69 nm from 163 ns to 200 ns. For chain B of γ-tubulin in the $ZnCl_2$ simulation, the value of dCOM of H7 and S6 is ~ 1.7 nm from 170 ns to 180 ns, being at the range of 1.65 nm - 1.66 nm from 150 to 170 and 183 to 200 ns. The dCOM of chain B in the $MgCl_2$ simulation various from 1.58 nm - 1.61 nm from 150 ns to 200 ns, which resembles the curved conformation. (**Figure 3.11 B**)

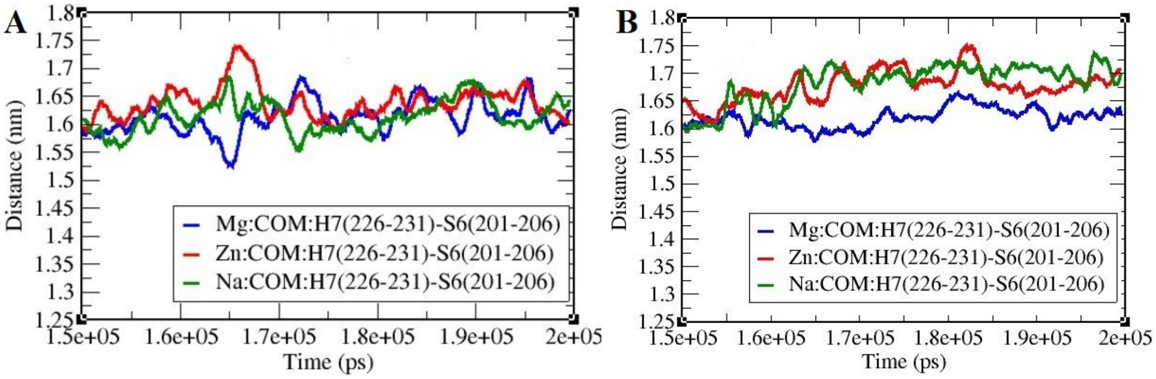

Figure 3.11: The dCOM of H7 helix and S6 strand for both chains A and B. **(A)** The dCOM of H7 helix (226-23) from S6 strand (201-206) for chain A. (**B**) for chain B. They are colored in blue, green, and red for $MgCl_2$, NaCl, and $ZnCl_2$ simulations, respectively.

The result of the evaluation of dCOM of the H7 helix (Phe225-Leu231) and the S6 strand (Cys201-Asp206) shows that in apo-γ-tubulin dimer, the curved and intermediate conformations are dominant in NaCl and $ZnCl_2$ simulations. The γ-dimer has a lower conformational change in $MgCl_2$ simulation because curved was the dominant conformation with a dCOM of less than 1.60 nm in both chains, and it was more stable. (**Figure 3.11**)

The straight conformation was not observed in these simulations; this finding further supports the view that soluble tubulins can be found in the curved and intermediate conformations. (**Figure 3.12**)

The value of H7 from S6 dCOM for A and B chains is not the same for $MgCl_2$, $ZnCl_2$, and NaCl simulations. This indicates A and B chains' straightness or curvature is related to the cations in the simulations and is independent of each other. The $MgCl_2$ simulation has shown the same value of ~ 1.55 nm - 1.62 nm for dCOM of H7 and S6 for the chains A and B without any large fluctuations. Except for some insignificant changes at 165 ns, 167 ns, 180 ns, and at 190 ns with chain A that increase the value to 1.62 nm of intermediate conformation. (**Figure 3.12 A**)

In contrast, in $ZnCl_2$ and NaCl simulations dCOM of H7 and S6 between chains A and B are more irrelative to each other compared to $MgCl_2$. In $ZnCl_2$ simulation, the dCOM of H7 and S6 for chain B is greater than chain A ranging from 165 ns to 190 ns, which is ~ 1.67 nm of the intermediate conformation. (**Figure 3.12 B)**

The dCOM of the H7 and S6 in chain B in NaCl simulation is ~ 0.8 Å higher than chain A within 160 ns to 200 ns that shows the state of conformational changes between chain A and B are independent of each other, and with three simulations, the dominant conformation is curved and intermediate. (**Figure 3.12 C)**

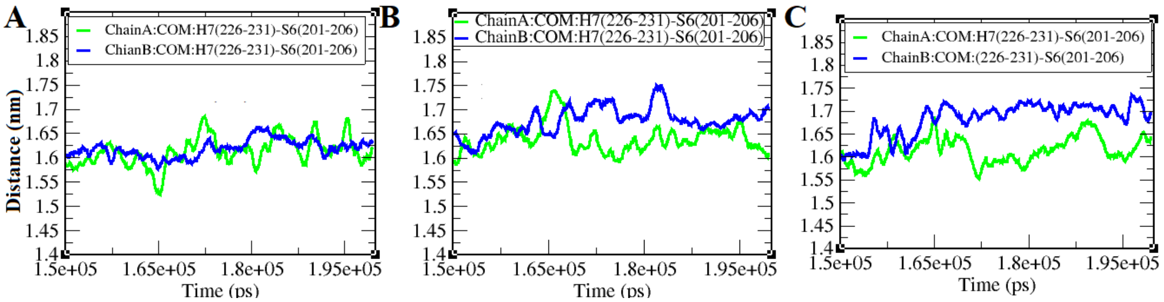

Figure 3.12: Comparison of dCOM of H7 helix and S6 strand between chains A and B. **(A)** The distances in $MgCl_2$ simulation. (**B**) In the $ZnCl_2$ simulation. (**C**) In NaCl simulation. For all simulations, the dCOM of the H7 and S6 strand is colored in blue for chain B and green for chain A.

The 200 ns conformations of the γ-dimer in three simulations were extracted to evaluate the straightness or curvature by superimposing it on the β-curved (1SA0) and straight (1JFF) conformations.

Chain A of γ-tubulin at 200 ns in $MgCl_2$ simulation has adapted a curved conformation. Secondary structure segments contributing to straight and curved conformations such as the H6 (Asn207-Asp216), H7 (Phe225-Leu243) helices as well as S7 (Phe268-Tyr273), S8 (Tyr317-Gln325), S9 (Ile356-Ser361), and S10 (Ser374-His381) strands, are aligned to curved β-tubulin.

The H7 helix of chain B at 200 ns is aligned to the H7 helix of curved β-tubulin. The conformation and coordination of H6 and S7, S8, and S10, are aligned to the curved β-tubulin. (**Figure 3.13 A and B)**

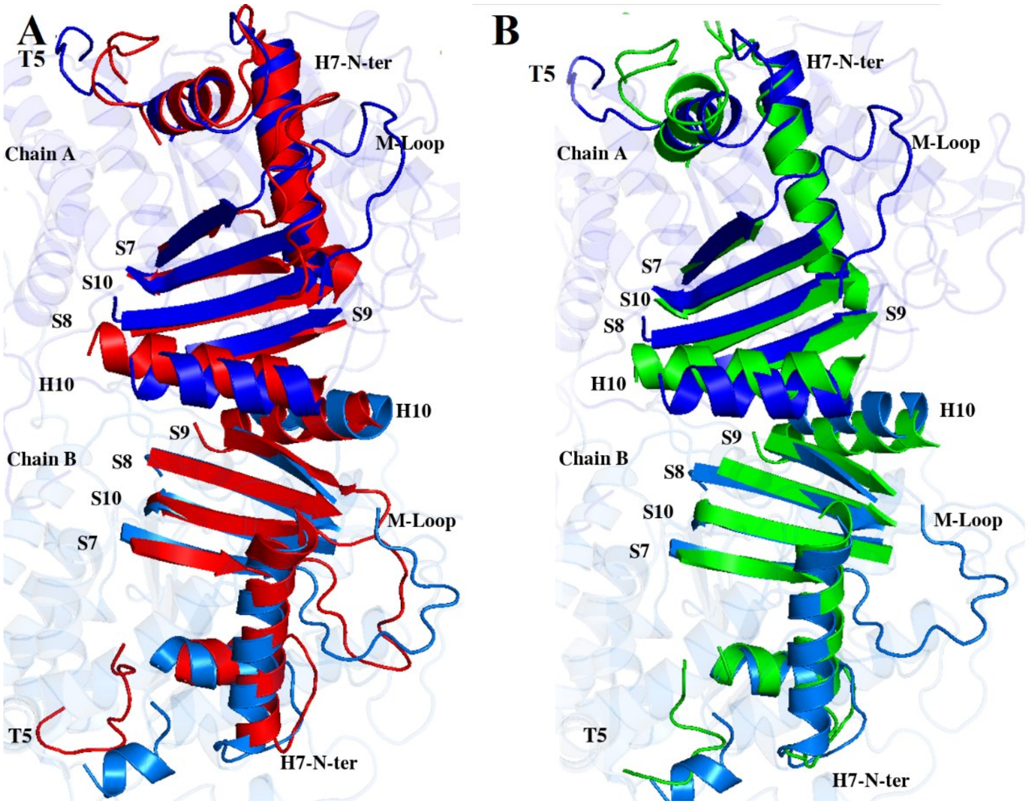

Figure 3.13: Superimposition of a 200 ns conformation of the γ-tubulin dimer in $MgCl_2$ simulation on to β-curved (1SA0) and β-straight (1JFF). (**A**) γ-tubulin dimer at 200 ns of $MgCl_2$ simulation in blue superimposed on straight β-tubulin (1JFF) in red. (**B**) γ-tubulin dimer in blue superimposed on curved β-tubulin (1JFF) in green.

Unliganded γ-dimer at 200 ns in $ZnCl_2$ was extracted from its trajectory and was superimposed on both β-curved and β-straight conformations.

Chain A at 200 ns adapted an intermediate conformation. The helices and strands that are contributing to the straight and curved conformations are not aligned to the straight or curved β-tubulins. The H7 helix was aligned to the curved H7 helix at C-terminal, and not aligned with the N-terminal of the H7 helix of curved tubulin. Also, the orientation of H6, H10, and four strands of S7 to S10 were aligned with none of the curved or straight β-tubulins, and an intermediate conformation that partially resembles both straight and curved conformations is a dominant conformation. (**Figure 3.14 A and B)**

Chain B of γ-tubulin at 200 ns in $ZnCl_2$ simulation adapted a curved conformation. The H7 helix (Phe225- Leu243) was aligned with the H7 helix of the curved β-tubulin.

The whole H6 and H10 orientations for Pro330 - Val333, and T5 loop (Pro173-Gln184) has also been aligned with curved β-tubulin. (**Figure 3.14 A and B)**

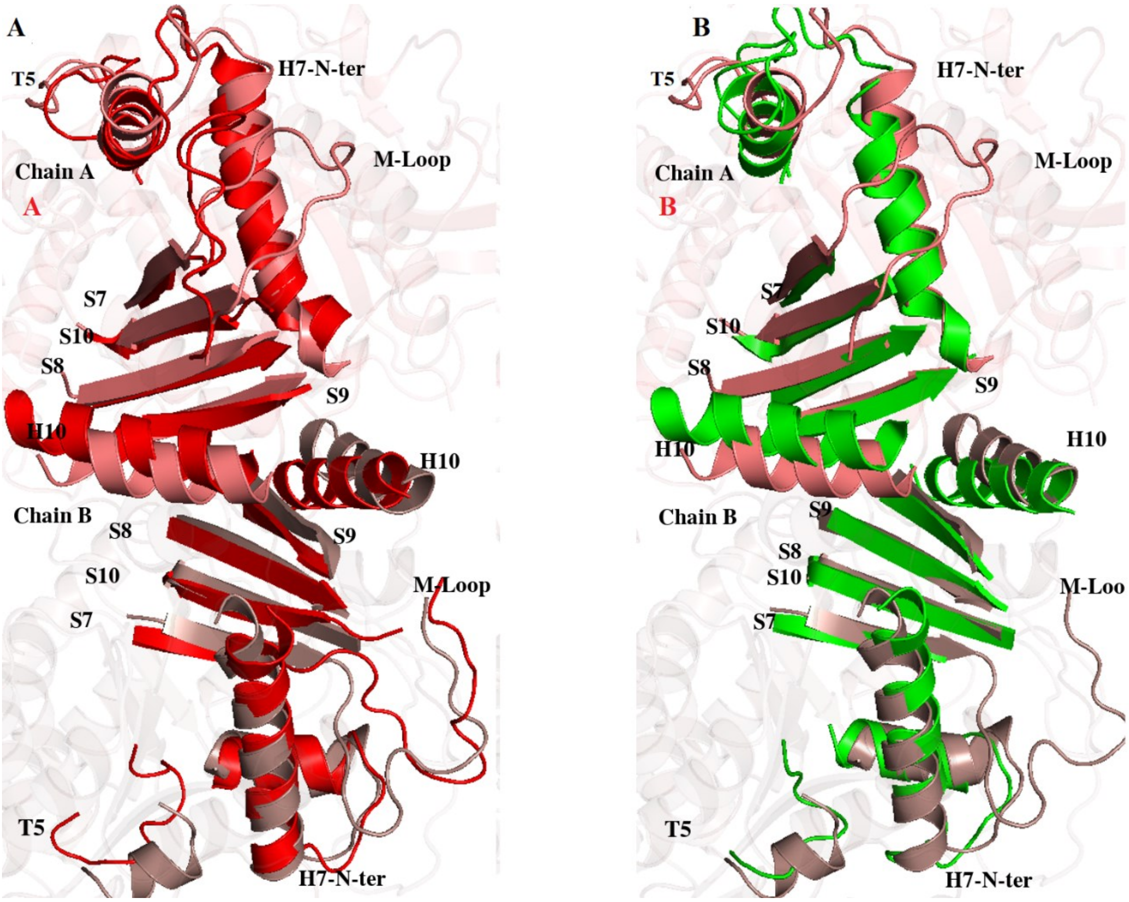

Figure 3.14: Superimposition of a conformation of the γ-tubulin dimer in $ZnCl_2$ simulation on β-curved (1SA0) and β-straight (1JFF). (**A**) γ-tubulin dimer in pink superimposed on straight β-tubulin (1JFF) in red. (**B**) γ-tubulin dimer in pink superimposed on curved β-tubulin (1JFF) in green.

Chain A of γ-tubulin at 200 ns in NaCl simulation is adapted to an intermediate conformation. The H7 helix (Phe225-Phe242) was aligned to the H7 helix of the curved β-tubulin, the orientations of other contributing elements consisting of the S7 (Phe268-Tyr273), S8 (Tyr317-Gln325), S9 (Ile356-Ser361), S10 (Ser374-His381) strands, and H6 helix (Asn207-Asp216) are resembling the intermediate conformation that has shown similarities to both curved and straight β-tubulins. The most significant differences are obvious with the conformation of the H10 helix (Pro330-Arg343), which is not aligned to conformation of H10 of the straight or curved β-tubulin. (**Figure 3.15 A and B)**

Chain B of the γ-tubulin at 200 ns of NaCl has adapted a curved conformation, which can be found by comparing the conformations of the secondary segments that contribute to the curvature such as H7, H6, and the beta-strands of the S7 - S10 to the curved β-tubulin. (**Figure 3.15 A and B)**

Both H6 and H7 helices were aligned to the H6 and H7 helices of the curved β-tubulin. Orientations of the intermediate domain strands of the S7 to S10 are mostly identical or aligned with the curved β-tubulin. The H10 was not aligned with the H10 helix of the straight (SA0) or curved (1JFF) β-tubulins. (**Figure 3.15 A and B)**

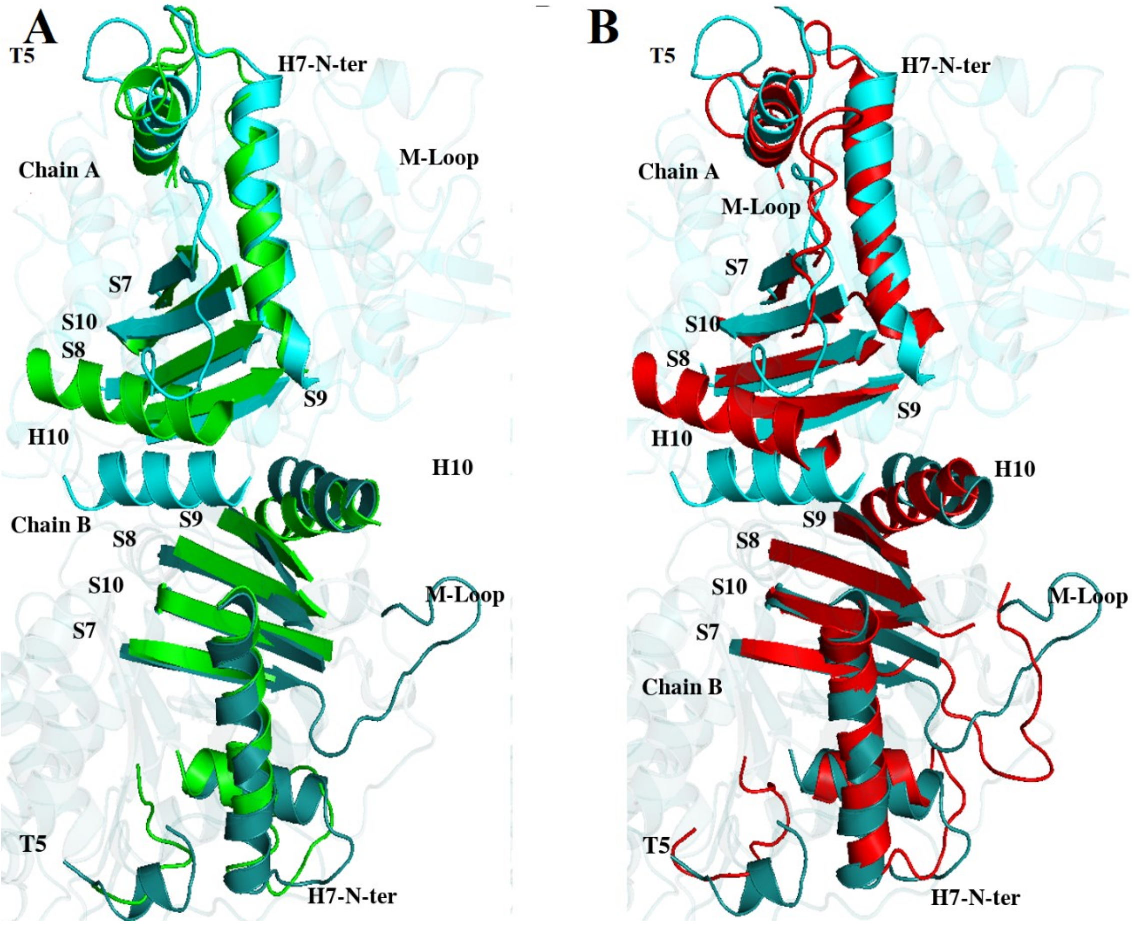

Figure 3.15: Superimposition of a conformation of the γ-tubulin dimer in NaCl simulation on β-curve (1SA0) and β-straight (1JFF). (**A**) γ-tubulin dimer in cyan superimposed on curved β-tubulin (1JFF) in green. (**B**) γ-tubulin dimer in cyan is superimposed on straight β-tubulin (1JFF) in red.

It is unclear and was not addressed whether the motion of the contributing region in straightness and curvature of the γ-tubulin is related or whether there are anti-correlated motions. Also, it is unclear whether the H7 motion affects the motion of the H10 helix or intermediate strands of S7 to S10 or not.

Dynamic cross-correlation analysis was used to determine the extent to which the displacement or fluctuation of Cα atoms of one secondary segment is correlated to another one, e.g., the H7 helix to the H10 helix. To address correlation between γ-dimer secondary segments, the dynamic cross-correlation was evaluated in NaCl simulation from 150 ns to 200 ns by using Bio3D package. The motion of the Cα of the H6-H7 segment of chain A from the H10 helix of chain A demonstrates no correlation with a zero value, and this shows that they fluctuate independently. The positive correlation has a value of 1 for the highest correlation and zero for no correlation; the highest anti-correlated motion has the value of -1 with no unit. The dynamic cross-correlation between the H6-H7 region of chain A with regards to the S8-H10 region of chain B was shown no correlation as well.

The T5 loop (Pro173-Gln184) of chain A was seen to have no positive or negative correlation with respect to the H6-H7 region (Asn207- Leu243) of chain A or B, although it had an anti-correlated motion of 0.3 - 0.4 to S8-H10 helix of chain A. (**Figure 3.16**)

The motion of C-ter helices of H11-H12 with respect to the H6-H7 segment of chains A and B has shown no positive or negative correlation. A positive correlation was found between C-ter helices of H11-H12 and the S8-H10 segment of chain A with a value of 0.2 - 0.3, and zero correlation to chain B. Also, for chain B, the dynamic cross-correlation of the C-ter helices from T5, M loop, and H6-H7 helices was similar to chain A. (**Figure 3.16**)

The S8-H10 and T5 loop of the chain B had no correlation in their motion with respect to the H6-H7 segment of chain B.

It can be concluded that the motion of the H6-H7 segment, which is responsible for the straightness and curvature of the tubulin family, is rather independent of other segments and secondary structures of the protein with no correlation.

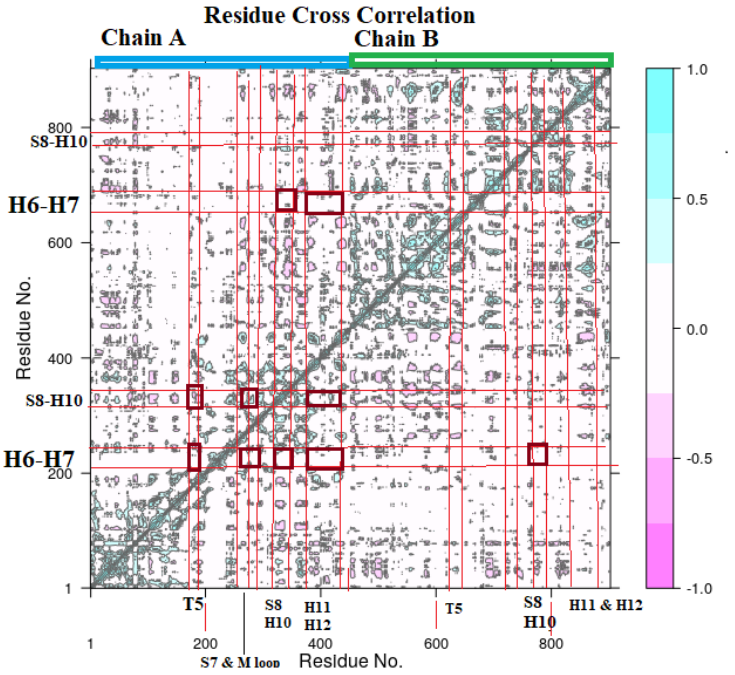

Figure 3.16: The residues dynamics cross-correlation functions of chain A and chain B in NaCl simulation. The extent to which Cα motions are correlated to each other is shown by colors and numbers; the zero with the white color means no correlation or independent motion. The positive correlation has a positive number from 0 to +1 colored in cyan. The negative or anti-correlated motion is from 0 to -1 colored in magenta.

3.1.3.3 Fluctuations of Chain A and B of the γ-Tubulin Dimer

The Root Mean Structural fluctuations (RMSF) of the residues in the dimer interface, including H8 (Leu253-Leu260), and H10 (Pro330-Arg343) helices of both chains, the C-terminal tail of the γ-tubulin for Try443-Trp446 with both chains, are ~ 1 Å - 2.5 Å in three simulations of NaCl, $MgCl_2$ and $ZnCl_2$. Their position is relatively stable during simulations. (**Figure 3.3**, **3.17, and 3.18)**

In NaCl simulation, the RMS fluctuation of H2 (Arg72-Asn79) helix is ~ 5 Å compared to more stable 3 Å and 2 Å in $MgCl_2$ and $ZnCl_2$ in chain A.

The RMSF value of the H11 (Ser385-Lys400) helix in NaCl simulation fluctuates ~ 6 Å, with a stable value of 3.2 Å and 3 Å in $MgCl_2$ and $ZnCl_2$ simulations in chain A. The RMSF value of the H12 (Asp419-Ala437) helix is 3 Å, 1.7 Å, and 4.5 Å in $MgCl_2$, $ZnCl_2$, and NaCl simulations, respectively. Therefore, the H2, H11, and H12 of chain A are not highly unstable in $MgCl_2$ and $ZnCl_2$ simulations. (**Figure 3.17)**

Both C-terminal helices of H11 (Ser385-Lys400) and H12 (Asp419-Ala437) have functional roles. The H11 paly an important role in the function of γ-tubulin as it acts as a nuclear localization segment[39] that facilitates its entry inside the nucleus. The function of H12 is necessary for the activity of γ-tubulin and its centrosome localization.[40] (**Figure 3.17)**

The RMSF of H4 helix (Thr145-Arg160) and H6-H7 (Arg217-Ser224) loop of chain A in the $MgCl_2$ simulation are ~ 3.8 Å and 3.7 Å, which are larger than the H4 helix and H6-H7 loop of the other two simulations with 2 Å, and 3 Å in $ZnCl_2$ and 1.5 Å and 3 Å in NaCl, respectively. (**Figure 3.17**)

The T5 loop (Pro173-Gln184) with chain B has a low fluctuation of 2.5 Å in $ZnCl_2$ simulation, 2 Å in the $MgCl_2$, and 2.1 Å in the NaCl simulation. The T5 loop (Pro173-Gln184) of chain A has 3 Å RMSF in $MgCl_2$ and NaCl and 2.5 Å in the $ZnCl_2$ simulation.

The H6-H7 loop (Arg217-Ser224) with chain B has a low RMSF value of 2.5 Å for $MgCl_2$ and in the NaCl simulation and 2 Å in the $ZnCl_2$ simulation. (**Figure 3.17-3.18**)

The RMS fluctuation of the intermediate domain strands S7 (Phe268-Tyr273), S8 (Tyr317-Gln325), S9 (Ile356-Ser361), and S10 (Ser374-His381) is lower than 1.5 Å for all the three simulations of chain A and B. (**Figure 3.17 and 3.18**)

The two loops of chain B, including M (Thr274-289Thr) and S8-H9 (Val303-Tyr316) loops in NaCl simulation, have large RMS fluctuations of 4 Å and 6 Ǻ. The RMS fluctuation of M (Thr274-289Thr) and H9-S8 (Val303-Tyr316) loops in $MgCl_2$ simulation is 3 Å and 5 Å, respectively, and for $ZnCl_2$, they have the RMS fluctuation of 2.5 Å and 4 Å, respectively. (**Figure 3.18**)

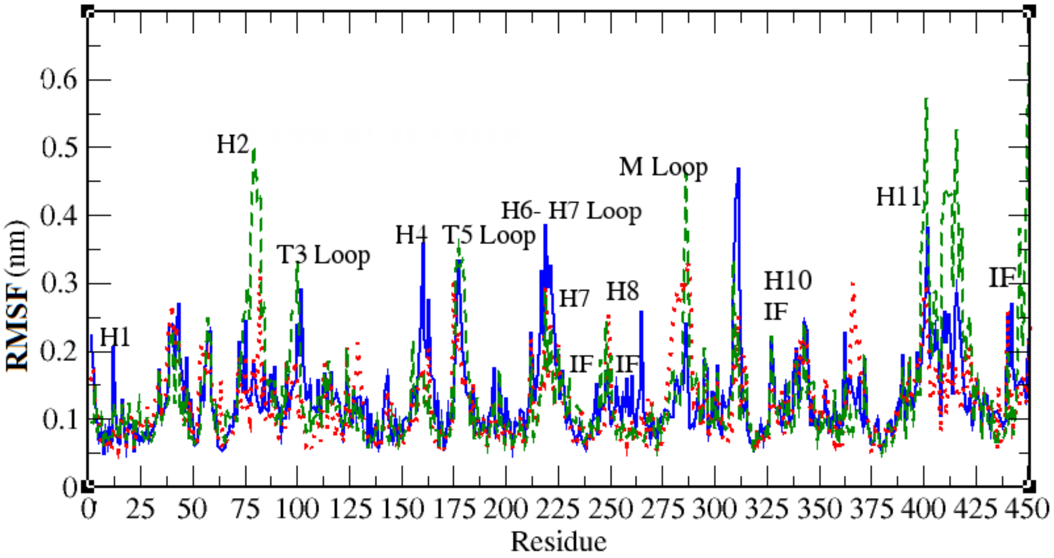

Figure 3.17: The root mean square fluctuations (RMSF) of residues of chain A with three simulations of NaCl, $MgCl_2$, and $ZnCl_2$. The RMSF is colored in blue, red, and green for $MgCl_2$, $ZnCl_2$’ and NaCl simulations, respectively. IF: interface residues.

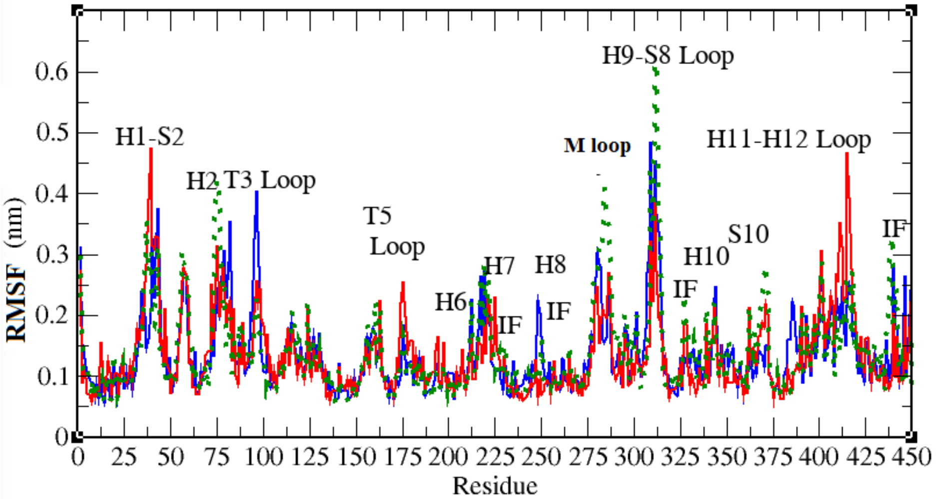

Figure 3.18: The root mean square fluctuations (RMSF) of residues of chain B with three simulations of NaCl, $MgCl_2$, and $ZnCl_2$. The RMSF is colored in blue, red, and green for $MgCl_2$, $ZnCl_2$' and NaCl simulations, respectively. IF: interface residues.

3.1.3.4 Interaction of Cations with the γ-tubulin Dimer

The number of interactions between cations and chains A and B at a cut-off of 4 Å was evaluated to investigate the interactions of cations and both chains.

The number of interactions between Zn^{+2}, Mg^{+2}, and chain A is at the range of 9 - 10 without fluctuations from 150 ns - 200 ns. This number in NaCl simulation changes from 2 to 15 interactions and has large fluctuations; for example, at 157 ns, 168 ns, 185 ns, and 200 ns number of interactions are 3, 15, 12, and 4. (**Figure 3.19 A)**

The number of interactions between cations and chain B fluctuates largely for Na^+ and is almost stable for Mg^{+2} and Zn^{+2} cations. This number in $MgCl_2$ is 10 - 12 and 7 interaction for $ZnCl_2$ simulations. But in the NaCl simulation, it changes from 3 - 7 interactions from 150 ns to 200 ns of its simulation. **(Figure 3.19 B)**

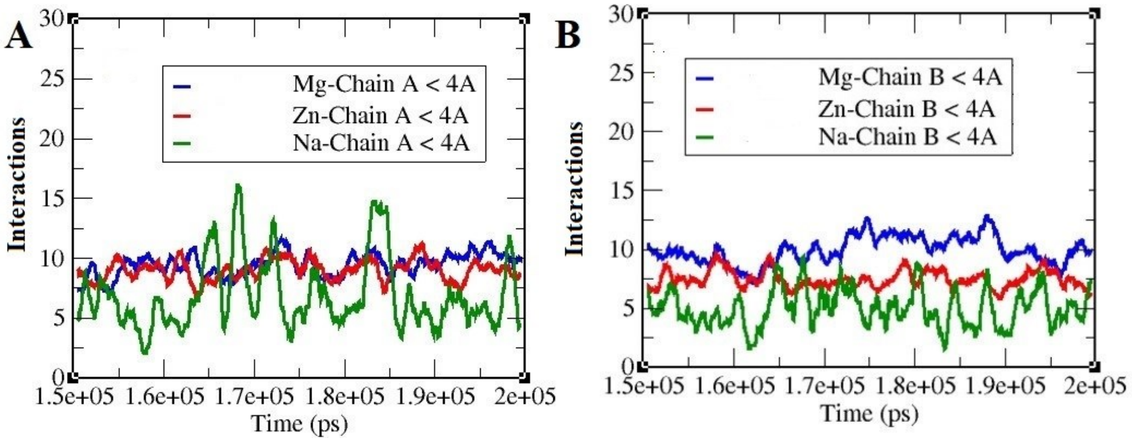

Figure 3.19: The number of interactions between each chain with Na^{+}, Mg^{+2}, and Zn^{+2} cations at 4 Ǻ. (**A**) The number of interactions for chain A. (**B**) for chain B. The number of interactions in $MgCl_2$ is represented in blue, red for $ZnCl_2$, and green under NaCl simulation.

Several residues of both chains were found at ≤ 4.5 Å from the Zn^{+2} cations at 200 ns conformation in the $ZnCl_2$ simulation. In chain A, the interactions include Glu58 at 3.9 Å, Asp180 at 2.1 Å, Glu112 at 3.9 Å, and Asp433 at 4.3 Å from the Zn^{+2} cations. In chain B Glu43 at 4.0 Å, Glu116 at 4.2 Å, Asp127 at 4.1 Å, and Asp433 at 2.2 Å were found in interaction with Zn^{+2} cations. **(Figure 3.20)**

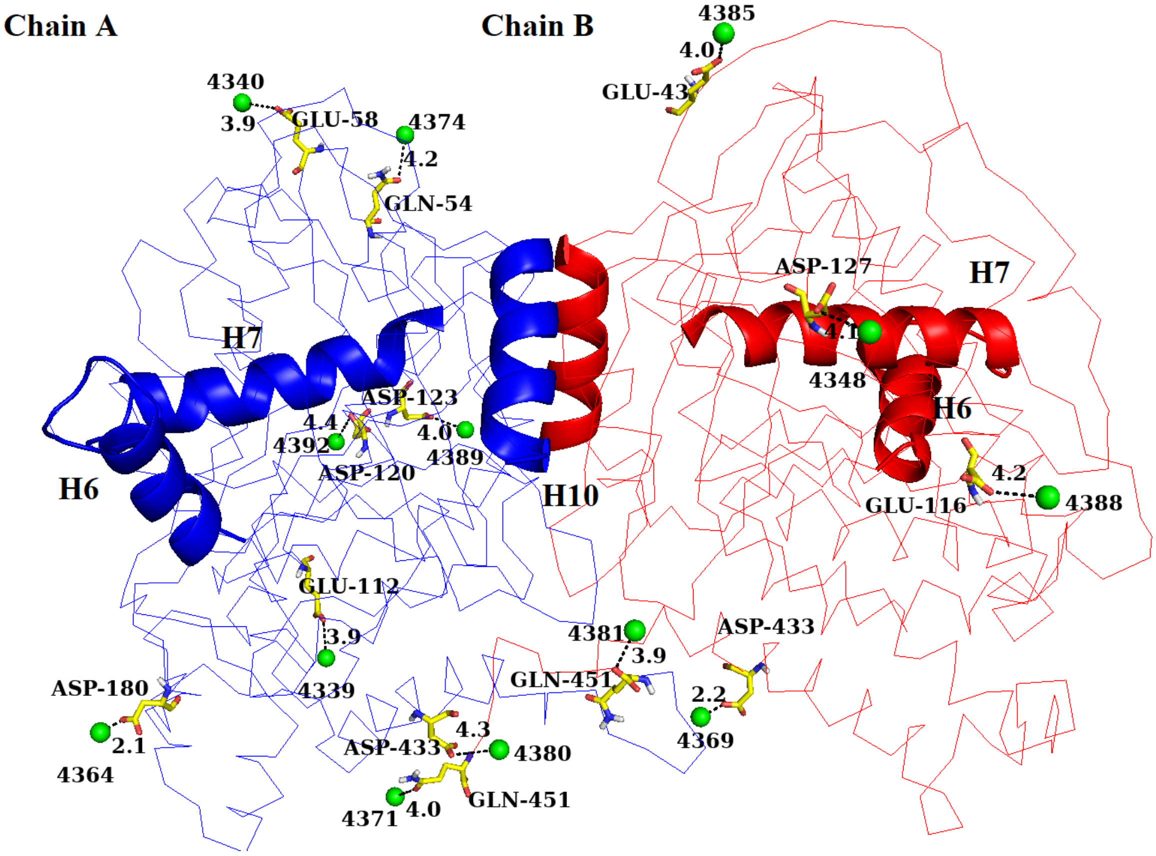

Figure 3.20: The 200 ns conformation of a γ-tubulin dimer in $ZnCl_2$ simulation with interacting Zn^{+2} at ≤ 4.5 Å. The Zn^{+2} are depicted in the red sphere and residues in the yellow stick.

Most residues (Glu58, Asp180, Glu112, Asp433), contributing to interaction with the Zn^{2+} cations, are part of the nucleotide-binding domain and C-terminal domain of the two chains and not the intermediate domain. Also, strong electrostatic energy is affecting the NBD and C-terminal domains compared to the intermediate domain (ID), as was shown.

In order to find whether the interactions between residues and Zn^{+2} cations are stable or not, the minimum distance between the aforementioned residues that had an interaction at ≤ 4.5 Å from Zn^{+2} cations at 200 ns was calculated for the last 50 ns.

The minimum distances between Zn^{+2} and Asp180 of chain A and Asp433 of chain B are stable at ~ 2 Å from 150 ns to 200 ns. The minimum distance between Zn^{+2} cations and Glu112 of chain A is fixed around ~ 4 Å with two changes that reach a minimum distance of 6 Å and 11 Å at 158 ns and 162 ns, respectively. In addition, the minimum distance between Glu116 and Asp127 of chain B to Zn^{+2} cations is fluctuating at the range of 4 Å - 8 Å from 150 ns to 200 ns. The large fluctuations from 5 Å to more than 10 Å are observed between the minimum distance of Glu34 of chain B, Glu58 and Asp433 of chain A from Zn^{+2}. (**Figure 3.21**)

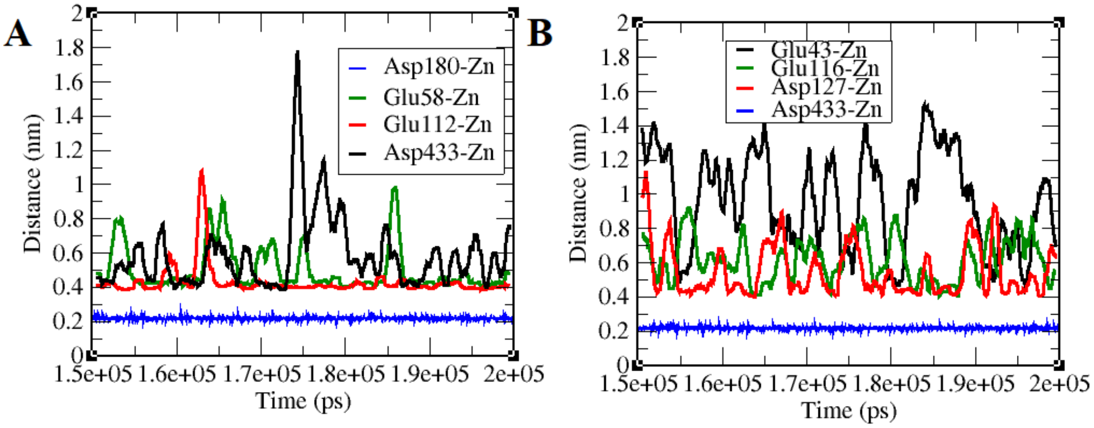

Figure 3.21: The minimum distances between residues of the ZnCl$_2$ simulation from Zn^{+2} cations. (**A**) The minimum distance for chain A. (**B**) The minimum distance for chain B.

One conformation as a representative of the γ-tubulin dimer at 200 ns of $MgCl_2$ simulation was selected to study cations that interact at ≤ 4.5 Å. (**Figure 2.22**)

The two residues of Asp180 (Chain A) and Asp433 (Chain B) are found at a distance of 2.1 Å and 2.2 Å from Mg^{2+}, respectively. The Asp127 (Chain B) and Glu89 (Chain B) were found at a distance of 3.9 Å of Mg^{2+}, respectively. Other interacting residues include Glu426 (Chain B) at 4 Å, Asp442 (Chain B) at 4.1 Å, and Asp200 (Chain B) at 4.1 Å. **(Figure 3.22)**

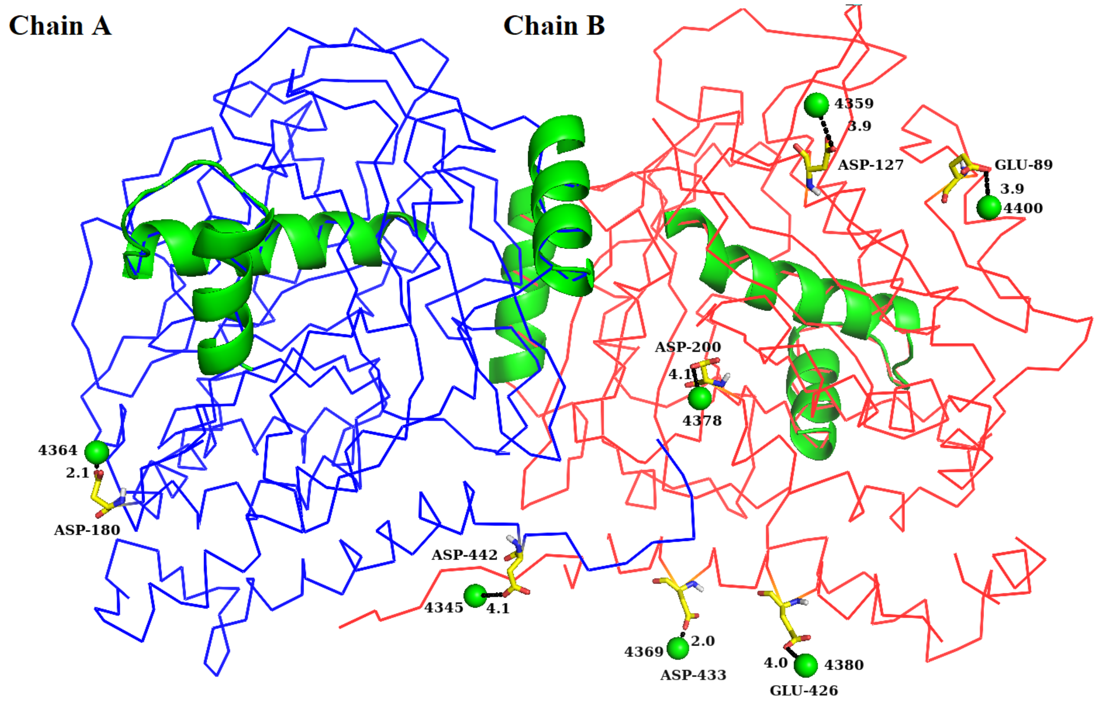

Figure 3.22: The conformation of γ-tubulin dimer at 200 ns of $MgCl_2$ simulation with all interacting Mg^{+2} at ≤ 4.5 Å of residues of both chains. The Mg^{+2} are depicted in the green sphere and residues in a yellow stick. Chain A in blue ribbon and chain B in red ribbon.

Asp180 (Chain A) and Asp433 (Chain B) interact at a minimum distance of 2 Å from Mg^{2+} cations; their interactions are stable from 150 ns to 200 for both residues. Asp433 (Chain A) is found with a minimum distance of 4 Å from 150 ns to 160 ns and 173 ns to 200 ns. The minimum distance between Glu89 (chain B) and Glu450 (chain A) has a large fluctuation in the range of 4 Å - 14 Å from 150 ns to 200 ns. (**Figure 3.23)**

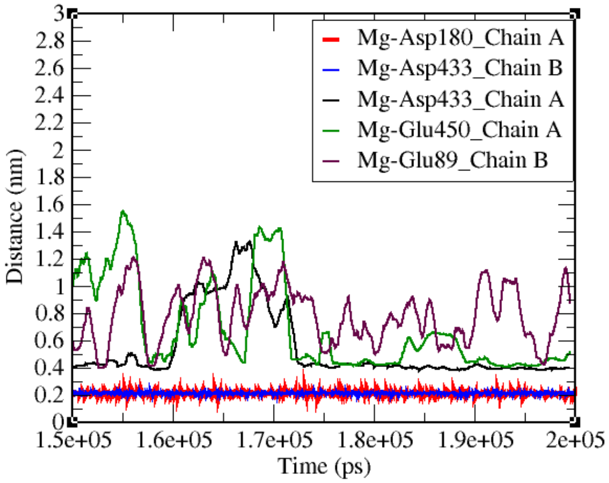

Figure 3.23: The minimum distances between residues of chain A and B in $MgCl_2$ simulation from Mg^{+2} cations. The selected residues are those that had an interaction at ≤ 4.5 Å from Mg^{+2} at 200 ns. The minimum distances are evaluated for Glu89, Glu450, Asp433, and Asp180 from 150 ns to 200 ns.

Two residues of Asp180 and Asp433 in $MgCl_2$ and $ZnCl_2$ simulations contribute to the stable interactions at ~ 2 to 2.5 Å from Mg^{2+} and Zn^{2+} cations. This stable interaction can have an impact on the function of the γ-tubulin inside the γ-ring. These two residues are located within the necessary region for the function of the γ-tubulin.[13] The Asp433 of

H12 at C-terminal and Asp180 belong to T5 of NBD. Both the T5 loop and H12 play an important role in the nucleation of MT and the functionality of the γ-tubulin. The H12 mutation impairs MTs nucleation, and the function of the T5 loop has been shown to switch between the curved and straight conformations.[13, 40]

The interacting residues of chain A in NaCl simulation include Glu39 at 2.4 Å and Glu58 at 4.1 Å of Na^+. With chain B, the residues of Gln221 at 3.8 Å, Glu125 at 2.6 Å, Asp127 at 4.2 Å, and Asp416 at 4.2 Å with respect to Na^+ cations contributed to the interaction at ≤ 4.5 Å. (**Figure 3.24**)

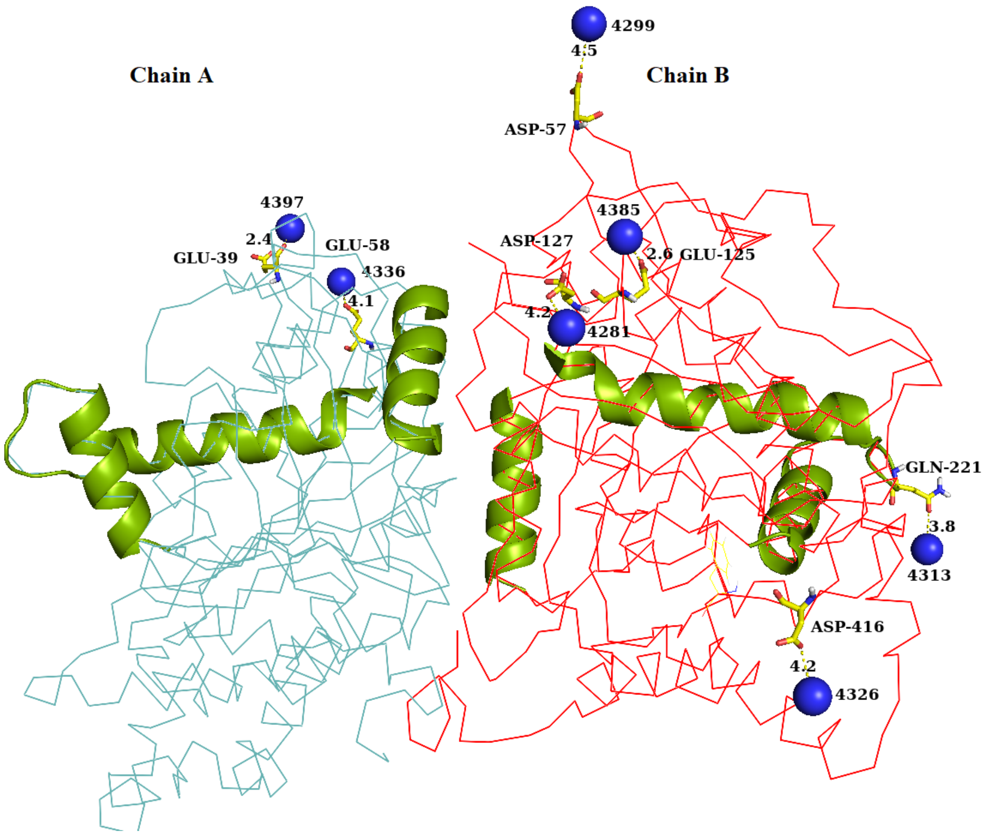

Figure 3.24: The 200 ns conformation of a γ-tubulin dimer in NaCl simulation with all interacting Na^+ at ≤ 4.5 Å. The Na^+ cations are depicted in blue and interaction residues in the yellow stick.

In contrast to $MgCl_2$ and $ZnCl_2$ simulations, the interactions between Na^+ and residues of both chains of the γ-tubulin are not stable. It was shown that their electrostatic energy with both chains in Na^+ was almost ¼ compared to Mg^{2+} and Zn^{2+} with - 453.5 kJ/mol for chain A and -333.2 kJ/mol for chain B. This indicates that the effect of Na^+ on the function of the proteins cannot be strong enough to have a considerable impact on their functions in contrast to the divalent cations with stable and strong interactions. None of the residues that were at 4.5 Å from Na^+ at 200 ns make close and stable interactions with Na^+. By considering the concentration of electrolytes such as $MgCl_2$ and $ZnCl_2$, 1~2 mml/L and ~ 0.016 mml/L respectively, and ~ 136 mml/L of NaCl in plasma cells, it can be assumed that the high concentration of the divalent cation can affect the interactions and functions of the important protein inside the cells. The minimum distance between Glu39 and Glu58 of chain A is at the range of 6 Å - 7 Å from 150 ns to 200 ns in NaCl simulation. Other residues, including Asp419 of chain A and Glu125, Gln221 of chain B, were found with large fluctuation, and their minimum distance is about 10 Å or higher in NaCl simulation. (**Figure 3.25)**

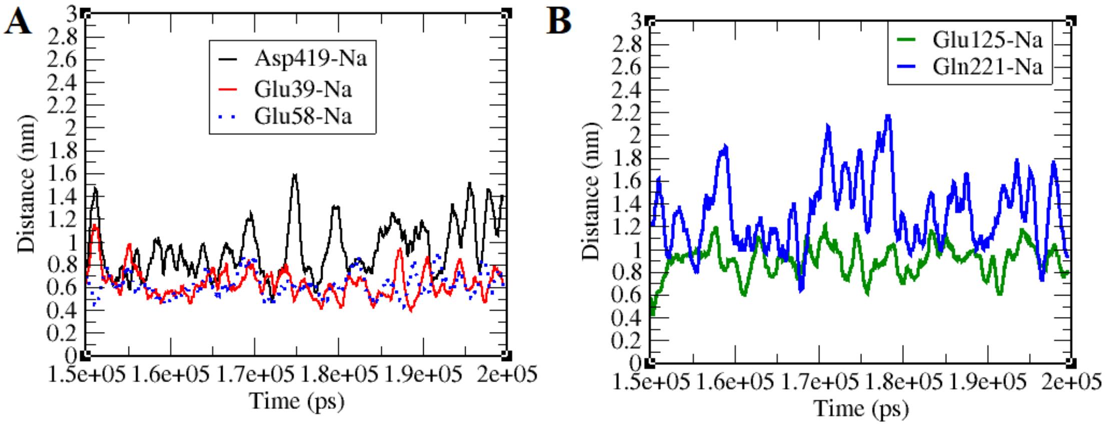

Figure 3.25: The minimum distances between residues of NaCl simulation from Na^+ cations. The selected residues are those at ≤ 4.5 Å of Na^+ at 200 ns (**A**) The minimum distance for chain A. (**B**) The minimum distance for chain B.

In order to study the collective motion of the γ-tubulin dimer and get an insight about significant motions of the protein related to the biological functions [41-43] the Principal Component Analysis (PCA) was performed.

For conducting the PCA and according to the description discussed in the introduction, the covariance matrix of atomic fluctuation was calculated first. Before obtaining the covariance matrix, the translational and rotational degrees of freedom were removed by fitting the data to the last conformation of the equilibrium simulation. The fitting was done by using the last frame of equilibration simulation as a reference. The atoms that are selected for covariance studies are the Cα atom from the last 50 ns of the NaCl simulation. The diagonalization of the C-matrix was conducted, and eigenvectors and their corresponding eigenvalues were obtained. In this calculation, both Gromacs and Bio3D tools were used for obtaining the graphs.[44-46] Whether the H6-H7 secondary structure segment that is known to play a role in the function of α, β-tubulin heterodimer is taking part in collective motion or not is tried to be answered here. Eigenvalue decomposition of the covariance matrix generates the orthogonal collective modes or eigenvectors. Each eigenvector has its corresponding eigenvalue. Eigenvalue (variances) determines the magnitude of the motions, or it can be said that a large eigenvalue corresponds to a large-scale motion. The first five eigenvalues account for 58.4% of all variances of NaCl simulation. The first PC cover 25.48% of all the variability of the generated conformations in the unliganded NaCl simulation. (**Figure 3.26 A**)

The PC2 and PC3 account for 11.94% and 5.76% of variability among all conformations. The sum of all eigenvalues yields total mobility of the protein (100%). (**Figure 3.26 A**)

As discussed, the first three PC accounts for more than 50% of the variations; then, it is possible to obtain a map of the two-dimensional projected trajectories. To further clarify, the MD simulation generates billions of different conformations that can be projected on the two-dimensional map for the PC1- PC2, PC3-PC2, or another combination is PC1- PC3 as these three PC vectors account for most motions of the protein. After projection, each blue or red circle represents one conformation projected on each determined PC. (**Figure 3.26 B-D**)

PC represents the direction and magnitude of the motion of the protein for all the Cα atoms, and its value is determined by the corresponding eigenvalue, which shows the mean square displacement. The projections of Cα atoms of the last 50 ns of the unliganded NaCl simulation on the first three PC map the direction of the motion and major generated conformations with respect to the first, second, and third PCs. The two-dimensional projections show how conformers are spread out between the first three PC axes. (**Figure 3.26 B-D**)

However, a question arises with each PC which secondary segment of the γ-tubulin dimer contributes to the motion. This provides information on the collective motion, which is important to the function of the protein. For instance, most variances are linked to PC1, but which helices and strands with PC1 are involved in larger motion. This can be investigated by the projection of trajectories on PC1 and evaluating the RMS displacement of the protein for PC1, PC2, or PC3.

Fluctuations of each residue in PC1 to PC3 reveals the nature of the most important displacement related to the biological function of the γ-tubulin.

With unliganded dimer in NaCl simulation, the H2 (Arg72-Asn79) and H3 (Trp104-Asp127) helices have significant displacement with PC vector one. This indicates they are involved in the collective motion of the γ-tubulin-dimer. For every single PC it is possible to evaluate which secondary structure segments are mostly involved in motion, and their displacement can be measured accordingly. (**Figure 3.26 and 3.27**)

Displacement for H2 and H3 were 4 Å and 2 Å, respectively, with chain A. The T5 (Pro173-Gln184) loop has a displacement of 2.2 Å with PC vector one; this is an indication of collective motion related to this loop with chain A. (**Figure 3.26)**

It was shown that the curved conformation is almost dominant with both chains A and B. Around 1.5 Å and 1 Å displacements were observed with vector 1 of chain A for M loop (Thr274-289Thr) and H10 helix (Pro330-Arg343), which shows that they are contributing to the collective motion. A significant fluctuation was measured with PC1 for H11 (Ser385-

Lys400) and H12 (Asp419-Ala437) helices at the C-terminal of chain A. The role of both helices (H11 and H12) in the biological functions of the γ-tubulin has been documented elsewhere [39], and here they show large displacement with vector one as mentioned above. (**Figure 3.27**)

With chain B of unliganded γ-dimer of NaCl simulation, both H2 (Arg72-Asn79) and M loop (Thr274-289Thr) are found to have a displacement around 2 Å. (**Figure 3.27)** Major fluctuations are observed with vector one. PC1 accounts for more than 25% of all variables seen with both chains A and B.

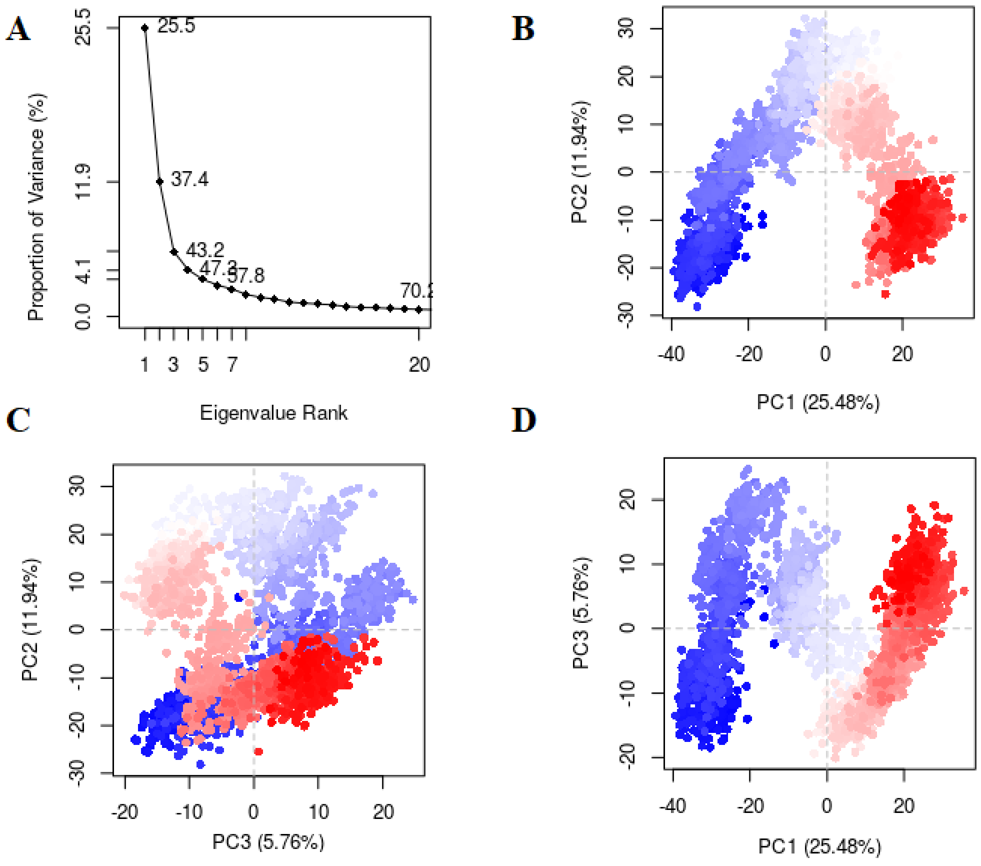

Figure 3.26 Result of PC analysis on the unliganded γ-tubulin dimer in NaCl simulation. (**A)** Eigenvalue spectrum: the index of the number of eigenvalues which are ordered from the strongest to weakest contribution to variances (mean square displacement) on X-axis, and the Y-axis gives the proportion of variances for each eigenvalue. (**B-D**) The two-dimensional trajectory projection of the PC plot shows the projection of the motion of the conformations obtained from 150 ns to 200 ns of the Cα atoms along with the first three principal components (PC1 and PC2, PC2, and PC3, PC1 and PC3). The colored circle represents the generated conformations during the last 50 ns of MD simulation. The color changes from blue to white to red, which shows the periodic jumps among the conformations throughout the trajectory.

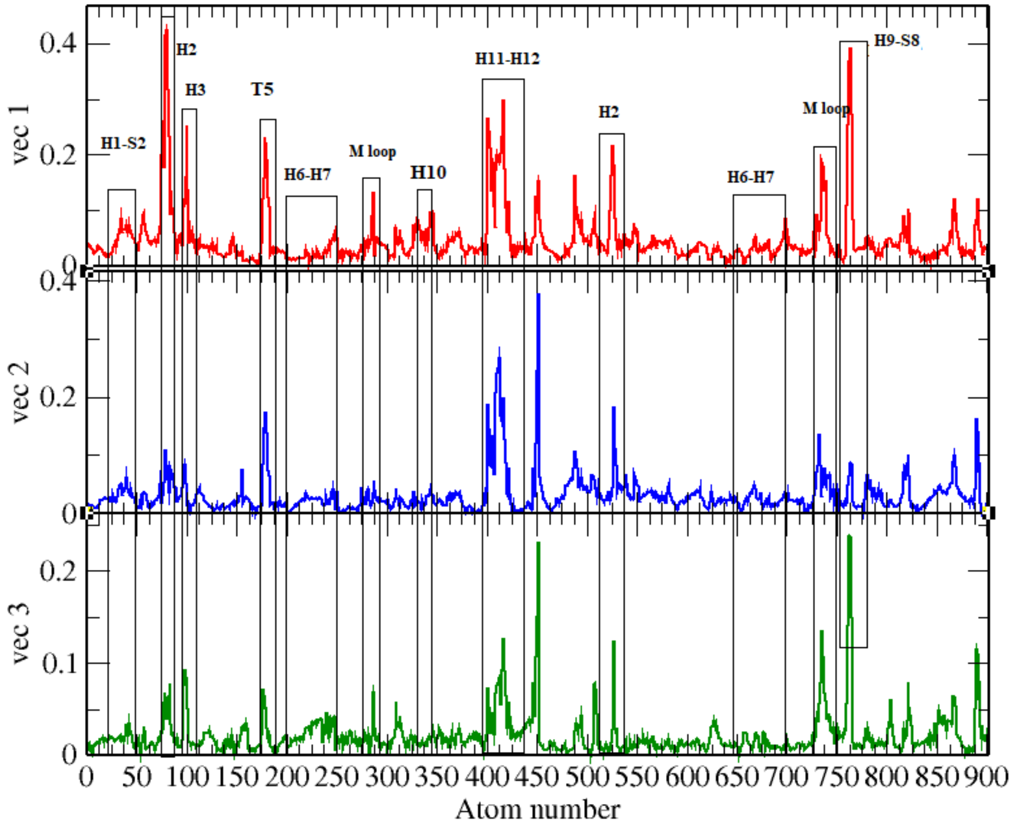

Figure 3.27 The plot of the RMS displacement per each Cα atoms of the unliganded γ-tubulin dimer in NaCl simulation for the first three eigenvectors. (**A**) The RMS displacement for PC vector 1 is colored in red. (**B**) PC vector 2 colored in blue. (**C**) PC vector 3 colored in green.

3.2 MD Simulation of GDP and GTP-Bound γ-Tubulin Dimer Under $MgCl_2$, $ZnCl_2$, and NaCl Ionic Conditions

3.2.1 MD Simulation of γ-tubulin Dimer in Association of Bound GDP

The RMSD of chain A and B of the GDP-dimer are monitored in the backbone atoms to evaluate the stability of the protein during the course of MD simulations. The RMSD for chain A of γ-tubulin in NaCl simulation gradually increases to 3 Å from the starting point of the production run up to 137 ns. Then, it reaches the 3.5 Å at its convergence point at 153 ns and until the end of simulation at 200 ns remained stable at 3.5 Å with no high fluctuation. (**Figure 3.28 A**)

The RMS deviation of chain A in $MgCl_2$ and $ZnCl_2$ simulation rises to ~ 2.5 Å from the starting point with no fluctuation after that. The RMSD for both simulations is around 2 Å - 2.3 Å. Their convergence point is 125 ns. (**Figure 3.28 A**)

Chain B showed almost the same RMSD with all three simulations until 75 ns with a ~ 2.2 Å. After 75 ns, the RMSD of chain B in NaCl simulation is reduced to 2 Å at 110 ns and was stable until the end of the simulation at 200 ns. The convergence point in $ZnCl_2$ and $MgCl_2$ simulations is at 130 ns for chain B. (**Figure 3.28 B**)

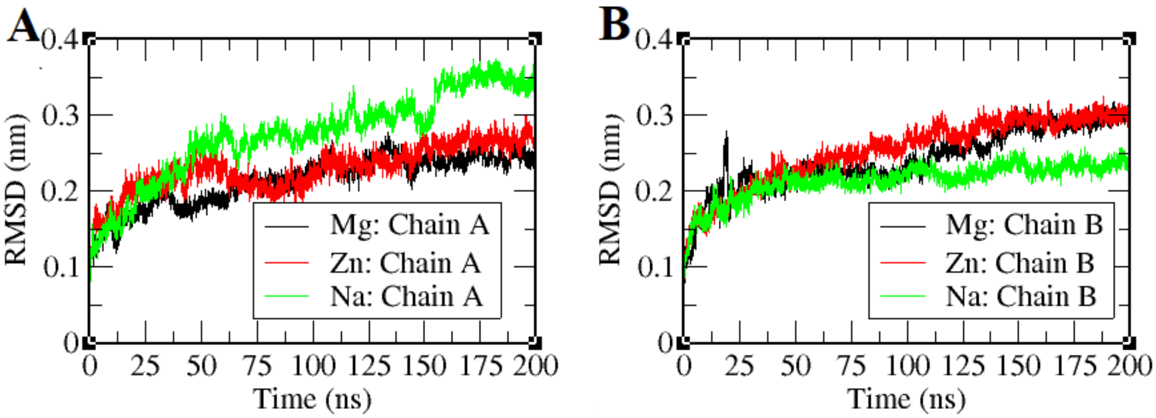

Figure 3.28: The root mean square deviation of backbone atoms of chain A and chain B of the GDP-bound γ-tubulin dimer. (**A**) Chain A. (**B**) Chain B. For both chains, the $MgCl_2$ is colored in black, $ZnCl_2$ in red, and NaCl in green.

3.2.1.1 The Dominant Model Obtained from MD Simulations of GDP-Bound γ-dimer Support Lattice

Whether the nucleotide, GTP, or the lateral interactions induce the straightness on the structure of the curved β-tubulin is a challenging subject in structural biology.[1] According to the allosteric model, the nucleotide, which is GTP, is the main factor behind the changes from curved to straight conformation in the α, β-tubulin heterodimer. It should be clarified that conformation due to the effect of GTP is with soluble α, β-tubulin heterodimer, and not αβ-dimer, which is already part of the MTs lattice. The soluble α, β-tubulin heterodimer is not assembled as part of MTs and has no lateral contacts.

There are no studies that show the dynamic effect of GDP on the straightness of the γ-tubulin. Most studies are focusing on the allosteric role of the GTP in inducing straightness.[1, 47] The only difference between GTP and GDP is the third γ phosphate, which is absent in GDP. The GTP has both structural and functional roles in the α, β-tubulin heterodimer[20, 48], not GDP.

If GDP is unable to induce the straight conformation and the GTP induces, this is attributed to γ-oxygens of the GTP. The straightness and curvature of both chains are evaluated by measuring the dCOM of the H7 helix (Phe225-Leu231) from the S6 strand. Then conformation at 200 ns of a γ-tubulin dimer superimposes on the curved and straight β-tubulins.

The result of the evaluation of dCOM of H7 and S6 shows that the curved and intermediate conformations are dominant. No straight conformation was observed with chain A or chain B of γ-tubulin with all three simulations. The dCOM from H7 helix to S6 strand for chain A of $MgCl_2$ simulation gradually increases from 1.60 nm at 150 ns to 1.70 nm at 182 ns then reaches 1.66 nm at 185 ns and at 200 ns has a value of 1.68 nm of intermediate conformation. (**Figure 3.29 A**)

As it was discussed, the dCOM of H7 and S6 for curved conformation is ≤ 1.6 nm, between 1.6 nm – 1.7 nm for intermediate conformation, and larger than 1.7 nm accounts for straight conformation.

The dCOM of the H7 helix and the S6 strand of chain A in the $ZnCl_2$ simulation has large fluctuations. It starts from 1.57 nm at 150 ns reaches 1.52 nm at 160 ns, being 164 nm at 172 ns. It decreases to 155 nm at 188 ns and at 200 ns, is 1.57 nm. In contrast to dCOM of

H7 and S6 strand of chain A in $ZnCl_2$, in NaCl simulation has low changes, and it almost fluctuates at the range of 1.55 nm - 1.55 nm for the entire last 50 ns of the NaCl simulation. (**Figure 3.29 A**)

For chain B, the dCOM between H7 helix and S6 strand (Cys201-Asp206) in the $MgCl_2$ simulation moderately increases to 1.60 nm from 153 ns until 1.65 ns of intermediate conformation. Then it falls to 1.5 nm at 170 ns and until the end of simulation at 200 ns fluctuates around ~ 1.57 nm, which resembles the curved conformation. The dCOM of the H7 helix from the S6 strand of chain B in $ZnCl_2$ and NaCl simulations are 1.62 nm of curved conformation with small fluctuation ~ 0.2 Å from 150 ns to 170 ns. The dCOM of H7 helix and S6 strand in NaCl simulation changes around 1.58 nm - 1.60 nm until the end of the simulation. Chain B in the $ZnCl_2$ simulation reaches 1.65 nm at 185 ns, then until 200 ns fluctuates with values between 1.58 nm - 1.6 nm. (**Figure 3.29 B**)

Overall, the value of dCOM of H7 helix and S6 strand for both chain B and chain A shows that the curved and intermediate conformations are dominant. (**Figure 3.29 A and B**)

GDP binding has not induced the curved to straight conversion. It is to say; that there is not enough and convincing evidence to rely on allosteric modifications as the main driving force behind the transition from curved to straight conformation. With both chains of A and B, curved and intermediate conformations are dominant, or in other words, the straight conformation was not observed. (**Figure 3.29 A and B**)

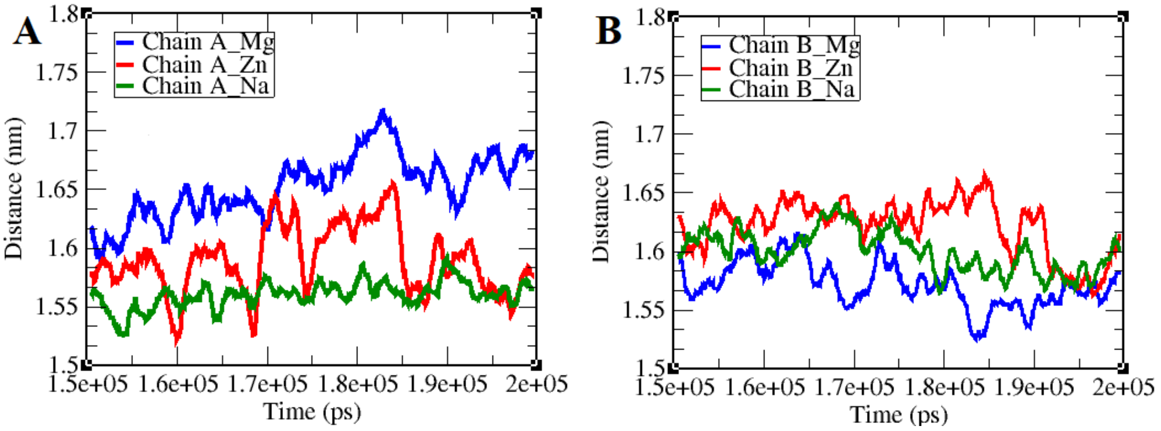

Figure 3.29: The dCOM of H7 helix and S6 in GDP-dimer simulations in $MgCl_2$, $ZnCl_2$, and NaCl. **(A)** The distances for chain A (**B**) Chain B. The color for $MgCl_2$, $ZnCl_2$, and NaCl simulations are blue, red, and green, respectively.

In addition to monitoring H7 and S6 dCOM, 200 ns conformation in three simulations were compared to curved and straight β-tubulins.

The 200 ns conformation of the γ-tubulin dimer in $MgCl_2$ simulation was superimposed on both curved (1SA0) and straight β-tubulins (1JFF).

The H7 helix of chain A is aligned to the H7 helix of the straight β-tubulin. H7 helix determines the straightness and curvature related to the conformation of the β-tubulin.[13]

The conformation of H6 (Asn207-Asp216) and H10 (Pro330-Arg343) helices of chain A are not fully aligned to H6 or H10 helices of curved or straight conformation of the β-tubulin. The intermediate domain strands of S7 (Phe268-Tyr273), S8 (Tyr317-Gln325), S9 (Ile356-Ser361), S10 (Ser374-His381) of γ-tubulin are not fully aligned to the β-tubulin curved or straight conformation, and the intermediate conformation better explains their arrangements. (**Figure 3.30 chain A**)

In chain B, the conformation of H7 helix of chain B of the γ-tubulin dimer is not aligned to the H7 helix of β-tubulin. The orientations of four intermediate domain strands of S7, S8, S9, and S10, are aligned with that of curved S7 to S10 strands. For chain B at 200 ns, the intermediate conformation is dominant. (**Figure 3.30 chain B**)

The 200 ns conformation of a γ-tubulin dimer in $ZnCl_2$ simulation was superimposed on both curved (1SA0) and straight β-tubulin (1JFF).

The conformation of the H7 helix of chain A is aligned to the H7 helix of the curved β-tubulin. Also, the intermediate domain strands of S7 to S10, and H6 of γ-tubulin are aligned to the same secondary segment structures (S7-S10 and H6) of curved β-tubulin. The H10 helix conformation of γ-tubulin is not aligned with the H10 helix of either curved or straight β-conformation. Overall, the conformation of chain A in $ZnCl_2$ simulation is adapting the curved conformation. (**Figure 3.31 chain A**)

Chain B of γ-tubulin in $ZnCl_2$ shows alignment with the curved β-tubulin because its H7 and H6 helices are aligned to the same helices of curved β-tubulin. The conformations of S6, S7, S8, and S10 are also aligned to the same strands of the curved β-tubulin. The conformation of H10 helix, M, and T5 loops are not aligned after superimposition to their counterparts (H10, M, and T5 loops) of curved or straight β-tubulin.

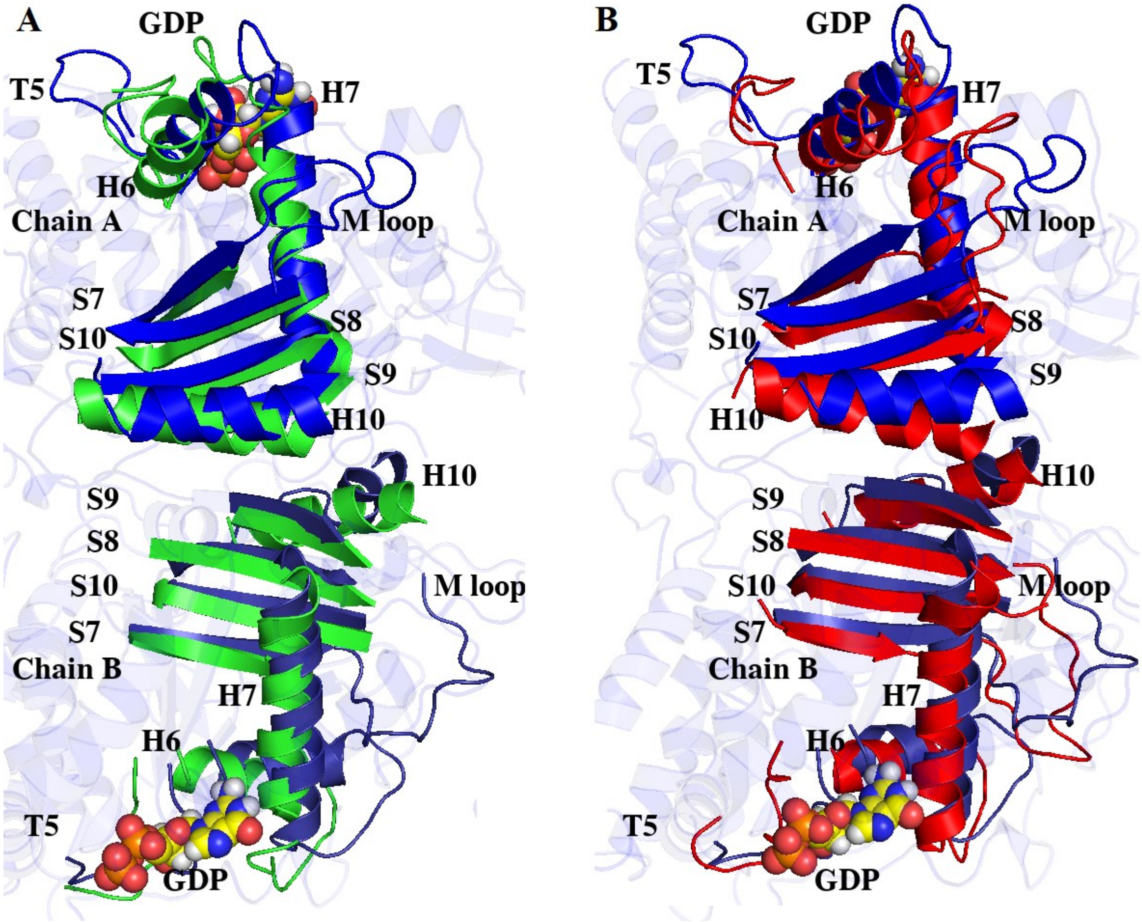

Figure 3.30: Superimposition of a conformation of GDP-bound γ-tubulin dimer in $MgCl_2$ simulation on β-curve (1SA0) and β-straight (1JFF). (**A**) 200 ns conformation of γ-tubulin dimer in blue superimposed on curved β-tubulin (1JFF) in green. (**B**) γ-tubulin dimer at 200 ns in blue superimposed on straight β-tubulin (1JFF) in red.

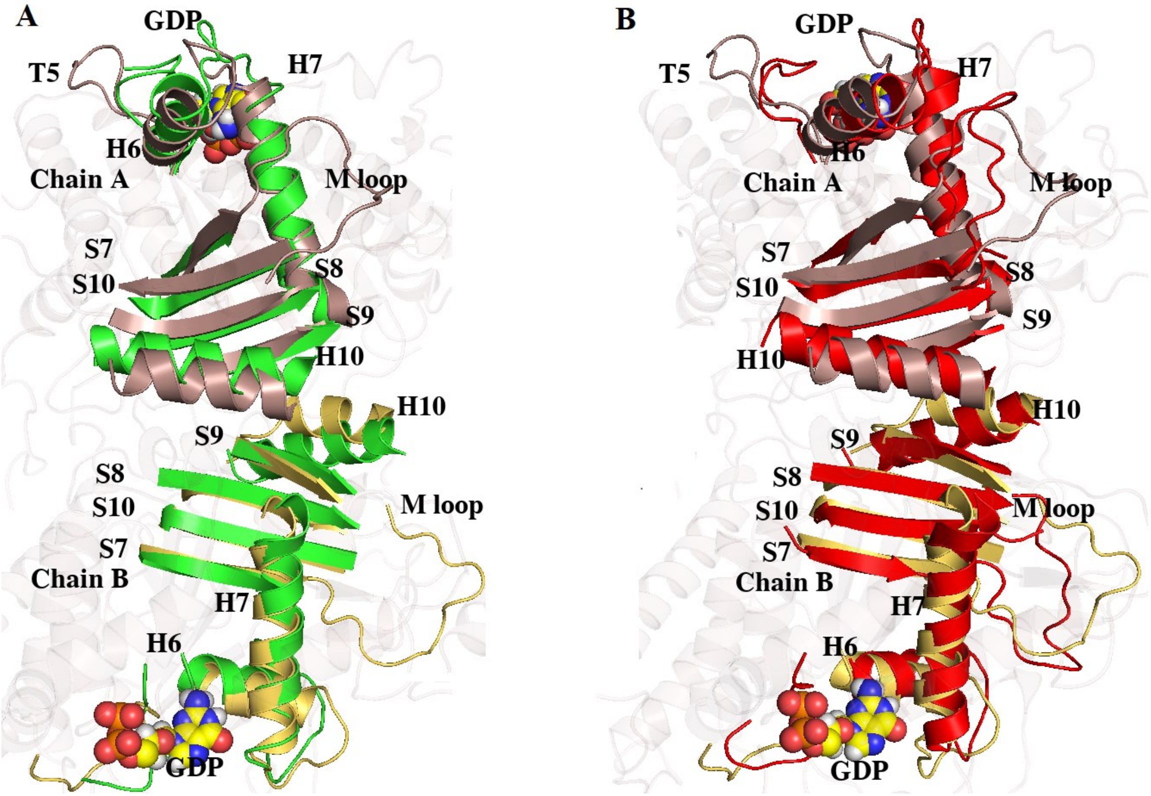

Figure 3.31: Superimposition of a conformation of GDP-bound γ-tubulin dimer in $ZnCl_2$ simulation on β-curve (1SA0) and β-straight (1JFF). (**A**) 200 ns conformation of γ-tubulin dimer in pink for chain A and yellow in chain B superimposed on curved β-tubulin (1JFF) in green. (**B**) γ-tubulin dimer at 200 ns in pink for chain A and yellow for chain B superimposed on straight β-tubulin (1JFF) in red.

A conformation of the γ-tubulin dimer in NaCl simulation at 200 ns was superimposed on the curved (1SA0) and straight β-tubulin (1JFF). The chain A of γ-tubulin in NaCl simulation is not aligned to the chain A of the straight β-tubulin.

The conformation of its H7 (Phe225-Leu243) and H6 (Asn207-Asp216) helices are aligned with respect to H7 and H6 helices of the curved β-tubulin. Also, the conformations of four intermediate domain strands were aligned to curved β-tubulin. The H10 helix (Pro330-Arg343) is not fully aligned to the H10 helix of the straight or curved conformation of the β-tubulin. The curved conformation is dominant with chain A in NaCl simulation. (**Figure 3.32 chain A**)

In chain B of γ-tubulin in NaCl, the conformations of H7, H6, the N-terminal of H10 helices for Pro330, Thr331, Gln332, Val333, and His334 are aligned to curved β-tubulin. Both N and C-terminal of H7 helix are aligned to the H7 helix of curved β-tubulin. The orientations of S7 to S10 strands of the intermediate domain of γ-tubulin are aligned to the S7 to S10 strands of the curved β-tubulin (1SA0) as well. The conformation of chain B of γ-tubulin is adapting a curved conformation in NaCl simulation at 200 ns.

(**Figure 3.32 chain B**)

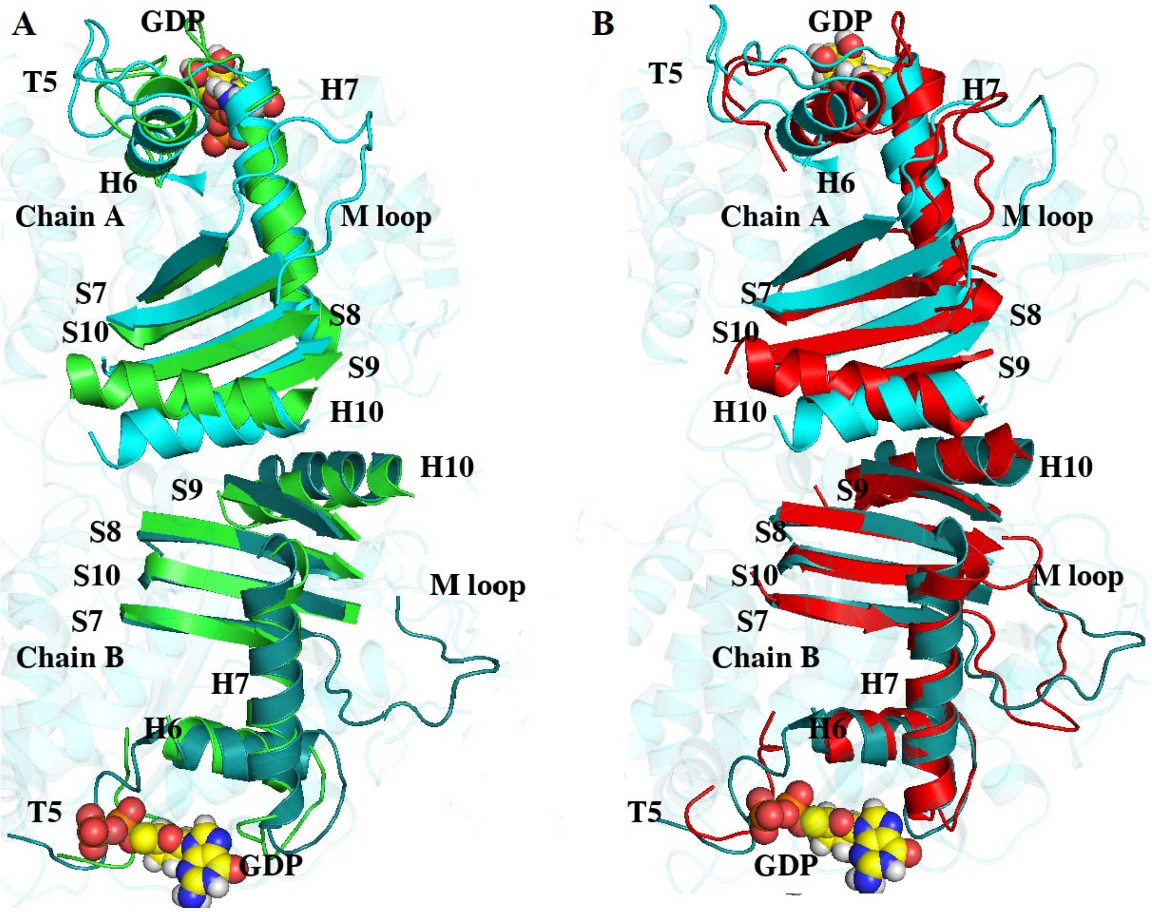

Figure 3.32: Superimposition of a conformation of GDP-bound γ-tubulin dimer under NaCl simulation on β-curve (1SA0) and β-straight (1JFF). (**A**) γ-tubulin dimer at 200 ns in cyan superimposed on curved β-tubulin (1JFF) in green. (**B**) γ-tubulin dimer at 200 ns in cyan superimposed on straight β-tubulin (1JFF) in red.

Chain A of $MgCl_2$ simulation at 182 ns, is adapting an intermediate conformation. Also, the conformation of chain A of $ZnCl_2$ at 165 ns is found to be curved. (**Figure 3.29**)

Both conformations were superimposed on each other in order to compare their curvature or straightness. There is no expectation that they aligned with each other because of the value of dCOM of H7 helix (Phe225-Leu231) from the S6 strand (Cys201-Asp206) was 1.70 nm and 1.52 nm in $MgCl_2$ and $ZnCl_2$ simulations, respectively.

Here the conformations of the two H7 (Phe225-Leu243) helices are important because the curved β-tubulin is determined by the deviation of its H7 helix [13, 14]. H7 helix of chain A in $MgCl_2$ at 182 ns is not aligned to the curved conformation at 165 ns in $ZnCl_2$ simulation. The deviation is observable at H7 N-terminal; the dCOM of the H7 from S6 is 1.59 nm in $ZnCl_2$ and about 1.7 nm in the $MgCl_2$. In addition to the H7 helix, other secondary segment structures include intermediate domain strands of S7 (Phe268-Tyr273), S8 (Tyr317-Gln325), S9 (Ile356-Ser361), S10 (Ser374-His381), H6 (Asn207-Asp216), and H10 (Pro330-Arg343) helices are not aligned to each other. (**Figure 3.33**)

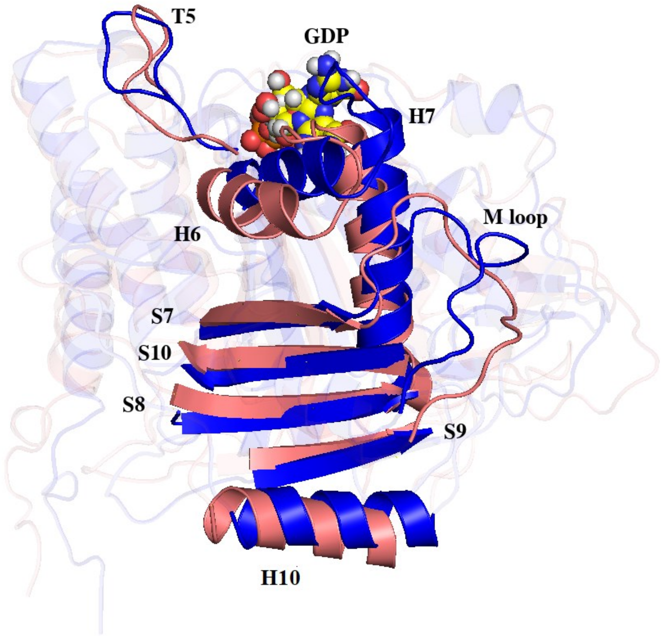

Figure 3.33: Structural superimposition of a conformation of the trajectory of chain A at 182 ns $MgCl_2$ on chain A of $ZnCl_2$ at 165 ns. The conformation of γ-tubulin in $MgCl_2$ is colored in blue and is pink in the $ZnCl_2$ simulation.

3.2.1.2 Study of the GTP Hydrolysis Mechanism and Interactions in the GDP Binding Sites

The major uncertainty about the mechanism of GTP hydrolysis is the exact mechanism for the phosphoryl transfer during the reaction, which has not been fully understood. There are two proposed mechanisms, one is fully associative, and the other is a dissociative mechanism.[49] In a fully associative mechanism, the nucleophilic attack on γ phosphate of the GTP occurs before the departure of the leaving group (γ phosphate is the leaving group). In the dissociative or elimination-addition pathway, the nucleophilic reaction follows the departure of the leaving group. The dissociative pathway is an intrinsic ability of the oxygen atoms of the γ phosphate of GTP molecule to contribute to the reaction.[49, 50]

Another uncertainty in GTP hydrolysis is the nucleophilic group for this reaction and the mechanism of its activation. The water OH^- is assumed as a nucleophile; it deprotonates by a general base in which one water molecule losses a proton and another one accepts it. The exact mechanism of the nucleophilic activation is still not well explained. Although rejected, there is a discussion about Gln role in activating the nucleophilic water.[50, 51]

The formation or hydrolysis of a bond cannot be addressed by conventional MD simulation. Attempts have been made to investigate whether there are strong interactions between waters and γ phosphate or not at the GTP binding site. This further supports the associative mechanism as waters act as the nucleophile to facilitate the reaction. The GTP binding site at 200 ns in $MgCl_2$ was studied to find the interacting residues and waters with the γ phosphate. Two water molecules make an interaction at 3.4 Å from γ phosphate and one water molecule at 4 Å to the γ phosphate. Waters make effective interactions and act as a nucleophile to facilitate the reaction in favor of associative reaction. **(Figure 3.34)**

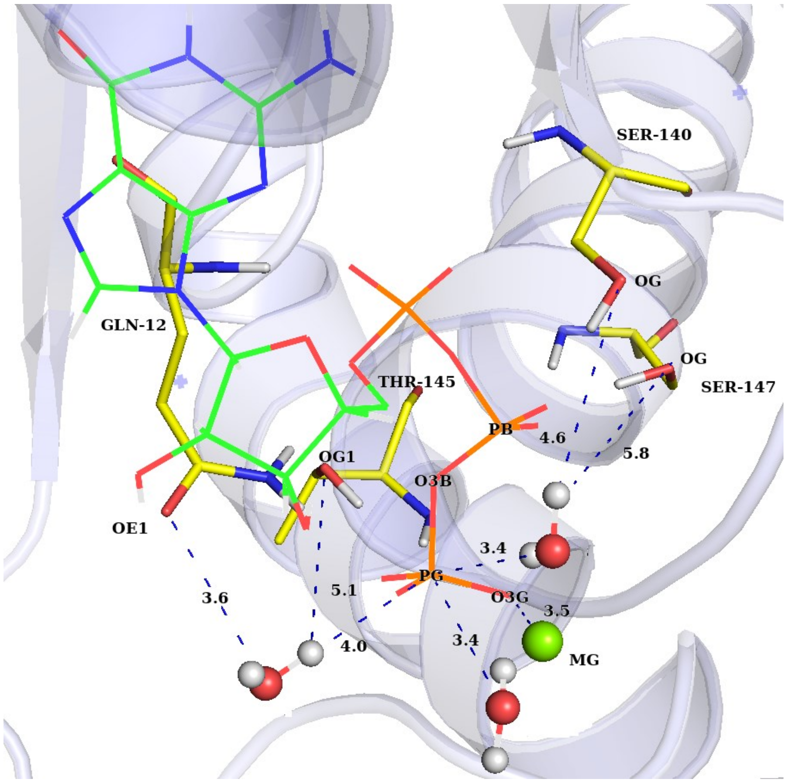

Figure 3.34: Interactions of waters and GTP at the binding site. The 200 ns conformation of the $MgCl_2$ in which the GTP is depicted in the yellow stick. Oxygen atoms of water are shown as red spheres.

The minimum distances make by water molecules and GTP γ-phosphate were monitored in GTP-bounded simulations from 150 ns - 200 ns. In three simulations, the minimum distance of water and γ phosphate is fluctuating in the range of 2.4 Å - 2.5 Å in the $MgCl_2$, ~ 2.5 Å in $ZnCl_2$, and in NaCl ~ 2.6 Å. This can prove that the position of γ-phosphate of the GTP in the binding site of the γ-tubulin allows water molecules to make an interaction at ≤ 3 Å, and hence the possibility of the associative mechanism of GTP hydrolysis gets stronger support. **(Figure 3.35)**

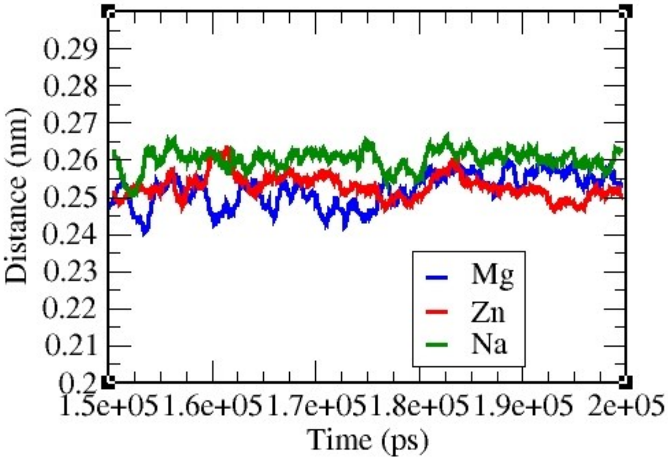

Figure 3.35: The minimum distances between γ phosphate of GTP and water molecules in GTP bounded simulation. The distances are colored in blue, red, and green for $MgCl_2$, $ZnCl_2$, and NaCl, respectively.

To study whether water molecules make H-bonds with γ-oxygens and evaluate it in different simulations, the number of H-bond generated at ≤ 4 Å were evaluated. The number of H-bonds between Og atoms of the γ phosphate of the GTP and water molecules fluctuates ~ 5 bonds in $MgCl_2$ simulation, 3 – 4 bonds in $ZnCl_2$, and 3 H-bonds in NaCl simulation. This further supports the possibility of the associative mechanism as the water molecules interact with the γ phosphate and its three oxygen atoms. **(Figure 3.36)**

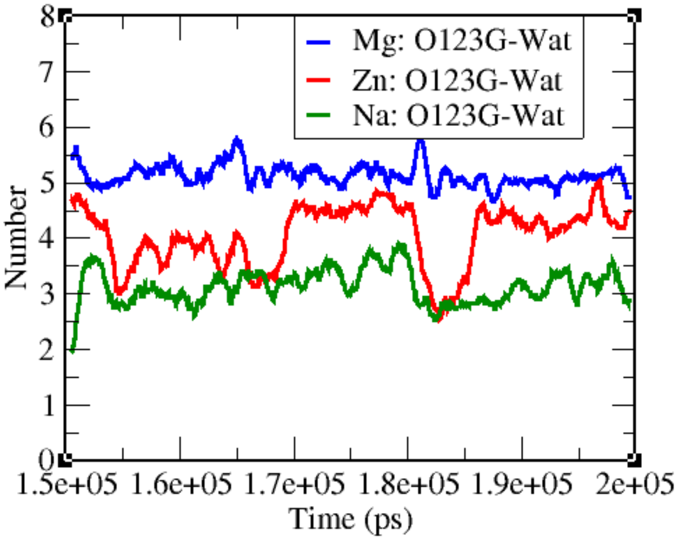

Figure 3.36: Number of generated H-bond between waters and oxygen atoms of the γ phosphate of GTP. Number of H-bonds are colored in blue, red, and green in $MgCl_2$, NaCl, and $ZnCl_2$ simulations, respectively.

In order to study which residues have effective and close interactions with the GDP, one conformation of chain A in $ZnCl_2$ at 180 ns was selected, and residues at a distance of 4 Å from the GDP were studied. Only those atoms which are able to make H-bonds were evaluated. Therefore, all interactions are between H-N, H-O atoms with oxygen, and nitrogen of either the GDP or γ-tubulin residues. Accordingly, H-N atom of Asn207 at 3.5 Å generates a H-bond with a nitrogen of the purin ring. The oxygen atom of Asn229 makes H-bond at 1.6 Å with H-N of the purin ring of GDP. The oxygen atom of ribose of the GDP has one interaction with H-O atom belonging to Ser140 at 3.9 Å. The rest of the interactions are between the oxygen atoms of α phosphate or β phosphate with the residues of the binding site. Two α phosphate oxygens make H-bonding with H-N atom of Gln12 at 2.6 Å and H-O of Thr145 at 3.1 Å. Three β-Phosphate oxygens make H-bonds with H-N atoms of Gly146 at 3.1 Å, Gly144 at 3.1 Å, and Gly143 at 2.0 Å. (**Figure 3.37)**

The conformation at 180 ns was selected because, at 182 ns, it makes an intermediate conformation with dCOM of H7 to S6 with ~ 1.65 nm; all conformations at 200 were investigated for the cation interactions and conformational changes.

The interaction energies (sum of electrostatic and L-J) for the three GDP-bound simulations of NaCl, $MgCl_2$, and $ZnCl_2$ from 150 ns to 200 ns were calculated to study which residues contribute and how effective it is to the binding energy of the GDP in its binding site. (**Figure 3.37 and 3.38**)

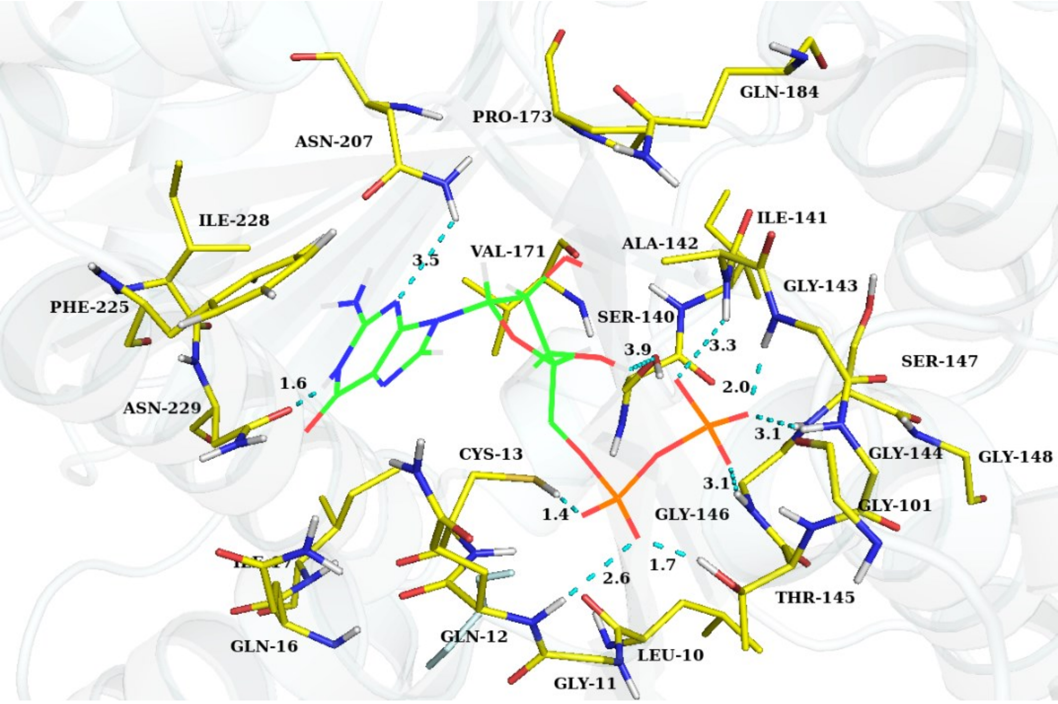

Figure 3.37: The conformation at 180 ns of chain A of $ZnCl_2$ simulation with interactions of GDP and residues of the binding site at ≤ 4 Å. The GDP is depicted in line representation, and the residues of the binding site are in stick yellow.

The interaction energy (IE) between GDP and the residues of the binding site is stronger in the $MgCl_2$ simulation. Similar to the GTP-bound simulation, this is an indication that specific cations at the binding site contribute to stronger interactions of the nucleotide with its binding site. (**Figure 3.38**)

IE is the average of electrostatic and L-J energy between chain A and GDP, in $MgCl_2$, $ZnCl_2$, and NaCl is -1122.3 kJ/mol, -944.4 kJ/mol, and -935.9 kJ/mol, respectively. The residues that have a larger contribution to the IE with GDP for three simulations include

Gln12, Thr145, Cys13, Ser147, Gly143, Gly144. These IE evaluations are from 150 ns to 200 ns, and the value given here is the average over the last 50 ns. (**Figure 3.38**)

The IE between Gln12, Thr145, Cys13, Ser147, and GDP under $MgCl_2$ simulation is -152.3 kJ/mol, -133.8 kJ/mol, -117.6 kJ/mol, -119.2 kJ/mol respectively. These values for the same residues of Gln12, Thr145, Cys13, Ser147 in $ZnCl_2$ simulation is -85.1 kJ/mol, -159.6 kJ/mol, -118.2 kJ/mol, -80.9 kJ/mol and in NaCl simulation is -177.1 kJ/mol, -32.5 kJ/mol, -128.1 kJ/mol, -134.2 kJ/mol respectively. (**Figure 3.38)**

There are residues at the binding site that have different values of IE under three simulations. For instance, the IE for Arg72, is -64.1 kJ/mol, -2.5 kJ/mol, -13.7 kJ/mol in $MgCl_2$, $ZnCl_2$, and NaCl simulation, respectively. The GDP binding site at 180 ns in $ZnCl_2$ has no interaction at a cut off of 4 Å to the Arg72. (**Figure 3.37 and 3.38)**

It was shown in the GTP-bound monomer Arg72 decreases its distance to the γ phosphate atom of the GTP from 12 Å at 100 ns to around 3 Å at 153 ns. (**Figure 3.34**)

The interaction energy between Gln12 and GTP is considerably stronger in the $MgCl_2$ simulation, with a value of -238.8 kJ/mol. This lies in comparison to -198.8 and -176.2 kJ/mol in NaCl and $ZnCl_2$ simulations, respectively. The interaction energy for Thr145 with three simulations of $MgCl_2$, $ZnCl_2$ and NaCl is -171.3 kJ/mol, -170.0 kJ/mol, -163.5 kJ/mol, respectively. And for Cys13 this value in $MgCl_2$, $ZnCl_2$, and NaCl is -122.8 kJ/mol, -125.7 kJ/mol, -120.1 kJ/mol, respectively. The interaction energy between the GTP and Ala100 shows a difference in the $ZnCl_2$ simulation with -90.6 kJ/mol, and two other simulations, including $MgCl_2$ with +3.7 kJ/mol, and NaCl with a value of +1.3 kJ/mol, respectively. In $MgCl_2$, NaCl and $ZnCl_2$ simulations, the interaction energy between Ser147 and GTP is -120.5 kJ/mol, -5.2 kJ/mol, -123.8 kJ/mol, respectively. (**Figure 3.39**)

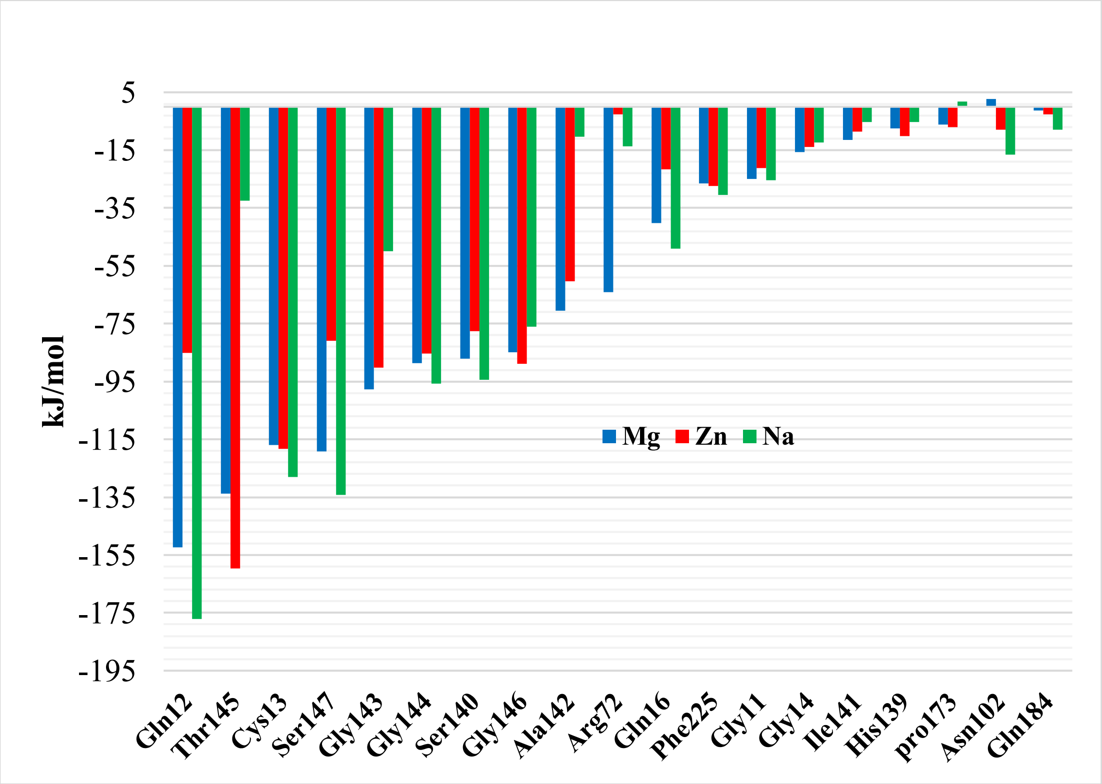

Figure 3.38: Interaction energy between each residue of the GDP binding site and GDP in chain A from 150 ns to 200 ns. The IE for each residue of the binding site is colored in blue, red, and green for $MgCl_2$, NaCl, and $ZnCl_2$ simulation, respectively.

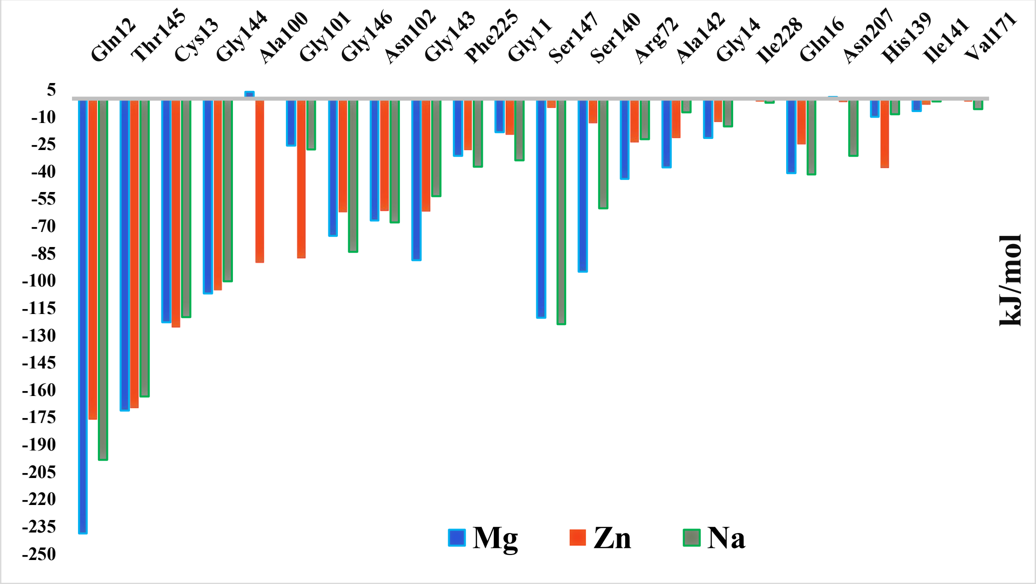

Figure 3.39: Interaction energy between each residue of the binding site and GTP from 150 ns to 200 ns. The interaction energy is colored in red for $ZnCl_2$, blue for $MgCl_2$, and green for NaCl simulation. The Interaction energy is the sum of L-J and electrostatics (chain A of monomer).

The abovementioned evaluation was done to reveal the residues at the binding site that makes stronger interactions with the GDP and GTP. All evaluation was done from 150 ns to 200 ns, and the residues, including Gln12, Cys13, Thr145 with both GDP, and GTP made stronger interactions. This is consistent with the wet-lab study of the GTP binding energy in yeast Tub4 γ-tubulin in which it was shown that Gln12, Cys13, and Thr145 play an important role in the binding of the GTP inside its binding site. [20]

3.2.1.3 Study of the High-Affinity Metal Binding Site with GDP-Bound γ-Tubulin Dimer

The major high-affinity metal-binding site is known in the GTP binding site in α, β-tubulin heterodimer.[52] It is not known whether, in the presence of GDP, strong and stable interactions with cations are possible or not similar to high-affinity metal-binding sites.

In each conformation of the three simulations, a γ-tubulin dimer was extracted from 150 ns for every 10 ns simulation. All cations at the GDP binding site in interaction with GDP were captured. For the last 50 ns of all simulations, the interactions of the cations with atoms of GDP were monitored. (**Figure 3.40**)

One Mg^{2+} interacts with O2a atom of the GDP in chain A and another Mg^{2+} with O3b atom in chain B. The distances between both Mg^{2} with GDP (Ota and O3b) are stable with no high fluctuations in the range of 3.8 Å - 3.9 Å from 150 ns to 200 ns. (**Figure 3.40 & 3.41**)

Two Zn^{+2} interacts to O3b and O2a atoms of the GDP with chain A and chain B. The interaction of one Zn^{2+} with O3b is stable at 3.9 Å from 150 ns to 194 ns and after that increases to 4.5 Å until 200 ns. The interaction of Zn^{2+} with respect to the O2a is not stable; the distances are mostly at 3.9 Å from 150 ns to 170 ns, then increases to 5.9 Å and again to 4 Å at 172 ns. After 185 ns, its interactions gradually rises to more than 20 Å at 190 ns, and then it leaves the GDP binding site. (**Figure 3.40**)

Tow Na^{+} cations are found in interaction with O2b and O1b atoms of GDP with chain A and chain B, respectively. (**Figure 3.40**)

The interaction between one Na^+ and O2b of chain A is stable during the last 50 ns from 150 ns to 200 ns at 2.2 Å. Also, the interaction of Na^+ and O1b of chain B is stable at around 2.3 Å with fluctuations around 2 Å at 165 and 175 ns. (**Figure 3.40**)

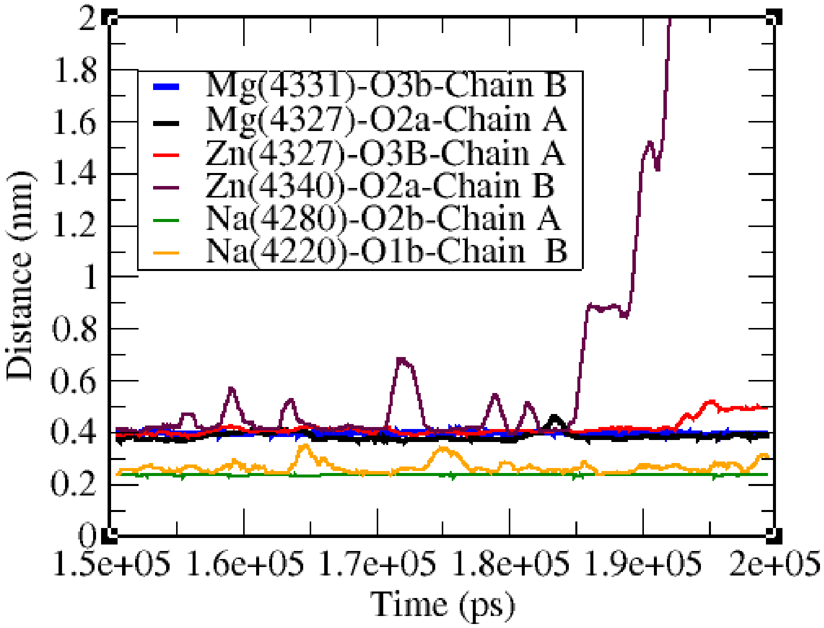

Figure 3.40: The distances between Mg^{+2}, Zn^{+2}, and Na^+ in their binding sites from the Ob1, Ob2, Ob3, Oa1, and Oa1 atoms of GDP. The cations with their codes are labeled, and their distances with respect to any oxygen atoms connect to the α or β phosphate of GDP are measured for the last 50 ns from 150 ns to 200 ns of all three simulations.

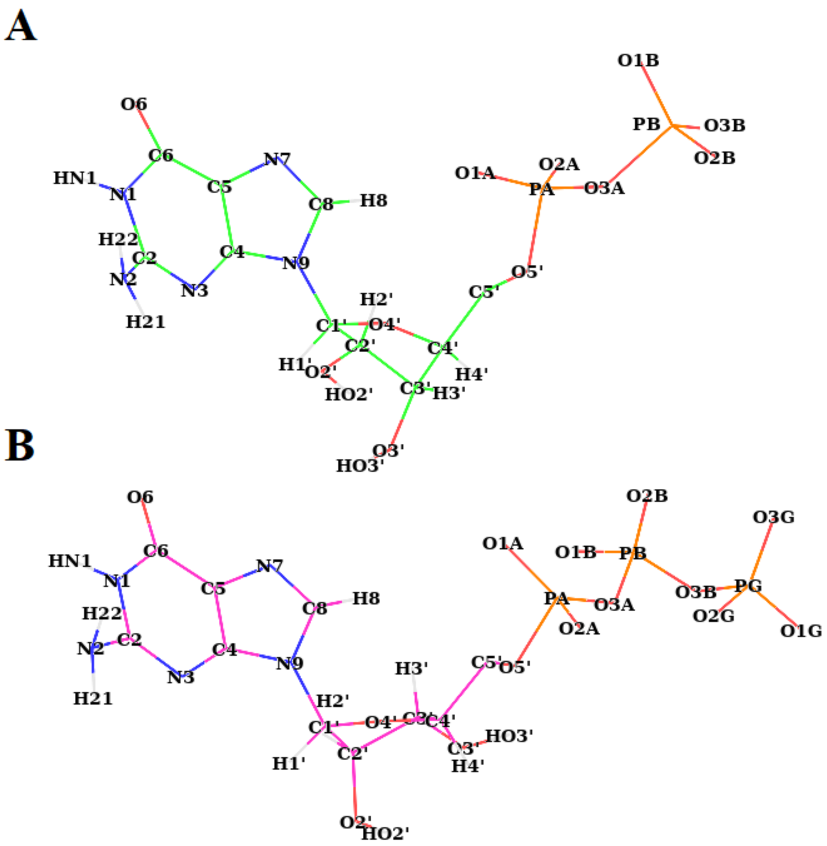

Figure 3.41: The structure of the GDP and GTP. (**A**) GDP. (**B**) GTP.

In contrast to GTP-bond simulations, in addition to oxygen atoms of the α-β phosphate N7 atom of GDP purin, make stable interactions with binding site cations. This generates a new high-affinity binding site, which for the first time, is addressed. Cations in interaction with oxygens atoms of γ phosphate are involved in the hydrolysis of the nucleotide, as discussed in section 2.1. However, the role of interaction with N7 is not known yet. (**Figure 3.42**)

The minimum distances between the N7 and the cations were monitored in each simulation. Two stable interactions at a distance of 2.3 Å were found. These interactions were found between N7 of chain B with Mg^{2+} and Zn^{2+} simulations with 2.2 Å from the Mg^{+2} and Zn^{+2} cations, respectively. In chain A of $MgCl_2$ and $ZnCl_2$ as well as both chains of NaCl simulation, the minimum distance of interactions between N7 and cations is more than 6 Å. This shows that N7 is a specific site of interaction for divalent cations, not Na^+. (**Figure 3.42**)

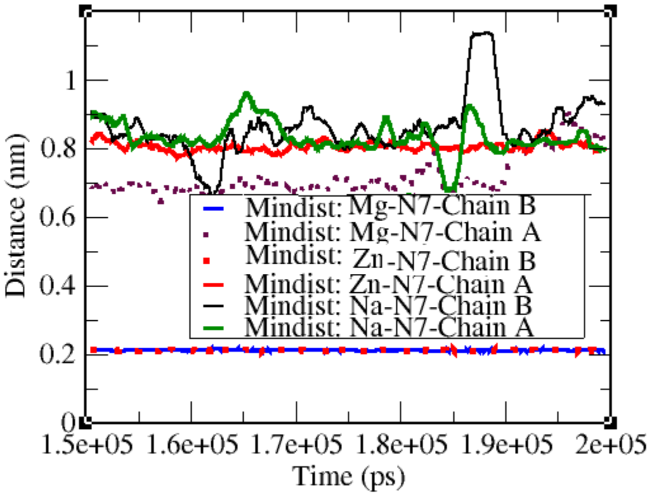

Figure 3.42: The minimum distances between Mg^{+2}, Zn^{+2}, and Na^+ in their binding sites from the N7 atoms of GDP purin ring.

In section 1.3.3, it is discussed how the PCA analysis is done. The GDP-dimer in ZnCl2 was selected for conducting the PCA, and it shows that 51.3% of all variances belong to the first six eigenvalues

The first PC cover 15% of the total variability of generated conformations. The first 20 eigenvalues account for 64% of variations. Also, the PC2 and PC3 cover 10.7% and 8.17% of all created variations. (**Figure 3.43 A)**

The projection of Cα motions on the first three PC map direction of motions and major generated conformations with respect to the first, second, and third PCs. (**Figure 3.43 B-D**). The projection of trajectories on PC1 and PC2 gives a two-dimensional map of generated conformations. (**Figure 3.43 B**)

The two-dimensional map of projected conformations for PC1-PC3 and PC2-PC was also generated. (**Figure 3.43 C and D**)

However, in order to reveal, which secondary segments structure are involved in the motion related to a specific PC, the RMS displacement of GDP γ-dimer for PC1, PC2, and PC3 was evaluated.

The RMS displacements of the H6-H7 region (Asn207-Leu243) of chain B with vector 3 and chain A of vector 1 are ~ 1.1 Å, and 0.7 Å, respectively, which compares to the highest fluctuation of the three vectors with 1.5 Å as significant value. (**Figure 3.44**)

The T5 (Pro173-Gln184) loop with vector 1 and vector 2 of chain A has an RMS displacement around 1.2 Å. (**Figure 3.44**)

The C-terminal helices of H11 (Ser385-Lys400) and H12 (Asp419-Ala437), contribute to structural motion with vector 1 of chain A and vector 3 of chain B; their RMS displacements are 1 Å - 1.2 Å.

The M loop (Thr274-289Thr) also shows high motion with chain B with vectors 1 and 3 for ~ 1.1 Å. The large RMS motion of 1.2 Å can be seen with the H2 helix (Arg72-Asn79), the H2 helix has shown to contribute to the collective motion of the γ-tubulin, but the exact role of the region is not well understood yet. (**Figure 3.44)**

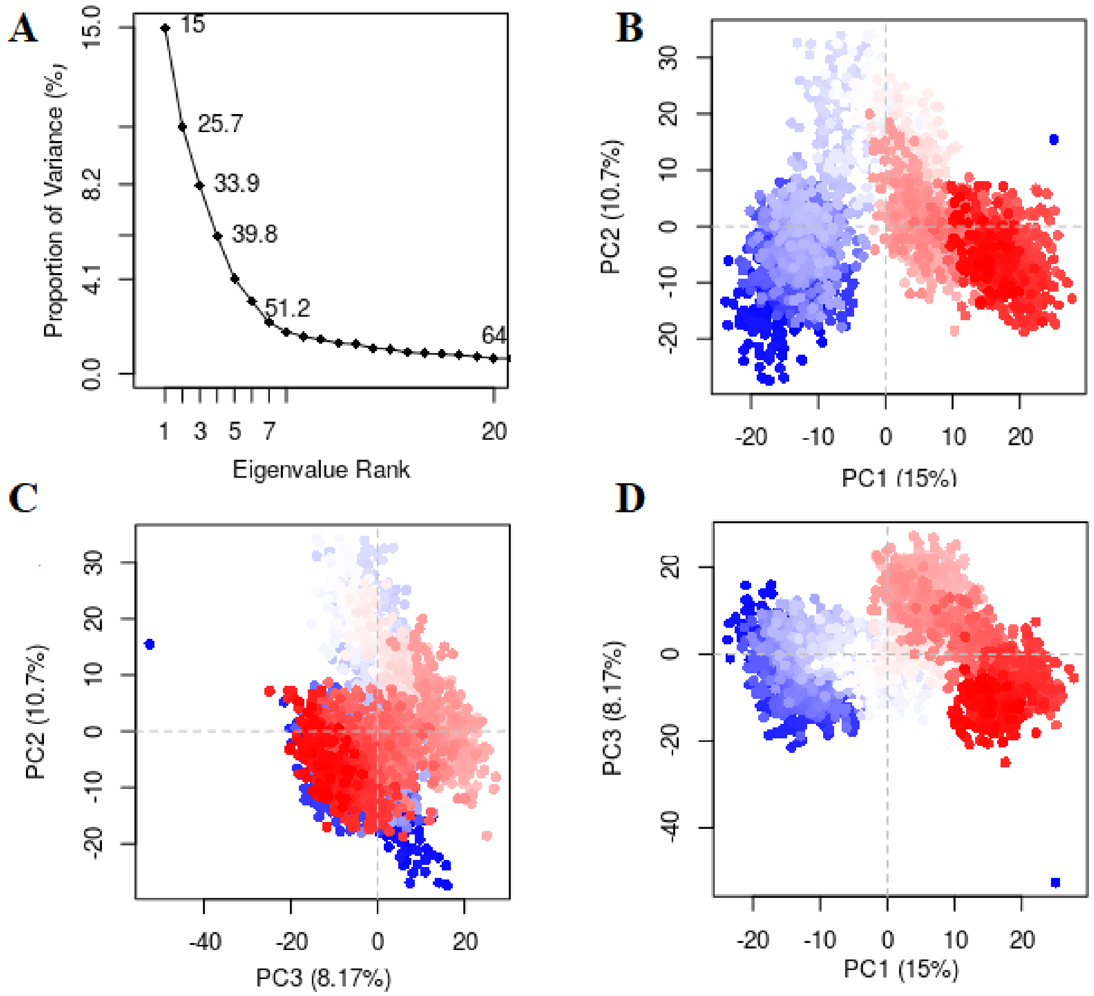

Figure 3.43 Result of PC Analysis on the GDP-bound γ-tubulin dimer in ZnCl$_2$ simulation. (**A)** Eigenvalue spectrum: the index of the number of eigenvalues which are ordered from the strongest to weakest contribution to variances (mean square displacement) on X-axis, and the Y-axis gives the proportion of variances for each eigenvalue. (**B-D**) The two-

dimensional trajectory projection of the PC plots show the projection of the motion of the conformations obtained from 150 ns to 200 ns of the Cα motions along with the first three principal components (PC1 and PC2, PC2, and PC3, PC1 and PC3). The colored circle represents the generated conformations during the last 50 ns of MD simulation.

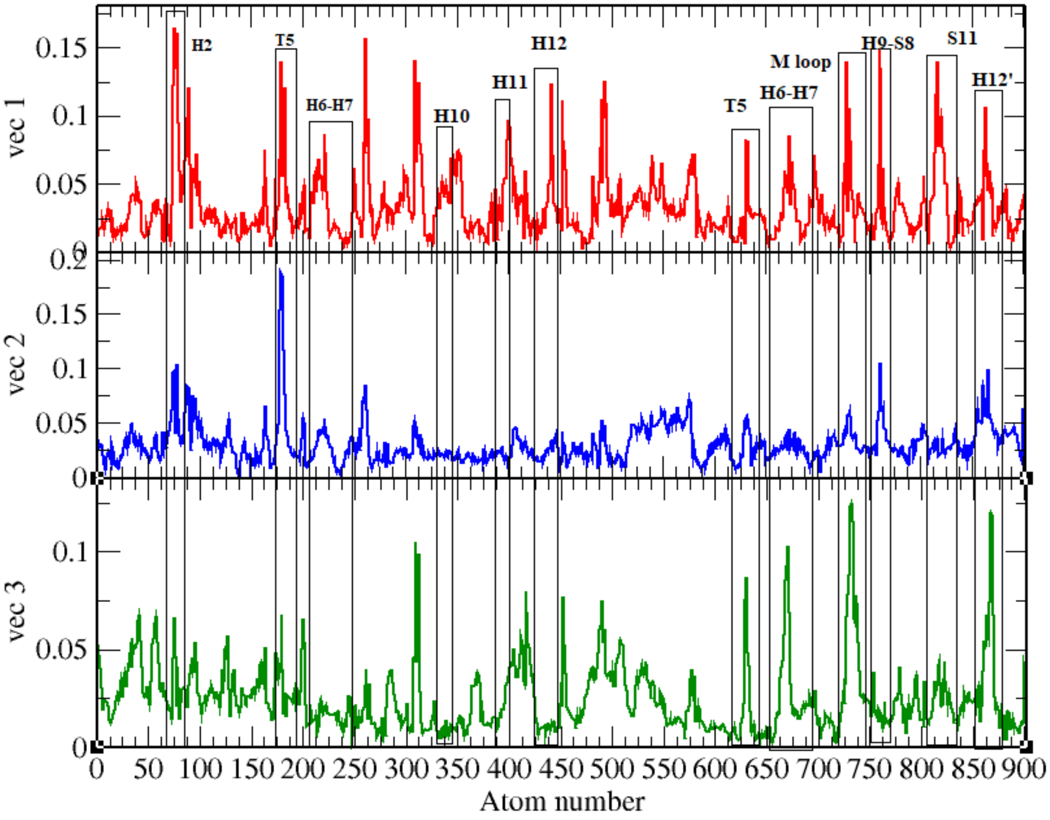

Figure 3.44 The plot of the RMS displacement per each Cα atoms of a GDP-bound γ-tubulin dimer in $ZnCl_2$ simulation for the first three eigenvectors. (**A**) The RMS displacement of atoms of vector 1 colored in red. (**B**) The RMS displacement of atoms of vector 2 colored in blue. (**C**) The RMS displacement of atoms of vector 3 colored in green.

3.2.2 MD Simulation of GTP-bound γ-Tubulin Dimer

For the GTP-bound simulation of the γ-dimer, in the presence of NaCl, $MgCl_2$, and $ZnCl_2$, the RMSD of the two chains of the GTP-bound γ-tubulin dimer shows that the structures of dimer under three experiments are stable. (**Figure 3.45**) The RMSD of backbone atoms of chain A in NaCl simulation increased to ~2 Å at 50 ns, and after that for the rest of the simulation was stable without any major fluctuation. The RMSD of chain A in $MgCl_2$ and $ZnCl_2$ simulations have shown almost a similar value of ~ 2.5 Å after 80 ns, and until the end of simulations at 200 ns were stable, they had the value of 2.4 Å to 2.5 Å, and converged at ~ 80 ns. (**Figure 3.45 A**)

Chain B for NaCl simulation converged at 150 ns, and the convergence point of $ZnCl_2$ and $MgCl_2$ simulations is at 130 ns. (**Figure 3.45 B**)

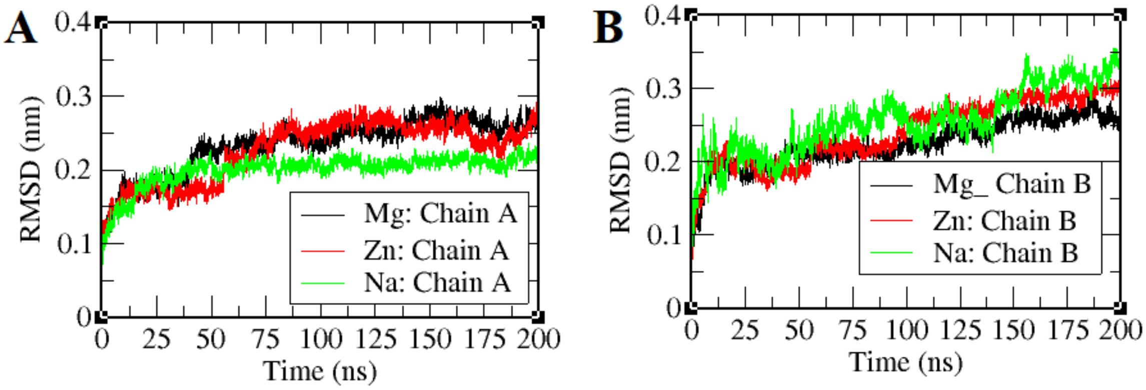

Figure 3.45: The RMSD of backbone atoms of chain A and chain B of the GTP-dimer of γ-tubulin. (**A**) The RMSD of chain A. (**B**) chain B. The $MgCl_2$ is colored in black, $ZnCl_2$ in red, and NaCl in green.

3.2.2.1 Does GTP Induces the Straight Conformation in GTP-Bound γ-Dimer

There is no study about the impact of the cations on the GTP bound γ-dimer on converting the curved to straight conformation with the γ-tubulin dimer, considering the impact of cations. It was shown that impact GDP was not effective enough to induce a straight conformation in γ-tubulin. (**Figure 3.29-3.32**)

The dCOM values for the H7 helix and the S6 strand was evaluated for chains A and B of three simulations. The dCOM between H7 and S6 is considered as a curved for ≤ 1.60 nm, and straight for more than 1.70 nm; the intermediate conformation is between 1.60 nm - 1.70 nm. (**Table 2.3**)

Chain A in $MgCl_2$ adapts an intermediate conformation as the dCOM of the H7 helix from the S6 strand fluctuates between 1.62 nm - 1.64 nm from 150 ns to 200 ns. The dCOM of H7 helix (Phe225-Leu231) from S6 strand (Cys201-Asp206) for chain A in $ZnCl_2$ simulation is 1.60 nm from 150 ns to 165 ns, then until 200 ns it is ~ 1.57 nm, which adapts a curved conformation. The dCOM H7 helix and the S6 strand for chain A in NaCl simulation is 1.55 nm from 150 ns - 165 ns and decreases to around 1.52 nm until 200 ns. The curved conformation is dominant with this chain as well. (**Figure 3.46 A**)

In chain B, dCOM of H7 and S6 fluctuates in the range of 1.58 nm to 1.60 nm for the last 50 ns, and curved conformation is dominant in $MgCl_2$. The dCOM with chain B in $ZnCl_2$ simulation various from 1.63 nm - 1.65nm, adapting an intermediate conformation. The dCOM of the chain B simulation of NaCl simulation decrease from 1.61 nm - 1.52 nm from 150 ns to 160, being 165 nm at 165 ns and with some small fluctuations at the range of 0.01 nm - 0.02 nm reaching 1.68 nm at 175 ns. Then it gradually decreases to 1.53 nm until 195 ns. From 195 ns to 200 ns, it is ~ 1.57 nm. The dominant conformation in chain B in NaCl is a curved conformation except for 168 ns to 175 ns, which adapts an intermediate conformation. (**Figure 3. 46 B**)

On the basis of evaluated simulations of the GTP-bound γ-tubulin dimer, curved and intermediate conformations are dominant. The straight state was not detected, and this is an indication that the GTP or allosteric model was not achieved to change the curved states to a straight conformation. Based on the allosteric model, the curved to straight transition depends on the allosteric impact of the GTP nucleotide, which was not observed here.[1]

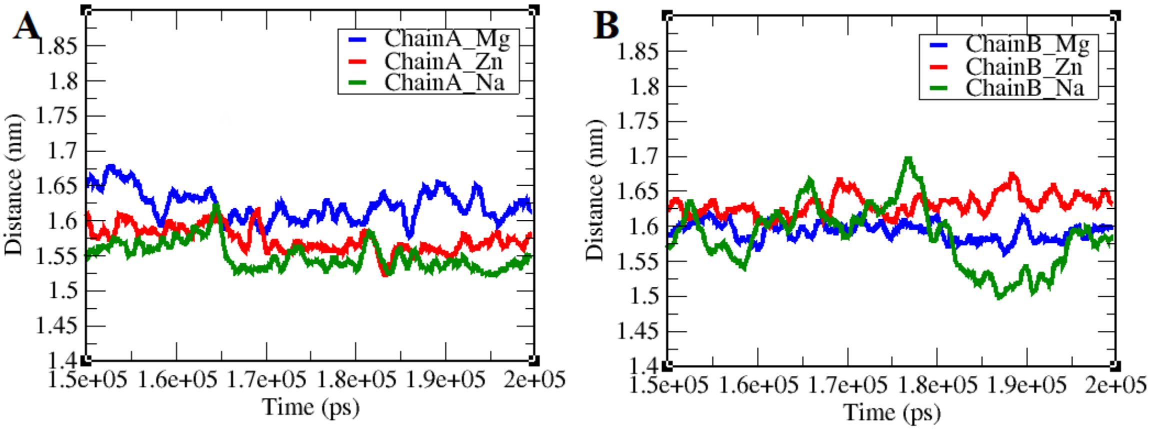

Figure 3.46: The dCOM of H7 helix and S6 strand for GTP-γ-tubulin dimer of three simulations. **(A)** Chain A simulation. (**B**) Chain B. The color in $MgCl_2$, $ZnCl_2$, and NaCl simulations are blue, red, and green, respectively.

200 ns conformation of γ-tubulin dimer in $MgCl_2$ was superimposed on both curved (1SA0) and straight (1JFF) β-tubulins. As it was described, the dominant conformation with chain A of $MgCl_2$ was an intermediate conformation. (**Figure 3.47 A**)

The conformation of H7 and H6 helices of chain A is aligned to the H7 and the H6 helices of the curved β-tubulin. The conformations of intermediate domain strands of the S7 (Phe268-Tyr273), S8 (Tyr317-Gln325), S9 (Ile356-Ser361), S10 (Ser374-His381) are not fully aligned to the curved conformation of β-tubulin. (**Figure 3. 47**)

Chain B of γ-tubulin in $MgCl_2$ simulation adapts a curved conformation as its H7 helix (Phe225-Leu243) is aligned with the H7 helix of the curved β-tubulin. The conformation of the H6 helix (Asn207-Asp216) and intermediate domain strands of the S7 (Phe268-Tyr273), S8 (Tyr317-Gln325), S9 (Ile356-Ser361), S10 (Ser374-His381) are aligned to the curved β-tubulin. (**Figure 3.47**)

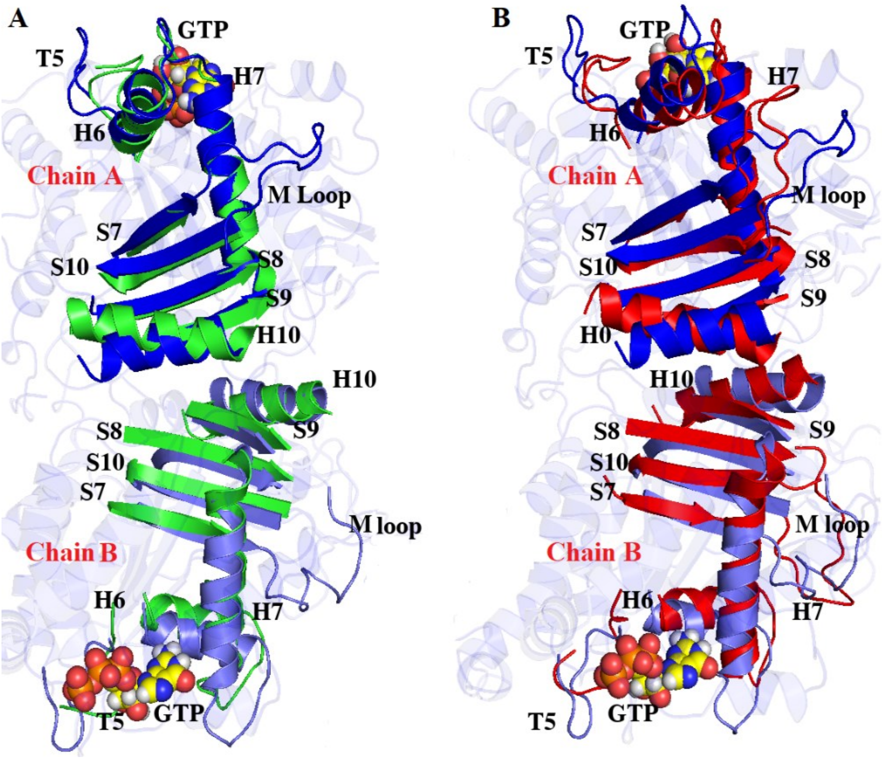

Figure 3.47: Superimposition of 200 ns conformation of the GTP-bound γ-tubulin dimer in $MgCl_2$ simulation on β-tubulin. (**A**) The 200 ns in blue superimposed on curved β-

tubulin (1JFF) in green. (**B**) The 200 ns in blue superimposed on straight β-tubulin (1JFF) in red.

The conformation of a γ-dimer in $ZnCl_2$ simulation at 200 ns was superimposed on both curved (1SA0) and straight β-tubulins (1JFF). (**Figure 3.48**)

With chain A in $ZnCl_2$ simulation, the H10 helix (Pro330-Arg343) is aligned well to the H10 helix of the curved β-tubulin. Instead, conformations of the H6 and S7 to S10 intermediate domain strands are not similar to the H6 or intermediate domain strands of curved or straight conformation as the whole protein adapt an intermediate conformation. The conformation of the H7 helix (Phe225-Leu243) is not fully aligned to H7 helix of straight or curved β-tubulin, which is a feature of the intermediate conformation. Chain A has H7 and S6 dCOM around 1.61 nm, and it can be said it adapts an intermediate conformation. (**Figure 3.48**)

An intermediate conformation is dominant in chain B, as well. The conformation of intermediate domain strands, S7, S8, S9, S10, and H10 helix, are aligned to the conformation of H10 and intermediate domain strands of the curved β-tubulin. The H7 and H6 helices are aligned to the H7 and H6 helices of the straight conformation of β-tubulin. (**Figure 3.48**)

The conformation of NaCl simulation at 200 ns was superimposed on both curved (1SA0) and straight β-tubulins (1JFF). Chain A is adapted a curved conformation. The conformation of the H7 (Phe225-Leu243) helix is relatively aligned to the conformation of the H7 helix of the curved β-tubulin. The conformation of the H6 (Asn207-Asp216) and H10 helices (Pro330-Arg343) are aligned to H6 and H10 helices of the curved β-tubulin. The shapes of S8 (Tyr317-Gln325), S9 (Ile356-Ser361), S10 (Ser374-His381) were aligned with the same counterpart in the curved β-tubulin as a references structure. Chain B in NaCl simulation adapts the curved conformation. The conformation of the H6 (Asn207-Asp216), H7 (Phe225-Leu243), and H10 (Pro330-Arg343) helices are aligned with the same counterpart in the curved β-tubulin. (**Figure 3.49**)

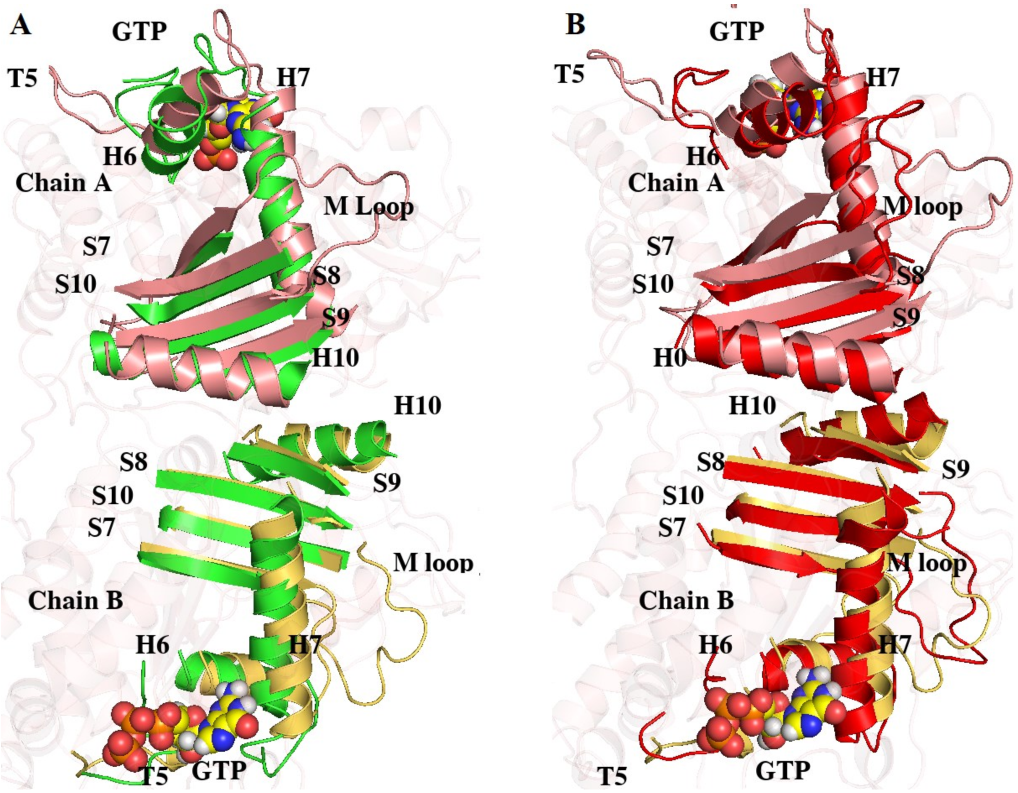

Figure 3.48 Superimposition of 200 ns conformation of the dimer of GTP-bound γ-tubulin in $ZnCl_2$ simulation on β-tubulin. (**A**) γ-tubulin dimer at 200 ns colored in pink for chain A and yellow in chain B superimposed on curved β-tubulin (1JFF) in green. (**B**) γ-tubulin dimer at 200 ns colored in pink for chain A and yellow in chain B superimposed on straight β-tubulin (1JFF) in red.

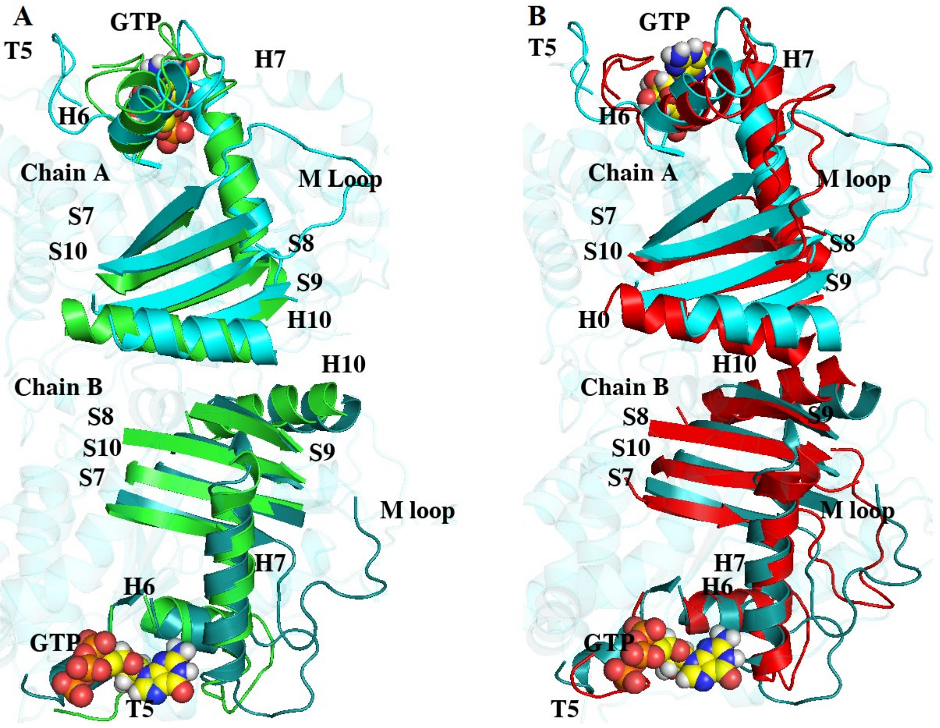

Figure 3.49 Superimposition of a conformation of the GTP-bound γ-tubulin dimer in NaCl simulation on β-tubulin. (**A**) γ-tubulin dimer at 200 ns colored in cyan for chain A and deep cyan in chain B superimposed on curved β-tubulin (1JFF) in green. (**B**) γ-tubulin dimer at 200 ns colored in cyan for chain A and deep cyan in chain B superimposed on straight β-tubulin (1JFF) in red.

3.2.2.2 Study of Changes of High-Affinity Metal Binding Sites in the Presence of GTP

The GTP binding sites were monitored for finding the cations interact GTP. Every 10 ns conformations of the last 50 ns of MD trajectories of the γ-tubulin dimer were extracted. All interacting cations inside the GTP binding site were founded, and then their distances from Og and Ob of the GTP were measured. (**Figure 3.50**)

In each chain of the NaCl simulation, two Na^+ cations are interacting at a close distance of ~ 2.4 Å with respect to O1g atom of the GTP in chains A and ~2.3 Å with respect to O2b atom of the GTP in chain B. The interaction between Na^+ of chain A with O1g atom of GTP and Na^+ of chain B with O2b atom of the GTP is stable at 2.4 Å for 50 ns from 150 ns to 200 ns. (**Figure 3.50**)

In $MgCl_2$ simulation, two Mg^{+2} in chain A and one Mg^{2+} in chain B are found in interaction at 3.9 Å - 4 Å with respect to O1g and O3g atoms of the GTP, respectively. Their interactions are stable at 4 Å distances. (**Figure 3.50**)

In $ZnCl_2$, one Zn^{+2} was found in stable interaction without any large fluctuations from 150 ns to 200 ns with the GTP; its interaction with O3g was stable around 4 Å. This interaction from 194 to 200 ns is at a distance of 5 Å. (**Figure 3.50**)

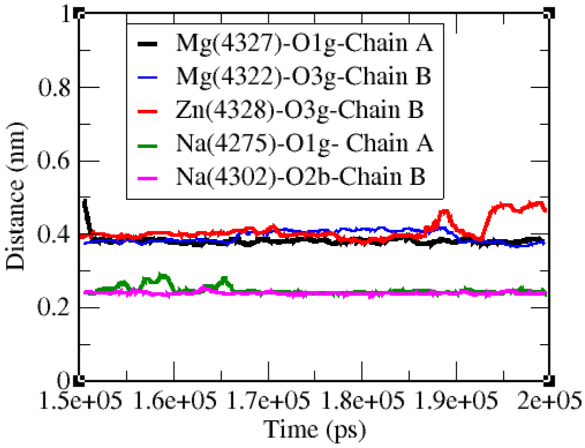

Figure 3.50 The distances between GTP and accommodated cations of Mg^{+2}, Zn^{+2}, and Na^+. The cations with their codes are labeled, and their distances with respect to oxygen

atoms connect to the β phosphate or γ phosphate of GTP are measured for the last 50 ns from 150 ns to 200 ns.

Interactions between Mg^{2+}- O1g, Mg^{2+}- O3g, Zn^{2+}- O3g, and Na^{+}- O1g was almost stable at the GTP binding site. **(Figure 3.50 and 3.41)**

Some other cations were found in interactions with the GTP with large fluctuations. They are in the binding site ~ 10 ns to 20 ns of trajectories and then leave it. The Zn^{+2} cation is found in interaction with O1g atom of the GTP with chain A at 4 Å from 150 ns to 175 ns; it gradually detaches from the binding site. One Zn^{+2} after 190 ns enters the binding site and until 200 ns made stable interactions at 3.9 Å with O1b atom of the GTP at chain A. Na^{+} was found at 3.7 Å from O2g of chain A from 150 ns to 163 ns and then left the binding site, and another Na^{+} interacts at 3.6 Å from O1g of chain A from 165 ns to 195 ns. (**Figure 3.51**)

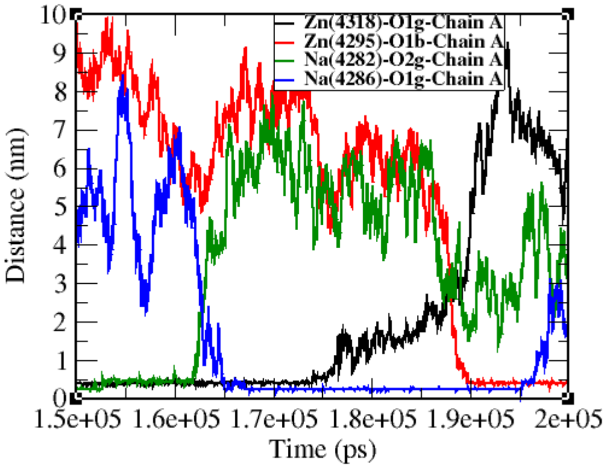

Figure 3.51 The distances between GTP and accommodated cations of Mg^{+2}, Zn^{+2}, and Na^{+} founded with large fluctuations. The distances with respect to oxygen atoms connected to the β - γ phosphate of GTP are measured for the last 50 ns from 150 ns to 200 ns in three MD simulations.

The interactions of the cations with N7 atom of the GTP in three simulations were evaluated for both chains to address the new high-affinity binding site. The minimum distance between N7 atom of GTP with chain A from Mg^{+2} cations in the $MgCl_2$ simulation and N7 atom of the GTP with chain B from Zn^{+2} cations is ~ 2.1 Å from 150 ns to 200 ns without high fluctuations. The N7 atom of chain A in NaCl simulation was in a stable interaction with Na^{+} at 4 Å from 163 ns until 200 ns. Other N7 atoms of the GTP, including N7 atom of the GTP in chain B of $MgCl_2$ simulation, chain A in $ZnCl_{2'}$ and chain B of NaCl simulations, were found at a minimum distance from 8 Å - 11 Å from Mg^{+2}, Zn^{+2}, and Na^{+}, respectively. (**Figure 3.52 A**)

In the GDP simulations, two stable interactions at a distance of 2.3 Å were found between N7 of chain B with Mg^{2+} and Zn^{2+} cations, respectively. In chain A of divalent simulations and both chains of Na^{+} simulation, the minimum distance of interaction between N7 and cations is more than 6 Å. (**Figure 3.52 B**)

Apart from the oxygen atoms of the β-γ phosphate belonging to the GTP/GDP, the N7 atoms of the GDP and GTP in the binding site can interact closely with the divalent cations and, therefore, potentially act as a high-affinity metal site.[52-54]

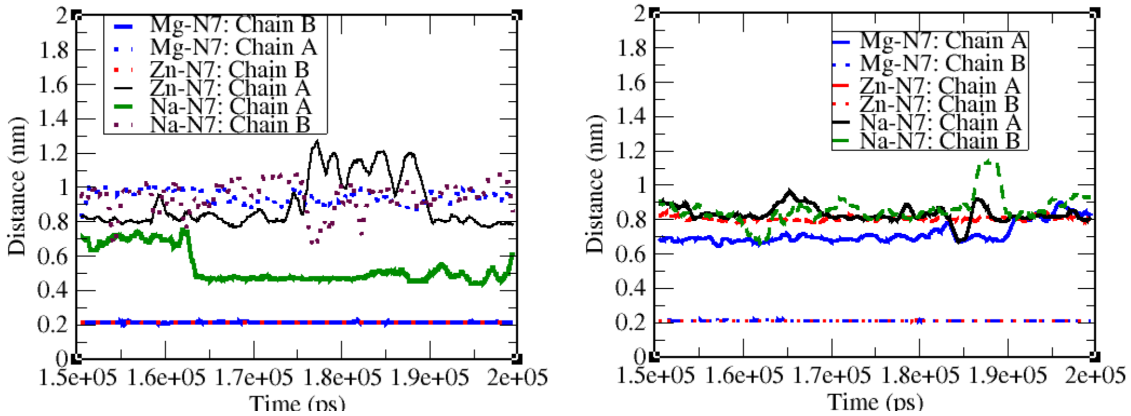

Figure 3.52 The minimum distances between accommodated cations into the GTP binding site from the N7 atoms of purin ring. The distances with respect to N7 are measured for the last 50 ns from 150 ns 200 ns of all three simulations. (**A**) GTP-bound dimer. (**B**) GDP-bound dimer.

In order to evaluate the role of GTP and $MgCl_2$ in collective motions of the protein, PCA was performed on the GTP-$MgCl_2$ dimer.

The PC1 covers 25% of the variability in the motions of the γ-tubulin under the impact of GTP and Mg^{+2} cations. (**Figure 3.53 A**)

The second and third PC is covering 11.19% and 6.24% of the variance with a displacement of the Cα atoms of the protein. (**Figure 3.53 B-D**)

The projections of trajectory on the first three PCs show that different conformers are spread out between PC1-PC2, PC2-PC3, and PC1-PC3 axis. The projection shows that there are a considerable number of different conformations. The motions related to each

PC gives information about the overall collective motion of the γ-tubulin that has a biological function. In GTP-Mg-dimer; the H6-H7 region, which includes the H6 helix, H6-H7 loop, and the core helix of the H7, has shown RMS displacement with chain A for 1 Å and 2 Å with PC vector 1 of chain B. (**Figure 3.54**)

Also, the M and T3 loops have shown large motions with PC vector 1 of chain A; their RMS motion is 2.6 Å. The M loop has a significant role in lateral interactions in the protofilament. However, the biological role of the T3 loop needs more investigation in order to be revealed. The H11 and H12 helices have relatively large RMS displacement here with a value of 1.5 Å. This shows the significance of the C-terminal domain in the collective motion and biological function of the γ-tubulin. (**Figure 3.54**)

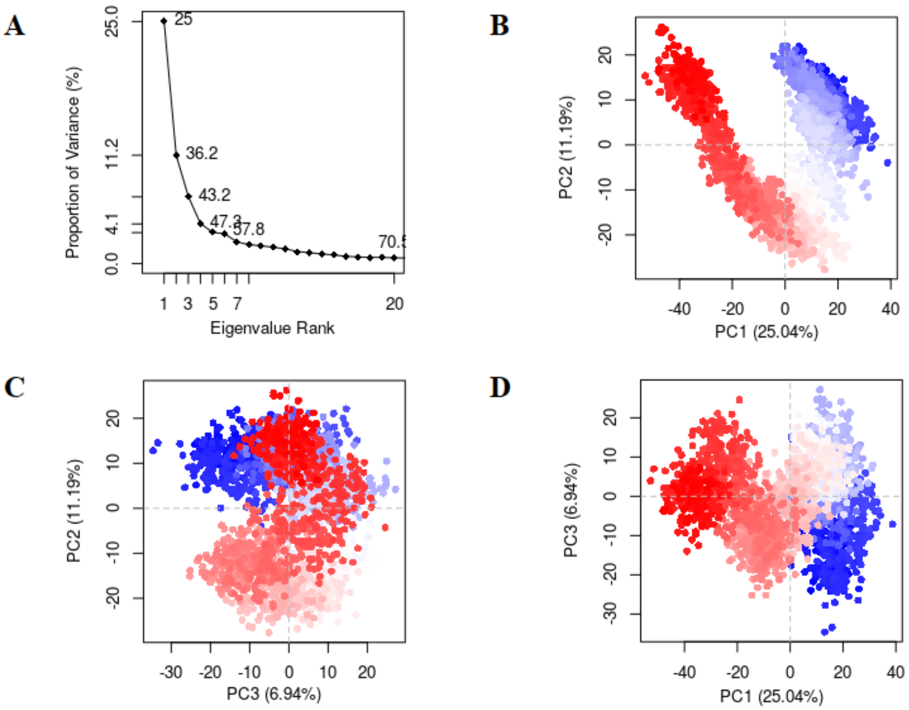

Figure 3.53 Result of PC Analysis on the GTP-bound γ-tubulin dimer in MgCl$_2$ simulation. (**A**) Eigenvalue spectrum: the index of the number of eigenvalues which are ordered from

the strongest to weakest contribution to variances (mean square displacement) on X-axis, and the Y-axis gives the proportion of variances for each eigenvalue. (**B-D**) The two-dimensional trajectory projections of the PC plot show the projection of the motion of the conformations obtained from 150 ns to 200 ns of the Cα atoms along with the first three principal components (PC1 and PC2, PC2, and PC3, PC1 and PC3). The colored circle represents the generated conformations during the last 50 ns of MD simulation.

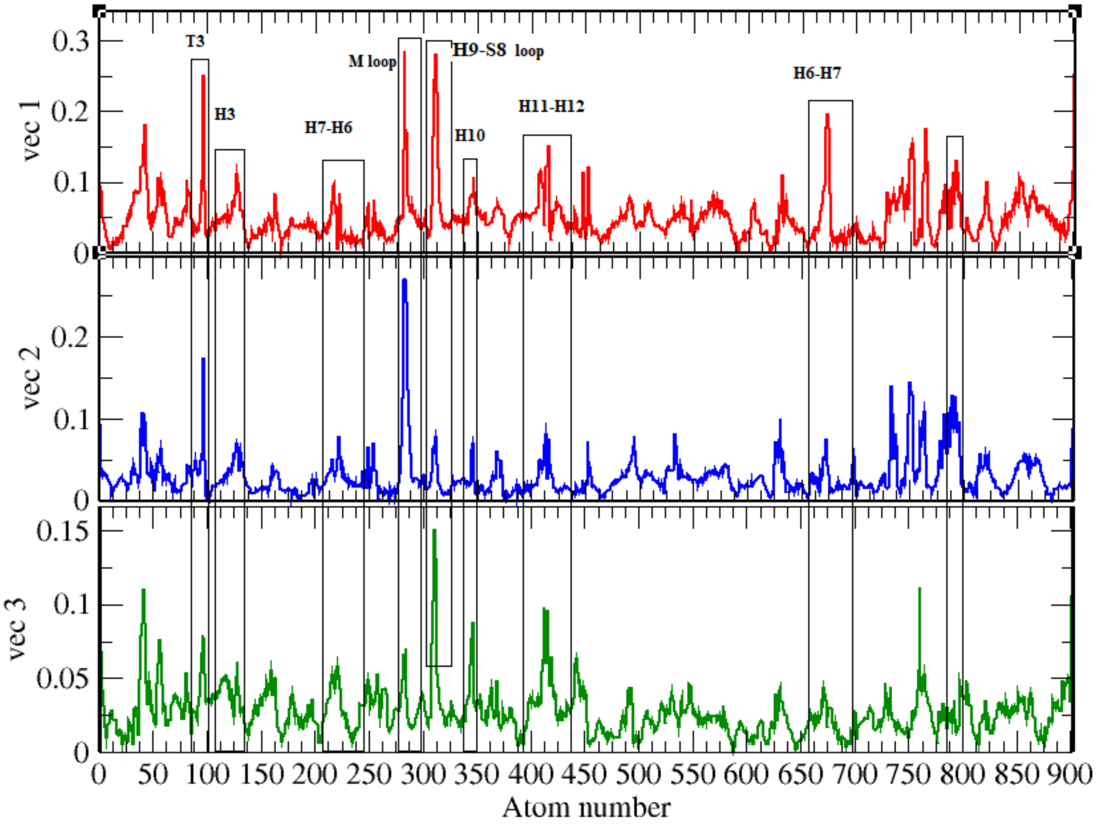

Figure 3.54 The plot of the RMS displacement per each Cα atoms of a GTP-γ-tubulin dimer in $MgCl_2$ simulation for the first three eigenvectors. **(A)** The RMS displacement for atoms of vector 1 colored in red. **(B)** The RMS displacement for atoms of vector 2 colored in blue. **(C)** The RMS fluctuation for atoms of vector 3 colored in green.

3.3 Discussions

The superimposition of the homo-sapiens γ-tubulin dimer on yeast γTuSC dimer shows lateral interactions and orientations of the two γ-dimers are not achieved through the contribution of similar secondary structure segments. Lateral interactions of Homo-sapiens γ-dimer achieved through the contribution of the H8 and H10 helices of both chains, the C-terminal tail for Tyr443-Trp446, and T7 loop Met249-Pro353. The H3, H9, H10, helices, and S2-S3 loop are involved in the lateral interactions in the yeast small complex, which are different from the homo-sapiens dimer. Also, the orientation of the H6-H7 helices, if considered as representative of two dimers, are different from homo-sapiens and yeast γ-dimer. The orientation of the H6-H7 of the homo-sapiens dimer is vertical, while horizontal in yeast dimer. The template model of MTs nucleation depends on ring shape lateral orientation of 7 γ-monomers, but the protofilament model states even one acting γ-monomer, regardless of exact orientation, nucleates MTs; these two models can be further investigated in a computational or a wet-lab study.

The GTP binding site of the *Homo-sapiens* γ-tubulin consists of key residues essential for developing the GTPase activity. It has been shown that three oxygen atoms of the γ phosphate make H-bonds with both water molecules as well as the GTP, which is one of the major criteria for developing the GTPase activity and as a necessary step of the reaction. The existence of some residues such as Arg and Lys are crucial for GTPase reaction; among them, the Arg72, Gln12, Gln184 make close interaction to the GTP. It was observed that the side chain of the Arg72 in $MgCl_2$ simulation lower its distances from 12 Å at 100 ns the Og atoms of the GTP to ~ 3 Å at 200 ns. However, more computational work is needed, especially QM/MM-based modeling, to investigate the GTP and its interactions in the binding site aiming to discover the exact mechanism of the reaction.

The average electrostatic energy between divalent cations of Zn^{+2}, Mg^{+2}, and each chain is more than four times as much as Na^+ simulation, -1982.4 kJ/mol in $MgCl_2$ and -2021.1 kJ/mol in $ZnCl_2$ simulation for chain A compared to the -453.5 kJ/mol in NaCl simulation. This was higher than the electrostatic interaction between cations and the monomer and is an indication that with the complexes of proteins, the higher number of monomers contribute to stronger electrostatic interactions with charged particles or molecules.

The electrostatic and L-J energy between chains A and B of the γ-tubulin dimer in three unliganded simulations was calculated to assess how interaction energy is varied in each simulation. The electrostatic and L-J energy between the two chains of the monomer of γ-tubulin was seen to be stronger and also with higher contributing atoms in the interface in simulations with Zn^{+2} and Mg^{+2} cations compared to the Na^+. The electrostatic energy between γ-tubulin chain A and B fluctuating around -1500.2 kJ/mol, and -1400.5 kJ/mol in $MgCl_2$ and $ZnCl_2$ simulations, respectively, and about -1250.3 kJ/mol in NaCl simulation. The number of interactions between residues of chains A and B involving interface interaction at ≤ 4 Å is higher by 100 in the $MgCl_2$ simulation compared to two other simulations containing $ZnCl_2$ and NaCl.

The H10 helix is an essential secondary segment contributing to interactions in the interface between two γ-tubulin chains. Considering the contribution of the H10 helix, which was around -575 kJ/mol, and compared to -1500.2 kJ/mol (interaction energy between chain A and B), it concluded that ~ 1/3 of the electrostatic energy between chain A and B originates from the contribution of both H10 helices in the chains interface. The H10 helix is part of the ID domain and undergoes strong rearrangement while the conversion occurred between the curved and straight conformation tubulin.

For both chains, the curved and intermediate conformations were dominant and most observed. In GDP, GTP-liganded, and unliganded simulations, the curved was the most seen state of the protein. In unliganded simulations for chain A, the curved conformation was seen to be a dominant conformation for all three simulations. For almost the last 50 ns, the dCOM between H7 and S6 for chain A of γ-tubulin was fluctuating in the range of 1.58 nm - 1.59 nm for all three simulations.

In chain B of the γ-tubulin dimer, the intermediate conformation is dominant in NaCl and $ZnCl_2$ simulations and a curved conformation in the $MgCl_2$ simulation. The dCOM of H7 helix and the S6 strand in the NaCl simulation was ~ 1.69 nm from 163 ns to 200 ns. In chain B of γ-tubulin in $ZnCl_2$ simulation, the value of dCOM of H7 and S6 was ~ 1.7 nm from 170 ns to 180 ns, being at the range of 1.65 nm - 1.66 nm from 150 to 170 and 183 to 200 ns. The dCOM of chain B in $MgCl_2$ simulation was mostly changed around 1.58 nm - 1.61 nm from 150 ns to 200 ns.

The dynamic cross-correlation between the H6-H7 segment of chain A from S8-H10 region exhibited almost zero correlation. The T5 loop of chain A, which has a switching role during converting curved and straight conformations was seen to have no positive or negative correlation with respect to the H6-H7 region of chain A or B. This rather shows motion of segments that participate in conformational rearrangement is independent of each other and might be dependent on other factors such as lateral interactions.

Two residues, Asp180 and Asp433 in $MgCl_2$ and $ZnCl_2$ simulations, were contributed to stable interactions at ~ 2 to 2.5 Å from Mg^{2+} and Zn^{2+} cations. These stable interactions might have biological impacts on γ-tubulin function inside the γ-ring. These two residues are located within the necessary region for the function of the γ-tubulin. The Asp433 of H12 located at C-ter and Asp180 belong to the T5 loop of the N-ter. Both T5 loop and H12 helix play important roles in the nucleation of MTs and the functionality of the γ-tubulin. The H12 mutation impairs the MTs nucleation, and the function of T5 loop has been shown to switch between the curved and straight conformation.

The principal component analysis is a useful method in structural biology. MD simulation generates several million conformations, each different from another one. The major conformational variances are not very clear and cannot even be examined by simple visualization tools due to a large number of produced conformers. On the other hand, the usefulness of the PCA method was proven in many studies that show consistency between the obtained results of the PCA with the analysis produced from wet lab-based experiments. The PCA is a useful method for evaluations of collecting motions that are involved in functionally related activities. Accordingly, it has been shown that biological functions of proteins such as substrate binding, product release, allosteric regulation, and hinge bending are examples of collective motion. These motions are different from local motions, which are not linked to the biological functions. Therefore the majority of the motions that are related to the functions of proteins are collective rather than local. Therefore the secondary segments with larger displacements in top-ranked PCA are contributing to the biological function of the proteins.

Around 1.5 Å and 1.Å displacement were observed with vector 1 in chain A of M loop and H10 helix, which show they are contributing to the collective motion. The significant fluctuation was measured with the PC vector one for H11 and H12 helices at the C-terminal of chain A. The role of both helices (H11 and H12) in the biological functions of the γ-tubulin has been documented elsewhere, and here they show large displacement with vector one, as mentioned above.

With chain B of unliganded γ-dimer in NaCl simulation, both H2 helix and M loop are found to have the displacement around 2 Å. The H6-H7 segment was also exhibited considerable displacement, which proves its role in the function of the γ-tubulin.

In contrast to the simulations with the GTP-bond monomer, not only oxygen atoms of the α-β phosphate but GDP N7 atom has also made stable interactions with the cations at the binding site. This generates a new high-affinity binding site, which for the first time, is addressed. Cations in interaction with oxygen atoms of γ phosphate are involved in the hydrolysis of the nucleotide. However, the role of interaction with N7 is not known yet.

3.4 Conclusions

In the *homo-sapiens* dimer, the strength of homo-monomers interactions was evaluated by monitoring the number of interactions, H-bonds, and calculating the L-J and electrostatic energy between them. In three simulations, the interface interactions were stronger in the $MgCl_2$ and $ZnCl_2$. The electrostatic energy between residues of chain A and B fluctuates at -1500.2 kJ/mol and -1400.5 kJ/mol in the $MgCl_2$ and $ZnCl_2$ simulations, respectively, and ~ -1250.3 kJ/mol in the NaCl simulation. Also, the L-J energy between chains A and B is stronger in the $MgCl_2$ ~ -840 kJ/mol; it fluctuates around -750 kJ/mol and -550 kJ/mol in $ZnCl_2$ and NaCl simulations, respectively.

The number of interactions and the H-bonds between chains A and B is higher in the $MgCl_2$ simulation by 100 interactions, and 10 H-bonds compared to either the NaCl or the $ZnCl_2$, respectively. This is an indication that electrolytes affect the interactions in multi-monomer complexes, which were stronger in Mg^{+2} simulation. It was also shown that the H10 helix is one of the key helices involved in interactions at the interface.

The main conformations in both chains of *homo-sapiens* γ-tubulin in three ionic conditions are the intermediate and curved conformations. Chain B of unliganded dimer almost always adapts the intermediate conformation in all simulations, and chain A in $MgCl_2$, NaCl, and $ZnCl_2$ simulations takes both curved and intermediate conformations. These findings support the model that the main driving force behind the conversion between curved and straight conformations cannot be GTP. The extent to which chain B in the NaCl and $ZnCl_2$ adapts intermediate conformation is similar to that of the GTP-bound γ-monomer, with the H7 and S6 dCOM value fluctuates between 1.60 nm - 1.65 nm.

The dynamic cross-correlation analysis has revealed secondary structure segments that contribute to straight and curved conversion are move rather independently.

The motion of Cα atoms of the H6-H7 region with respect to the H10 helix demonstrates no positive correlation but rather zero correlation, and this shows they move independently.

The T5 loop was seen to have no positive correlation with respect to the H6-H7 region in both chains A and B.

One of the key questions that can be addressed is the GDP role in inducing conformational changes compared to the role of GTP. Straight conformation was not observed in the GTP and GDP liganded simulations; the curved and intermediate conformations were the dominant conformations. It can be deduced that the curved or intermediate conformation was the major and active conformations in the active γ-ring responsible for the nucleation of MTs.

In opposition to the allosteric model, there is not enough evidence from GDP and GTP simulations of γ-dimer to show they contribute curved to straight conversion. No significant differences were observed in terms of the H7 and the S6 dCOM in GDP-bound or GTP-bound simulations. For instance, in chain A of GTP-bound γ-dimer, the intermediate and curved conformations with dCOM of H7 and S6 between 1.50 nm -1.68 nm were dominant in $MgCl_2$ and $ZnCl_2$.

In both GDP and GTP simulations, the nucleotide-binding sites accommodated Mg^{+2}, Zn^{+2} as well as Na^{+}. The exact location of the high-affinity site was found to interact closely to β-γ oxygens. This shows that the high-affinity metal site does not only depends on the availability of the oxygen atoms of γ phosphate, but in GDP simulations, the oxygen atoms of β phosphate can also interact with cations. It has been shown that the N7 atom of GDP or GTP interacts with the divalent cations at 2 Å. Therefore, the purin ring of the GTP or GDP can also be another potential high-affinity metal-binding site with an unknown function.

The interaction of Mg^{+2} with GDP contributes to larger interaction energy between GDP and the residues of the binding site, which was seen in the GTP binding as well. The IE between residues of chain A and GDP are -1122.3 kJ/mol, -944.4 kJ/mol, and -935.9 kJ/mol in $MgCl_2$, $ZnCl_2$, and NaCl simulations, respectively. Some residues have a larger contribution to the IE with GDP. For three simulations Gln12, Thr145, Cys13, Ser147, Gly143, and Gly144 were involved strongly in interaction with the GDP. The IE between Gln12, Thr145, Cys13, and Ser147, and GDP in $MgCl_2$ simulation are -152.3 kJ/mol, -133.8 kJ/mol, -117.0 kJ/mol, and -119.2 kJ/mol respectively. These values for the same residues of Gln12, Thr145, Cys13, Ser147 under $ZnCl_2$ simulation are -85.1 kJ/mol, -159.6 kJ/mol, -118.2 kJ/mol, -80.8 kJ/mol and for NaCl simulation are -177.1 kJ/mol, -32.5 kJ/mol, -128.1 kJ/mol, -134.2 kJ/mol respectively. The interaction energy between the Arg72 with chain A of GDP-bound simulations are -64.1 kJ/mol, -2.5 kJ/mol, and -13.7 kJ/mol for $MgCl_2$, $ZnCl_2$, and NaCl simulation, respectively.

The functional motions of the proteins are of significant importance to structural biology. The collective motions determine the key displacement with the domains of the proteins during allosteric changes, binding of substrate, movement of the hinge regions, and the release of the product. The PCA was performed on three different simulations, unliganded dimer in NaCl simulation, GTP-bond dimer in $MgCl_2$, and GDP-bound dimer under $ZnCl_2$ simulation. In both GTP-bound and GDP-bound simulations, the H6-H7 region was found to be involved in collective motion. The role of the H6-H7 region in the straightness and curvature of the tubulin is known in β-tubulin. The H11 (Ser385-Lys400) and H12 (Asp419-Ala437) helices at C-terminal domain of γ-tubulin, with chain A in GDP-bound in $ZnCl_2$ and unliganded dimer in NaCl simulations, have shown large RMS displacement with their first PCA vector with 2 Å and 1 Å. In chain A of the unliganded dimer in NaCl, GDP-bound in $ZnCl_2$, and GTP-bound in $MgCl_2$ simulations, H2 and H3 helices were shown to be involved in collective motions, but their functional role has not yet been discovered. In the liganded dimer, the H10 helix M and T5 loops were found to contribute to the collective movements. The role of the T5 loop is considered as switching between the transition from curved to straight conformations. T3 (Ser94-Asn103), H2 (Arg72-Asn79), and H3 (Trp104-Asp127) helices contributed to the collective motion, and their roles remain elusive.

3.5 Bibliography

1. Rice LM, Montabana EA, Agard DA: **The lattice as allosteric effector: structural studies of alphabeta- and gamma-tubulin clarify the role of GTP in microtubule assembly**. *Proceedings of the National Academy of Sciences of the United States of America* 2008, **105**(14):5378-5383.
2. Kollman JM, Merdes A, Mourey L, Agard DA: **Microtubule nucleation by γ-tubulin complexes**. *Nature Reviews Molecular Cell Biology* 2011, **12**:709.
3. Zheng Y, Wong ML, Alberts B, Mitchison T: **Nucleation of microtubule assembly by a γ-tubulin-containing ring complex**. *Nature* 1995, **378**(6557):578-583.
4. Zheng Y, Wong ML, Alberts B, Mitchison T: **Nucleation of microtubule assembly by a gamma-tubulin-containing ring complex**. *Nature* 1995, **378**(6557):578-583.
5. Kollman JM, Zelter A, Muller EG, Fox B, Rice LM, Davis TN, Agard DA: **The structure of the gamma-tubulin small complex: implications of its architecture and flexibility for microtubule nucleation**. *Molecular biology of the cell* 2008, **19**(1):207-215.
6. Choy RM, Kollman JM, Zelter A, Davis TN, Agard DA: **Localization and orientation of the gamma-tubulin small complex components using protein tags as labels for single particle EM**. *J Struct Biol* 2009, **168**(3):571-574.
7. Mishra RK, Chakraborty P, Arnaoutov A, Fontoura BMA, Dasso M: **The Nup107-160 complex and γ-TuRC regulate microtubule polymerization at kinetochores**. *Nature Cell Biology* 2010, **12**(2):164-169.
8. Roostalu J, Surrey T: **Microtubule nucleation: beyond the template**. *Nature Reviews Molecular Cell Biology* 2017, **18**:702.
9. Erickson HP, Stoffler D: **Protofilaments and rings, two conformations of the tubulin family conserved from bacterial FtsZ to alpha/beta and gamma tubulin**. *J Cell Biol* 1996, **135**(1):5-8.
10. Erickson HP: **γ-tubulin nucleation: template or protofilament?** *Nature Cell Biology* 2000, **2**(6):E93-E95.
11. Teixido-Travesa N, Roig J, Luders J: **The where, when and how of microtubule nucleation - one ring to rule them all**. *J Cell Sci* 2012, **125**(Pt 19):4445-4456.
12. Greenberg CH, Kollman J, Zelter A, Johnson R, MacCoss MJ, Davis TN, Agard DA, Sali A: **Structure of gamma-tubulin small complex based on a cryo-EM map, chemical cross-links, and a remotely related structure**. *J Struct Biol* 2016, **194**(3):303-310.
13. Ravelli RBG, Gigant B, Curmi PA, Jourdain I, Lachkar S, Sobel A, Knossow M: **Insight into tubulin regulation from a complex with colchicine and a stathmin-like domain**. *Nature* 2004, **428**(6979):198-202.
14. Löwe J, Li H, Downing KH, Nogales E: **Refined structure of αβ-tubulin at 3.5 Å resolution**. *Journal of Molecular Biology* 2001, **313**(5):1045-1057.

15. Kollman JM, Greenberg CH, Li S, Moritz M, Zelter A, Fong KK, Fernandez J-J, Sali A, Kilmartin J, Davis TN *et al*: **Ring closure activates yeast γTuRC for species-specific microtubule nucleation**. *Nature structural & molecular biology* 2015, **22**(2):132-137.
16. Nogales E, Wolf SG, Downing KH: **Structure of the αβ tubulin dimer by electron crystallography**. *Nature* 1998, **391**(6663):199-203.
17. Brouhard G, Sept D: **Microtubules: Sizing Up the GTP Cap**. *Current Biology* 2012, **22**(18):R802-R803.
18. Brouhard GJ, Rice LM: **The contribution of αβ-tubulin curvature to microtubule dynamics**. *The Journal of Cell Biology* 2014, **207**(3):323-334.
19. Aldaz H, Rice LM, Stearns T, Agard DA: **Insights into microtubule nucleation from the crystal structure of human γ-tubulin**. *Nature* 2005, **435**(7041):523-527.
20. Gombos L, Neuner A, Berynskyy M, Fava LL, Wade RC, Sachse C, Schiebel E: **GTP regulates the microtubule nucleation activity of γ-tubulin**. *Nature Cell Biology* 2013, **15**:1317.
21. Borisy G, Heald R, Howard J, Janke C, Musacchio A, Nogales E: **- Microtubules: 50 years on from the discovery of tubulin**. 2016, **- 17**:-.
22. Consortium TU: **UniProt: a worldwide hub of protein knowledge**. *Nucleic Acids Research* 2018, **47**(D1):D506-D515.
23. Waterhouse A, Bertoni M, Bienert S, Studer G, Tauriello G, Gumienny R, Heer FT, de Beer TAP, Rempfer C, Bordoli L *et al*: **SWISS-MODEL: homology modelling of protein structures and complexes**. *Nucleic Acids Res* 2018, **46**(W1):W296-w303.
24. **The PyMOL Molecular Graphics System, Version 1.2r3pre, Schrödinger, LLC.**
25. Oostenbrink C, Villa A, Mark AE, Van Gunsteren WF: **A biomolecular force field based on the free enthalpy of hydration and solvation: The GROMOS force-field parameter sets 53A5 and 53A6**. *Journal of Computational Chemistry* 2004, **25**(13):1656-1676.
26. Hess B, Bekker H, Berendsen HJC, Fraaije JGEM: **LINCS: A linear constraint solver for molecular simulations**. *Journal of Computational Chemistry* 1997, **18**(12):1463-1472.
27. Essmann U, Perera L, Berkowitz ML, Darden T, Lee H, Pedersen LG: **A smooth particle mesh Ewald method**. *The Journal of Chemical Physics* 1995, **103**(19):8577-8593.
28. Bussi G, Donadio D, Parrinello M: **Canonical sampling through velocity rescaling**. *The Journal of Chemical Physics* 2007, **126**(1):014101.
29. Malde AK, Zuo L, Breeze M, Stroet M, Poger D, Nair PC, Oostenbrink C, Mark AE: **An Automated Force Field Topology Builder (ATB) and Repository: Version 1.0**. *Journal of Chemical Theory and Computation* 2011, **7**(12):4026-4037.
30. Rarey M, Kramer B, Lengauer T, Klebe G: **A Fast Flexible Docking Method using an Incremental Construction Algorithm**. *Journal of Molecular Biology* 1996, **261**(3):470-489.

31. Bohm HJ: **The development of a simple empirical scoring function to estimate the binding constant for a protein-ligand complex of known three-dimensional structure**. *J Comput Aided Mol Des* 1994, **8**(3):243-256.

32. Schweins T, Geyer M, Scheffzek K, Warshel A, Kalbitzer HR, Wittinghofer A: **Substrate-assisted catalysis as a mechanism for GTP hydrolysis of p21ras and other GTP-binding proteins**. *Nature Struct Biol* 1995, **2**(1):36 - 44.

33. Cheng H, Sukal S, Callender R, Leyh TS: **γ-Phosphate Protonation and pH-dependent Unfolding of the Ras·GTP·Mg2+ Complex: A VIBRATIONAL SPECTROSCOPY STUDY**. *Journal of Biological Chemistry* 2001, **276**(13):9931-9935.

34. Joppe K, Roser A-E, Maass F, Lingor P: **The Contribution of Iron to Protein Aggregation Disorders in the Central Nervous System**. *Front Neurosci* 2019, **13**:15-15.

35. Vasconcellos LRC, Dutra FF, Siqueira MS, Paula-Neto HA, Dahan J, Kiarely E, Carneiro LAM, Bozza MT, Travassos LH: **Protein aggregation as a cellular response to oxidative stress induced by heme and iron**. *Proceedings of the National Academy of Sciences* 2016, **113**(47):E7474-E7482.

36. Ross CA, Poirier MA: **Protein aggregation and neurodegenerative disease**. *Nature medicine* 2004, **10 Suppl**:S10-17.

37. Downing KH, Nogales E: **Tubulin structure: insights into microtubule properties and functions**. *Current opinion in structural biology* 1998, **8**(6):785-791.

38. Nogales E, Wolf SG, Downing KH: **Structure of the alpha beta tubulin dimer by electron crystallography**. *Nature* 1998, **391**(6663):199-203.

39. Eklund G, Lang S, Glindre J, Ehlen A, Alvarado Kristensson M: **The nuclear localization of γ-tubulin is regulated by SadB-mediated phosphorylation**. *Journal of Biological Chemistry* 2014.

40. Leask A, Stearns T: **Expression of Amino- and Carboxyl-terminal γ- and α-Tubulin Mutants in Cultured Epithelial Cells**. *Journal of Biological Chemistry* 1998, **273**(5):2661-2668.

41. Stein SAM, Loccisano AE, Firestine SM, Evanseck JD: **Chapter 13 Principal Components Analysis: A Review of its Application on Molecular Dynamics Data**. In: *Annual Reports in Computational Chemistry.* Edited by Spellmeyer DC, vol. 2: Elsevier; 2006: 233-261.

42. Prathamesh M. Shenai ZXaYZ: **Applications of Principal Component**

Analysis (PCA) in Materials Science. 2012.

43. David CC, Jacobs DJ: **Principal component analysis: a method for determining the essential dynamics of proteins**. *Methods in molecular biology (Clifton, NJ)* 2014, **1084**:193-226.

44. Grant BJ, Rodrigues AP, ElSawy KM, McCammon JA, Caves LS: **Bio3d: an R package for the comparative analysis of protein structures**. *Bioinformatics (Oxford, England)* 2006, **22**(21):2695-2696.

45. Skjaerven L, Jariwala S, Yao XQ, Grant BJ: **Online interactive analysis of protein structure ensembles with Bio3D-web**. *Bioinformatics (Oxford, England)* 2016, **32**(22):3510-3512.

46. Hess B, Kutzner C, van der Spoel D, Lindahl E: **GROMACS 4: Algorithms for Highly Efficient, Load-Balanced, and Scalable Molecular Simulation**. *Journal of Chemical Theory and Computation* 2008, **4**(3):435-447.

47. Nogales E, Wang HW: **Structural mechanisms underlying nucleotide-dependent self-assembly of tubulin and its relatives**. *Current opinion in structural biology* 2006, **16**(2):221-229.

48. Brouhard GJ, Rice LM: **Microtubule dynamics: an interplay of biochemistry and mechanics**. *Nature Reviews Molecular Cell Biology* 2018, **19**(7):451-463.

49. Lassila JK, Zalatan JG, Herschlag D: **Biological phosphoryl-transfer reactions: understanding mechanism and catalysis**. *Annual review of biochemistry* 2011, **80**:669-702.

50. Carvalho ATP, Szeler K, Vavitsas K, Åqvist J, Kamerlin SCL: **Modeling the mechanisms of biological GTP hydrolysis**. *Archives of Biochemistry and Biophysics* 2015, **582**:80-90.

51. Pai EF, Krengel U, Petsko GA, Goody RS, Kabsch W, Wittinghofer A: **Refined crystal structure of the triphosphate conformation of H-ras p21 at 1.35 A resolution: implications for the mechanism of GTP hydrolysis**. *The EMBO journal* 1990, **9**(8):2351-2359.

52. Menendez M, Rivas G, Diaz JF, Andreu JM: **Control of the structural stability of the tubulin dimer by one high affinity bound magnesium ion at nucleotide N-site**. *The Journal of biological chemistry* 1998, **273**(1):167-176.

53. Correia JJ, Beth AH, Williams RC: **Tubulin exchanges divalent cations at both guanine nucleotide-binding sites**. *Journal of Biological Chemistry* 1988, **263**(22):10681-10686.

54. Codaccioni F, Dell'Amico M, Bourdeaux M, Briand C, Lux B: **Influence of the guanine nucleotide phosphorylation state and of Mg2+ ions on the interaction of vinzolidine/tubulin 6 S: A fluorescence quenching study**. *Archives of Biochemistry and Biophysics* 1988, **267**(1):236-244.

3.6 Appendix

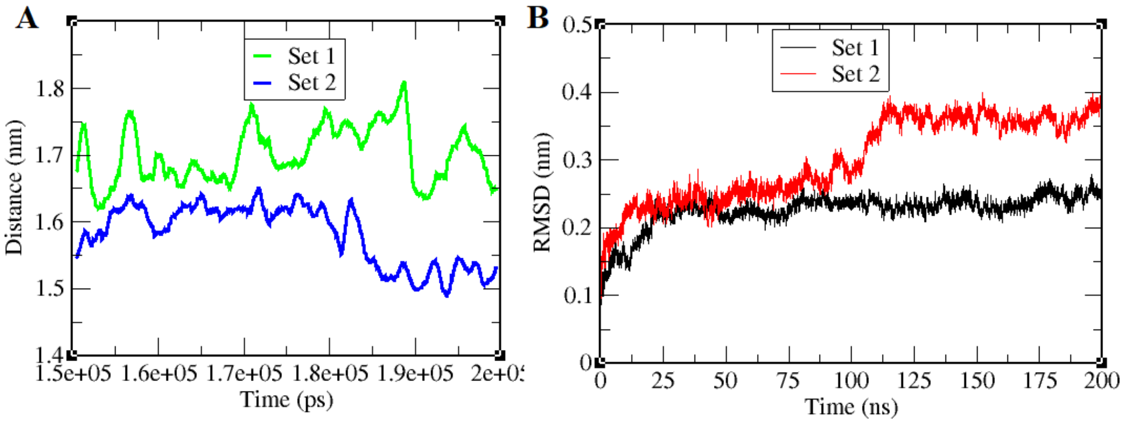

Figure A1: (A) The dCOM between H7 and S6 from 150 ns to 200 ns for unliganded monomer in $MgCl_2$. **(B)** The RMSD of 200 ns of simulations of unliganded $MgCl_2$ simulations.

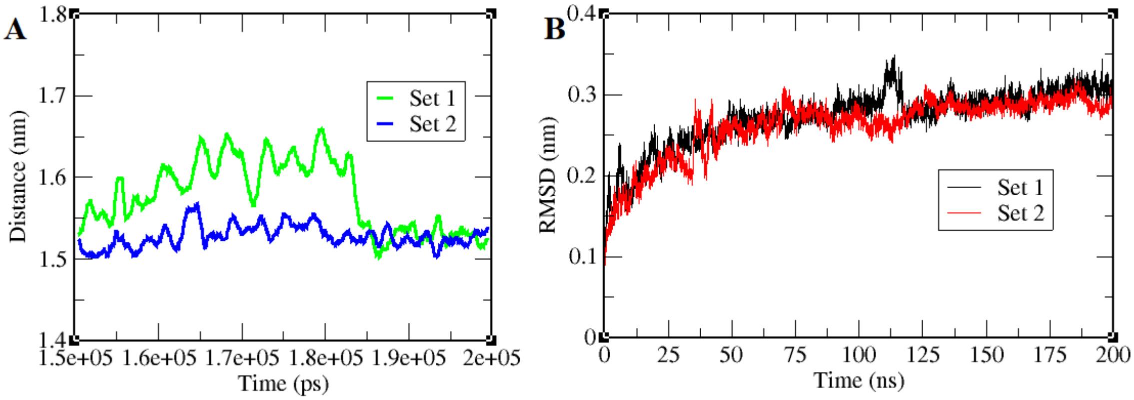

Figure A2: (A) The dCOM of H7 and S6 from 150 ns to 200 ns for unliganded monomer in $ZnCl_2$ simulations. **(B)** The RMSD of 200 ns of simulations of both sets of unliganded $ZnCl_2$.

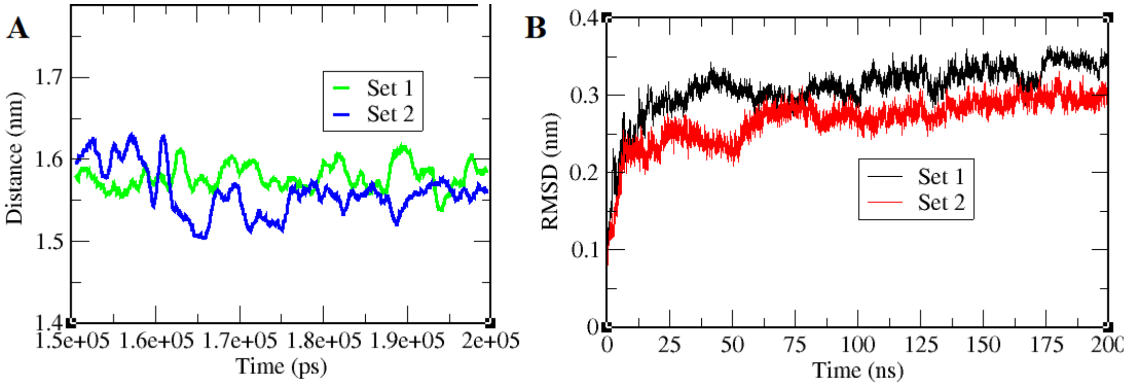

Figure A3: The dCOM of H7 and S6 from150 ns to 200 ns for unliganded monomer in NaCl simulations. **(B)** The RMSD of 200 ns of simulations of both sets of unliganded NaCl.

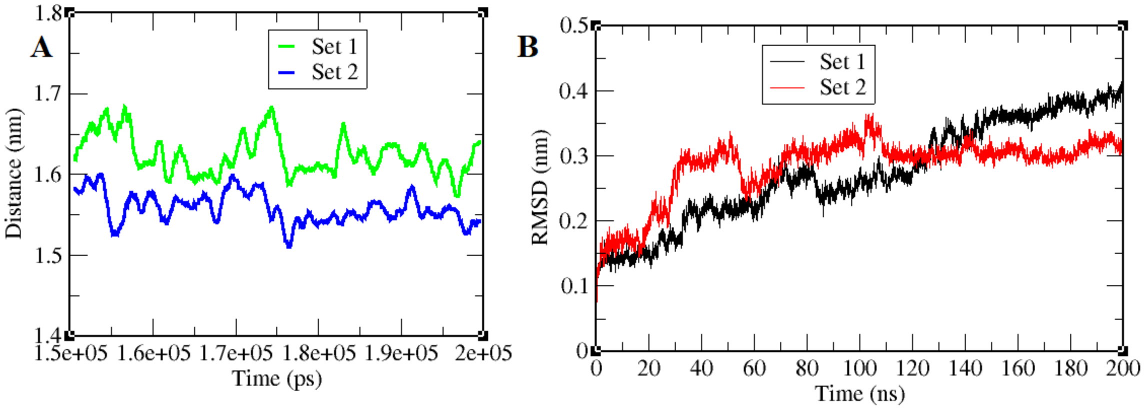

Figure A4: (A) The dCOM between H7 from S6 from 150 ns to 200 ns for GTP-liganded monomer in $MgCl_2$. **(B)** The RMSD of 200 ns of simulations of both sets of liganded $MgCl_2$.

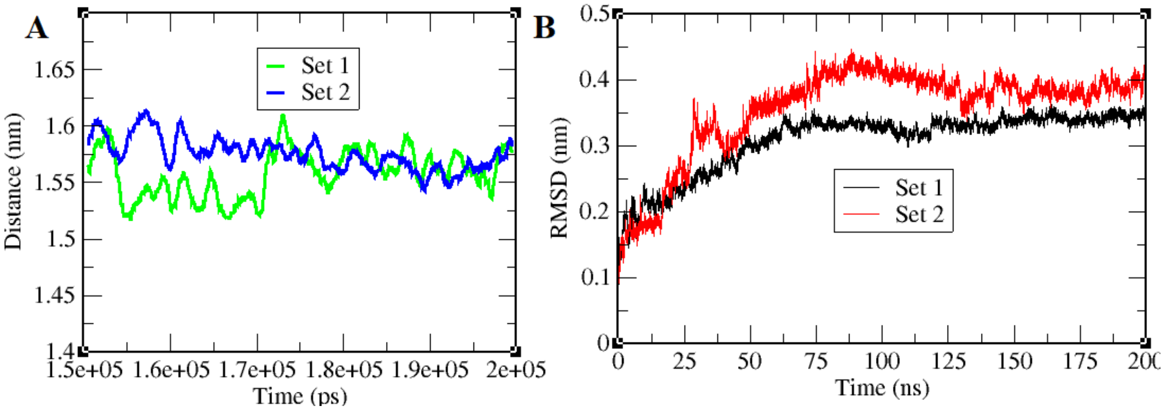

Figure A5: (A) The dCOM of H7 and S6 from 150 ns to 200 ns for GTP-liganded monomer in $ZnCl_2$. **(B)** The RMSD of 200 ns of simulations of both sets of liganded $ZnCl_2$.

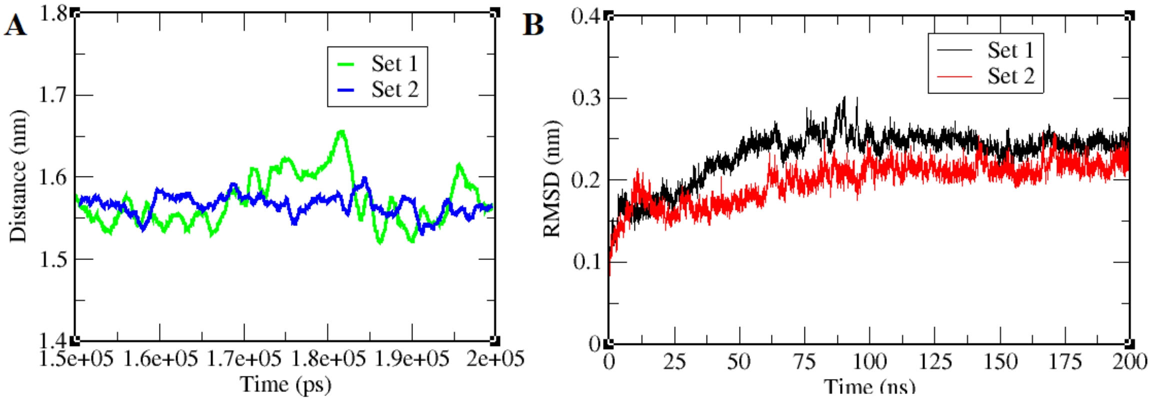

Figure A6 (A) The dCOM of H7 and S6 from 150 ns to 200 ns for GTP-liganded monomer in NaCl. **(B)** The RMSD of 200 ns of simulations of both sets of liganded NaCl.

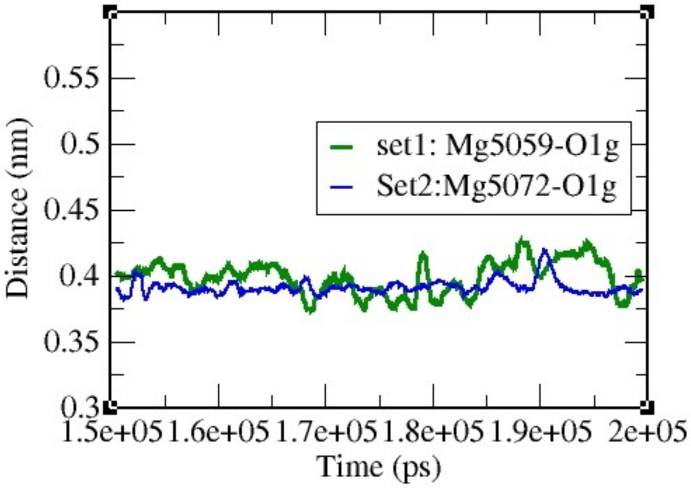

Figure A7: The min distances between Mg^{+2} and O1g atom of GTP colored in green in set 1, and Mg^{+2} with respect to O1g colored in blue in set 2 for GTP-liganded monomer.

.

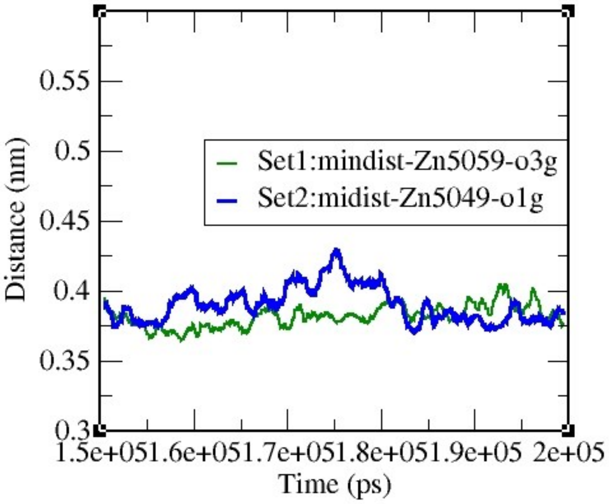

Figure A8: The min distances between Zn^{+2} and O3g atom of GTP with set 1 colored in green, and Zn^{+2} with respect to O1g colored in blue in set 2 for GTP-liganded monomer.

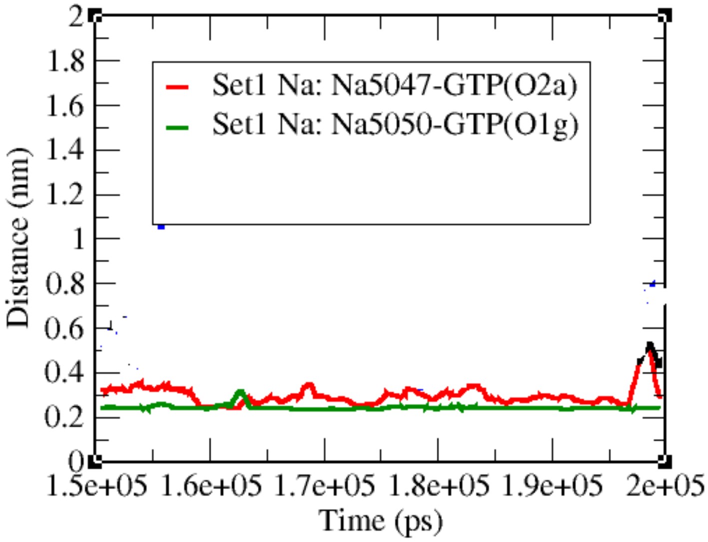

Figure A9: The distances between Na^+ and O2a atom of GTP with set 1 colored in red, and Na^+ with respect to O1g colored in green in set 2 for GTP-liganded monomer.

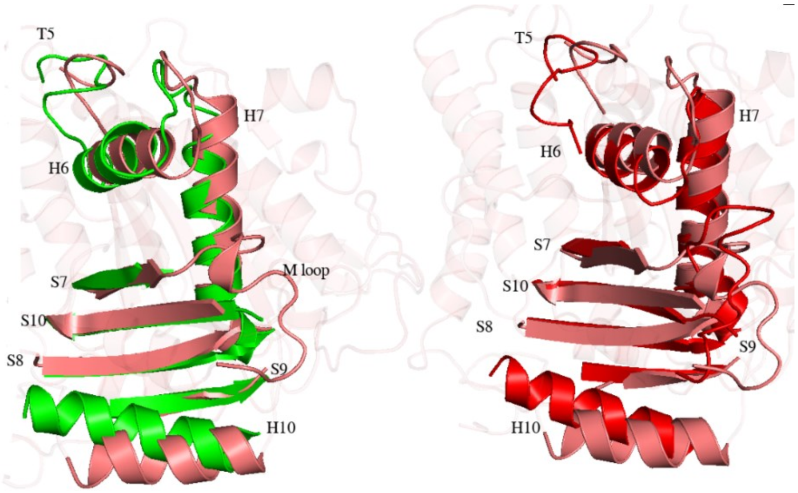

Figure A10: The conformation of unliganded γ-tubulin monomer at 173 ns superimposed on curved (1SA0) and straight (1JFF) conformation of β-tubulin. The Straight and curved β-tubulin colored in red and green and γ-tubulin in pink.

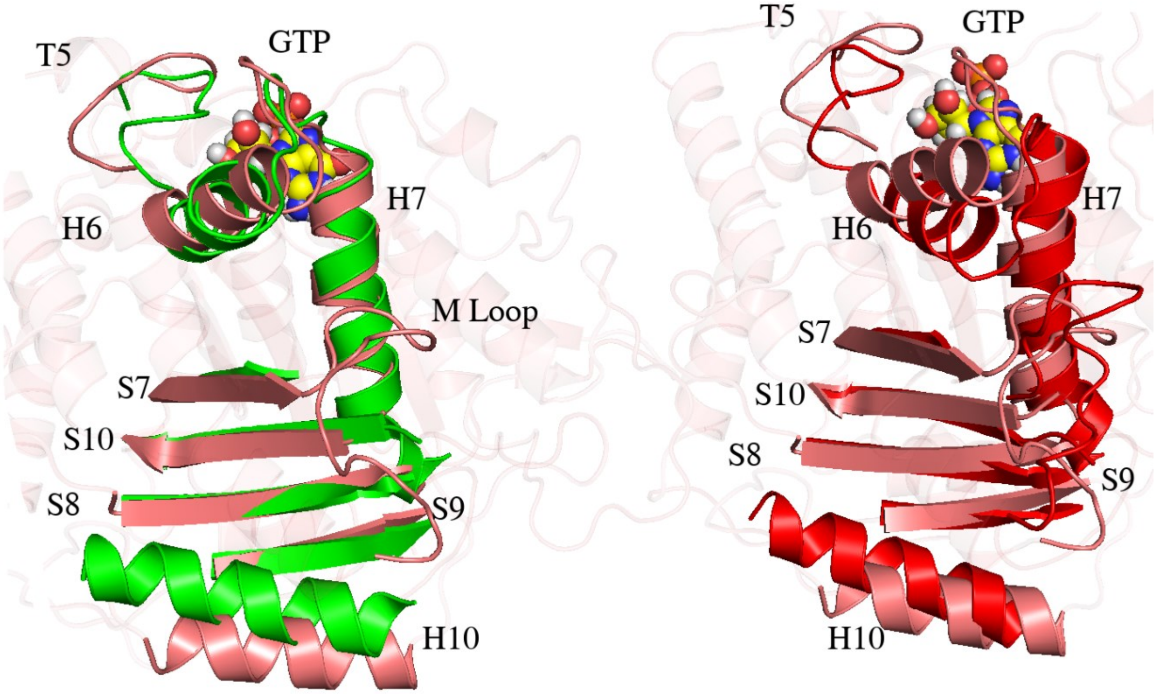

Figure A11: The conformation of set1 of GTP liganded monomer of $ZnCl_2$ at 170 ns superimposed on curved (1SA0) and straight (1JFF) conformation of β-tubulin. The Straight and curved β-tubulin colored in red and green and γ-tubulin in pink.

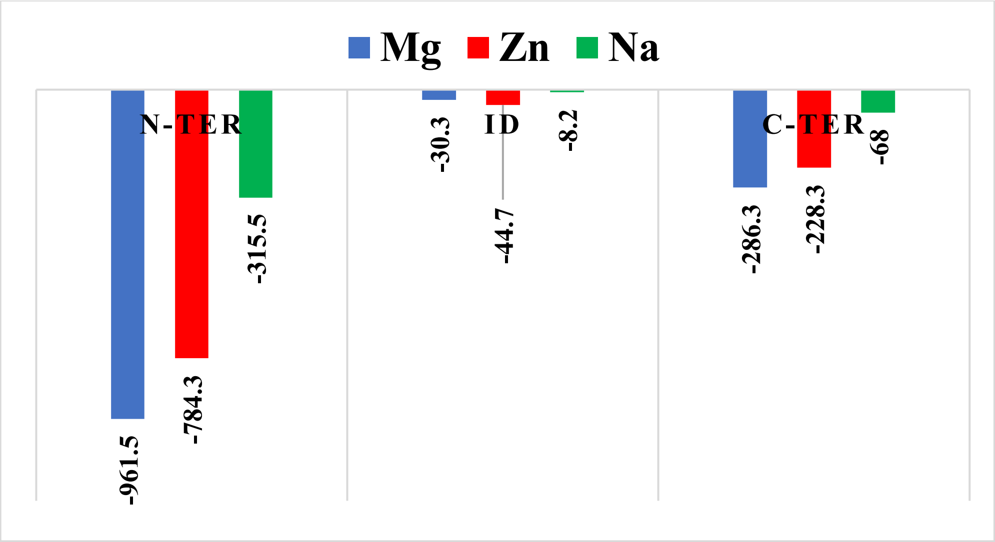

Figure A12: The electrostatic energy between cations and each domain of the γ-tubulin in set 1 of unliganded monomer simulations. The interaction energy between Mg^{2+} and protein coloured in blue, between Zn^{2+} and protein in orange and black for Na^{+} simulation.

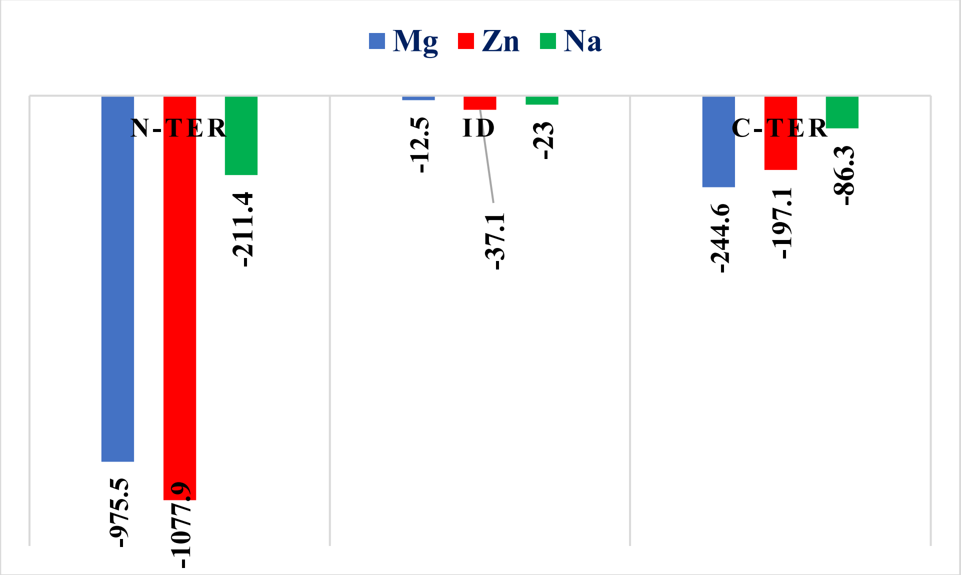

Figure A13: The electrostatic energy between set 1 of GTP liganded monomer and cations for each domain of the γ-tubulin. The interaction energy between Mg^{+2} and protein coloured in blue, between Zn^{+2} and protein in orange and black for Na^{+} simulation.

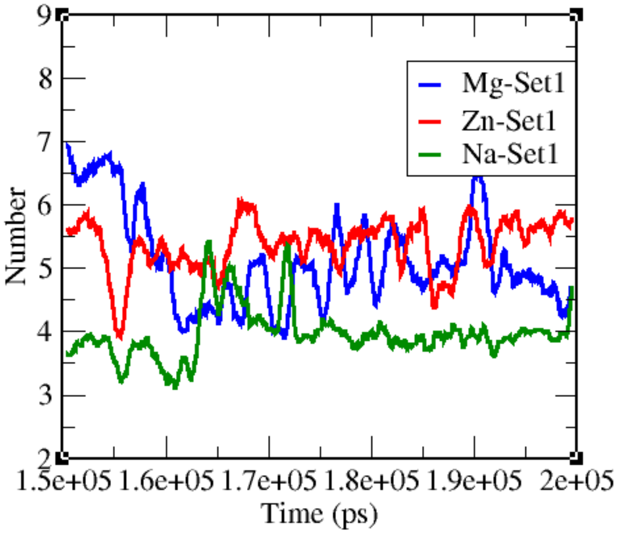

Figure A14: The number of H-bond between the oxygen atoms of γ phosphate (O1g, O2g, and O3g of GTP) and GTP binding site of γ-tubulin. Number of H-bond in set 1 of GTP-monomer simulation. The cut-off for both is set to 4 Å. Colored in blue, with $ZnCl_2$ represented in red and green in NaCl simulation.

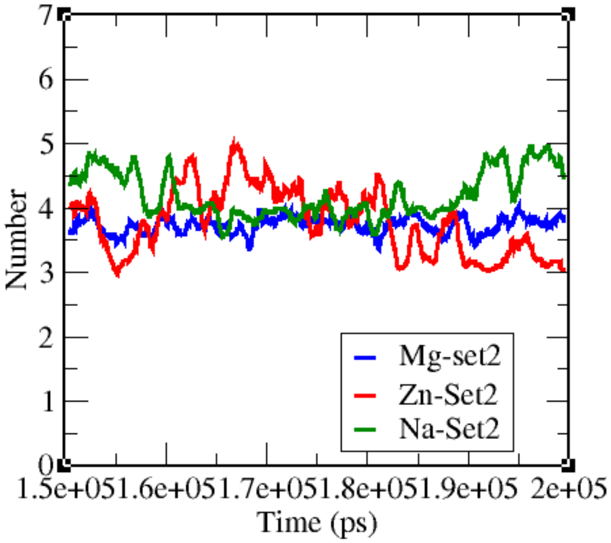

Figure A15: The number of H-bond between the oxygen atoms of γ phosphate (O1g, O2g, and O3g of GTP) and GTP binding site of γ-tubulin. Number of H-bond in set 2 of GTP-monomer simulation. The cut-off for both is set to 4 Å. Colored in blue, with $ZnCl_2$ represented in red and green in NaCl simulation.

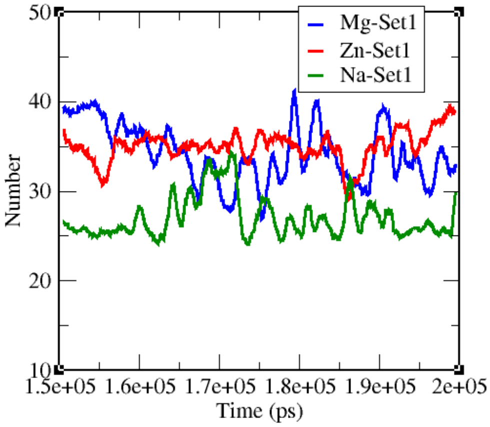

Figure A16: The number of interactions between the oxygen atoms of γ phosphate (O1g, O2g, and O3g of GTP) and GTP binding site of γ-tubulin. Number of H-bond in set 1 of GTP-monomer simulation. The cut-off for both is set to 4 Å. Colored in blue, with $ZnCl_2$ represented in red and green in NaCl simulation.

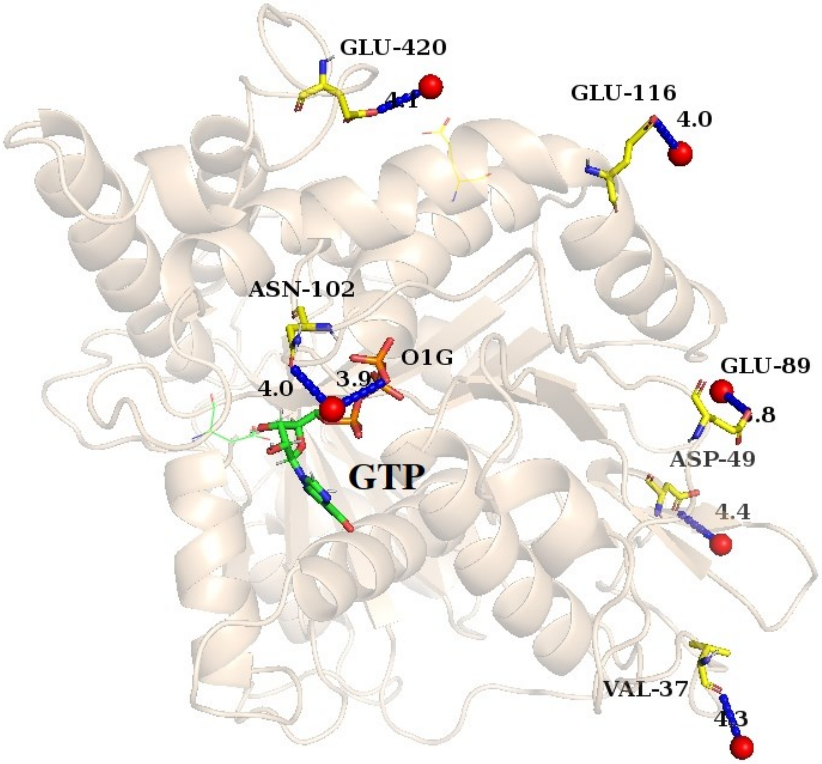

Figure A17: The conformation of set 1 of γ-tubulin at 200 ns with interacting Zn^{+2} at ≤ 4.5 Å. Zn^{+2} is colored in sphere red and interacting residues in a stick. The GTP in stick representation with its interacting Zn to O1g.

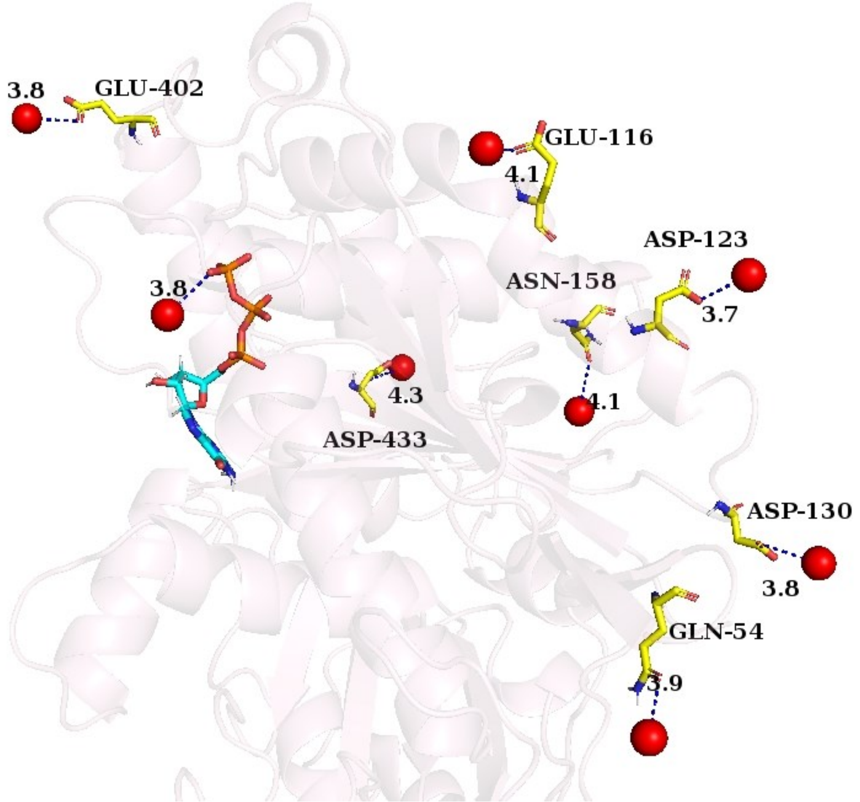

Figure A18: The conformation of set 1 of γ-tubulin at 200 ns with interacting Mg^{+2} at ≤ 4.5 Å. Mg^{+2} is colored in sphere red and interacting residues in a stick. The GTP in stick representation with its interacting Mg to O1g.